

**Deformation and Annealing of Quartz and Feldspar in the Lower Crust:
a detailed microstructural investigation of polyphase rocks from the
Highland Complex, Sri Lanka**

Inaugural-Dissertation
zur
Erlangung des Doktorgrades
der Mathematisch-Naturwissenschaftlichen Fakultät
der Universität zu Köln

vorgelegt von
Marina Kemperle
aus Düsseldorf

Berichterstatter: Prof. Dr. Reiner Kleinschrodt
(Gutachter) Prof. Dr. Sandro Jahn

Tag der letzten mündlichen Prüfung: 16. August 2021

Zusammenfassung

Die vorliegende Arbeit präsentiert eine detaillierte mikrostrukturelle Untersuchung von deformierten und statisch getemperten Quarz-Feldspat-Gesteinen des Highland Complex, Sri Lanka. Deformation und statische Temperung erfolgten unter trockenen granulitfaziellen Bedingungen der unteren Kruste bei Minimum-Deformationstemperaturen von $\sim 770\text{--}830\text{ }^{\circ}\text{C}$.

Mikrostrukturen zeigen, dass Deformation von Quarz und Feldspat maßgeblich mittels Versetzungskriechen und dynamischer Rekristallisation durch Korngrenzwanderung erfolgte. EBSD-basierte Analysen einer vollständigen Sequenz von quarz-armen hin zu quarz-reichen Domänen zeigen, dass Quarz im Zuge der dynamischen Korngrenzwanderung selektiv vergrößerte begünstigt durch eine vorteilhafte Orientierung für die Aktivität von Prismen $\langle c \rangle$, Basis $\langle a \rangle$ und Rhomben $\langle a \rangle$ Gleitsystemen. In Alkali-Feldspat und Plagioklas dominierten Gleitsysteme mit (010) als Hauptgleitebene in verschiedenen Gleitrichtungen. In Alkali-Feldspat führte die Beteiligung multipler Gleitsysteme zu einer moderaten kristallographischen Vorzugsregelung (CPO). In Plagioklas war zudem das Gleitsystem (021)[1-12] beteiligt, welches vermutlich in Körnern in ungünstiger Orientierung für (010)-Gleiten in Sprödbrüchen initiiert wurde. Kompositionell bedingte Unterschiede im Deformationsverhalten von Plagioklas werden deutlich in einer verstärkten CPO und dem Zurücktreten des (021)[1-12] Gleitsystems in Anorthit-armen Plagioklasen, welches auf eine geringere Festigkeit von letzteren deutet. Die Analyse von Korngrößen und Kornformen in Domänen mit unterschiedlichem Modalbestand von Quarz, Alkali-Feldspat und Plagioklas zeigen, dass Deformationsmechanismen von der Konnektivität abhängen. Bei mangelnder Konnektivität dominiert diffusions-begünstigte Phasengrenzwanderung, welche sanft gekrümmte Phasengrenzen und schwache CPOs hervorruft. Mit zunehmender Konnektivität dominiert Korngrenzwanderung. Für Quarz in quarz-armen Domänen werden Konnektivität und assoziierte Mikrostrukturen vom Modalbestand kontrolliert. In quarz-reichen Domänen bestimmt der Anteil und die Verteilung der Sekundärphase Feldspat die mikrostrukturelle Entwicklung. In Domänen mit dem höchsten Quarz-Gehalt ($>\sim 80\text{ Vol.-%}$) und geringer Feldspat-Streuung werden Mikrostrukturen maßgeblich von dynamischer Rekristallisation gesteuert.

Deformations-Mikrostrukturen von Quarz und den beiden Feldspäten wurden durch statische Temperung modifiziert. Das betrifft Subkorn Grenzen und damit assoziierte Misorientierungen und Gleitsysteme. Zudem wurden Korngrenzen equilibriert, indem die

Krümmung reduziert und 120° Öffnungswinkel zwischen drei Körnern erstellt wurden. Plagioklase in reinen Domänen wurden dabei am stärksten equilibriert. In Alkali-Feldspäten wurde das Equilibrieren durch Entmischungen und Plagioklas-Filmen entlang von Korngrenzen teilweise unterdrückt. In Quarz führte vermutlich eine kristallographisch-bedingte Stabilisierung von Korngrenzen zur Erhaltung einer hohen Krümmung der Korngrenzen, wohingegen ausreichend 120° Öffnungswinkel Equilibrierung andeuten. CPOs von Quarz, Alkali-Feldspat und Plagioklas blieben weitestgehend erhalten.

Abstract

This study deals with deformation and annealing microstructures of quartz and feldspar in lower crustal rocks of the Highland Complex, Sri Lanka. Deformation occurred under dry granulite facies conditions at minimum temperatures of ~770–830 °C.

Microstructures show that quartz, alkali feldspar and plagioclase deformed dominantly by dislocation creep accommodated by dynamic grain boundary migration (GBM) recrystallization. EBSD-based analyses of a complete sequence of quartz-poor to quartz-rich domains show that, during GBM recrystallization, quartz in suitable orientation for combined prism[c], basal<a> and rhomb<a> slip underwent selective coarsening. In feldspars, intracrystalline slip was dominantly achieved on the (010) plane in various slip directions. In alkali feldspar, activity of multiple slip systems resulted in moderate crystallographic preferred orientations (CPO). In plagioclase, further (021)[1-12] slip was active, probably initiated by fracturing of grains in unsuitable orientation for slip on (010). Furthermore, strong CPOs and minor (021)[1-12] slip in Anorthite (An)-poor plagioclase point to a compositional dependence of strength with An-poor plagioclase being weaker than An-rich plagioclase.

Analysis of grain size and shape in domains with differing modal content of quartz, alkali feldspar and plagioclase show that deformation mechanisms depend on the connectivity. At weak connectivity diffusion-assisted phase boundary migration is dominant causing smoothly curved phase boundaries and weak CPOs. With increasing connectivity GBM recrystallization becomes dominant. For quartz in quartz-poor domains connectivity and microstructural evolution depend on the modal content. In quartz-rich domains microstructures are controlled by feldspar second phase content and distribution. In domains with highest quartz content (>~80 Vol.-%) and low feldspar dispersion, microstructures are controlled by dynamic recrystallization.

Deformation microstructures of quartz and feldspars were partly modified during annealing. This concerns subgrain boundaries and associated misorientations and slip systems. Grain boundaries between same phases were equilibrated by the reduction of curvature and establishment of 120° dihedral angles. In plagioclase of pure domains, grain boundaries are most equilibrated. Alkali feldspar equilibration was hampered by exsolutions and plagioclase films along grain boundaries. In quartz, crystallographically stabilized grain boundaries probably inhibited reduction of curvature while abundant 120° dihedral angles infer equilibration. CPOs of quartz, alkali feldspar and plagioclase are largely preserved.

Acknowledgment

I received much support during my doctoral studies which helped me to accomplish this work. I am thankful to Reiner Kleinschrodt who accompanied me through this time and always had an open ear for my ideas and need for discussions. I am grateful to Jolien Linckens who helped to supervise this project. Her thorough reviews significantly improved this work. She also provided image files of *test quartz*. Sören Tholen is acknowledged for helpful discussions and further support during EBSD measurements and data processing. Moreover, Sören prepared thin sections for the review of sample and device coordinate systems during EBSD measurements. Nathalie Thor also deserves acknowledgement because she professionally accompanied me during the early stages of my PhD studies in the course of her own master thesis. Ruth Keppler and Jacek Kossak are thanked for conducting Neutron Diffraction Texture analytical measurements on my samples. The results were not included in this work, but significantly helped to interpret EBSD-based texture data. I am grateful to Hanna Cieszynski who was anytime available for support during the Secondary Electron Microscope usage. Kathrin Jung is thanked for sample preparation.

I would like to offer very special thanks to my family and friends who gave me support and encouragement and witnessed all ups and downs which accompany doctoral studies. Special mention deserve Stephanie Grad, Jennifer Janssen-Džanić, Lena Firiss, Jennifer Jabilonski, Leonard Pleschberger, Sabrina Klaes, Magret Damaschke, Nadine Günther, Swea Klipsch, Sarah Esteban-Lopez, Niklas Leicher and Jens Barosch.

This work was supported by a doctoral scholarship of the Bischöfliche Studienförderung Cusanuswerk. I am immensely grateful for this support which enabled me to place all my focus on this work. Furthermore, I received several travel grants from the Graduate School of Geosciences of the University of Cologne which enabled me to participate in numerous conferences and training courses outside the University of Cologne. In this context, I would also like to thank Karin Boessenkool, the head of the Graduate School, who always provided support and advice during my entire doctoral studies.

This work is dedicated to my grandfather Tomislav Kemperle who encouraged me to embark on an academic path.

Table of Contents

1. Introduction	1
1.1. General Introduction	1
1.2. Deformation of Quartz and Feldspar in the Lower Crust	2
1.3. Analyzing Microstructures	4
1.4. Set-Up of this Study	8
2. Geological Background	10
2.1. Metamorphic Basement	10
2.2. Geotectonic Evolution	12
2.3. Deformation History	13
2.4. Sample Collection Site	17
3. Sample Description	19
3.1 Classification and Description of Domains	20
3.2 Microstructures	22
3.2.1 Quartz	22
3.1.2 Feldspar	24
3.1.3 Quartz-Feldspar Boundaries	27
4. Methods	28
4.1. Sample Preparation and Microscopic Examination	28
4.2. Thermometry	28
4.2.1. Two-Feldspar Thermometry	28
4.2.1.1. Thermometric Expression and Correction for Slowly Cooled Rocks	28
4.2.1.2. Reintegration of Exsolved Feldspars and Measuring Conditions	31
4.2.2. TitaniQ Thermometry	32
4.3. Electron Backscatter Diffraction (EBSD) Analysis	34
4.3.1. Principles	34
4.3.2. Measuring Conditions	35
4.3.3. Data Collection and Processing	36
4.3.4. Misorientation Analysis	39
4.4. Analysis of Modal Content, Grain Size, Shape and Connectivity	41
4.4.1. Quantified Parameters	41
4.4.2. Zener Parameter	45
4.5. Curvature and Dihedral Angle Analysis	46
5. Thermometry	48
5.1. Results	49
5.1.1. Two-Feldspar Thermometry	49
5.1.2. TitaniQ Thermometry	53

5.2. Discussion	54
5.2.1. Two-Feldspar Thermometry	54
5.2.2. TitaniQ Thermometry	56
5.2.3. Comparison of Temperatures	57
6. EBSD Analysis	59
6.1. Results	59
6.1.1. Quartz	59
6.1.2. Feldspar	73
6.1.2.1. CPO	73
6.1.2.2. Misorientation Analysis	76
6.1.2.3. Boundary Trace Analysis	81
6.2. Discussion	85
6.2.1. Quartz	85
6.2.2. Feldspar	94
7. Modal Content, Grain Size, Shape and Connectivity	102
7.1. Results	102
7.1.1. Quartz	102
7.1.2. Feldspar	111
7.2. Discussion	121
7.2.1. Challenges in Analysing Grain Size, Shape and Connectivity	121
7.2.2. Quartz	121
7.2.3. Feldspar	129
8. Curvature and Dihedral Angle Analysis	133
8.1. Results	134
8.1.1. Equilibrated and Deformed Quartz	134
8.1.2. Sri Lanka Samples	135
8.2. Discussion	142
9. Summary and Conclusion	149
10. Outlook	154
References	155
Appendix	I

1. Introduction

1.1. General Introduction

Quartz and feldspar are the most abundant minerals in the Earth's crust and their mechanical properties are commonly used to model the rheology of large parts of the ductile crust (e.g., Bürgmann and Dresen, 2008; Ranalli, 2000). Therefore, the deformation behaviour of quartz and feldspar was subject to numerous studies in experiments (e.g., Gleason et al., 1993; Hirth and Tullis, 1992; Muto et al., 2011; Stünitz et al., 2003; Tullis and Yund, 1991, 1992; Willaime et al., 1979) and in natural samples (e.g., Ceccato et al., 2017; Hippertt et al., 2001; Menegon et al., 2013; Rosenberg and Stünitz, 2003; Svahnberg and Piazzolo, 2010; Stipp et al., 2002b). However, deformation of quartz and feldspar is not yet fully elucidated, especially not under lower crustal conditions of amphibolite and granulite facies. For one reason, this is due to limitations in experiments to simulate natural conditions. Furthermore, in natural samples deformation fabrics and microstructures developed under lower crustal conditions are often overprinted by annealing or later deformation events in the upper crust. A further constraint on experimental studies is that most experiments investigate monomineralic aggregates (e.g., Blacic, 1975; Griggs and Bell, 1938; Tullis and Yund, 1991; Willaime et al., 1979) and only few consider polymineralic aggregates (e.g., Cross et al., 2017; Dell'Angelo and Tullis, 1986). However, most natural rocks are polymineralic and display complex strain partitioning processes (e.g., Handy, 1994; Hunter et al., 2019; Martelat et al., 1999). Second phases may exert a pinning effect on major matrix phases thereby governing grain sizes which in turn control deformation mechanisms (e.g., Herwegh and Berger, 2004; Linckens et al., 2011; Passchier and Trouw, 2005). Second phases also influence the microstructural evolution during static recrystallization and annealing (e.g., Brodhag et al., 2011; Herwegh et al., 2008).

The aim of this study is to investigate deformation and annealing microstructures of quartz and feldspar and their interrelationships to contribute to a better understanding of microstructural evolution in the lower crust. For this purpose, a detailed microstructural analysis combined with geothermometry was performed on quartzofeldspathic granulites from Sri Lanka. The investigated samples are particularly suitable for this effort for several reasons. The samples constitute mainly of quartz and two feldspars, plagioclase and alkali feldspar, and provide a continuous sequence of feldspar rich to quartz rich domains deformed and annealed under same extrinsic conditions. This enables the investigation of microstructural development within polymineralic and nearly pure aggregates. Deformation and annealing microstructures in the Sri Lankan samples developed under dry granulite facies conditions and are preserved during exhumation (e.g., Voll and Kleinschrodt, 1991; Voll et al., 1994). Microstructures are indicative for dynamic grain boundary migration recrystallization of both, quartz and feldspar, and display extensive coarsening of quartz with increasing quartz content. Natural samples with comparable microstructures evolved under similar conditions are scarce, especially of plagioclase and alkali feldspar (e.g., Egydio-Silva et al., 2002; Gower and Simpson, 1992; Hippertt et al., 2001; Martelat et al., 1999). Therefore, the study of Sri Lankan samples offers a valuable completion to the poor record of quartz and feldspar deformation and annealing in the lower crust. Furthermore, the sequence from feldspar to quartz rich domains facilitates the attempt to decipher between deformation and annealing. This is possible because deformation and annealing microstructures vary in degree between individual domains.

1.2. Deformation of Quartz and Feldspar in the Lower Crust

In the lower crust, quartz is reported to deform by dislocation creep accommodated by grain boundary migration (GBM) recrystallization (e.g., Cavalcante et al., 2018; Little et

al., 2013; Neumann, 2000; Stipp et al., 2002b). Common microstructures are lobate to amoeboid grain boundaries, pinning microstructures, left-over grains, and dissection microstructures (Fig. 1a, c-e) (e.g., Jessel, 1987; Stipp et al., 200b; Urai et al., 1986). At high temperatures, fast recrystallization and recovery cause most grains to have a strain free appearance (e.g., Passchier and Trouw, 2005). However, square subgrains forming chessboard extinction patterns are restricted to high grade conditions and may result from combined basal and prism slip or due to the α - β transition in quartz (e.g., Kruhl, 1996; Mainprice et al., 1986). In polyphase rocks, where growth is restricted, quartz forms elongated ribbons with straight grain boundaries (e.g., Handy, 1994; Hippertt et al., 2001). At high temperatures ($\sim >500$ °C) prism $\{m\}$ $\langle a \rangle$ slip becomes important and above ~ 700 °C $\{m\}[c]$ slip is active (Fig. 2a, b) (e.g., Mainprice et al., 1986; Stipp et al., 2002b). Multiple active slip systems are also common in the GBM recrystallization regime (e.g., Kruhl, 1996; Little et al., 2013 Stipp et al., 2002b).

Feldspar deformation in the lower crust is frequently reported to occur by climb accommodated dislocation creep associated with subgrain rotation (SGR) recrystallization (e.g., Lapworth et al., 2002; Miranda et al., 2016; Svahnberg and Piazzolo,

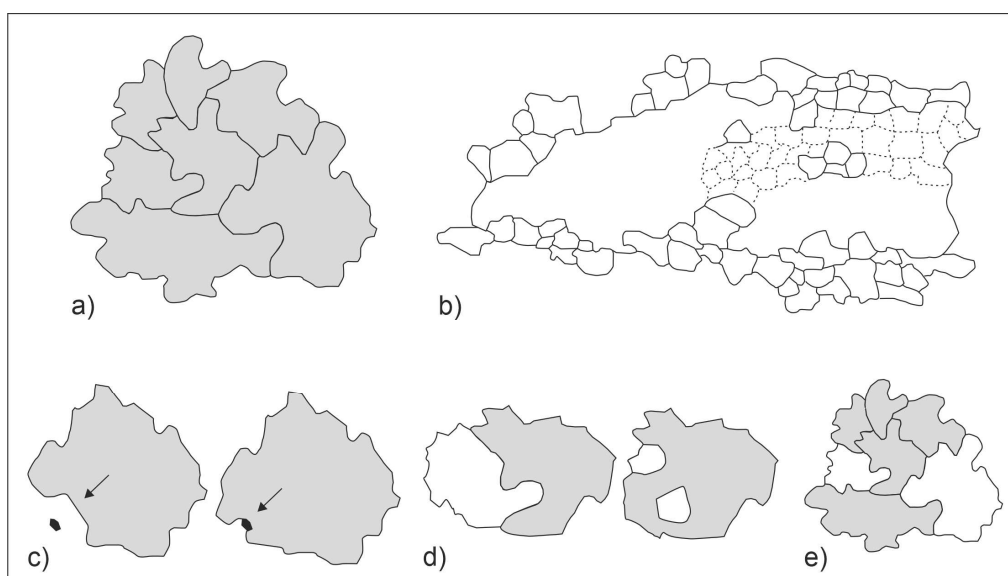


Fig. 1: Recrystallization microstructures: a) lobate to amoeboid grain boundaries due to GBM recrystallization; b) SGR recrystallization microstructures (stippled lines are subgrain boundaries); c) pinning of a migrating grain boundary (arrow) by an obstacle (black); d) left-over grains (white grains); e) dissection microstructure (white grains).

2010). Resulting microstructures are elongated old grains with abundant subgrains and recrystallized slightly elongated grains of similar size as subgrains (Fig. 1b) (e.g., Passchier and Trouw, 2005). A gradual transition from subgrain (low angle) to grain (high angle) boundaries is characteristic (e.g., Neumann, 2000; Passchier and Trouw, 2005). Associated grain size reduction promotes grain size sensitive deformation mechanisms as diffusion creep and grain boundary sliding (e.g., Menegon et al., 2013; Miranda et al., 2016; Svahnberg and Piazzolo, 2010). Recrystallization may be chemically driven resulting in decomposition of the host into coexisting alkali feldspar and plagioclase of new composition (e.g., Franek et al., 2011; Menegon et al., 2013). GBM recrystallization is only rarely reported at very high temperatures close to the solidus (~ 900 °C Lafrance et al., 1998; ~ 670 °C Rosenberg and Stünitz, 2003). Associated microstructures are similar to quartz. Smoothly curved and protruding phase boundaries between quartz and feldspars are attributed to diffusion assisted phase boundary migration (Gower and Simpson, 1992; Martelat et al., 1999; Menegon et al., 2013). Fracturing can occur even at temperatures as high as 700-900 °C and fractures can provide sites of dislocation generation (e.g., Menegon et al., 2013; Stünitz et al., 2003). At high temperatures several slip systems can be active in feldspars with slip on (010) in [001] and [100] being most frequently reported (e.g., Egidio-Silva et al., 2002; Miranda et al., 2016; Rosenberg and Stünitz, 2003; Schulmann et al., 1996; Stünitz et al., 2003; Svahnberg and Piazzolo, 2010).

1.3. Analyzing Microstructures

The determination of deformation and annealing requires the investigation of microstructures. Indicators for intracrystalline deformation are for instance undulose extinction, subgrain boundaries and a crystallographic preferred orientation (CPO) (e.g., Passchier and Trouw, 2005). The latter reflects active slip systems and gives information about deformation kinematics as strain and strain symmetry (Fig. 2) (e.g., Schmid and

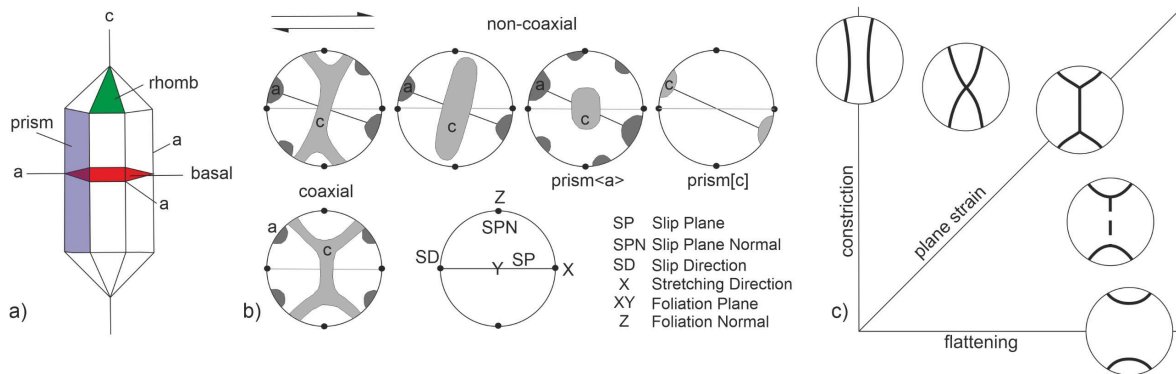


Fig. 2: Crystallographic preferred orientations (CPO), slip systems and deformation kinematics presented for quartz (redrawn after Passchier and Trouw, 2005): a) slip planes (basal, rhomb, prism) and directions (a, c); b) pole diagrams presenting contoured CPO patterns of c and a axes in a kinematic reference frame; note asymmetry in patterns in non-coaxial deformation; quartz CPOs for prism<a> and prism[c] are indicated; c) c-axis pattern in constriction, plane and flattening strain in coaxial deformation (Flinn diagram).

Casey, 1986). Multiple active slip systems and competing deformation mechanisms may impede a conclusive interpretation (e.g., Cavalcante et al., 2018; Menegon et al., 2013; Svahnberg and Piazzolo, 2010). The analysis of misorientations can shed further light on intragrain and intergrain processes during deformation (e.g., Kruse et al., 2001; Lloyd et al., 1997; Neumann, 2000; Prior et al., 2002; Wheeler, et al., 2001). Misorientation angle distributions give information about physical interaction of neighbouring grains or inheritance from a precursor microstructure (Wheeler et al., 2001). The combined analysis of misorientation angles and axes (axis-angle pairs) displays crystallographic relationships along grain (misorientation angle $>10^\circ$) and subgrain boundaries (misorientation angle $<10^\circ$) such as twinning and may allow the identification of contributing slip systems (Kruse et al., 2001; Lloyd et al., 1997; Lloyd, 2004). The latter is referred to as boundary trace analysis (Prior et al., 2002) and is based on a geometric relationship between misorientation axes associated with specific subgrain boundaries and the orientation of slip systems (Fig. 3) (e.g., Kruse et al., 2001; Lloyd, 2004; Neumann, 2000). Subgrain boundaries that are build up by edge dislocations are called tilt boundaries (Fig. 3a). Along tilt boundaries the trace of the boundary is perpendicular to the slip plane and the slip direction. The referring misorientation axis is aligned parallel

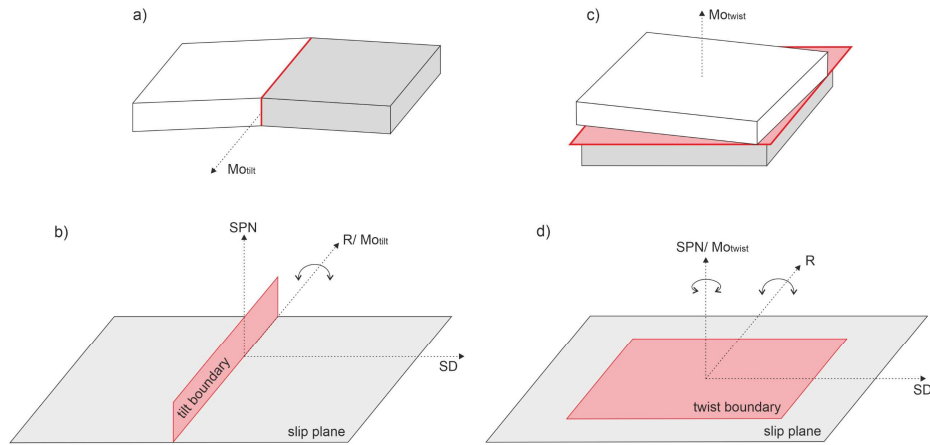


Fig. 3: Geometric relationship between misorientation axes of tilt (a, b) and twist (c, d) boundaries and slip systems (MO_{tilt} : tilt boundary misorientation axis, MO_{twist} : twist boundary misorientation axis, R: rotation axis, SPN: slip plane normal, SD: slip direction).

to a slip system specific rotation axis and is perpendicular to the slip plane normal and the slip direction (Fig. 3b). Twist boundaries constitute of screw dislocations (Fig. 3c). The trace of a twist boundary is parallel to the slip plane with the misorientation axis being parallel to the slip plane normal and perpendicular to the rotation axis and slip direction (Fig. 3 c, d).

Grain size distributions and grain shapes can help to identify recrystallization during dynamic and static conditions (e.g., Berger et al., 2011; Heilbronner and Tullis, 2002). For instance, dynamic recrystallization by strain induced GBM gives rise to interlobate and amoeboid grain boundaries (Fig. 4) and leads to synkinematic grain growth with broad grain size distributions (e.g., Platt and Behr, 2011; Stipp et al., 2002b, 2010; Urai et al., 1986). During static conditions (annealing) surface energy driven grain boundary migration (grain boundary area reduction) produces polygonal frameworks with straight grain boundaries and equilibrated dihedral angles of approximately 120° (Fig. 4) (e.g., Elliott et al., 1997; Evans et al., 2001; Passchier and Trouw, 2005). Furthermore, during static conditions abnormal or discontinuous grain growth may lead to bimodal grain size distributions due to selective growth of some large grains and/ or grains with a preferred orientation at the expense of small matrix grains (e.g., Evans et al., 2001; Stöckhert and



Fig. 4: Change of dynamic recrystallization microstructures during static recrystallization/ annealing (redrawn and modified after Passchier and Trouw, 2005): left: typical microstructure after dynamic grain boundary migration (GBM) recrystallization; during static recrystallization grains grow, grain boundaries become straight and equilibrated dihedral angles of approximately 120° develop.

Duyster, 1999). In the case of quartz, it could be shown that curved grain boundaries persist even after annealing, but that such grain boundaries consist of straight segments representing equilibrated grain boundary configurations (Kruhl and Peternell, 2002). Therefore, grain shape or curvature of a grain boundary is not necessarily representative to determine the degree of equilibration. Another approach to identify textural equilibrium is the measurement of apparent dihedral angles (e.g., Elliott et al., 1997; Riegger and Van Vlack, 1960). Moreover, in polyphase rocks diffusion assisted phase boundary migration causes curved phase boundaries between different minerals (Gower and Simpson, 1992). In such a case, grain shapes cannot be used to infer recrystallization mechanisms in the proper sense which refers to recrystallization within the same mineral (e.g., Urai et al., 1986). Therefore, in polyphase rocks, the state of grain boundaries between minerals of the same phase (like-like boundaries) constitutes a useful supplement for deciphering between deformation and annealing microstructures.

In polyphase rocks the effect of second phases on microstructural evolution can be evaluated using the Zener parameter (e.g., Brodhag et al., 2011; Herwegh and Berger, 2004; Herwegh et al., 2008; Hunter et al., 2016; Linckens et al. 2011). The Zener parameter Z is defined as the ratio of the mean second phase grain size d_p and volume

fraction f_p (Herwegh and Berger, 2004). The evolution of a matrix grain size (D) with Z is illustrated in a Zener plot (Fig. 5). A small value of Z is characterized by a high second phase fraction which exerts a pinning effect on the matrix phase resulting in a small mean matrix grain size. For deformed rock aggregates, a second-phase controlled microstructure will develop (blue shaded in Fig. 5) (Herwegh and Berger, 2004). With increasing Z and decreasing second phase content, the interparticle spacing between second phases reduces and so does the pinning effect. During deformation, a recrystallization-controlled microstructure evolves which is marked by a change in slope

in the Zener plot (blue trend in Fig. 5). The matrix grain size does no longer increase with Z as a steady-state grain size is achieved which results from a balance between grain growth and grain size reducing mechanisms during deformation

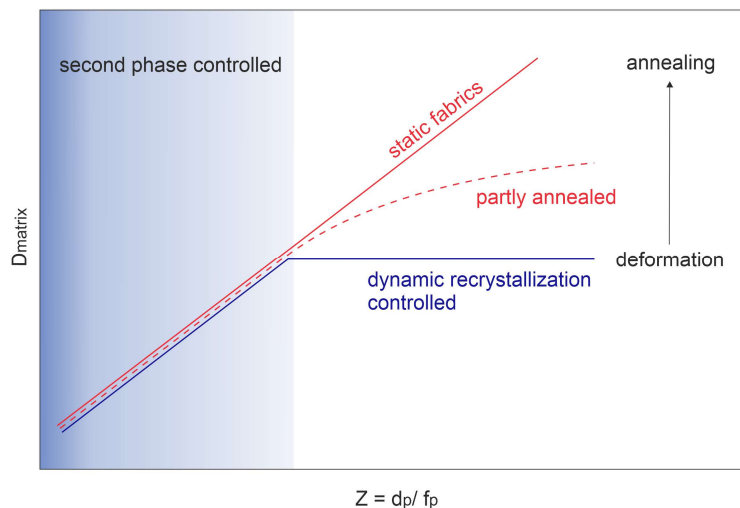


Fig. 5: Zener plot: presented is the grain size relation of a dominant matrix phase (D_{matrix}) with the Zener parameter (Z) in deformed and static fabrics (modified after Herwegh et al., 2008).

(De Bresser et al., 1998). In the static case during annealing, the matrix grain size will increase continuously with increasing Z or, in the case of partially annealed samples, the Zener trend flattens (red trends in Fig. 5) (Herwegh et al., 2008). However, this approach is applicable in homogeneous aggregates with a dominant matrix phase (>50 Vol.-%). In aggregates with heterogeneous phase distribution and fraction comparable relations may be established by estimating the connectivity of a phase (e.g., Hunter et al., 2016).

1.4. Set-Up of this Study

The investigation of deformation and annealing of quartz, alkali feldspar and plagioclase encompasses a detailed analysis of microstructures within different domains of varying

quartz-feldspar contents. In a first step (chapter 5), two-feldspar and TitaniQ geothermometers are applied to constrain temperature conditions during deformation. In a second step (chapter 6) EBSD (electron backscatter diffraction) based texture analysis is conducted encompassing investigation of CPOs, distribution of misorientation axes/ angles and boundary trace analysis to identify deformation mechanisms and slip systems in the different subdomains. The results are evaluated including microstructural observations (chapter 3) with respect to preservation and alteration of deformation microstructures during annealing. Furthermore, the attempt is made to create a model for misorientation axes and corresponding slip systems for feldspars. In chapter 7 modal content, grain size, shape and connectivity of quartz and feldspar are analyzed and correlated based on image analysis. Dependencies of grain size and shape development are elucidated and related with deformation mechanisms and alteration during annealing. Furthermore, in quartz rich domains the attempt is made to apply a modification of the Zener parameter. In chapter 8 curvature and apparent dihedral angles of like-like boundaries are analyzed to estimate equilibration of quartz and feldspar microstructures. For comparison, curvature and apparent dihedral angles of monophasic deformed and equilibrated test quartz aggregates are measured and stated as endmembers for deformation by GBM recrystallization and equilibration. The results are evaluated with respect to the applicability to distinguish between deformation and annealing in polyphase rocks.

2. Geological Background

2.1. Metamorphic Basement

The Paleoproterozoic to Neoproterozoic basement of Sri Lanka is divided into three major units based on petrography, geochemistry and geochronology (Fig. 6) (Kehelpannala, 1991, 1997; Milisenda et al., 1994). From northeast to southwest, these units are i) the Wannai Complex (WC), ii) the Highland Complex (HC) and iii) the Vijayan Complex (VC).

The HC is comprised of a supracrustal sequence of metasediments such as quartzites, marbles, calcsilicate gneisses, garnet-sillimanite bearing gneisses (khondalites) and psammo-pelites. Metasediments are intercalated with metaigneous rocks like charnockites and metagabbros (Braun and Kriegsman, 2003; Kleinschrodt et al., 1991; Kleinschrodt and Voll, 1994; Malaviarachchi, 2018). The HC is the oldest unit in Sri Lanka and yields Nd model ages of 2.0 – 3.4 Ga (Kröner et al., 2003, 2013; Milisenda et al., 1988, 1944). HC rocks were metamorphosed and deformed under high grade granulite facies conditions around 610–550 Ma based on U-Pb data (Hözl et al. 1994; Kröner and Williams, 1993). Metamorphic conditions decrease from 8-9 kbar and 800–900 °C in the east-southeast to 4.5–6 kbar and 600–700 °C in the southwest (Dharmapriya et al., 2015; Sajeev et al., 2010; Schumacher et al., 1990; Schumacher and Faulhaber 1991). Locally, ultra-high temperature (UHT) conditions of 925–1150 °C and pressures of ~ 9–12.5 kbar are reported (Osanaï et al., 2016a, b). For the retrograde path of HC rocks near isobaric cooling is suggested from high temperatures prior to uplift (Dharmapriya et al., 2017; Schenk et al., 1988; Schumacher et al., 1990). This is followed by rapid uplift along a near isothermal decompression path (Dharmapriya et al., 2017; Raase and Schenk, 1994). Peak metamorphism and isobaric cooling is estimated to amount for a time span from ~610–450 Ma based on cooling ages of biotites (closure temperature ~300 °C) (Hözl et al., 1991, 1994).

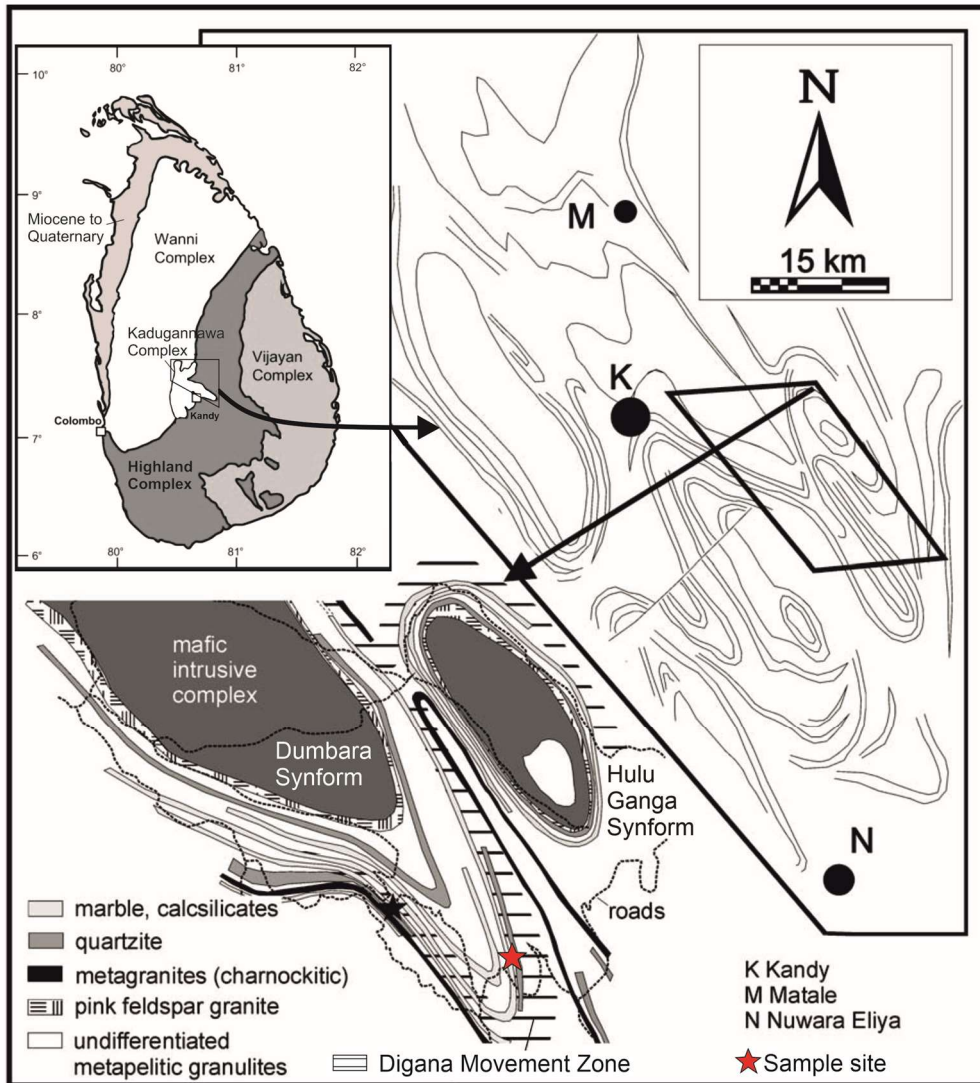


Fig. 6: Geological overview of the Sri Lankan Basement and sample site (modified after Kleinschrodt and Duyster, 2002).

The WC is dominated by metaigneous rocks with granitic, granodioritic to dioritic composition and metasediments are scarce (Cooray, 1994; Malaviarachchi, 2018). The VC consists mainly of granodioritic to dioritic gneisses and tonalite-trondhjemite-granodiorite (TTG) gneisses. Of minor occurrence are quartzites and calc-silicate rocks close to the HC boundary (Cooray, 1994; Malaviarachchi, 2018). Both, the WC and the VC, yield lower Nd model ages compared to the HC of 2–1 Ga and 1.9–1 Ga, respectively (Milisenda et al., 1988, 1994). U-Pb data yield metamorphic ages of 590–540 Ma and 510–460 Ma for the WC and VC, respectively (Hözl et al., 1994; Kröner and Williams, 1993; Malaviarachchi, 2018, references therein). Metamorphism in the WC reached amphibolite to granulite facies conditions at 600–900 °C and 3.5–7.5 kbar (Faulhaber and Raith, 1991;

Schenk et al., 1991). In the VC metamorphism reached predominantly amphibolite facies conditions but locally found charnockites indicate granulite facies conditions (De Maesschalck et al., 1990; Jayawardene and Craswell 1967; Kröner et al., 2013; Wijeratne and Malaviarachchi, 2017).

Metamorphism in the HC, WC and VC is correlated with the juxtaposition of these terrains during the final assembly of the supercontinent Gondwana (Kröner et al., 1994; Ranaweera and Kehelpannala, 2019; Santosh et al., 2014; Takamura et al., 2015;). There is a general agreement that the boundary between the HC and VC represents a sub-horizontal thrust/ shear zone along which the HC was thrust over the VC. The transport direction is marked by a NNE-SSW oriented stretching lineation (Kehelpannala, 1997; Kleinschrodt, 1994; Kröner et al., 2013; Vitanage, 1985). The nature of the boundary between HC and VC is not yet consistently determined. Kehelpannala and Ranaweera (2007, 2019) suggest that the boundary represents a lower crustal shear zone. However, the WC represents a shallower crustal level than the HC as indicated by peak pressure estimates (e.g., Dharmapriya et al., 2020; Faulhaber and Raith, 1991; Raase and Schenk, 1994).

2.2. Geotectonic Evolution

The geotectonic evolution of the Sri Lankan basement is at present still under discussion (see review in Malaviarachchi, 2018; Ranaweera and Kehelpannala, 2019). Kehelpannala (2004) and Santosh et al. (2014) proposed two contrasting models. The model of Kehelpannala (2004) suggests two separate plate collisions following two separate convergent margins. According to the author, the first collision occurred between a Paleoproterozoic microcontinent (HC) and a late Meso- to Neoproterozoic Andean-type magmatic arc (WC). This collision was the result of the subduction of the plate containing the HC below the WC. Subsequently, an oceanic plate upstream of a Mesoproterozoic

island arc (VC) was subducted beneath the WC-HC entity. In his model, Kehelpannala (2004, 2016) assigns granulite facies and UHT metamorphism in the WC and HC to the first collision and amphibolite (to granulite) facies metamorphism in the VC to the second metamorphism. Further, the author interprets two thermal events around 620–580 Ma and 560–535 Ma (Dharmapriya et al., 2016; Osanai et al., 2016a, b; Santosh et al., 2014;) to correlate with the two-stage plate collision.

The model of Santosh et al., (2014) includes a double-sided two-staged subduction at an active convergent margin setting. In this scenario, the WC and VC represent early Neoproterozoic magmatic arcs with the HC as (paleo) ocean located between these arcs. The WC is suggested to originate during a first subduction after Rodinia dispersal. The HC ocean was formed as part of the Mozambique ocean. A second subduction beneath pre-Gondwana continents resulted in arc formation of the VC. Lithologies in the HC are regarded as fragments of pre-Gondwana crustal blocks, accretionary remnants of the subducting lithosphere and trench sediments interpreted as MORB remnants (Takamura et al., 2015, 2016). Subsequent collision during Late-Neoproterozoic-Cambrian amalgamated WC, HC and VC and led to simultaneous metamorphism (Dharmapriya et al., 2015; He et al., 2016a, b; Takamura et al., 2015, 2016). The time span between the two subduction events is not yet precisely determined but estimated to amount for several million years (Malaviarachchi, 2018).

2.3. Deformation History

The deformation history of the metamorphic basement of Sri Lanka is subdivided into up to six detected deformation events D₁ to D₆ (e.g., Berger and Jayasinghe, 1976; Kehelpannala, 1991, 1997; Sandiford et al., 1988; Voll and Kleinschrodt, 1991; Yoshida et al., 1990). Kehelpannala (1997) proposed a first deformation D₁ and foliation S₁ by the preferred orientation and internal folding and crenulation of inclusion minerals in garnet

porphyroblasts within different rock types of Sri Lanka. The author discussed the possibility of D_1 being the initial stage of D_2 where the major compositional layering arised from a crenulation cleavage of the first foliation. The crenulation cleavage is preserved as inclusion trails and crenulation fold hinges in garnet porphyroblasts in some metapelites (Kehelpannala, 1997). The deformation event D_1 is interpreted to took place during the prograde path before granulite facies peak metamorphism in Sri Lanka (Kehelpannala, 1997; Raase and Schenk, 1994; Voll and Kleinschrodt, 1991).

The second deformation D_2 is characterized by a foliation S_2 parallel to the major compositional layering and a stretching Lineation L_2 (S_1 and L_1 in Kleinschrodt and Voll, 1991). D_2 represents the strongest deformation of the basement in Sri Lanka (Kehelpannala, 1997; Kleinschrodt and Voll, 1991; Voll and Kleinschrodt, 1991). S_2 is accompanied by a strong flattening of about 80 % (Kehelpannala, 1997; Voll and Kleinschrodt, 1991). L_2 is defined by long axes of quartz and feldspar grains, c-axes of hornblende, pyroxene and sillimanite, and long axes of recrystallized aggregates. A zone of increased strain was reported by Voll and Kleinschrodt (1991) which is prominent close to Digana but also found in the surroundings of the Dumbara and Hulu Ganga synforms in the central Highlands (Fig. 6). This Digana Movement Zone is characterized by increased flattening and stretching parallel to L_2 , which is concentrated in a 10 – 15 m wide zone in the centre. Folding during D_2 produced mainly rootless, isoclinal and intrafolial folds F_2 with hinges mostly parallel but also oblique to L_2 . F_2 folds were interpreted to result from progressive rotation during non-coaxial deformation (Kehelpannala, 1997). D_2 occurred under peak metamorphic conditions as inferred from geothermobarometry and parallel alignment to S_2 and L_2 of high-grade minerals like pyroxene and sillimanite (Berger and Jayasinghe, 1976; Kehelpannala, 1997; Voll and Kleinschrodt, 1991). In some parts of the HC, D_2 continued to decreasing temperatures as

reported in the Digana Movement Zone (Voll and Kleinschrodt, 1991; Voll et al., 1994). Raase (1998) estimated ~ 710 °C for recrystallisation and deformation of feldspars in the Digana Movement Zone using two-feldspar thermometry.

The evolution of the compositional layering is still under discussion. Kleinschrodt and Voll (1994) found evidence for the sequence still representing primary relationships as characteristic horizons can be found in identical positions within different synforms. In this context, magmatic rocks were interpreted to intruded as sills parallel to the sedimentary layering before deformation. On the other hand, Kröner et al. (1991, 1994) and Kehelpannala (1991) argued that the compositional layering was tectonically induced. After Kröner et al. (1994), magmatic rocks intruded into the sequence at various stages during deformation and the layered units represent now straight gneisses.

The deformation event D_3 produced refolding of S_2 and developed F_3 folds with axes mostly parallel – in fewer cases subnormal to L_2 – and an axial plane foliation S_3 parallel to the compositional layering (Kehelpannala, 1997; Kleinschrodt and Voll, 1994; Yoshida et al., 1990). F_3 folds are small to km-scale, tight to isoclinal and some of them are recumbent (Kehelpannala, 1997). Kehelpannala (1997) interpreted these folds as the result of simple shear deformation D_3 in the same direction as D_2 with progressive rotation. The author underpinned his explanation with the occurrence of variable tightness and intensity of deformation of F_3 folds and fold axes parallel to L_2 in the central Highlands and subparallel to L_2 in the SE of the HC. The latter folds are thought to represent not further rotated folds.

A deformation event D_4 was proposed by Kehelpannala (1991) due to local occurrence of large, E-W trending gentle to open folds. In places (from E of Colombo to E of Kandy) where the amplitudes of F_4 folds are large enough, a nearly E-W striking axial plane foliation S_4 is developed. S_4 was locally folded by D_5 deformation which is mainly found in

synforms around and west of Kandy. Both, D₃ and D₄, are estimated to took place under granulite facies conditions (Kehelpannala, 1997). Kehelpannala (1991, 1997) argued, that D₄ proceeded at the onset of exhumation from deep lower crustal levels and that a change in the stress field during initial stages of uplift caused folding of F₄.

D₅ is the second strongest deformation event detected in Sri Lanka and is characterized by large scale upright folds F₅ (Kehelpannala, 1997; Kleinschrodt et al., 1991; Kleinschrodt and Voll 1994). Fold axes of F₅ are mostly parallel to the prominent stretching lineation L₂ and axial directions vary from NE-SW in the NE of Sri Lanka to NE-SW in the central part and nearly E-W in the southern regions (Kehelpannala, 1997; Voll and Kleinschrodt, 1991). F₅ folds are reported mainly in the HC and WC where they cause refolding of former structures such as the Digana Movement Zone (Voll and Kleinschrodt, 1991). An axial plane cleavage S₅ is marked by flattened quartz and feldspar aggregates and reorientation of (001) of biotite and (100) of hornblende in rock samples. S₅ is mostly developed close to the hinge zones of F₅ folds and in closure areas. Kleinschrodt and Voll (1994) reported for the Dumbara synform – one of the F₅ folds in the central Highlands – that S₅ is most intense in the central part of the synform and is less developed in the margins. S₅ produced an intersection lineation L₅ with S₂ (Kehelpannala, 1997). Metamorphic conditions of D₅ were still at granulite facies conditions, but at lower temperatures than peak metamorphism as isobaric cooling from 850 °C to 700–750 °C due to uplift is recorded and interpreted to proceeded from D₂ to D₅ (Evangelakakis et al., 1991; Kleinschrodt and Voll, 1994; Schumacher et al., 1990).

A last deformation event D₆ was proposed by Kehelpannala (1993) based on analysis of spot and satellite images which record refolding F₆ of some F₅ folds. F₆ folds are smaller than F₅ folds and their axial planes are mostly subvertical and nearly parallel to those of the F₅ folds. Quartz-feldspar granitic veinlets may represent an axial plane cleavage S₆

which caused dragging and shearing of the major compositional layering S₂ (Kehelpannala, 1991; Voll and Kleinschrodt, 1991; Yoshida, 1990). The presence of biotite and hornblende in the veinlets infers deformation of D₆ under amphibolite facies conditions during uplift (Voll and Kleinschrodt, 1991; Yoshida et al., 1990). Kehelpannala (1997) mentioned the possibility that D₆ could be related to the D₆ event of Kleinschrodt (1994).

All units of the Sri Lankan basement were affected by static annealing which outlasted all deformation during long lasting cooling and uplift (Voll and Kleinschrodt, 1991; Voll et al., 1994). Annealing resulted in a partial overprint of deformation microstructures by grain coarsening, development of polygonal grain shapes and equilibrated dihedral angles of 120° (Voll and Kleinschrodt, 1991).

2.4. Sample Collection Site

The samples treated in this study are quartzo-feldspathic granulites from marginal parts of the Digana Movement Zone east of Kandy within the HC. The collection site (7°12'56"N 80°46'00"E) is located at the southern tail of the Dumbara Synform (Fig. 6). The samples were collected from fresh road-cuts from a quartzitic succession intercalated with quartzo-feldspathic metasediments. The samples were collected in 1992 by Reiner Kleinschrodt within the scope of a special research project "Composition, Structure and Evolution of the lower continental crust". The rocks derive from a metasedimentary unit consisting of marbles, calcsilicates, quartzites, and metapelites (Kleinschrodt and Voll, 1994). Overall structures around the sample site are dominated by F₅ folds (Dumbara and Hulu Ganga Synforms) but foliation and lineation within the Digana Movement zone are strictly parallel to S₂ and L₂. Recrystallization and deformation in the Digana Movement Zone occurred at ~ 710 °C (Evangelakakis et al., 1991; Raase 1998; Voll and Kleinschrodt,

1991). However, around Kandy feldspar recrystallization temperatures of >800 °C are reported (Voll et al., 1994).

3. Sample Description

The sample description is based on microscopic investigation of thin sections and Backscattered Electron (BSE) images (for details see section 4.1).

The studied samples are deformed quartzo-feldspathic granulites which are coarsened due to post-deformation annealing (Kleinschrodt and Voll, 1994). The granulites display varying amounts of quartz and two feldspars, alkali feldspar and plagioclase, ranging from ~20 to >90 Vol.-% in quartz (Fig. 7). Almandine-rich garnet is locally accumulated in feldspar rich domains and represents a minor to major component depending on the observed layer. Sillimanite is a minor constituent and often associated with garnet in feldspar dominated domains. Kyanite, zircon, monazite, rutile, and opaque minerals (hercynite, magnetite, ilmenite) occur as accessory phases. Feldspars show various exsolution features which generated at different stages during cooling history (Evangelakakis et al., 1993; Voll et al., 1994; Raase, 1998). Most common are film perthites, string/ spindle perthites and antiperthites. Film perthites in feldspars from the Highland Complex of Sri Lanka were interpreted by Evangelakakis et al. (1993) as final late stage exsolution features. A dry mineral assemblage is accompanied by intracrystalline low OH-contents of quartz and was determined in preliminary Fourier Transformation Infrared (FTIR) Spectroscopic investigations (results are not shown in this study).

The samples reveal a pronounced flattening foliation defined by alternating quartz-feldspar-layers of variable thicknesses. In thin sections, the foliation is marked by long axes of quartz ribbons and elongated feldspar aggregates (Fig. 7). These features are visible in both, sections cut perpendicular to the foliation and parallel to the stretching lineation (XZ sections) and perpendicular to foliation and lineation (YZ sections) (Fig. 7c).

In XZ sections long axes of elongated garnet, opaque minerals, and c-axes of sillimanite are aligned to the foliation.

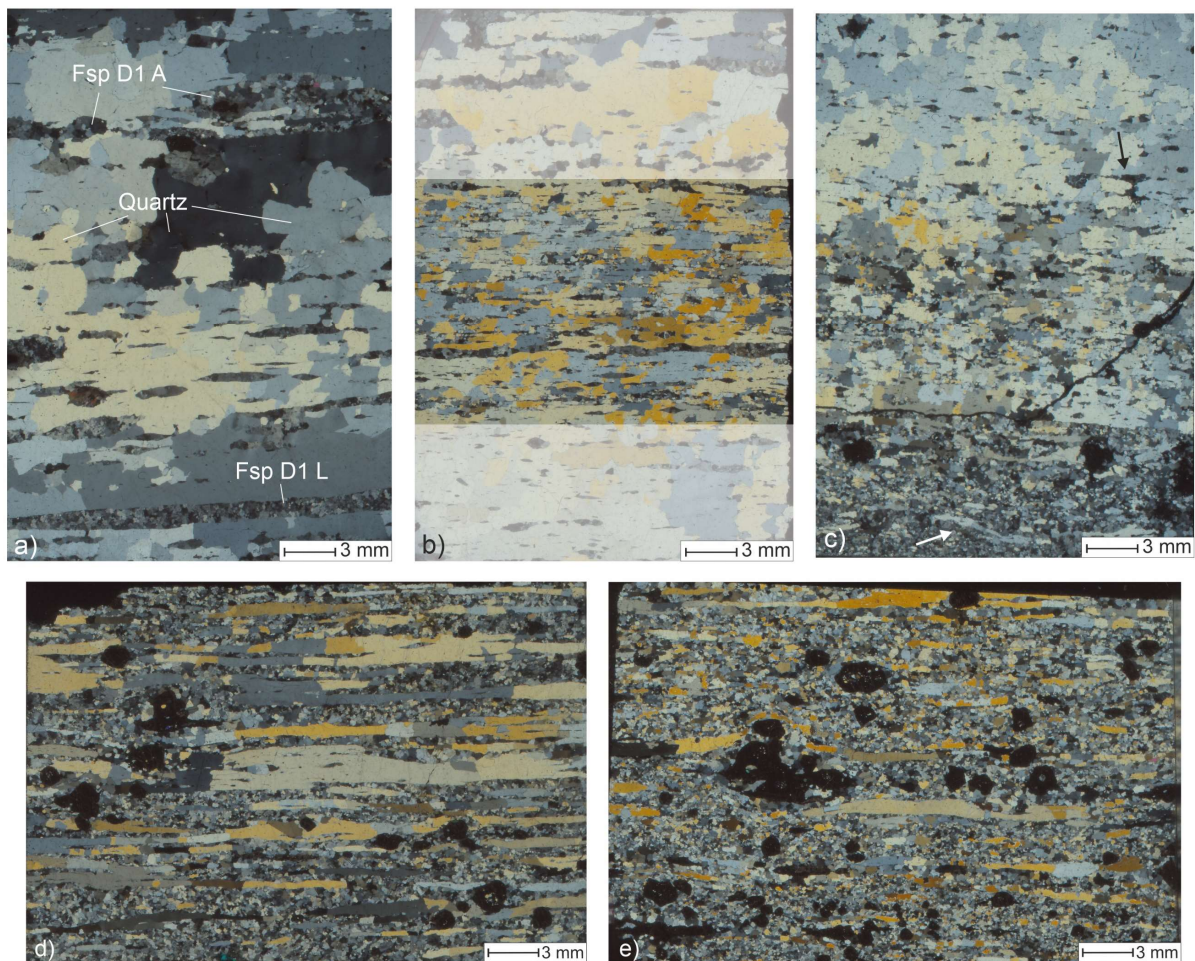


Fig. 7: Main domains in the investigated samples (thin section scans recorded with polarization filter): a) quartz domain D1 and feldspar domains D1 A and D1 L, b) D2 (highlighted) c) YZ-section showing flattening foliation of feldspar (black arrow) and quartz ribbons (white arrow); d) D3; e) D4.

3.1 Classification and Description of Domains

The investigated samples are subdivided into domains based on their quartz content. A first subordinate classification is made by defining a *quartz dominated domain* (Qdd, sample 2997) and a *feldspar dominated domain* (Fdd, sample 3054). In the Qdd quartz is the dominant phase with a content of >50 Vol.-%. Quartz builds an interconnected network of up to millimetre sized grains and feldspars are dispersed at varying degrees (Fig. 7a, b) The Fdd consists of a matrix consisting of quartz-alkali feldspar-plagioclase with embedded quartz ribbons (Figs. 7d, e, 8c-e).

Based on quartz content, the Qdd and Fdd are further subdivided into the following main domains:

- Domain 1 (D1), ~75–90 Vol.-% quartz
- Domain 2 (D2), ~65–75 Vol.-% quartz
- Domain 3 (D3), ~30–40 Vol.-% quartz.
- Domain 4 (D4), ~20–30 Vol.-% quartz

In D1 feldspars are accumulated into aggregates and layers (Fig. 7a). These are referred to as *D1 aggregates* (D1 A) and *D1 layers* (D1 L). D1 A constitute of varying amounts of alkali feldspar and plagioclase. In D1 L antiperthites dominate over alkali feldspar. In D2 feldspars are dispersed (Fig. 7b) and are mainly represented by alkali feldspar. In D3 most quartz is accumulated in ribbons while the matrix is depleted by quartz (Fig. 7d, 8c, d). Feldspars often occur in layers dominated by one feldspar phase. These are referred to as *kfs dominated domains* (Fig. 8c) and *pl dominated domains* (Fig. 8d). Well mixed layers of alkali feldspar, plagioclase and minor quartz are also common. In D4 more quartz is

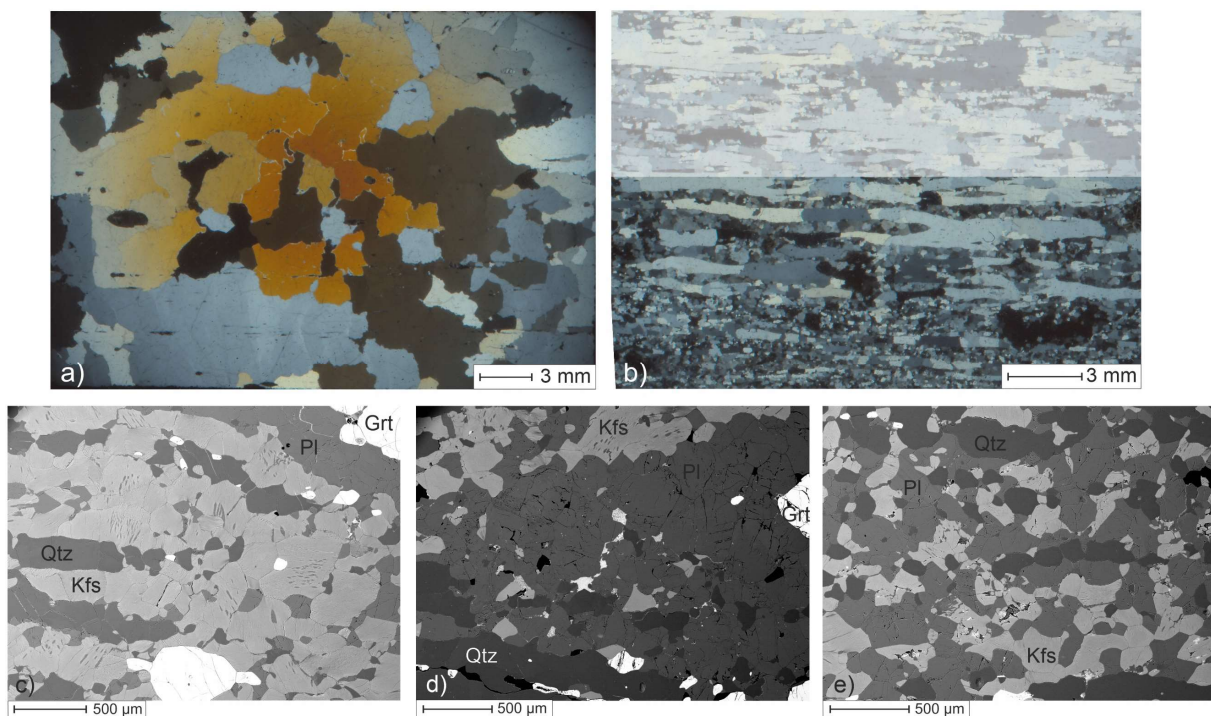


Fig. 8: Subdomains in the Qdd and Fdd (a, b: thin section scans recorded with polarization filter; c-e: BSE images): a) D0; b) 2997 ribbons (highlighted); c) kfs dominated domain, D3; d) pl dominated domain, D3; e) D4 matrix.

present in the matrix which comes along with less ribbon forming quartz (Figs. 7e, 8e). In D4 alkali feldspar and plagioclase rich domains are less common, and the matrix constitutes of a mixed assemblage of two feldspars and quartz (Fig. 8e).

For analysis of grain size, shape and like-like boundaries (chapter 7, 8) a *Domain 0* (D0) (sample 2531, >90 Vol.-% quartz) (Fig. 8a) is introduced to supplement the data set of quartz rich domains in the Qdd. In sample 2997 a feldspar rich layer occurs in which quartz forms ribbons (Fig. 8b). These are designated as *2997 ribbons* and are additionally treated for texture analysis (chapter 6). Feldspars of D1 A and D1 L are only treated for texture analysis (chapter 6) because a high weathering grade impeded identification of individual grain boundaries for analysis of grain size, shape and like-like boundaries (chapter 7 and 8). Further subdivisions are specifically mentioned in relevant cases.

3.2 Microstructures

3.2.1 Quartz

In D1 and D0 the framework of quartz is constituted of inequigranular and interlobate aggregates of mm to cm-sized grains (Figs. 7a, 8a). In D2 quartz grain size is reduced and ranges between several 100s of micrometres and a few millimetres depending on feldspar distribution (Figs. 7b, 9a). Quartz shape is variable in D2. Irregular shaped grains with interlobate grain boundaries coexist with ribbons and small equidimensional grains forming polygonal frameworks (Figs. 7b, 9a). Quartz ribbons in D3 and D4 are poly- to monocrystalline ranging in width from ~200 μm up to a few millimetres (Fig. 9b). Some ribbons are constituted of single grains which are strongly elongated up to a few centimetres in x-direction (Fig. 7d, e). Matrix quartz is mostly aligned to layers parallel to the foliation (Fig. 9i). Locally, matrix quartz grains appear to coalesce to form incipient ribbons (Fig. 9c, d).

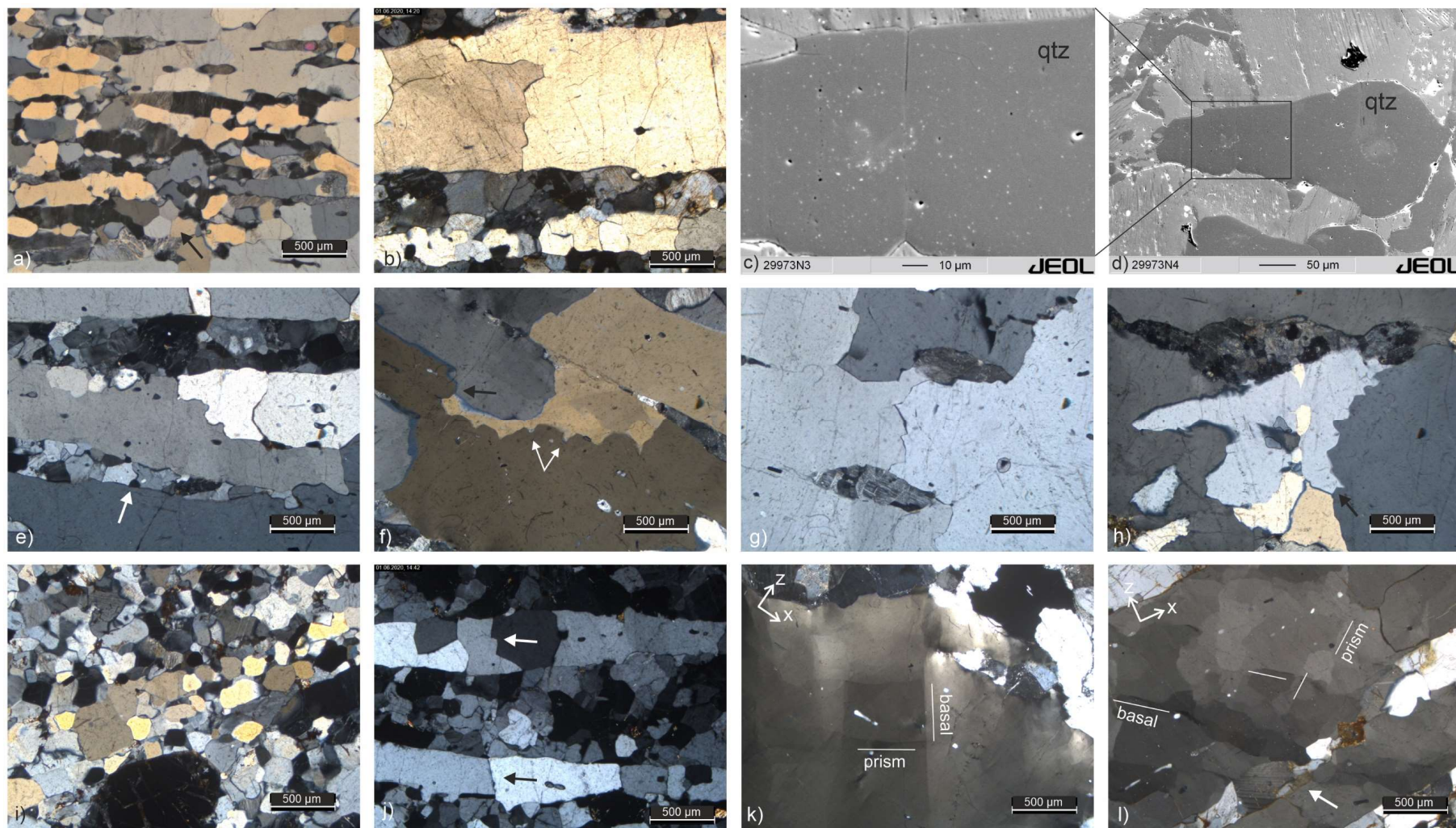


Fig. 9: Quartz microstructures (a-b, e-l: microscopic images with polarization filter; c, d: BSE images): a) small-sized quartz in D2 with locally (arrow) polygonal frameworks; b) nearly mono (upper) and polycrystalline (lower) ribbons in the Fdd; note dissection of the bright yellow ribbon (upper); c-d) coalescing matrix quartz; e-h) lobate (e, f, h), serrate (g) and straight (e, h) grain boundary segments; black arrows in f) and h) point to equilibrated dihedral angles established by short boundary facets; in f) lobate boundaries are produced by small pinning grains (white arrows); h) dissection microstructures of light blue and light yellow grains; i) matrix quartz (yellow-brownish grains) in the Fdd aligned to layers; j) straight (black arrow) and irregular (white arrow) grain boundaries in D4 ribbons; k-l) chessboard extinction in D1 (k) and D3 (l); prism and basal plane parallel boundaries are indicated oblique to the foliation (X-direction); white arrows in e) and l) point to lenticular feldspar aggregates.

Quartz grain boundaries are irregular in all subdomains of the Qdd and Fdd. Grain boundary geometries are lobate, serrate, or straight (Fig. 9b, e-h, j). Ribbons often display straight grain boundaries perpendicular to the foliation (Fig. 9j). Pinning (Fig. 9f) and dissection microstructures (Fig. 9b, h) are common indicating GBM recrystallization. Dissection microstructures (Urai et al., 1986) are identified by identical extinction and interference colours of separated grain fragments in thin section and are predominantly observed in large grains in D1, D0 and in ribbons of D3 and D4. Equilibrated dihedral angles of 120 ° are most common in polygonal frameworks of small grains (D2) (Fig. 9a). Between large grains (D1, D0, D3/ D4 ribbons) these are often accomplished by short boundary facets (Fig. 9f, h) (Kruhl, 2001). Quartz exhibits undulose chessboard extinction with subgrain walls and boundaries oblique to the foliation (Fig. 9k, l). Subgrain boundaries forming chessboard patterns are parallel to prism and basal-planes (Fig. 9k, l) (determined on grains with c-axes subparallel to the thin section using a λ -plate; see also Kruhl, 1996). Smallest quartz grains within polygonal frameworks are visibly free of subgrains.

3.1.2 Feldspar

In the Qdd and Fdd feldspar microstructures are characterized by inequigranular polygonal to interlobate fabrics (Fig. 10). In the Fdd interlobate fabrics are more common in alkali feldspar rich domains while plagioclase rich domains often develop polygonal frameworks (Fig. 10b, c). Grain size of feldspars is variable but largest grains are found in aggregates and layers with a predominant feldspar phase without quartz. Irregular grain shapes, dissection and pinning microstructures and left-over grains indicate GBM recrystallization (Figs. 10a, b, d-g, j) (e.g., Jessel, 1987; Urai et al., 1986). This is underpinned for plagioclase by truncation of twin lamellae (Fig. 10f). In string perthites truncation of exsolved cores and pinning of migrating boundaries by strings/ spindles

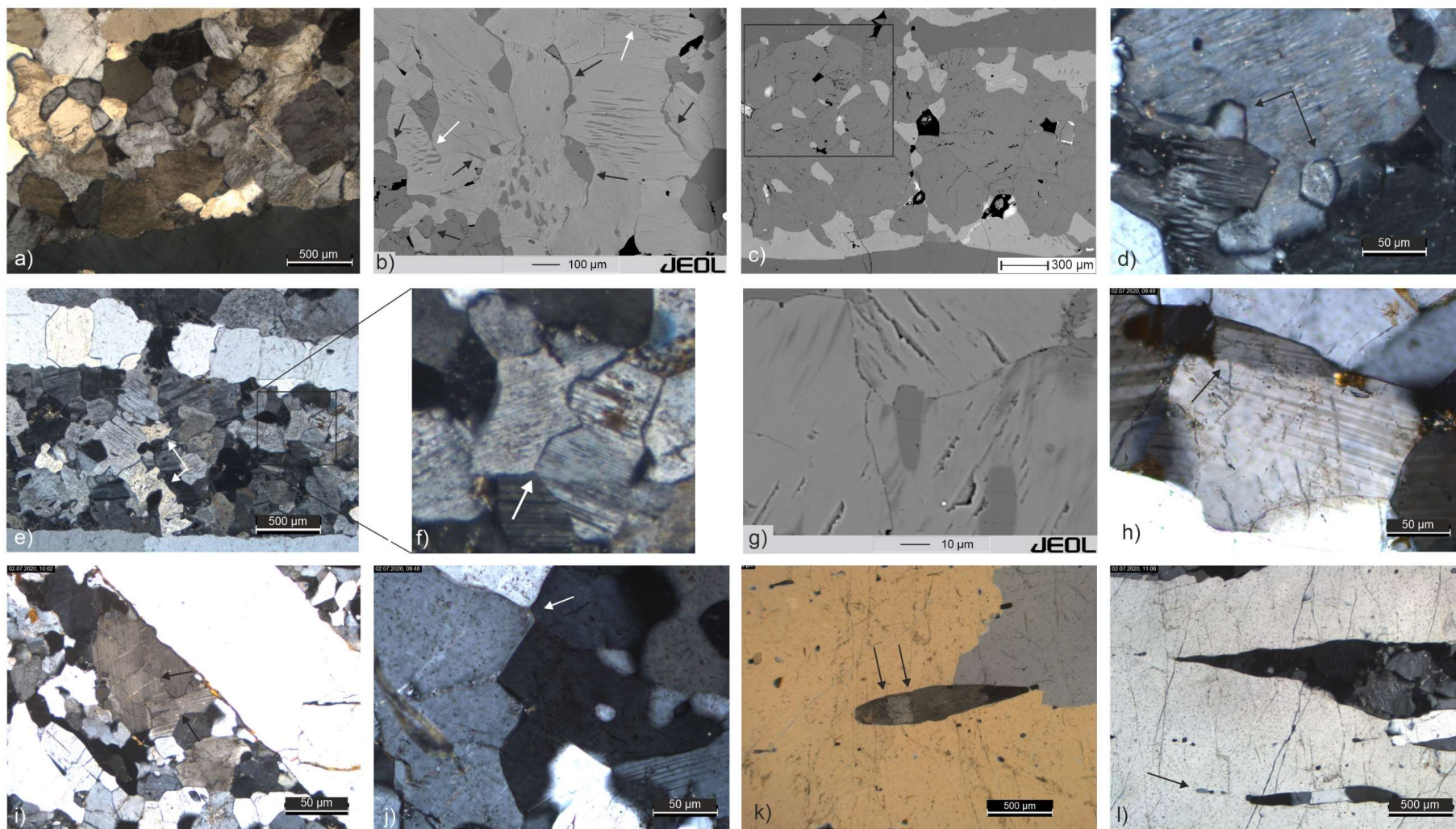


Fig. 10: Feldspar microstructures (b, c, g: BSE images; all others are microscopic images with polarization filter): a-c), e) inequigranular, interlobate fabrics; b) alkali feldspar (kfs) (light grey)-rich domain in D3; note bands and patches (black arrows) of plagioclase (pl) (grey) and quartz (dark grey) along kfs and pl grain boundaries; white arrows indicate truncation of exsolved cores; c) pl-rich domain; rectangle marks polygonal grain fabrics; note interstitial kfs; d) left-over grains (arrows); e) dissection microstructures (white arrows); f) truncation of pl twins; white arrow marks 120° triple junctions; g) pinning of migrating boundaries by exsolved spindles in kfs; h) deformation twins and subgrain boundary (arrow) in pl; i) undulose extinction and slightly bended twin lamellae (arrows) in pl; j) serrated boundaries and 120° triple junctions established by short boundary facets; k) kinking (arrow) in lenticular kfs in D2; l) kfs in D2; note ribbon shape and pinched-off particles (arrow) in the lower image part (foliation plane is parallel to the horizontal in k) and l)).

suggest exsolution prior or simultaneous to deformation (Fig. 10b, g). Further, in in alkali feldspars films and patches of plagioclase occur along grain boundaries indicating diffusion (Fig. 10b). Similar films of quartz occur also in plagioclase (Fig. 10b). Further, interstitial quartz, plagioclase and alkali feldspar occur at triple junctions, between two grain boundaries or as inclusions within the feldspar matrix (Fig. 10b, c). Plagioclase reveals deformation twins and bended twin lamellae (Fig. 10h, i).

Grain boundaries of both feldspars are smoothly curved, serrated or straightened and triple junction angles of 120° are common (Fig. 10a-c, f, j). In both feldspars undulose extinction is less frequent and mostly patchy. In plagioclase undulose extinction is only observed in grains with irregular grain shapes (Fig. 10i) while plagioclase in polygonal frameworks is visibly strain free. In single cases, subgrain boundaries in plagioclase are aligned parallel to twin lamellae (Fig. 10h).

Alkali feldspar in D2 shows partly different microstructures. Aggregates and single grains reveal lenticular shapes (Fig. 10k, l). These display acute tips in X-direction which display concave boundaries towards the surrounding quartz. Locally, small fragments with a few 10s of micrometres in diameter are pinched off at the tips and aligned in the direct continuation of the tip in X-direction (Fig. 10l). Aggregates with a single grain in width reveal straight grain boundaries perpendicular to the foliation similar to ribbon quartz (Fig. 10l). Moreover, kinking structures occur (Fig. 10k). Such microstructures are also observed in the Fdd when small feldspar layers or individual grains are enclosed by quartz ribbons (white arrows in Fig. 9e, l). Coarse aggregates in D2 display comparable microstructures with feldspars from other domains.

3.1.3 Quartz-Feldspar Boundaries

Quartz-feldspar boundaries are smoothly curved in all domains (Fig. 11). In D1 of the Qdd boundaries between quartz and feldspar are mainly determined by boundaries of feldspar aggregates and layers (Fig. 11a, b). Feldspar aggregates show more indentations by quartz than layers. In the former indentations are accompanied by locally developed asymmetric pinch and swell structures (Fig. 11a). Along triple junctions quartz and feldspar form slight indentations which are referred to as cusps (Fig. 11e, f) (Gower and Simpson, 1992). Such cusps can also be assigned to pointy ends of lenticular feldspars in D2 parallel to the foliation (Fig. 10k, l). In the matrix of the Fdd smoothly curved and indenting boundaries also occur between individual grains of quartz and feldspar and between alkali feldspar and plagioclase (Fig. 11d).

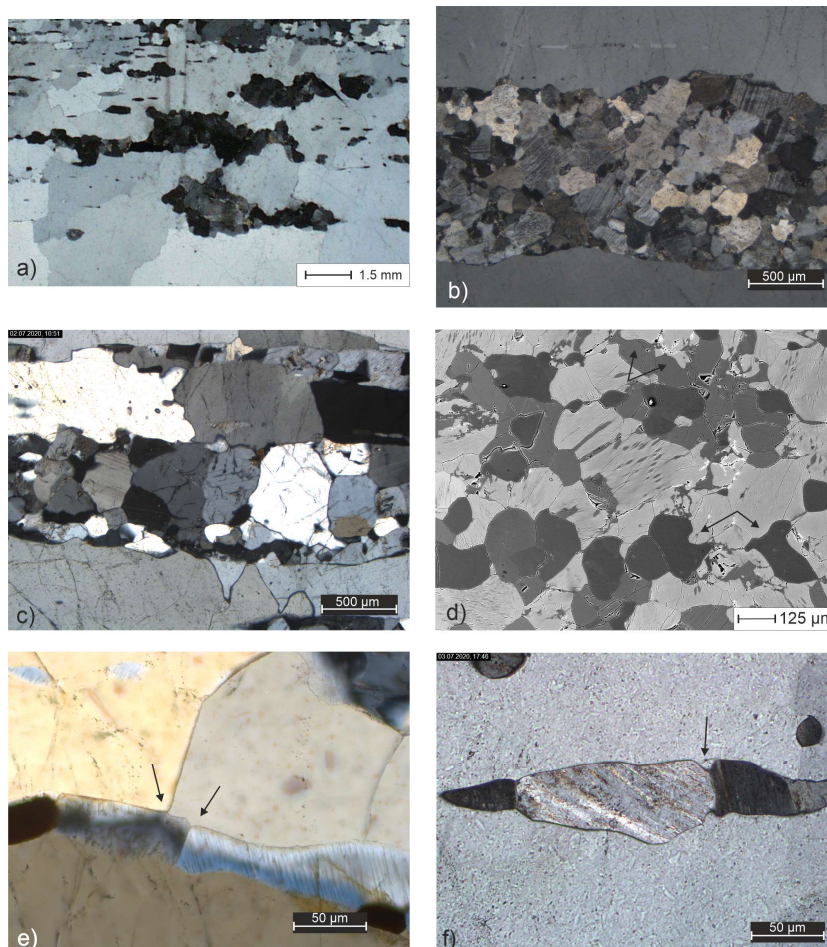


Fig. 11: Quartz (qtz)-Feldspar (fsp) boundaries (a-c, e, f: microscopic images with polarization filter; d: BSE image; foliation plane is parallel to the horizontal): a) D1 fsp aggregate-qtz; b) D1 fsp layer-qtz; c) qtz ribbon-fsp; d) indentations between matrix qtz and fsp (arrows); e-f) cusp forming indentations (arrows).

4. Methods

4.1. Sample Preparation and Microscopic Examination

Investigation of samples was conducted on thin sections cut perpendicular to the foliation and parallel to the lineation (XZ section). A second set of thin sections perpendicular to foliation and lineation (YZ section) was prepared for microscopic investigations only. Thin sections have a thickness of approximately 30–40 μm (estimated with the Michel-Levy Chart) resulting in grey to orange interference colours of quartz. Thin sections considered for EBSD and electron microprobe analyses were polished with colloidal silica and carbon coated.

Microstructures were optically examined by means of polarization microscopy and Backscatter Electron (BSE) imaging. BSE images were recorded on the same devices which served for EBSD and thermometric analyses (see section 4.2 and 4.3). Microstructures of millimetre-sized quartz were further analyzed on scans encompassing whole thin sections. Scans were recorded with and without a polarization filter.

4.2. Thermometry

Mineral chemical compositions required for the application of geothermometers were quantitatively determined by electron microprobe analyses. Measurements were conducted on a JEOL JXA-8900RL Superprobe at the Institute of Geology and Mineralogy, University of Cologne.

4.2.1. Two-Feldspar Thermometry

4.2.1.1. Thermometric Expression and Correction for Slowly Cooled Rocks

Two-feldspar thermometry is based on the temperature dependent composition of coexisting plagioclase and alkali feldspar (e.g., Fuhrman and Lindsley, 1988). Thermometric expressions for ternary feldspars consider that at high temperatures a (limited) solution exists between all feldspar components albite (Ab), anorthite (An) and

orthoclase (Or) (e.g., Benisek et al., 2010; Fuhrman and Lindsley, 1988). In this study, the two-feldspar thermometer for ternary feldspars of Fuhrman and Lindsley (1988) (FL) is used. The FL thermometer is applied in several studies on feldspars from the Sri Lankan Highland Complex (Kroll et al., 1993; Voll et al., 1994; Raase 1998). Thus, the application of the same thermometer ensures a reasonable comparison of calculated temperatures. Furthermore, the thermometer of FL was applied in several studies on high-grade rocks and proved to be effective (Hokada et al., 2001; Pilugin et al., 2009; Jiao and Guo, 2011). Fuhrman and Lindsley (1988) revised a thermodynamic model for ternary feldspars using experimental data of Seck (1971 a, b). The authors considered that for coexisting feldspars in ternary systems activities of all their components must be equal resulting in the following equilibrium conditions:

$$a_{Ab}^{kfs} = a_{Ab}^{pl} \quad (1)$$

$$a_{Or}^{kfs} = a_{Or}^{pl} \quad (2)$$

$$a_{An}^{kfs} = a_{An}^{pl} \quad (3)$$

Substitution of activity expressions (equations 11–13 in Fuhrman and Lindsley, 1988) into equations 1–3 permits the calculation of three temperatures T_{Ab} , T_{An} and T_{Or} with an error of approximately ± 40 °C. T_{Ab} , T_{An} and T_{Or} represent equilibrium temperatures and should be equal for coexisting feldspars in equilibrium. Re-equilibration due to slow cooling modifies Or and Ab contents in coexisting feldspars resulting in non-equilibrium compositions and different temperatures of T_{Ab} , T_{An} and T_{Or} . Such feldspars do not plot on a common isotherm in ternary feldspar phase diagrams and show Or-contents in plagioclase too low compared to An components in alkali feldspar (Voll et al., 1994; Pilugin et al., 2007; Jiao and Guo, 2011). Kroll et al. (1993) proposed a correction method for slowly cooled rocks from Sri Lanka to offset the retrograde K-Na exchange. Their

approach assumes that the K-Ca exchange between coexisting feldspars ceases at high temperatures whereas Na-K-exchange continues during cooling. This is because K-Ca exchange is coupled to Si-Al exchange (due to charge balance) which diffusivities are very low at dry conditions (which is assumed for Sri Lankan granulites) (Grove et al., 1984; Liu and Yund, 1992; Voll et al., 1994; Yund, 1986). During further cooling (and exsolution) the An component remains constant. Kroll et al. (1993) proposed to reverse the K-Na exchange of slowly cooled feldspars by adjusting measured Ab and Or components of coexisting feldspars at constant An-content until the equilibrium tie-line and a common isotherm on the ternary feldspar solvus are found (Raase, 1998). Resulting temperatures are estimated to have an error of ± 50 °C. The procedure was proved effective by various studies on high grade rocks (Jiao and Guo, 2011; Kroll et al., 1993; Pilugin et al., 2007; Raase, 1998).

In this study the correction procedure of Kroll et al. (1993) is applied using the Excel Spreadsheet of Benisek et al. (2004). Input data are molar Ab, Or and An contents of alkali feldspar-plagioclase pairs. The spreadsheet includes thermometric calculations. To this end, Margules parameters determined by Fuhrman and Lindsley (1988) were entered into the Spreadsheet. For thermometric calculations, the pressure was set to 8 kbar and is derived from orthopyroxene-garnet pairs in granulite facies rocks from the Highland Complex (e.g., Schumacher and Faulhaber, 1994). Output data include recalculated molar compositions and equilibrium temperatures. Ternary phase diagrams with isotherms and tie lines are obtained with the software SOLV CALC (Wen and Nekvasil, 1994) using the model of Fuhrman and Lindsley (1988). In this study feldspar compositions are given in mol% normalized to Ab+Or+An=100 mol%.

4.2.1.2. Reintegration of Exsolved Feldspars and Measuring Conditions

Exsolution of feldspars requires a reintegration of exsolved components to determine the bulk composition. Reintegration of exsolved feldspars was conducted by two methods (Raase, 1998). The first method of reintegration was carried out on film perthites and antiperthites. Film perthites were measured with a defocused beam diameter of 3 to 5 μm , thereby encompassing both, exsolved films and host grain. About 10 to 30 measurements per grain were conducted to average the bulk composition of alkali feldspars. In small and fractured/ damaged grains less measurement points were taken, but at least five. Measurement points were manually set, and care was taken to avoid fractures and other impurities. For reintegration of antiperthites a defocused beam diameter of 50 μm was selected to encompass large areas of host and coarse exsolution rods which further display perthitic exsolution themselves. A beam diameter of 100 μm was also tested but results yielded a loss of about 10 % in total weight percentages of oxides. About three to five measurement points were set along a traverse through exsolved core regions and reintegrated compositions were averaged for each grain.

The second method of reintegration was applied on coarsely exsolved string perthites. Host and string compositions were measured individually. For the measurement of strings, the probe diameter had to be adjusted to 1 μm to exclude host areas. On BSE images, volume percentages of strings and host were acquired by image analysis with the software Fiji (Schindelin et al., 2012). Volume percentages were then converted into weight percentages using densities of alkali feldspar (2.57 g/ cm^3) and plagioclase (2.67 g/ cm^3) (Smith, 1974). Finally, the molar bulk composition of alkali feldspars was calculated using weight percentages and compositions of strings and host. Only string perthites largely free of irregular and late stage exsolution were selected for the second method as these inhibit a reliable determination of string and host volume fractions.

Raase (1998) mentioned that the second method is preferred for reintegration as the first method implies a matrix-effect error. The author estimated the error to account for about 10 % for the An-content and 2 % for the Or-content. The former yields temperatures that are about 10–20° C too low. However, Raase (1998) estimated that the error in K-Na composition does not yield a significant error in two-feldspar thermometry as isotherms are nearly parallel to the Ab-Or join. Further, the author assumed the error of An to be insignificant as the An component in string perthites is mainly derived by the composition of strings. This was justified by the authors by constant An-contents in strings. This is also assessed to be true for investigated perthites in this study.

Feldspar measurements were conducted at an accelerating voltage of 10 kV, a probe current of 10 nA and a defocussed beam diameter of 1 to 5 μm (see above). These settings were selected to avoid Na evaporation. Counting times were raised to 20 seconds on peak positions and 10 seconds on upper and lower background to compensate low counting rates due to low voltage, current and defocussed beam. Si, Al and Na were detected with TAP crystals, K and Ca on PET crystals. For standard calibration natural orthoclase, plagioclase and albite minerals were used.

4.2.2. TitaniQ Thermometry

Titanium in Quartz (TitaniQ) thermometry is based on the temperature and pressure dependent substitution of Ti^{4+} for Si^{4+} on the fourfold tetrahedral site in quartz (Wark and Watson, 2006; Thomas et al., 2010; Huang and Audétat, 2012). Different TitaniQ calibrations exist which applicability depend on pressure conditions during Ti equilibration in quartz (Acosta et al., 2020; Huang and Audétat, 2012; Thomas et al., 2010; 2015). The calibration of Thomas et al (2010) was proposed for quartz deformed at high pressures and evident quartz growth (Ashley et al., 2014) and was applied in this study.

The calibration of Thomas et al. (2010) allows an estimation of TitaniQ temperatures with an error of ± 20 °C. Temperatures are calculated following the authors equation 12:

$$T(^{\circ}\text{C}) = \frac{a + c \times P}{b - R \times \ln X_{\text{TiO}_2}^{\text{Qtz}} + R \times \ln a_{\text{TiO}_2}} - 273.15 \quad (4)$$

Parameters a, b and c are the same as in Thomas et al. (2010), R is the gas constant $8.314472 \text{ J K}^{-1} \text{ mol}^{-1}$, P is the pressure in kbar and a_{TiO_2} is the activity of titania. $X_{\text{TiO}_2}^{\text{Qtz}}$ is the mole fraction of TiO_2 in quartz which is converted from the measured Ti concentration (in ppm by weight) using the appendix equation of Thomas et al. (2010):

$$X_{\text{TiO}_2}^{\text{Qtz}} = \frac{\frac{\text{Ti (ppm)}}{1\text{E}4 \times 0.599 \times 79.87}}{\frac{\text{Ti (ppm)}}{1\text{E}4 \times 0.599 \times 79.87} + [(100 - \frac{\text{Ti (ppm)}}{1\text{E}4 \times 0.599 \times 79.87}) \times \frac{1}{60.09}]} \quad (5)$$

In this study an activity a_{TiO_2} of 1 is chosen for quartz in the Qdd and is justified by the presence of rutile (Wark and Watson, 2006; Thomas et al., 2010). In the Fdd the presence of ilmenite allows to set a_{TiO_2} to 1 (Ashley et al., 2013; Ashley and Law, 2015; Ghent and Stout, 1984). The same pressure estimates of 8 kbar were selected for TitaniQ thermometry as for the two-feldspar thermometry (e.g., Schumacher and Faulhaber, 1994).

Measuring conditions were set to 100 nA probe current, accelerating voltage of 20 kV and a defocused probe diameter of 5 μm . Ti and Si concentrations were measured simultaneously on two spectrometers with PETH and TAP analyzer crystals, respectively. The measuring time for Ti was 300 and 150 s for peak and background, respectively, and for Si 10 and 5 s. Natural wollastonite and rutile standards were used for calibration of Si and Ti, respectively. For low abundant Ti in quartz the detection limit was calculated after Batanova et al. (2018). Prior to quantitative measurement quartz

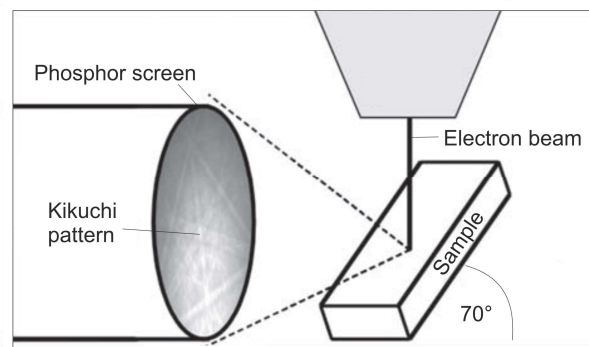
grains were inspected with a polarization microscope and by means of Cathodoluminescence (CL) (Ashley et al., 2014) and BSE imaging. CL and BSE imaging did not reveal any zonation pattern in quartz. Selected quartz grains were free of inclusions and impurities. Large grain size of quartz (100s of micrometres up to millimeters!) enabled selection of measuring areas with a distance to grain boundaries and rutile or ilmenite. For each analyzed grain 20 measurement points were sufficient to reach a constant mean value in single quartz grain analysis (Tholen, 2015).

4.3. Electron Backscatter Diffraction (EBSD) Analysis

4.3.1. Principles

Electron Backscatter Diffraction (EBSD) is a technique to determine complete crystallographic orientations of minerals (e.g., Prior et al., 1999b; Stojakovic, 2012).

EBSD measurements are performed in Scanning Electron Microscopes (SEM) in which a focussed electron beam hits a



sample surface resulting in diffraction of (redrawn after Stojakovic, 2012).

electrons (Fig. 12). The sample is tilted by 70° with respect to the horizontal to increase the interaction surface for more electrons to be diffracted. Electrons which are diffracted among lattice planes and fulfil the Bragg condition produce diffraction or Kikuchi patterns captured on a phosphor screen (Fig. 12) (Bragg, 1915; Nishikawa and Kikuchi, 1928; Prior et al., 1999b; Stojakovic, 2012). The arrangement of Kikuchi patterns reflects crystal properties: 1) the symmetry of the crystal, 2) band width and intensity are related to the atomic spacing within crystallographic planes, and 3) angles between bands reflect angles between crystallographic planes (Stojakovic, 2012). The orientation of a crystal is determined in three steps including 1) Kikuchi band detection by Hough Transformation,

2) indexing of the pattern by comparison with an integrated data base, and 3) calculation of the crystal lattice within a reference frame by rotation operations in which the orientation of the crystal lattice is defined by three Euler angles ($\varphi_1, \varphi_2, \varphi_3$) (Stojakovic, 2012).

4.3.2. Measuring Conditions

EBSD measurements were conducted at the Institute of Geology and Mineralogy of the University of Cologne on a Zeiss Sigma 300-VP field emission Scanning Electron Microscope (SEM) equipped with an EBSD NordlysNano detector (Oxford Instruments). Measuring conditions were set to an accelerating voltage of 20 kV at high vacuum of $\sim 2 \times 10^{-6}$ mbar and working distances between 8 and 15 mm depending on the position of the region of interest within the thin section. An aperture of 120 μm was chosen and a resulting high dead time was compensated by the lowest processing time adjustment of 1 ($\sim 10\text{--}20\%$ dead time). The background was subtracted (static, about 100 frames) to improve the contrast of Kikuchi patterns which were indexed based on edge detection with a Hough resolution of 70. Five to seven Kikuchi bands were defined for phase indexing. For EBSD mappings the binning modulus was set to 2x2 at a frame number of 2. Step sizes ranged between 5 and 30 μm depending on grain size. The compliance of primary (sample) and secondary (device) coordinate systems was reviewed by the measurement of a quartz standard sample with known crystallographic orientation. For data acquisition the Aztec Software of Oxford Instruments was used. Integrated libraries for crystallographic data of HKL and American Mineralogist were used for automatic indexing of quartz (*Quartznew*, HKL) and alkali feldspar (*Orthoclase*, American Mineralogist). Best indexing of plagioclase was achieved using data of *OligoclaseAn28* (Phillips et al., 1971) obtained from the external data base *American Mineralogist Crystal Structure Database* (rruff.geo.arizona.edu/AMS/amcsd.php). EBSD data processing was

performed with the Mambo, Tango and Project Manager programs of the HKL Channel 5 software of Oxford Instruments.

4.3.3. Data Collection and Processing

4.3.3.1. EBSD Point Measurements

Point measurements were conducted to determine CPOs of quartz and feldspar. To this end the orientation of about 100–170 grains per phase and domain was manually measured. In the case of coarse-grained quartz care was taken to avoid double measurement of individual grains dissected in multiple fragments in thin section. This was accomplished by double checking interference colours on thin section scans in combination with recurrence of identical orientations. Misindexing between alkali feldspar and plagioclase was a common problem due to similar crystal structure. This was prevented by double checking grains of interest on simultaneously recorded BSE images. CPOs are presented in contoured pole figures in equal area lower hemisphere projections. Contouring of pole figures is produced using a halfwidth of 10° and a cluster size of 5. The contouring shows the clustering of individual grain orientations with respect to a random distribution as multiples of uniform distribution (mud) and the texture strength is defined by the maximum value.

4.3.3.2. EBSD Mapping

EBSD mappings were conducted to analyse internal misorientations of single grains, domanical misorientation relationships and for the boundary trace analysis. EBSD maps were recorded as single maps and large area maps. The latter is constituted of multiple fields which were merged for coherent analysis. Coarse-grained quartz in D1 ideally requires EBSD mappings of entire thin sections for measuring sufficient grains and grain boundaries. However, this cannot be achieved without a loss in Kikuchi pattern quality because the pattern quality depends on a close position between sample and phosphor

screen (Fig. 12) (Halfpenny, 2010). Due to sample tilting, the acquisition of EBSD data in lower parts of a thin section requires that the sample stage is moved away from the phosphor screen. This increases the distance between the sample surface in lower thin section areas and the phosphor screen because the EBSD detector is fixed to a specific position. Thus, trajectories of diffracted electrons are prolonged resulting in bad pattern quality. For the sake of good pattern quality, it was decided to conduct large area mappings without stage movement away from the detector and to compensate small datasets of coarse-grained quartz by acquisition of multiple individual maps.

For error correction raw EBSD maps were automatically and manually processed with respect to wild spikes, zero solutions, artefacts and misindexing following the procedure described by Bestmann and Prior (2003). Misindexing was significant for feldspars (see above) and was checked by comparison with simultaneously acquired element maps and BSE images. Once a misindexed feldspar was identified the phase transition tool of Tango was applied.

EBSD maps are displayed as pattern quality maps overlain by orientation maps which show crystallographic orientations of individual grains with respect to the X-direction of the sample reference frame (inverse pole figure colour coding). Grain boundaries are defined by a misorientation of $>10^\circ$ and black coloured. Subgrain boundaries are presented for misorientations $>2^\circ$ (yellow), $>3^\circ$ (green) and $>5^\circ$ (pink). For quartz additionally Dauphiné twin boundaries are highlighted in red. EBSD maps are further processed for Schmid factor and GROD angle representation. Their constituents are in the following briefly explained:

The *Schmid factor* describes the relationship between external normal stresses and shear stresses caused in a slip system (Schmid and Boas, 1950). It is a measure of how easy it is for slip to occur on a specific slip system. In Tango the Schmid factor is calculated at each

measuring point within a grain and displayed as colour in the map. Additionally, a frequency distribution of Schmid factors is given in histograms. In this work, the Schmid factor was calculated for quartz with a load direction parallel to Z of the sample reference frame. The following slip systems were considered: basal<a>, rhomb {r}<a>, prism<a>, prism[c].

The *Grain Reference Orientation Deviation* (GROD) is a measure of the internal misorientation within a grain. The GROD angle is defined as the deviation of a single point orientation from an average orientation within a single grain. The average orientation calculation per grain is based on the user-defined grain detection. In twinned grains GROD angles are biased towards high values of average orientation because twin boundaries are characterized by misorientations $>10^\circ$ (e.g., 60° misorientation for quartz Dauphiné twin boundaries). Therefore, twin boundaries are considered as grain boundaries for the calculation of the GROD angle to highlight internal grain misorientation defined by misorientations $<10^\circ$. GROD maps are colour coded with respect to the GROD angle (0– 10°).

Grain size determinations were conducted in Channel 5 for further quartz classification. To this end grain areas were determined in each map with the *grain area determination* function in Tango. Determined grain areas were converted to equivalent circular diameters and, for each category, the mean grain size was calculated based on area weighting (Berger et al. 2011). EBSD based grain size estimations are complementary to the orientation dependent classification of quartz and do not contribute to chapter 7, which deals with grain sizes. EBSD grain size estimation was not conducted for coarse-grained quartz in D1 as corresponding maps do not contain enough quartz grains.

4.3.4. Misorientation Analysis

The misorientation analysis was performed on processed EBSD maps and includes the presentation of misorientation angle distributions, misorientation axis/ angle pair distributions and boundary trace analysis. The minimum misorientation angle was always set to 2° as the angular uncertainty increases for small misorientation angles (Prior; 1999a; Wheeler et al., 2001).

Misorientation angles are displayed in frequency distribution diagrams and give relative frequencies. Misorientation angle distributions are given for correlated and uncorrelated data pairs and theoretical random distributions are inserted. For uncorrelated distributions, the number of misorientations was set to a standard value of 1000 data points. Quartz correlated misorientation angle distributions are presented for the complete data set and for on one point per boundary disregarding Dauphiné twin boundaries. The latter was chosen because few long grain boundaries and abundant Dauphiné twin boundaries bias the misorientation angle distribution. Misorientation angle distributions are obtained from representative large area maps.

The distribution of misorientation axes is shown for specific misorientation angles (axis-angle pairs). Misorientation axis-angle pairs can be defined by several equivalent axis/ angle pair combinations. By convention, the combination with the smallest misorientation angle was chosen (Wheeler et al., 2001). Axis-angle pairs were grouped with respect to misorientation angle classes. For quartz and feldspar, the class of misorientation angles $2\text{--}10^\circ$ refers to internal misorientations associated with subgrain boundaries. Misorientation axis-angle pairs for angles $>10^\circ$ refer to grain and twin boundaries. For quartz, these classes are $10\text{--}55^\circ$, $55\text{--}65^\circ$ and $65\text{--}110^\circ$ and are based on one point per boundary data sets. For feldspars, a subdivision gives classes $10\text{--}170^\circ$ and $170\text{--}180^\circ$ and is based on the complete data set. In quartz and alkali feldspar large misorientation angles

are restricted to specific crystallographic regions due to symmetry constraints (Lloyd, 2004; Wheeler et al., 2001). Crystallographic areas outside these regions are referred to as "forbidden regions" and are indicated in inverse pole figures.

Feldspar misorientation axes are presented in contoured pole (sample coordinates) and inverse pole figures (crystal coordinates). Contouring was performed under same settings as for pole figures presenting CPOs. Quartz misorientation axes are presented in pole/inverse pole figures presenting point data. Point data presentation was preferred over contoured data presentation because in the latter misorientation data of only few grain and subgrain boundaries bias contoured misorientation distributions in individual maps. To approach representative bulk misorientation distributions in each domain, misorientation data of all EBSD maps per domain were combined. The combination of misorientation data was conducted with the image analysis software Fiji (Schindelin et al., 2012) (command "AND-adding") by merging image files of pole/ inverse pole figures presenting point data. The resulting image files could not further be contoured.

The boundary trace analysis (Prior et al., 2002) was conducted along individual subgrain boundaries (Fig. 13a). The orientation of the corresponding misorientation axis was identified in crystal (inverse pole figures) and sample coordinates (pole figures) (Fig. 13b). The slip system specific rotation axis was determined in pole figures following the dispersion path procedure (Fig. 13c) (Prior et al., 2002). The interpretation of the boundary trace analysis was based on a tilt boundary model (see chapter 1, Fig. 3a, b).

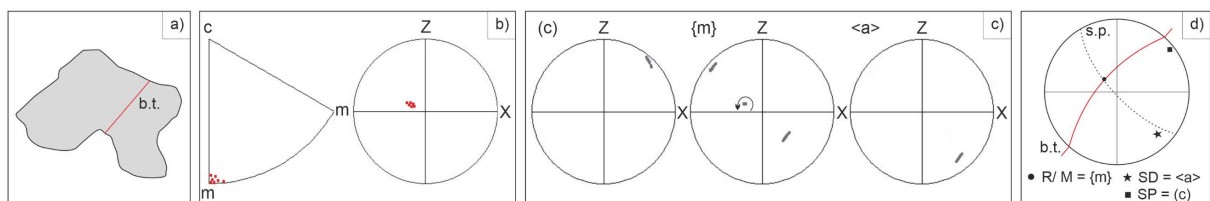


Fig. 13: Procedure of a boundary trace analysis in exemplary fashion for quartz: a) subgrain boundary in quartz (red line); b) misorientation axis plots around m-direction of quartz (inverse pole figure) and around the foliation plane (pole figure); c) orientation of quartz presented by poles to (c), {m} planes and <a> direction; one of the {m} poles shows least dispersion (arrow circle) and is the rotation axis; d) final interpretation of (c)<a> slip system (b.t.: boundary trace, R: rotation axis, M: misorientation axis, SD: slip direction, SP: slip plane).

4.4. Analysis of Modal Content, Grain Size, Shape and Connectivity

Quantification of modal content grain size, shape and connectivity was made via image analysis with the image analysis software Fiji (Schindelin et al., 2012) and JAZY macros (by Rüdiger Kilian, available at <https://earth.unibas.ch/micro/index.html>). Image analysis was conducted on grain maps which display each grain of a particular phase (Figs 14, 15). Grain maps were established by hand tracing and by image processing. Grain maps produced by hand tracing were established using the graphic software Corel Draw Graphic Suits (2020) (Fig. 14). This procedure was mainly applied for coarse-grained quartz (Qdd and Fdd ribbons) on thin sections scans in which entire thin sections represent subdomains. The second method is based on image processing of BSE images using Fiji. This method utilizes the compositional information in BSE images represented by individual grey scales for each phase (Fig. 15a). The method implies a multistep procedure including noise reduction, segmentation of phases based on grey values, and different copy commands and is based on the principle described by Heilbronner and Barrett (2013). This method was applied on matrix grain maps in the Fdd.

4.4.1. Quantified Parameters

The modal content was estimated as area fraction. According to Heilbronner and Barrett (2013), the measured area fraction of a phase can be assumed as estimation of the volume

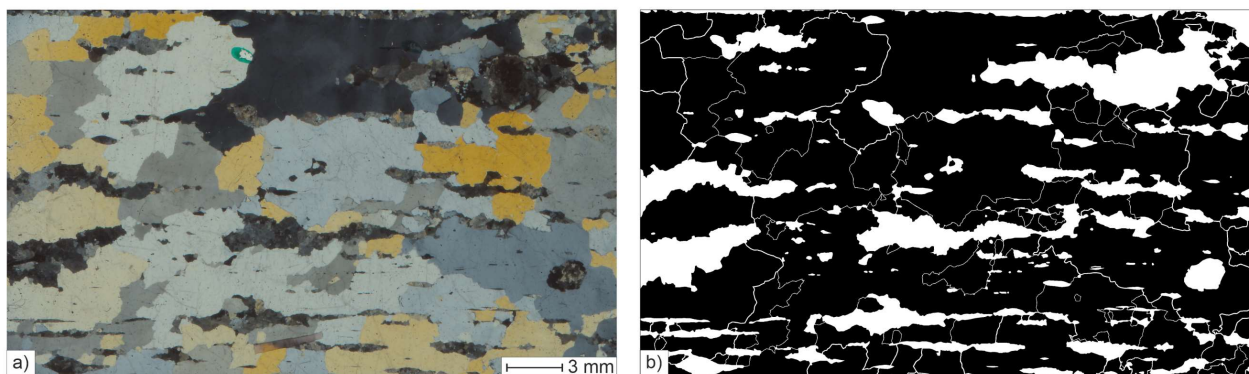


Fig. 14: Quartz grain map (b) established by hand tracing of grain boundaries on thin section scan (a) (recorded with polarization filter).

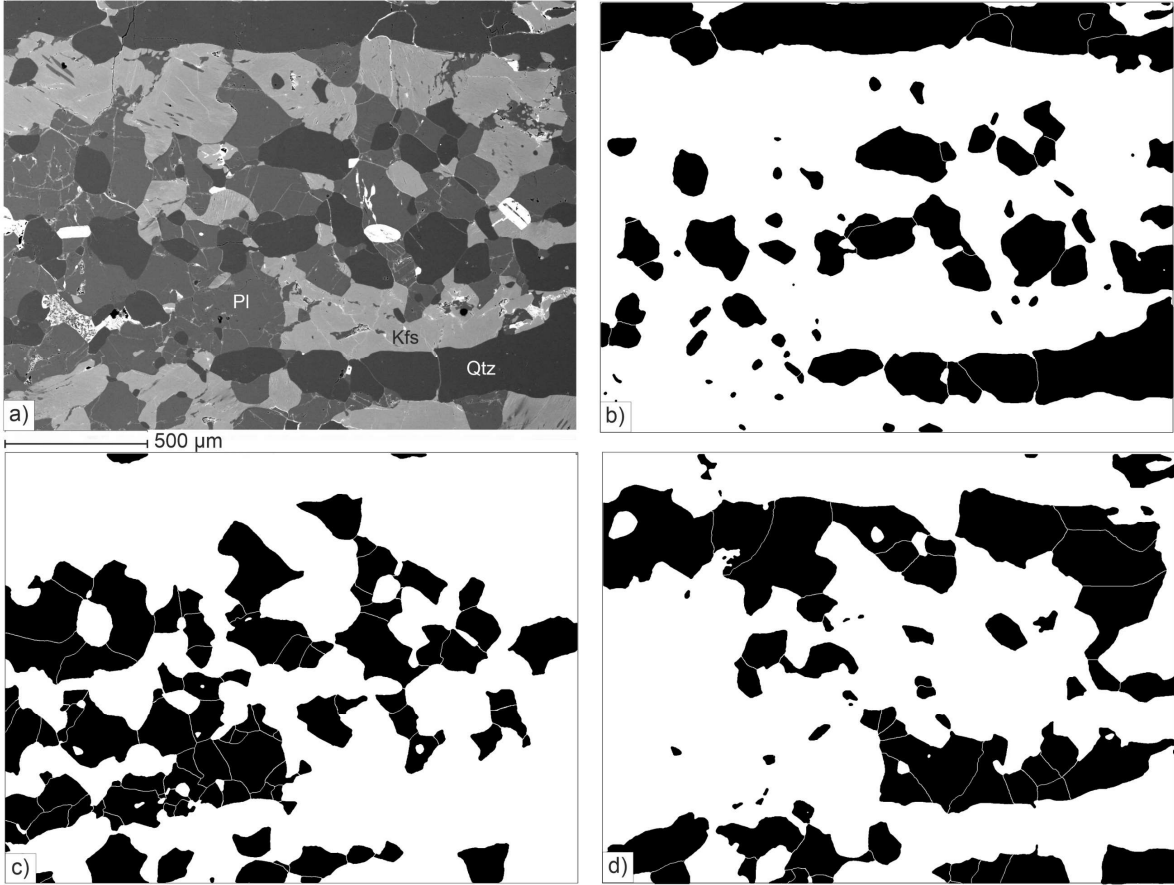


Fig. 15: Grain maps of quartz (b), plagioclase (c) and alkali feldspar (d) established by image processing of BSE image files (a).

fraction of this phase. In this work the area fraction of a phase is herinafter designated as volume fraction.

Grain sizes are given as Feret diameter. The Feret diameter is defined as the longest distance between two points in a cross-sectional area of a grain. Mean grain sizes are area weighted to avoid underestimation of real grain sizes due to sectioning effects. The mean area weighted grain size \bar{d} was calculated using the following equation (Berger et al., 2011):

$$\bar{d} = \frac{w}{\sum_{i=1}^{n_{tot}} A_i} \times \sum_{j=1}^{j_{tot}} (j \times \sum_{i=1}^i A_{ji}) \quad (6)$$

where w is the class width of grain size classes, n_{tot} is the number of measured grains, A_i is the area of the i th grain, j_{tot} is the number of grain size classes j . From equation 6 it becomes evident that the value of \bar{d} depends on the number of classes at a given class

width. It could be shown that the mean grain size decreases with increasing number of classes until it reaches a constant value (Thor, 2019). Therefore, \bar{d} is given as minimum value at the maximum reasonable number of grain size classes at a given class width. Grain size distributions are presented in frequency diagrams based on area weighting and the frequency is given as percentage. Grain size distributions are presented for main domains only (D1+D0, D2, D3, D4) ensuring a sufficient number of grains (at least 200, Berger et al., 2011).

Aspect ratios were determined to quantify the elongation of a grain. In Fiji, the aspect ratio is determined from a fitted ellipse of each grain as quotient of the major axis (longest) and minor axis (shortest). An aspect ratio of 1 defines a circular shape and aspect ratios increase with elongation of grains.

Paris factor and angularity were analyzed to describe the irregularity and smoothness of grain boundaries. The Paris factor (introduced by Panozzo and Hürlimann, 1983) is defined as the percentile average relative indented surface and gives the deviation of a grain area from the area of its convex hull enveloping this grain. For fully convex grain shapes the Paris factor is 0 % and increases with indentation of grain shapes. In Fiji, the Paris factor was calculated using the macro JAZY_Env_map.

The angularity is a measure of smoothness of grain boundaries (Heilbronner and Barrett, 2013). To estimate angularity, outer angles of polygonal chains were measured which define the outline of a grain. These angles are referred to as vertex angles. The sum of vertex angles defining a grain is 360° . The angularity of a grain is given as Ω and/ or Ω' defined as the fraction of vertex angles smaller 0° and between -10 and -180° , respectively. In this work it will be referred to Ω' because small negative angles usually occur as artefacts of improper digitization (Heilbronner and Barrett, 2013). The angularity was determined with the software iSHAPES (by Rüdiger Kilian, available at

<https://earth.unibas.ch/micro/index.html>). Input data were generated in Fiji with the macro `Jazy_XY_export_header`. The macro produces files with smoothed, interpolated coordinates of particles from a binary image. The spacing between nodes (points between recorded coordinates) was set between 6 and 10 pixel and was adjusted to the shortest straight section of a grain within a grain map.

The connectivity was measured in terms of a dispersion factor C_k and contact frequencies. The factor C_k is defined as the sum of k -order connectivity ratios of a given phase (Hunter et al., 2016; Zhanga et al., 1992):

$$C_k = \sum \frac{b_k}{(b_0 + b_c)} \quad (7)$$

where b_k is the number of connected grains of k -order, b_c is the number of adjacent grains, and b_0 is the number of isolated grains. Values approaching 0 for C_k refer to isolation of a phase and C_k of 1 refers to an interconnected framework. In Fiji neighbour analysis was conducted with the BioVoxel Toolbox for Fiji (Brocher, 2015). The neighbour analysis tool of BioVoxel calculates the number of neighbours for each grain on a bitmap.

Contact frequencies were calculated for boundaries of the same phase referred to as like-like boundaries (grain boundaries). In this sense, contact frequencies are a measure of connectivity. The frequency of like-like boundaries was calculated as the fraction of grain boundaries:

$$\text{like - like boundaries} = \frac{\text{length } gb}{\text{length } pb + \text{length } gb} \times 100 \quad (8)$$

where gb and pb refer to grain and phase boundaries. The length of boundaries was determined in Fiji by pixel counting of phase and grain boundaries.

All measures of modal content, grain size, shape descriptors and connectivity are given for individual grain maps and as average values for main domains. In grain maps grain

size, aspect ratio, Paris factor and angularity are mean values. For the determination of grain size and shape grains were excluded which were truncated by the edge of the grain map. For the calculation of the dispersion factor C_k grains touching edges were only considered as neighbours of grains not truncated at edges.

4.4.2. Zener Parameter

The Zener parameter relates the volume fraction f_p with the area weighted mean grain size d_p of a second phase and is $Z=d_p/f_p$ (Herwegh and Berger, 2004). In a Zener plot the grain size D of a dominant matrix phase is related with the Zener parameter (Fig. 5). This relation was applied in the present study in the Qdd where quartz is the dominant matrix phase and feldspar constitutes the second phase. Pinning of quartz grain boundaries occurs rather by feldspar aggregates than by single feldspar grains. Therefore, the Zener parameter was modified with respect to d_p which is represented by the feldspar aggregate size (Fig. 16). Feldspar aggregate size was determined in aggregate maps (Fig. 16b). Aggregate maps were created in Fiji by inversion of black and white pixels in quartz grain maps (compare Figs. 14 and 16) and quartz grain boundaries were removed. Aggregate size estimation was performed following the same procedure as for grain size analysis.

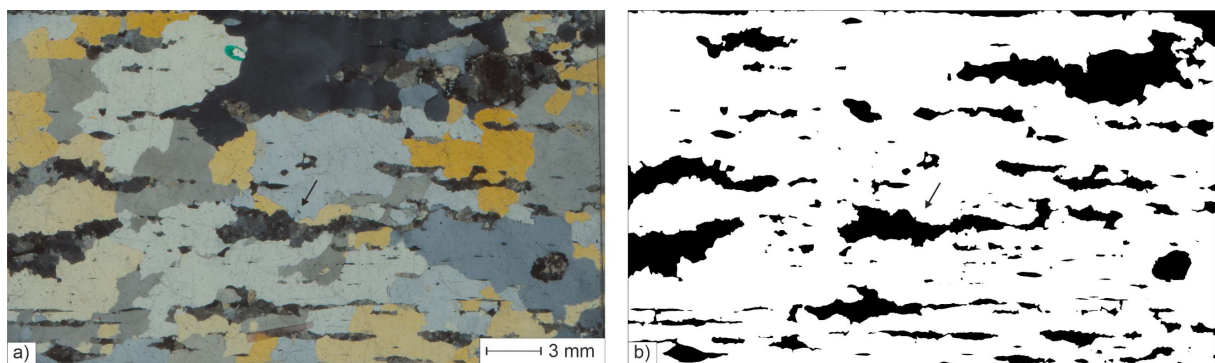


Fig. 16: Feldspar aggregate map: a) same thin section as shown in Fig. 14a; b) Feldspar aggregate map (arrows point to same aggregates).

4.5. Curvature and Dihedral Angle Analysis

For the analysis of curvature 150 like-like grain boundaries per domain were measured (when available). Only grain boundary sections between triple junctions were considered because otherwise the curvature of the perimeter of isolated grains/ grain fragments would be included. The measurement of grain boundaries was carried out on polarization microscopy image files and on BSE images at same resolution. The measurement of grain boundaries was conducted with the Kappa plugin (Mary and Brouhard, 2019) for Fiji. In Kappa a boundary segment is traced manually by setting control points to establish a B-spline curve. This curve is fitted to the control points by a least square based minimization algorithm. The curvature is defined as $1/r$ which describes the curvature of a circle at a specific point of a curve with r being the radius of the circle. The curvature of a boundary segment is given as the average curvature in μm^{-1} of all circles defining this segment. In this work the average curvature of a grain boundary is abbreviated as curvature.

Frequency distributions of measured curvature are presented in histograms in absolute frequencies and the value of maximum curvature is given. The parameter C_s is introduced to quantify the grade of straightness of a grain boundary and is defined as the fraction of measured grain boundaries with *straight curvature* of $<0.004 \mu\text{m}^{-1}$. In a testing phase, this value turned out to define straight grain boundaries adequately. A high value of C_s approaching 100 % gives a high fraction of straight grain boundaries and C_s of 0 % is characteristic for highly curved grain boundaries.

The analysis of apparent dihedral angles included the measurement of 150 angles per domain (when available). The measurement was conducted with the angle tool of Fiji. Only apparent dihedral angles with a sum of $360^\circ \pm 5^\circ$ for each triple junction were considered to keep the error small. The measurement was conducted on polarization microscopy and BSE images at same resolution. The parameter Tj_{120} is introduced as

measure for equilibrated textures and is defined by the percentage of measured angles of $120^{\circ} \pm 10^{\circ}$. In a testing phase an angle of 90° was frequently detected in deformed assemblages. 90° angles were also observed in other studies investigating deformed quartz (e.g., Lister and Dornsiepen, 1982; Little et al., 2013; Pennacchioni et al., 2010). Therefore, T_{j90} is introduced as percentage of measured angles of $90^{\circ} \pm 10^{\circ}$ and is tested as indicator for deformed assemblages.

Apparent dihedral angles are plotted in histograms in absolute frequencies and as cumulative frequency curves. The latter serves for comparison with results of Elliott et al. (1997). The authors conducted three-dimensional numerical simulations to generate equilibrated and unequilibrated monomineralic textures and analyzed dihedral angle distributions. For comparison only their curves for fully crystallized textures are used. In this study the term apparent dihedral angle is abbreviated to dihedral angle.

5. Thermometry

The composition of feldspar-pairs considered two-feldspar thermometry was investigated in D1 A, D1 L, D3 and D4. In D3 and D4 feldspars were analyzed in kfs dominated domains (D3), *boundary layers* (D3, D4) and in D4 domains with about equal amounts of alkali feldspar and plagioclase (Fig. 17). Boundary layers are characterized by adjacent kfs and pl dominated domains (Fig. 17f). This subdivision was conducted to determine possible compositional differences with respect to different deformation behaviour in pure and mixed domains.

D1 L and kfs dominated domains are characterized by large grain sizes of the dominant

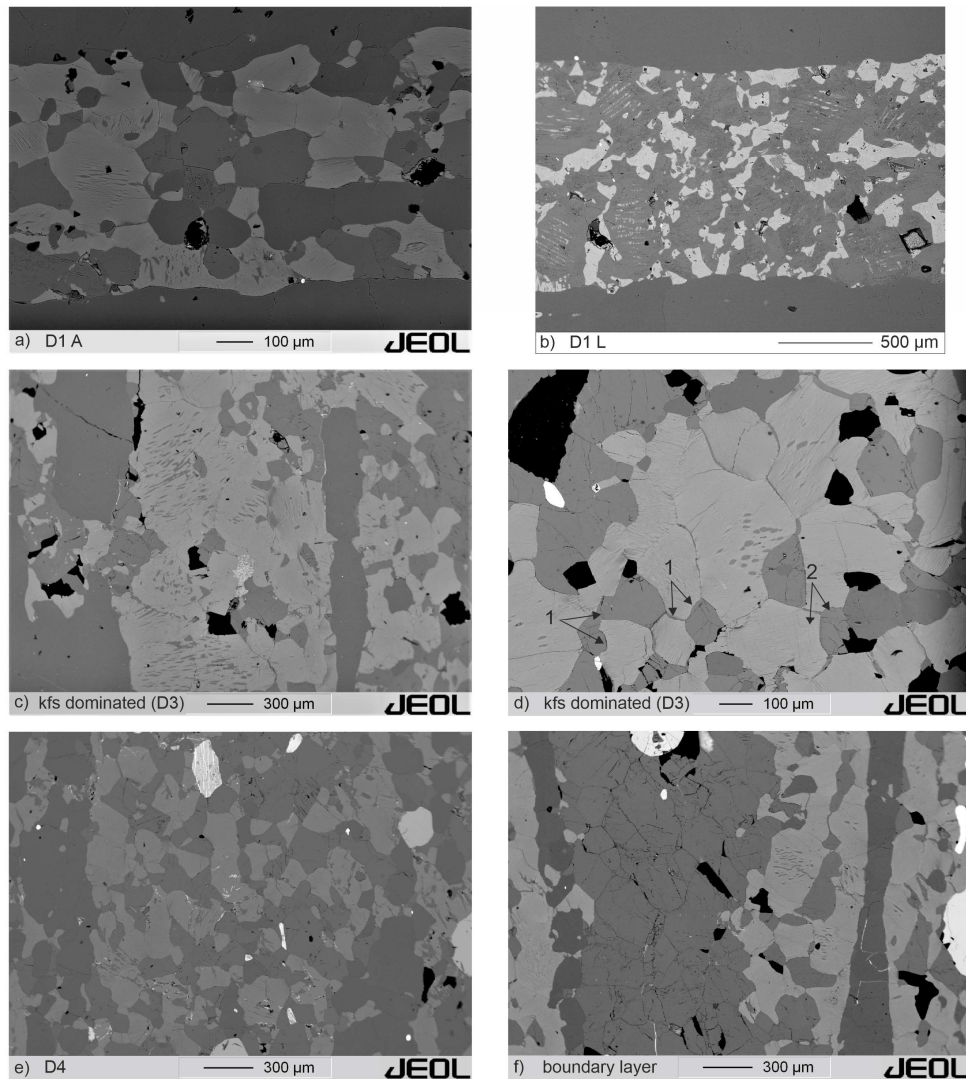


Fig. 17: Measuring Domains for two-feldspar thermometry (BSE images): d) feldspar pairs of similar grain size (1) and pairs of small pl grains and rim regions of large kfs (2); f) boundary layers of pl dominated domains (centre) and adjacent kfs dominated domain (on the right-hand side) (for further explanation see text.).

feldspar and small grain sizes of the minor feldspar (Fig. 17b-d). Only similar sized alkali feldspar and plagioclase were selected as feldspar pairs considering equivalent diffusion pathways (1 in Fig. 17d). In kfs dominated domains additionally non-exsolved rim areas of alkali feldspars were selected as thermometry partner (2 in Fig. 17d). Furthermore, reintegrated core compositions of string/ spindle perthites and antiperthites are given. For the application of the TitaniQ thermometer the Ti content was measured in quartz of D1, D2 and in quartz ribbons of D3 and D4.

5.1. Results

5.1.1. Two-Feldspar Thermometry

5.1.1.1. Remarks on Recalculated Compositions of Feldspar Pairs

Fig. 18 shows analyzed and recalculated compositions of alkali feldspar-plagioclase pairs in a ternary feldspar diagram (see also Table 1). Analyzed compositions of coexisting feldspars do not plot on a common isotherm. Recalculation shifts compositions on common isotherms with equilibrium tie lines while An-content is fixed. In general, recalculation generates a gain in Or-content for plagioclase whereas alkali feldspar loses some of its Or-component reflecting the reverse of Na-K exchange. Parallel tie lines between recalculated feldspar pairs within each domain indicate that recalculated compositions represent equilibrium compositions.

5.1.1.2. Composition and Temperature

In D1 A alkali feldspars yield a mean composition of $Ab_{31.6}Or_{66.7}An_{1.7}$ (Table 1, Fig. 18). The composition of plagioclase is in average $Ab_{75.0}Or_{10.7}An_{14.3}$. Recalculated compositions of feldspar pairs yield a mean temperature of $773\text{ }^{\circ}\text{C} \pm 36\text{ }^{\circ}\text{C}$ in D1 A (Table 1).

Feldspars pairs in D1 L yield mean compositions of $Ab_{19.7}Or_{79.9}An_{0.3}$ for alkali feldspar and $Ab_{83.0}Or_{4.9}An_{12.1}$ for plagioclase. The resulting temperature is $611\text{ }^{\circ}\text{C} \pm 42\text{ }^{\circ}\text{C}$. Alkali

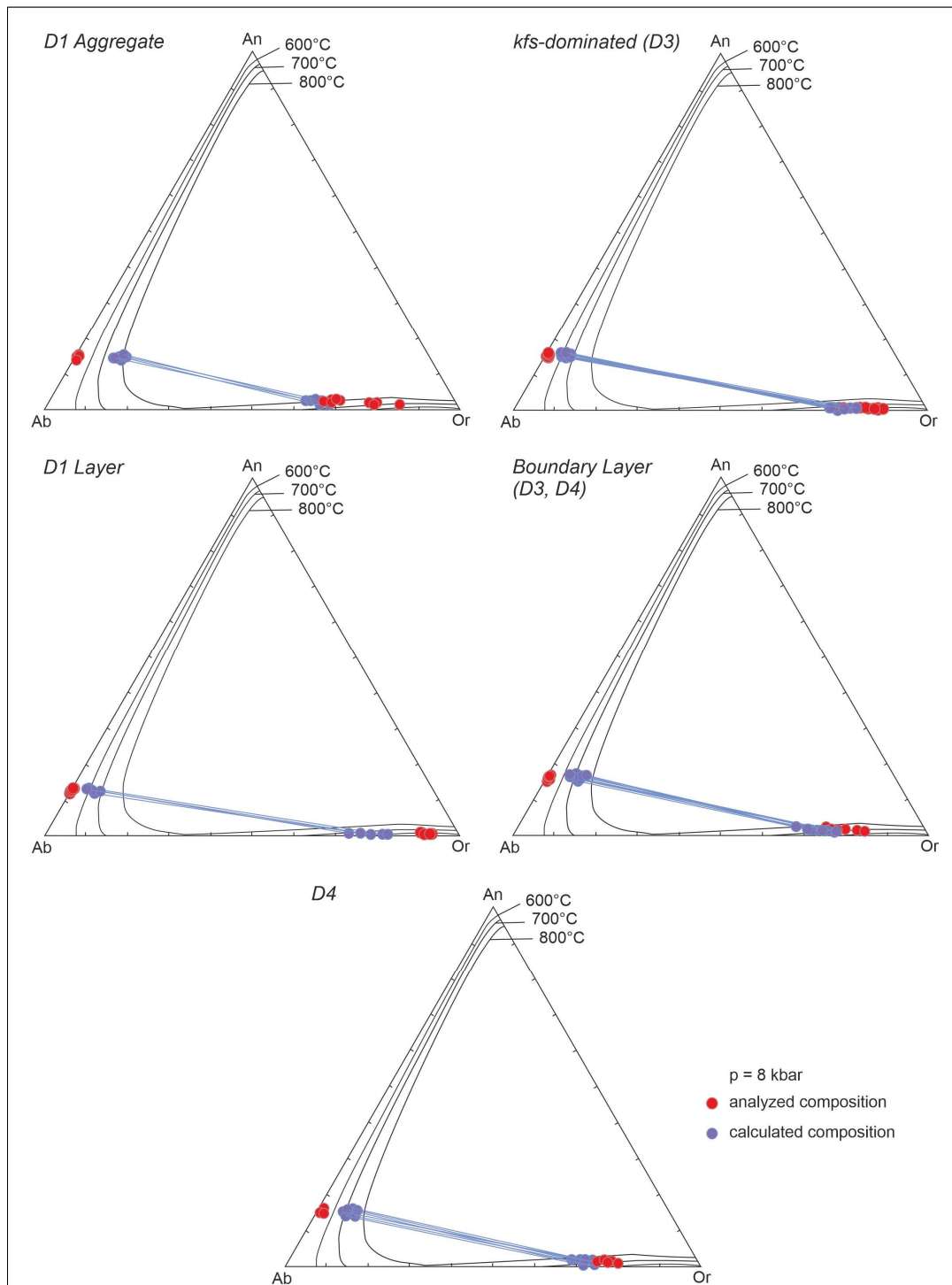


Fig. 18: Ternary feldspar diagrams: analyzed and recalculated compositions and isotherms; tie-lines are shown for calculated compositions.

feldspars in D1 L display lowest An-contents of all analyzed alkali feldspars of 0.3 mol.-% in average. Low An-contents of 0.1 mol.-% of individual alkali feldspars (P1, P3, P6) disable a recalculation of analyzed compositions after Kroll et al. (1993) resulting in discordant temperatures of T_{Ab} , T_{Or} and T_{An} (Table 2). However, T_{Ab} and T_{Or} are nearly

concordant, and T_{An} is ~ 100 °C lower suggesting inaccuracies in the detection of the An-content in alkali feldspar. In such cases, Fuhrman and Lindsley (1988) suggested that the mean temperature is best represented by concordant temperatures T_{Ab} and T_{Or} which were selected in this study.

Antiperthites in D1 L yield a reintegrated average core composition of $Ab_{77.8}Or_{12.8}An_{9.5}$. Core compositions plot on the same isotherm as average plagioclase compositions in D1 A (Fig. 19).

Table 1: Two-Feldspar Thermometry: analyzed and recalculated mean compositions and temperature estimates.

Sample	Fsp	Composition analyzed			Composition calculated			T (°C)	SD ^a (°C)
		Ab	Or	An	Ab	Or	An		
D1 A	kfs	23.2	75.1	1.7	31.6	66.7	1.7	773	36
	pl	84.8	0.9	14.3	75.0	10.7	14.3		
D1L	kfs	7.6	92.0	0.3	19.7	79.9	0.3	611	42
	pl	87.1	0.8	12.1	83.0	4.9	12.1		
	AP ^b				77.8	12.8	9.5		
D3	kfs	14.6	84.9	0.6	19.9	79.5	0.6	637	28
	pl	83.8	0.9	15.3	79.6	5.1	15.3		
	kfs rim	14.0	85.4	0.6	20.8	78.6	0.6		
	SP ^b				21.4	77.0	1.6		
D4	kfs	19.4	79.4	1.1	26.0	72.9	1.1	713	53
	pl	83.7	1.0	15.4	76.8	7.8	15.4		
BL ^a	kfs	19.7	79.1	1.2	26.0	72.9	1.2	718	35
	pl	83.0	1.1	15.9	76.3	7.8	15.9		

^a Standard Deviation (SD), Boundary Layer (BL)

^b Reintegrated core compositions of Antiperthites (AP) and String/ Spindle Perthites (SP).

Table 2: Discordant temperatures in D1 layers: only recalculated compositions are shown (see Appendix Table 1 for analyzed compositions).

Sample	Feldspar	Composition calculated			T(Ab)	T(Or)	T(An)	T (°C) ^a
		Ab	Or	An				
<i>D1L</i>								
P1	kfs	16.7	83.2	0.1	578	581	413	579
	pl	83.2	3.9	12.9				
P3	kfs	15.5	84.4	0.1	556	574	483	565
	pl	83.9	3.9	12.2				
P6	kfs	19.3	80.6	0.1	583	571	496	577
	pl	87.8	4.2	8.0				

^a mean of T(Ab) and T(Or).

In kfs dominated domains of D3 feldspar pairs yield mean compositions of $Ab_{19.9}Or_{79.5}An_{0.6}$ for small alkali feldspars, $Ab_{20.5}Or_{78.7}An_{0.8}$ for non-exsolved rim areas of string/ spindle perthites, and $Ab_{79.6}Or_{5.1}An_{15.3}$ for plagioclase. The resulting temperature is in average $637\text{ }^{\circ}\text{C} \pm 28\text{ }^{\circ}\text{C}$. There is no significant difference between temperatures calculated from small alkali feldspars and rim areas (Appendix Table 1). Reintegrated compositions of string/ spindle perthites display a mean of $Ab_{21.4}Or_{77.0}An_{1.6}$.

Feldspar pairs in D4 reveal recalculated mean compositions of $Ab_{26.0}Or_{72.9}An_{1.1}$ for alkali feldspar and $Ab_{76.8}Or_{7.8}An_{15.4}$ for plagioclase. Feldspar pairs from boundary layers yield compositions of $Ab_{26.0}Or_{72.9}An_{1.2}$ for alkali feldspar and $Ab_{76.3}Or_{7.8}An_{15.9}$ for plagioclase. Temperature estimates yield similar mean values of $713\text{ }^{\circ}\text{C} \pm 53\text{ }^{\circ}\text{C}$ and $718\text{ }^{\circ}\text{C} \pm 35\text{ }^{\circ}\text{C}$ in D4 and boundary layers, respectively, and agree with similar compositions (Table 1, Fig. 19). These temperatures agree with temperature estimates in D1 A within an error of $\pm 40\text{ }^{\circ}\text{C}$ (Fuhrman and Lindsley, 1988). Reintegrated core compositions of string/ spindle perthites in kfs dominated domains plot on the same isotherm as recalculated mean alkali feldspar compositions in D4 and boundary layers (Fig. 19).

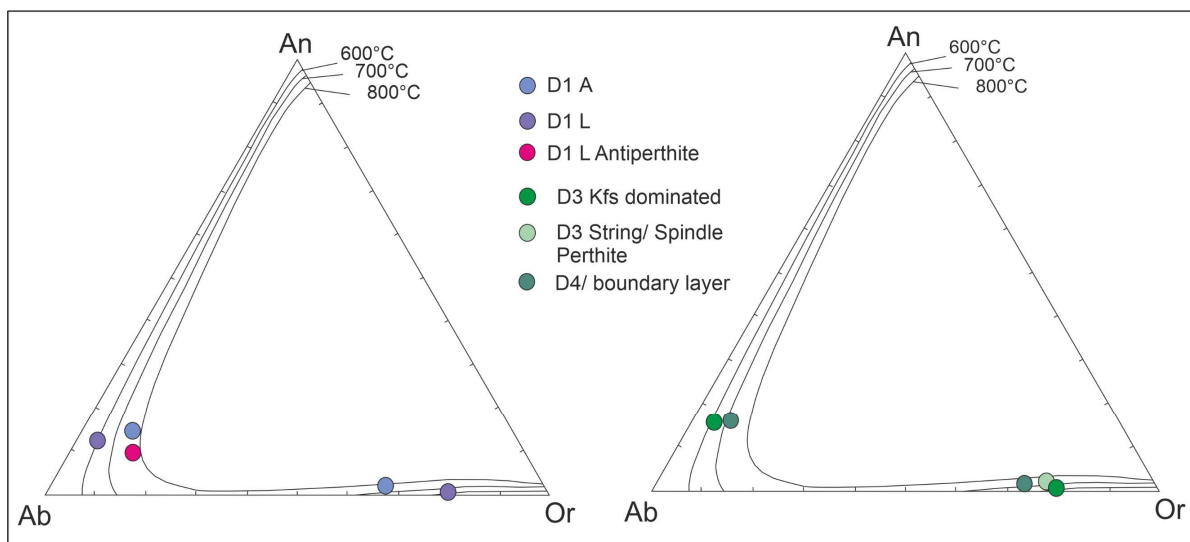


Fig. 19: Mean feldspar compositions in ternary diagrams.

5.1.2. TitaniQ Thermometry

The Ti content in quartz of D1 and D2 varies for less than 20 ppm which corresponds to the calculated detection limit (Table 3). The average Ti content of quartz in the Qdd is 284 ppm. The resulting average temperature is $836 \text{ }^{\circ}\text{C} \pm 3 \text{ }^{\circ}\text{C}$.

In quartz ribbons of D3 and D4 the scatter of Ti content is somewhat higher than in the Qdd, but still minor of about 30 ppm. The average Ti content is 247 ppm and results in a mean temperature of $817 \text{ }^{\circ}\text{C} \pm 6 \text{ }^{\circ}\text{C}$.

Measured Ti contents are consistent within the Qdd and Fdd and mean temperatures are within error of $\pm 20 \text{ }^{\circ}\text{C}$ (Thomas et al., 2010).

Table 3: Results of Ti in Quartz analysis and thermometry.

Sample	N ^a	Ti (ppm)	DL ^b	SD ^b	T ($^{\circ}\text{C}$)
Qdd					
D1-1	24	294	17	6	840
D1-2	22	292	18	5	839
D1-3	20	285	19	5	836
D2-1	24	276	20	6	832
D2-2	20	281	20	5	834
D2-3	20	278	20	5	833
Mean ^c	6	284		7	836 ± 3
Fdd					
D3-1	20	239	17	9	813
D3-2	20	240	19	7	813
D3-3	20	260	19	6	824
D4-1	20	258	20	7	823
D4-2	20	254	20	7	821
D4-3	20	229	20	7	807
Mean ^c	6	247		12	817 ± 6

^a Number (N) of measurements per grain and analyzed grains per domain

^b Detection Limit (DL) and Standard Deviation (SD) of analyzed Ti concentrations per grain

^c Mean values refer to the number of analyzed grains.

5.2. Discussion

5.2.1. Two-Feldspar Thermometry

In both, the Qdd and Fdd, temperature estimates are lower in domains with a predominant feldspar phase (D1 L and kfs dominated domain, D3, Fig. 17b-d) compared to domains with similar amounts of plagioclase and alkali feldspar (D1 A, D4). Furthermore, in D1 L and D3 grain sizes of minor feldspar phases are considerably smaller compared to the dominant feldspar phase. Small sized grains have short diffusion paths. Hence, Na-K exchange is faster accomplished. Moreover, in D1 L and kfs dominated domains the minor feldspar phase is often surrounded by the dominant feldspar phase and exchange reactions can act on all grain boundary sites enhancing Na-K exchange during cooling. Enhanced exchange reactions are indicated in D1 L by a great shift between analyzed and calculated compositions of minor, small-sized alkali feldspar compared to major, coarse-grained plagioclase (Fig. 18). Following this argumentation, larger grain sizes in D1 A and D4 result in longer diffusion paths. Thus, exchange reactions during cooling affect mostly rim regions while high temperature compositions may be preserved in cores. This suggestion is supported by core compositions of coarse-grained antiperthites (D1 L) and string/ spindle perthites (kfs dominated domain, D3) which plot on same isotherms as feldspar pairs in D1 A, D4 and boundary layers, respectively (Fig. 19). A further explanation for lower temperature estimates of small-sized feldspar pairs may be chemically driven recrystallization at lower temperatures. Chemically driven recrystallization is commonly observed to result in decomposition of feldspar hosts into fine-grained plagioclase and alkali feldspar with new composition (e.g., Franek et al., 2011; Menegon et al., 2013). However, in kfs dominated domains of D3 small alkali feldspars have same compositions as rim areas of coarse grains indicating common compositional evolution (Table 1). Furthermore, small alkali feldspar grains might also

represent dissected grain fragments of large grains. Chemically driven recrystallization is also excluded in D1 L because only cores of large grains display antiperthitic exsolution (Fig. 17b). This implies that Na-K-exchange with coexisting alkali feldspar reduced K-content in rim regions of plagioclase whereas in core regions K-content remained high resulting in a supersaturation of K and antiperthitic exsolution. It is suggested that alkali feldspar coexisted with plagioclase at high temperatures thereby preventing exsolution in rim areas because plagioclase does not exsolve alkali feldspar below $\sim 800^{\circ}\text{C}$ under dry conditions (Raase, 1998). Therefore, low temperatures of small-sized feldspar pairs in D1 layers and D3 kfs dominated domains are suggested to result from enhanced compositional change between small grains due to shorter diffusion paths. Coarse-grained feldspar pairs in D1 A, D4 and boundary layers are interpreted to represent preserved high temperature compositions.

Temperature estimates of 773°C in D1 A and $713\text{--}718^{\circ}\text{C}$ in D4 and boundary layers are within error. However, temperatures are systematically lower in D4 and boundary layers compared to D1 A (Appendix Table 1). A compositional modification down to lower temperatures might result from a slightly higher water content in the Fdd which facilitates diffusion (Cherniak, 2010, references therein). However, a probable difference in water content cannot be striking because this would affect microstructures due to a hydrolytic weakening effect (e.g., Kronenberg et al., 1990; Menegon et al., 2011b) and feldspar microstructures are comparable in the Qdd and Fdd. Furthermore, feldspar recrystallization by GBM was reported in feldspars only at very high temperatures ($\sim 900^{\circ}\text{C}$, Lafrance et al., 1998) and in the presence of melt (Rosenberg and Stünitz, 2003). The presence of melt is not evident in the investigated samples. Therefore, it is concluded that temperature estimate of 773°C in D1 A best represents the deformation temperature. Furthermore, this temperature is regarded as minimum estimate of

equilibration after Ca exchange ceased (Kroll et al., 1993).

5.2.2. TitaniQ Thermometry

Calculated TitaniQ temperatures are consistent within the Qdd and Fdd. The lack of Ti zonation, as inspected by Cathodoluminescence, implies equilibration of Ti in quartz (Ashley et al., 2014, references therein).

Several studies indicate limitations of TitaniQ thermometry to reliably determine deformation temperatures (e.g., Ashley et al., 2014; Grujic et al., 2011; Negrini et al., 2014). This is due to sluggish Ti re-equilibration below ~ 540 °C and lack of poorly constrained driving forces for Ti resetting during crystal plastic flow (Ashley et al., 2014; Grujic et al., 2011). However, there is a general agreement that TitaniQ reports deformation temperatures in high temperature rocks with GBM as dominant deformation mechanism (Ashley et al., 2014; Grujic et al., 2011; Nachlas et al., 2018). This is, because sweeping grain boundaries through strained grains constitute high diffusivity pathways (Grujic et al., 2011; McCaig et al., 2007; Yund and Tullis, 1991). The investigated samples show evidence for GBM recrystallization of quartz. Furthermore, high temperatures result in fast volume diffusion of Ti (e.g., Cherniak et al., 2007). High Ti concentrations induce higher strain energies in the quartz lattice which additionally contribute to Ti redistribution (Ashley et al., 2014). Estimated TitaniQ and two-feldspar temperatures are high (>800 °C and >700 °C, respectively) in the investigated samples. Consequently, high temperatures, GBM recrystallization, high Ti-concentrations (~ 250 – 300 ppm, for comparison of Ti contents and temperatures see for instance Menegon et al., 2011b) and the lack of zonation infer equilibration of Ti in quartz during deformation.

The Sri Lankan samples were affected by postdeformation annealing during long-lasting cooling (Voll and Kleinschrodt, 1991). For Sri Lankan rocks the cooling rate was estimated to be ~ 3.5 °C/ Ma between peak metamorphism at ~ 610 Ma (850 – 900 °C) down to biotite

cooling ages at 450 Ma (300–350 °C) (Kroll et al., 1993, references therein). Recorded TitaniQ temperatures of >800 °C show that Ti-resetting in quartz was not significantly affected by annealing. Though, a modification of Ti in quartz during annealing cannot be excluded as grain boundary migration also occurs during static conditions (e.g., Passchier and Trouw, 2005). However, Kruhl and Peternell (2002) suggested to regard grain boundaries from dynamically recrystallized quartz as annealed and equilibrated fabrics which are stable against subsequent annealing. Therefore, temperature estimates of 817–836 °C are regarded as minimum deformation temperatures.

5.2.3. Comparison of Temperatures

Temperature estimates of 817–836 °C by TitaniQ and 773 °C by two-feldspar thermometry are largely within error. Lower feldspar temperatures can be attributed to the greater ease of Ca-Na-K diffusion in feldspars at high temperatures (e.g., Cherniak, 2010) while in quartz Ti redistribution is promoted by migration of grain boundaries (e.g., Ashley et al., 2014; Grujic et al., 2011).

Temperature estimates in this study correlate with geothermometric results of other studies conducted on rocks around the Digana Movement Zone: Voll et al. (1994) calculated feldspar temperatures of ~850 °C related to D₁ (in this study D₂) and near-peak metamorphism for feldspars from a coarse-grained psammopelitic mobilisate. Their samples are from the eastern limb of the Hulu Ganga synform beneath a marble-quartzite assemblage and correspond to the geological position of samples investigated in this study (Fig. 6). Schumacher et al. (1990) reported similar temperatures of 830 °C determined by pyroxene-garnet thermometry for samples from the same geological position. These temperatures are consistent with peak metamorphic temperatures and conditions of D₁ (D₂ this study) (Raase and Schenk, 1994; Dharmapriya et al., 2017; chapter 2). Raase (1998) further reported deformation and recrystallization temperature

of feldspars at about 710 °C in the Digana Movement Zone. However, samples investigated in this study are from a marginal part of the Digana Movement Zone and microstructures are consistent with deformation at higher temperatures >710 °C. Therefore, it is concluded that deformation of the investigated samples occurred under temperatures of 773~836 °C and is related to the deformation event D₂ in the Highland Complex of Sri Lanka.

6. EBSD Analysis

6.1. Results

6.1.1. Quartz

6.1.1.1. CPO

Quartz CPOs from the Qdd display similar patterns in D1 and D2 (Fig. 20). Quartz c-axes display a non-random distribution with maxima between about 10 (D2) and 12 (D1) mud. c-axes are symmetrically distributed and build four clusters between X, Y, and Z. Some clusters are elongated towards the periphery of the pole figure and/ or cross YX and YZ planes. For D2 quartz there are further few c-axis poles scattering around Y. Poles to prism {m} planes and <a> axes are arranged in more or less pronounced girdles perpendicular to c-axis maxima. Peripheral maxima between Z and X are partly concordant with c-axis maxima. Patterns of positive rhomb {r} planes have orthorhombic symmetry with maxima around X, Y, and Z forming a girdle along the YZ plane. Poles to the negative rhomb {z} and acute positive { π } and negative { π' } rhomb planes display less distinct pattern. Combined <a+c> directions show patterns similar to {r} plane poles and build girdles along XY and YZ planes.

The pole figures of quartz ribbons in sample 2997 show a cross-girdle distribution for c-axes with a maximum of about 10 mud located at the north-eastern periphery of the pole figure between Z and X. The crossgirdle consists of two girdles oriented in NE-SW and NW-SE directions of the pole figure intersecting at Y. This pattern can be attributed to cross-girdle of type II (e.g., Schmid and Casey, 1986). Poles to {m} planes display a girdle trending in NW-SE direction in accordance with the c-axis maximum. Patterns of <a> directions are similar to D1 and D2 but display a higher concentration around X. Distribution patterns of rhomb plane poles and <a+c> direction are similar to D1 and D2.

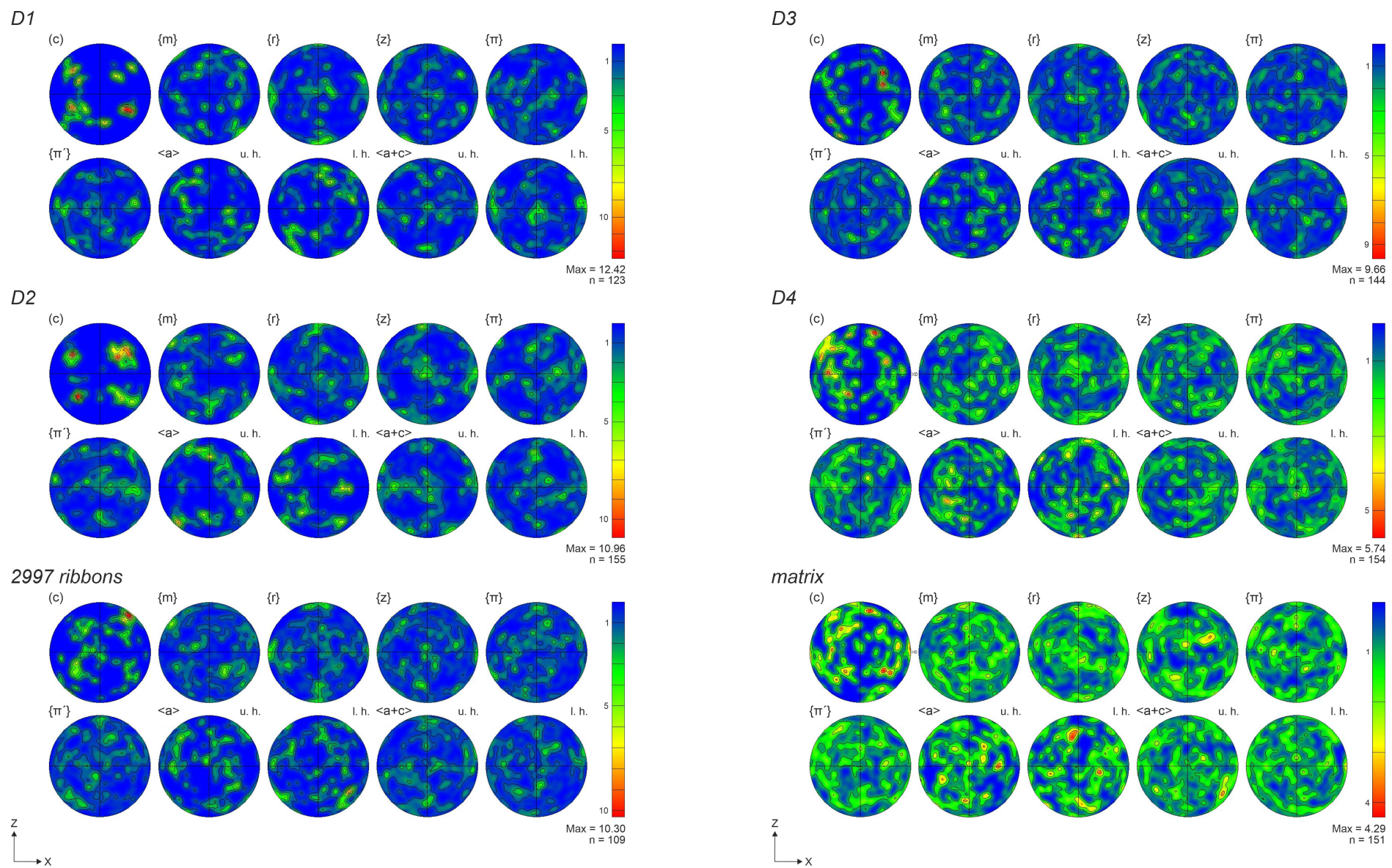


Fig. 20: Quartz CPO.

In the Fdd quartz displays strongest textures for D3 ribbons with maxima up to ~10 mud for c-axes (Fig. 20). The texture weakens towards D4 ribbons and matrix quartz considerably down to ~4 mud. There is no unequivocal pattern in c-axis distribution recognizable but D3 maxima are positioned between X, Y, and Z and are concordant with c-axis maxima of quartz in D1 and D2. In D3 positive rhomb {r} planes display a weak clustering around X, Y, and Z. This pattern weakens in D4 and matrix quartz. In D3 the concentration of the <a+c> direction is slightly enhanced around X with a maximum strength of about 4 mud. The poles to other planes and directions display a random distribution in D3, D4 and matrix quartz.

6.1.1.2. Misorientation Analysis

Misorientation analysis is based on EBSD Maps presented in Fig. 21 and Appendix Figs. 1 and 2.

Misorientation Angle Distribution

Correlated misorientation angle distributions (all data points) of quartz reveal two pronounced peaks (Fig. 22a). A prominent peak lies around 60° and can be attributed to Dauphiné twinning. A minor peak is detected for angles <5° and the frequency decreases towards 10°. The peak around 5° occurs also in uncorrelated distributions but is less intense (except for D1). Misorientation angles <10° indicate the presence of subgrain boundaries. However, GROD maps show that quartz of all domains display only minor internal misorientation (Fig. 23). For misorientation angles >10° (one point per boundary, Fig. 22b) two main features are distinguished. In coarse-grained quartz in D1 and D3 and to a minor extent in D2 large misorientation angles of approximately 60–90° are increased in frequency. This feature deviates from the correlated distribution. Furthermore, the correlated distribution reveals an increased frequency for angles 10–20° in all domains but D1 and this deviates from uncorrelated distributions.

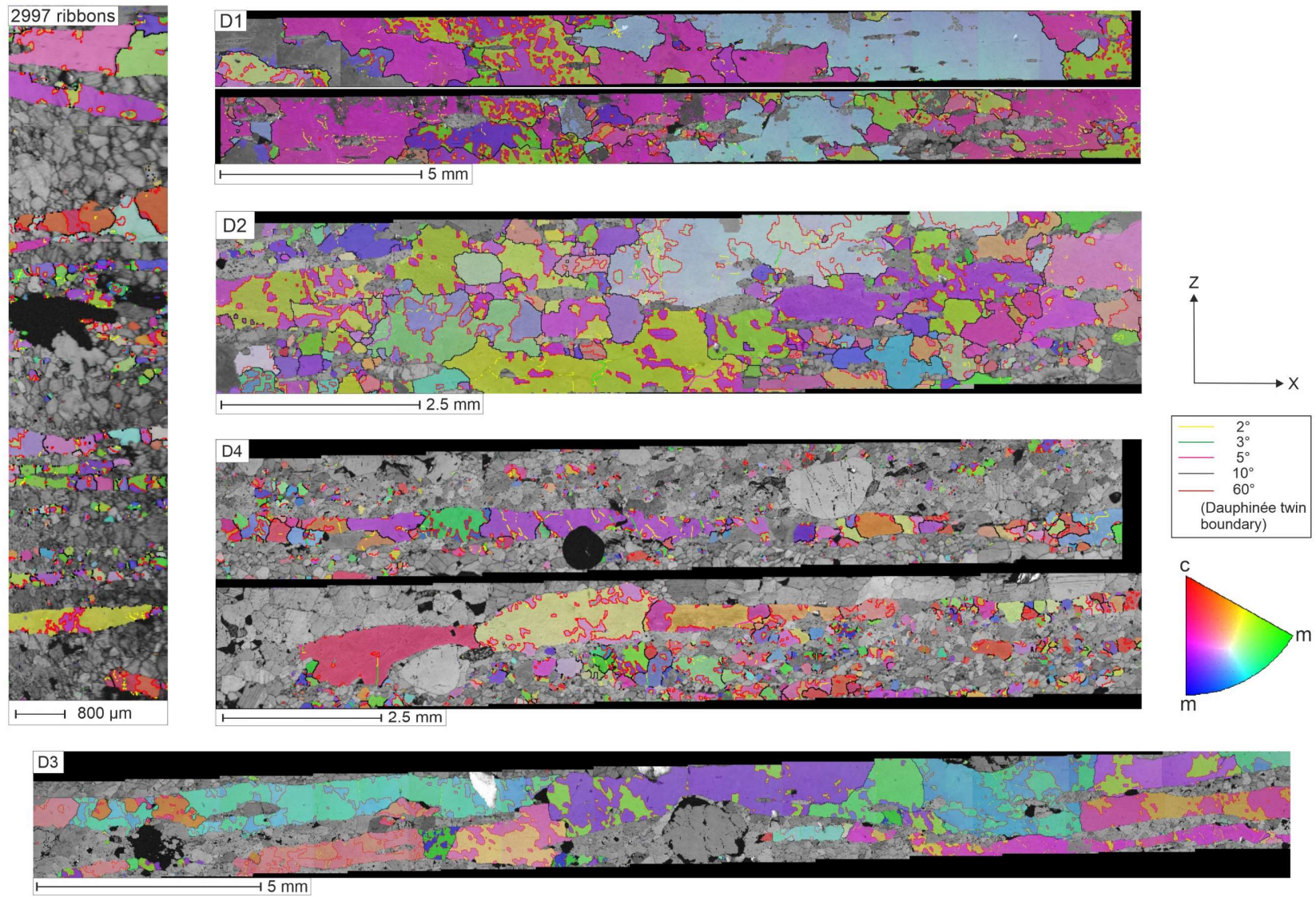


Fig. 21: Quartz EBSD Maps.

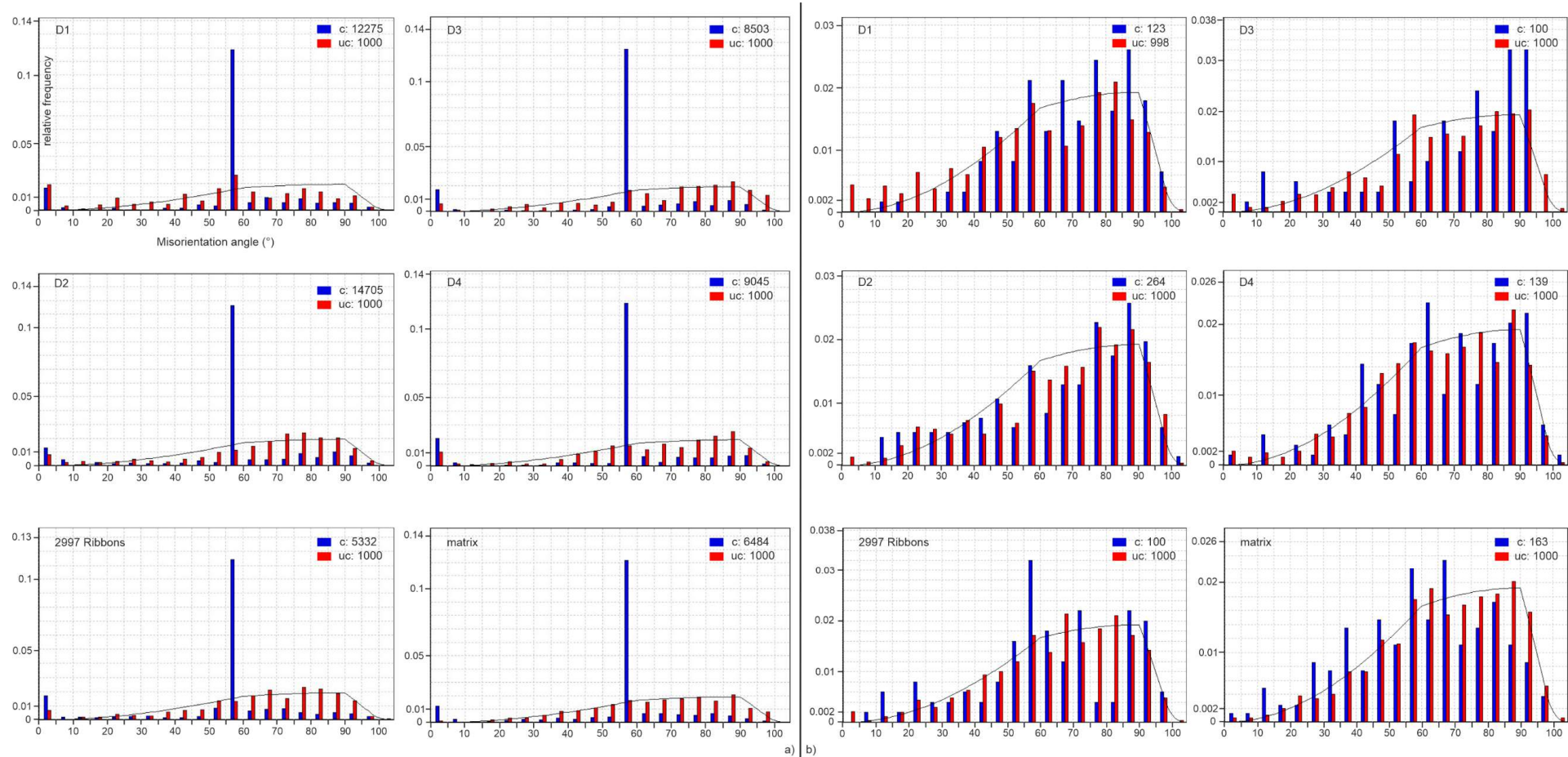


Fig. 22: Quartz misorientation angle distributions: a) complete data set; b) one point per boundary disregarding Dauphiné twin boundaries (c: correlated data points, uc: uncorrelated data points; solid line: theoretical random distribution; axis labels are inserted in D1 (a) and are the same in all diagrams; note in b) misorientation angles $< 10^\circ$ are not representative for correlated data points due to inaccuracies in determining low angle boundaries for the one point per boundary data set).

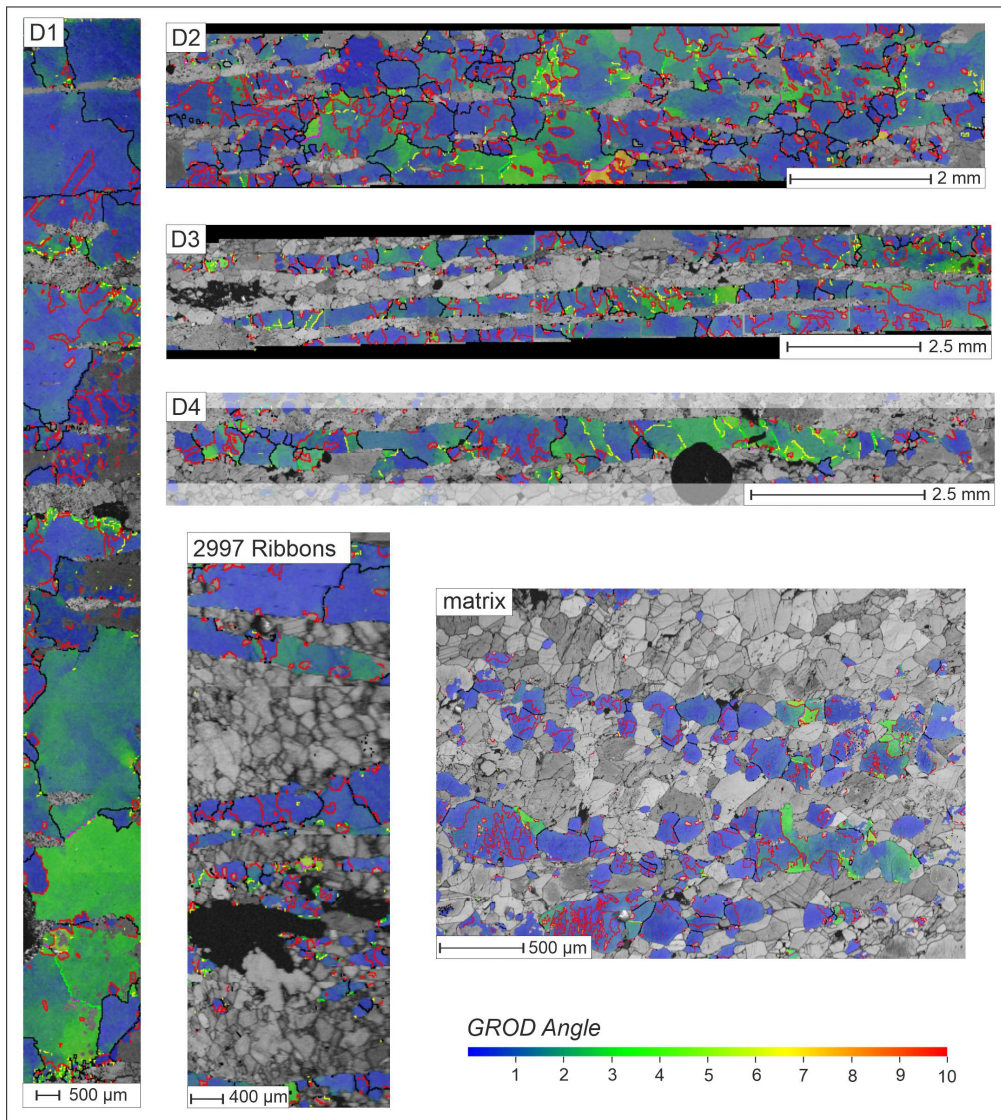


Fig. 23: EBSD GROD angle maps for quartz.

Misorientation Axis Distribution

Misorientation axis distributions for small angles $<10^\circ$ show a broad scatter in all investigated domains (Fig. 24). In crystal coordinates misorientation axes occur parallel to all crystallographic directions of quartz. In D2, there is a concentration of misorientation axes in three clusters around c , close to a and located between c and a quartz directions (Fig. 24a, c). This pattern was also observed in misorientation axis distributions of individual EBSD maps in D2 and D3, but the texture strength is weak (1.5–2 mud) (Fig. 24c). According to the model of Neumann (2000) such a distribution is indicative for combined prism slip in $\langle a \rangle$ and $[c]$ directions (Fig. 24d).

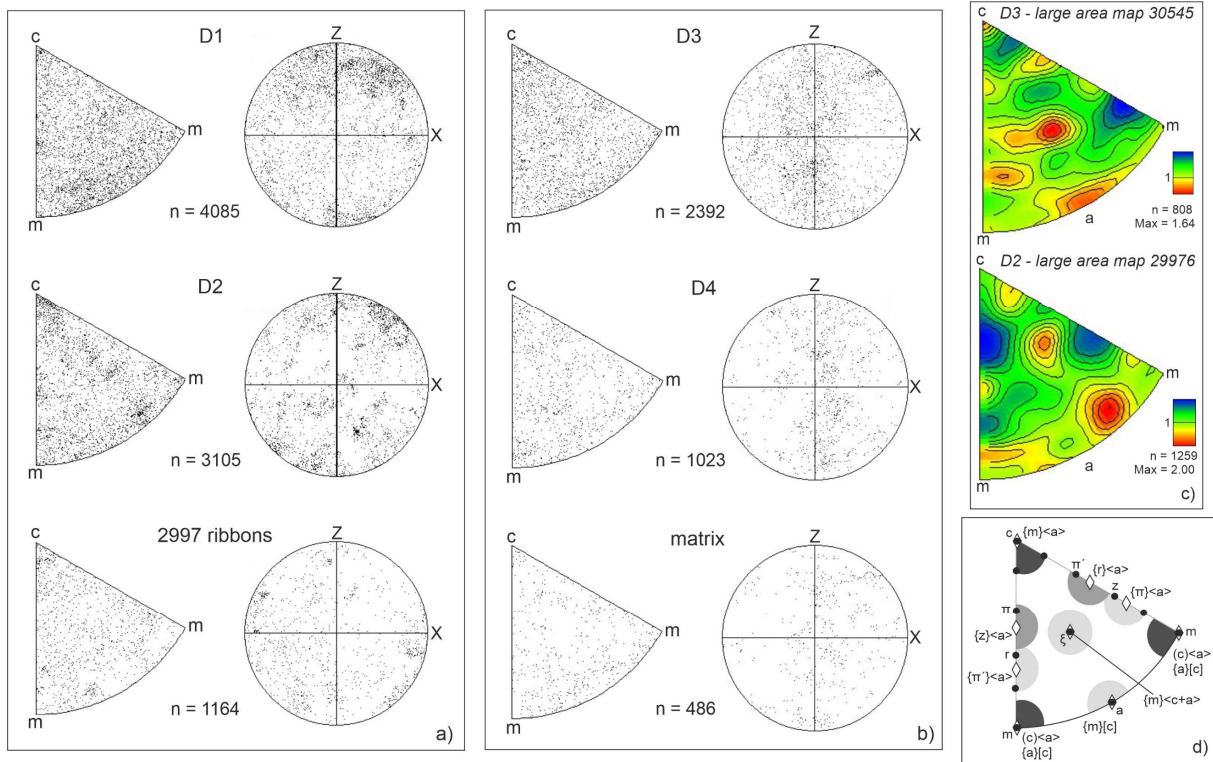


Fig. 24: Quartz misorientation axis distributions for misorientation angles 2-10°: a, b) distributions are presented for individual measuring points in inverse pole figure (left row) and pole figures (right row) in the Qdd (a) and Fdd (b); c) distributions in contoured inverse pole figures for selected maps of D3 and D2 (for corresponding maps see Appendix Figs. 1 and 2); d) interpretation of misorientation axes and corresponding slip systems (modified after Neumann, 2000; dark grey: most common slip systems; intermediate grey: common slip systems; light grey: uncommon slip systems).

In sample coordinates misorientation axis distributions differ between the Fdd and Qdd.

In D1 misorientation axes occur in all directions with a concentration around Z. In D2 similar accumulations occur and in 2997 misorientation axes are shifted towards X. In the Fdd a girdle distribution appears along the YZ plane. In D3 this pattern is most diffuse, but a peripheral maximum between X and Z is present similar to that in the Qdd.

Misorientation axis distributions for angles >10° are similar in both, the Qdd and Fdd, and show the following features (Fig. 25): 1) a pronounced accumulation around the c-axis for misorientation angles around 60° which can be assigned to Dauphiné twinning (Fig. 25b) (e.g., Frondel, 1962), 2) a dominance of misorientation axes for angles >65° over angles <55° (compare number n of data points in Fig. 25a and c). This is also evident in misorientation angle distributions of D1, D3 and D2 quartz (Fig. 22b), 3) random distribution of misorientation axes for angles 10–55° (Fig. 25a), 4) preferred orientation

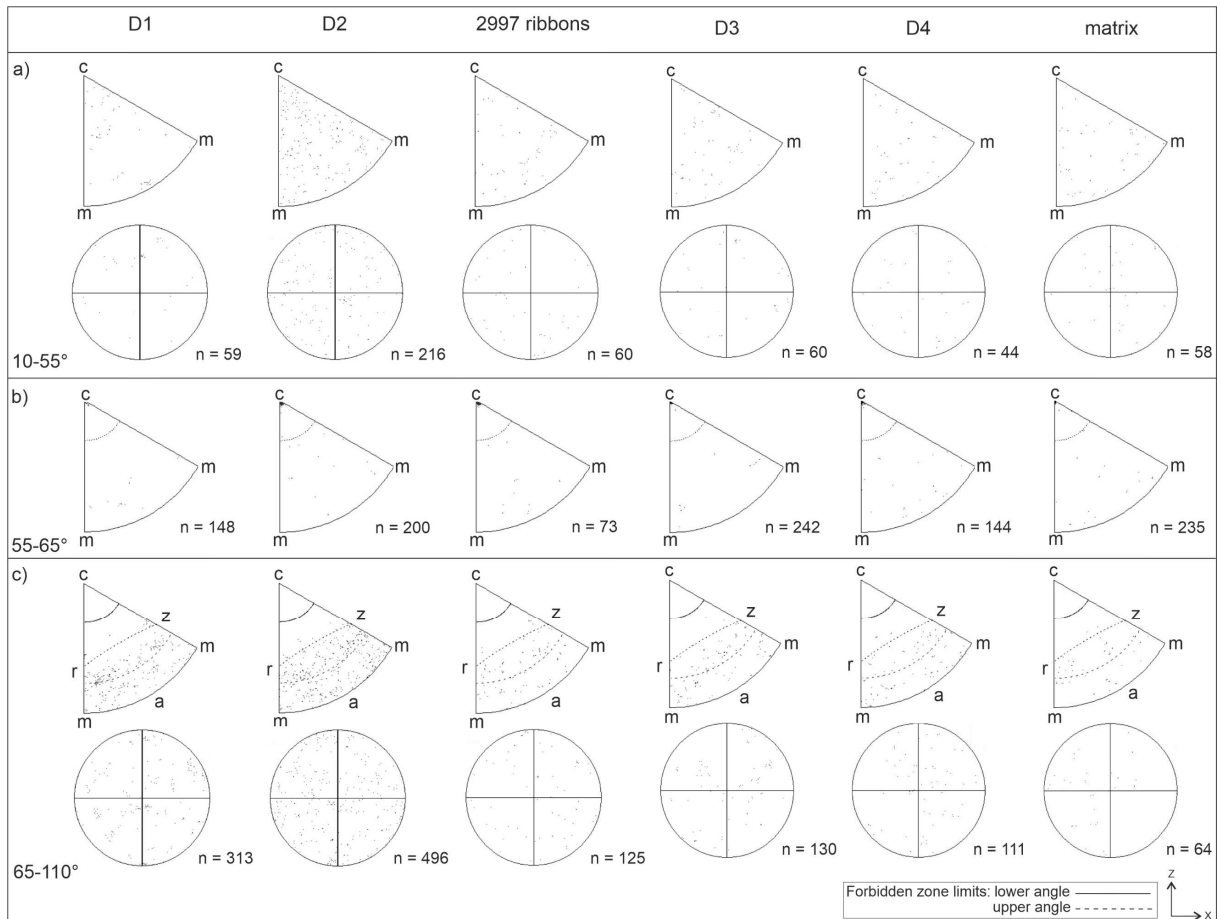


Fig. 25: Quartz misorientation axis distributions for misorientation angles $>10^\circ$: a, c) presentation in inverse pole figures and pole figures for misorientation angles $10\text{-}55^\circ$ (a) and $65\text{-}110^\circ$ (c); in c) r, z and a quartz crystal directions are indicated; b) inverse pole figure presentation for misorientation angles $55\text{-}65^\circ$; note black dots around the c-axis indicative for Dauphiné twinning.

of misorientation axes for angles $65\text{-}110^\circ$ aligned to positive and negative r and z rhombohedral directions and to a minor extent between m and a (Fig. 25c). The latter can be assigned to symmetrical restrictions for high misorientation angles in quartz (e.g., Lloyd, 2004).

6.1.1.3. Quartz Category A, B and C

The CPO of quartz strengthens from matrix quartz to D1 (Fig. 20). To specify texture strengthening, quartz is classified into three categories A, B and C with respect to the c-axis orientation (Fig. 26). In the following, each category will be described referring to the c-axis orientation, suitable orientation for specific slip systems and grain size. Subsequently, corresponding low angle ($<10^\circ$) misorientation axis distributions are presented. Results of the boundary trace analysis are related to each category.

Classification of Categories

Category A contains quartz grains with c-axes distributed along the YZ plane (Fig. 26). Characteristic slip systems resulting in such c-axes positions are basal and prism slip in $\langle a \rangle$ direction (e.g., Stipp et al., 2002). Furthermore, slip on rhomb planes results in c-axes positioned between Z and Y. Schmid factor maps show that category A quartz yields highest Schmid factors for prism $\langle a \rangle$ slip of ~ 0.45 (Fig. 27). Grain size analysis of category A quartz reveals smallest mean grain sizes compared to category B and C quartz (Table 4), but large grains of category A are also observed in D3 (Fig. 26, grain in the lower right corner).

Category B quartz is characterized by c-axes parallel to the lineation, viz. in direction of X (Fig. 26). {prism}[c] slip is adjudged to produce c-axes orientations around X (e.g., Stipp et al., 2002b) which is confirmed in Schmid factor maps with maximum values ~ 0.45 (Fig. 27). Mean grain sizes of category B quartz are usually larger than for A quartz within individual subdomains and always smaller than category C quartz (Table 4).

Category C quartz has c-axes positioned between X, Y and Z axes and extending towards the periphery (Fig. 26) which can be attributed to different active slip systems. Schmid

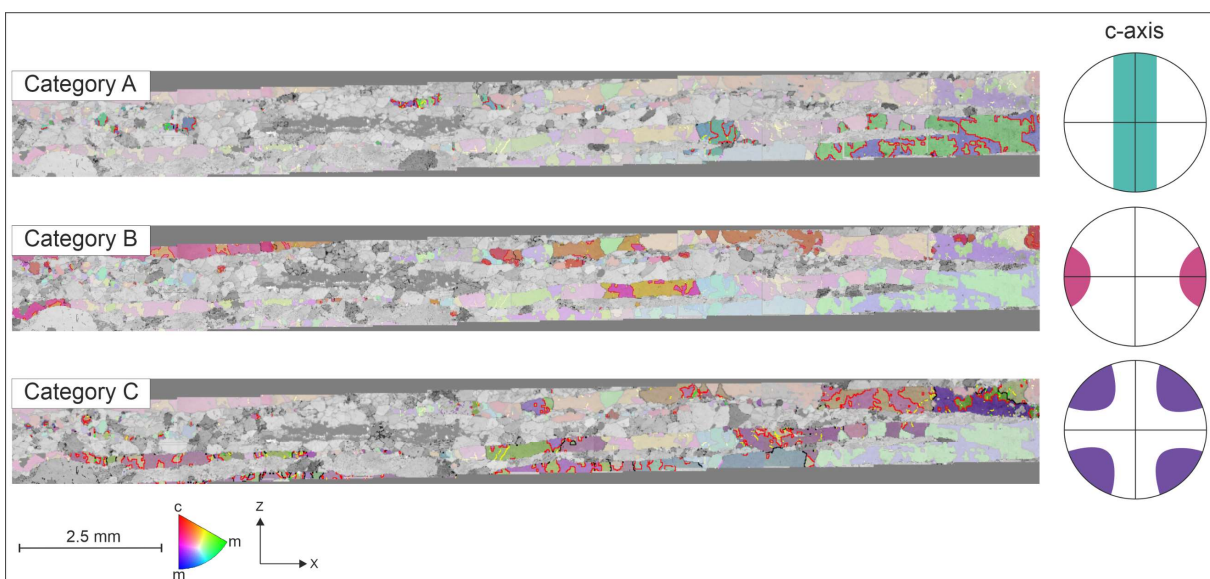


Fig. 26: Quartz Category A, B and C: presentation in EBSD maps and schematic illustration of corresponding c-axis distribution; category A, B and C grains are highlighted in corresponding maps.

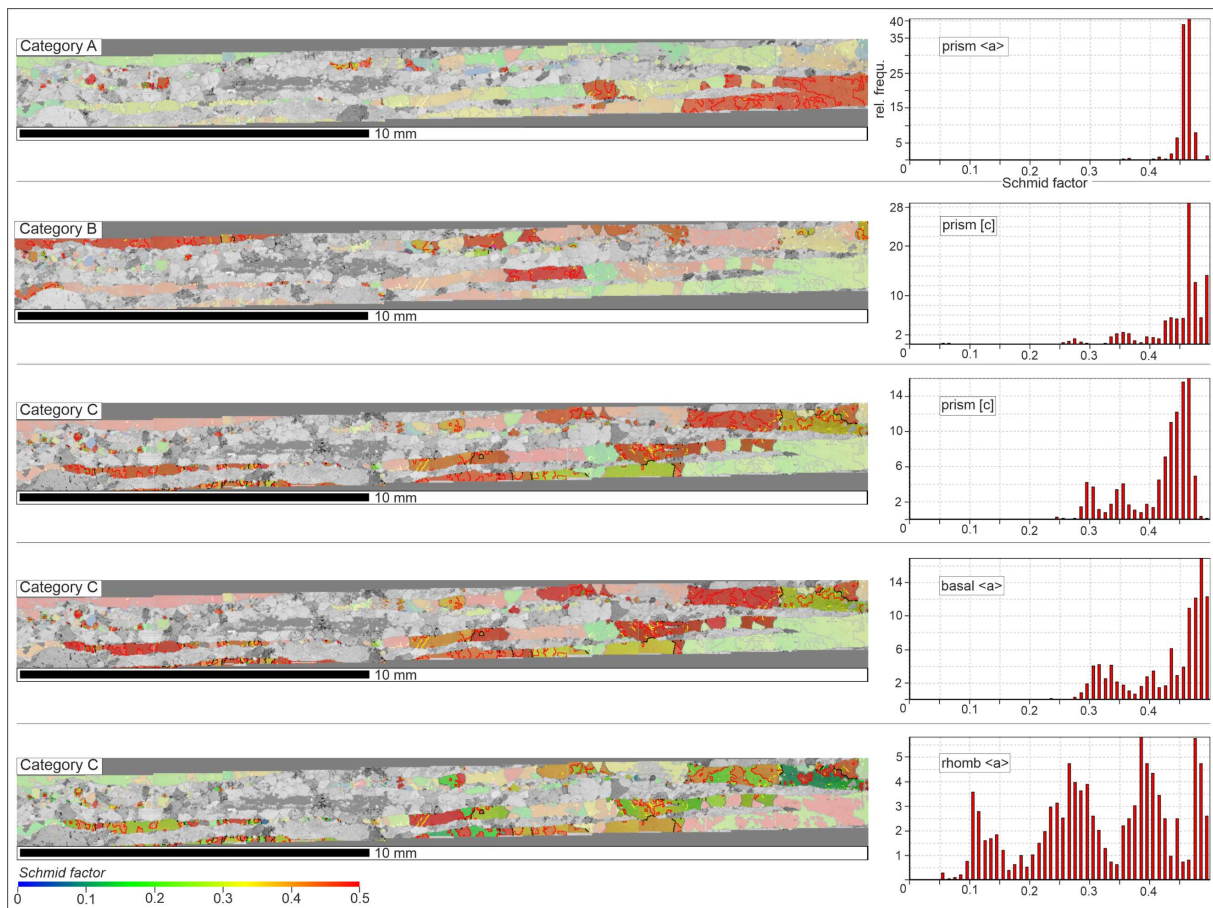


Fig. 27: Schmid factor in category A, B and C (same map as in Fig. 26): left: EBSD Schmid factor maps for each quartz category (grains of specific categories are highlighted) and corresponding slip systems (see text); right: corresponding frequency distribution histograms of Schmid factors (rel. frequ.: relative frequency; axis labels are the same for all diagrams).

factor maps show similar high Schmid factors for prism[c] and basal<a> with maximum values between 0.45 and 0.5 (Fig. 27). Schmid factors for rhomb<a> slip display a high variation and range between ~ 0.05 and 0.5. This variation can be related to Dauphiné twinning which causes a switch of positive {r} and negative {z} rhomb planes. (e.g., Menegon et al., 2011a). Category C quartz reveals largest mean grain sizes in all subdomains (Table 4). c-axis orientations are concordant with c-axis distributions of D1 and D2 (Fig. 20). Concordant c-axis pattern and largest grain sizes in all domains infer selective coarsening of category C quartz.

Table 4: Grain size of quartz category A, B and C.

Domain	d mean (μm)		
	A	B	C
D2	542	532	1125
2997 rb	292	537	846
D3	2064	1344	2088
D4	636	912	1108
Matrix	303	450	901

Misorientation Axis Distribution

The misorientation axis distributions for quartz does not reveal a repetitive pattern within individual categories (Fig. 28). Note that in D1 and D2, misorientation data for category A and B quartz are underrepresented due to the predominance of category C quartz. Misorientation axes occur in all quartz crystallographic directions in quartz of all categories and domains. Furthermore, the pattern of category C quartz resembles the bulk pattern of quartz in each domain (Fig. 24) demonstrating the predominance of category C. Further, distribution patterns of category A in D2 and matrix quartz and of category C in D2 display accumulations of misorientation axes around c, a, m and between c and a quartz directions. This is similar to bulk distributions in individual maps of D2 and D3 (Fig. 24c).

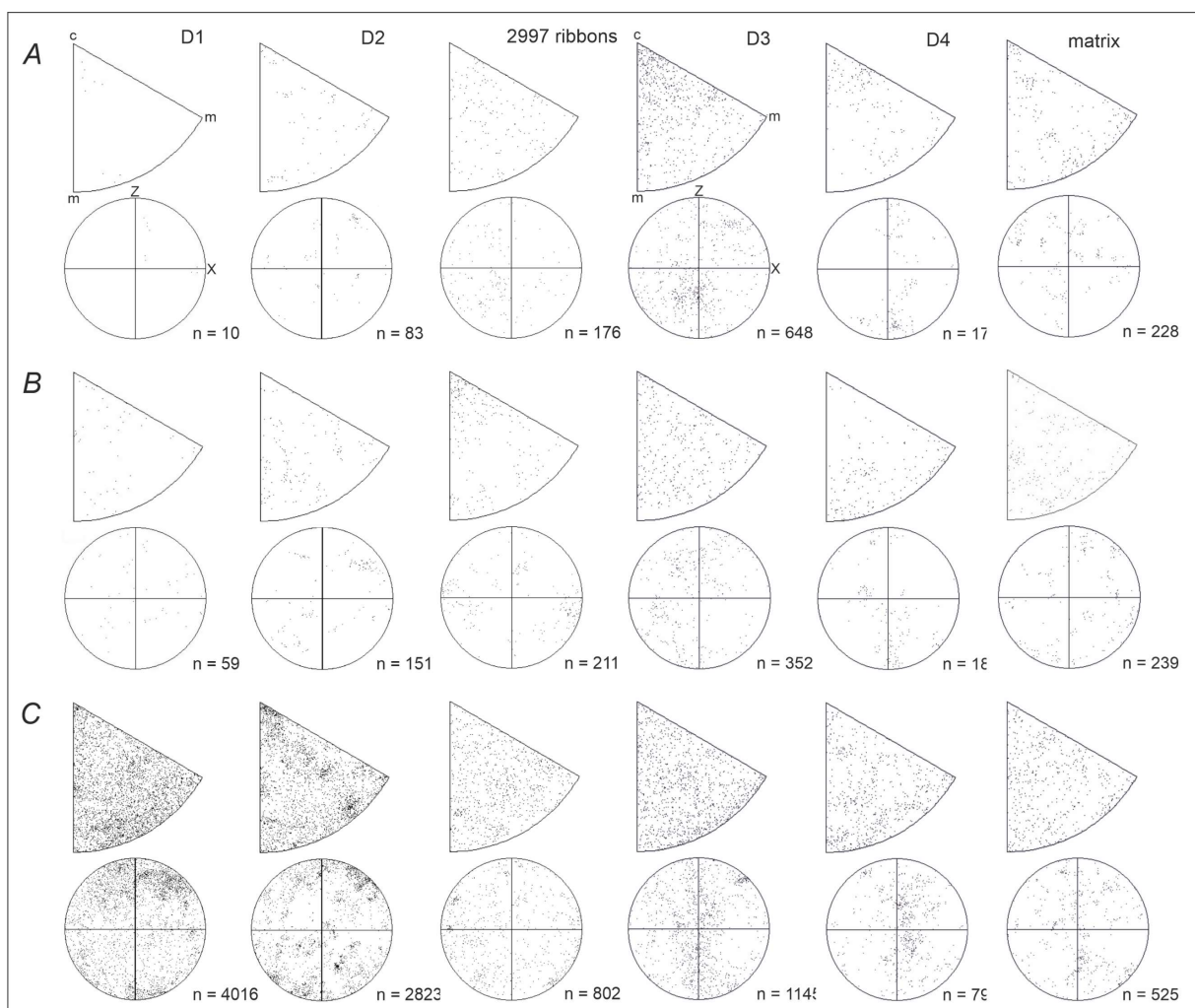


Fig. 28: Misorientation axis distributions for angles 2-10° of Category A, B, C quartz and for each domain.

To sum up, category C quartz dominates in number and displays largest grain sizes in all subdomains of the Fdd and Qdd. Based on misorientation axis distributions multiple active slip systems are indicated in all domains and categories. Combined prism slip in $\langle a \rangle$ and $[c]$ direction and basal $\langle a \rangle$ slip appear dominant in category C and A as inferred from characteristic misorientation axis distribution patterns. Indicated slip systems agree with Schmid factors in category C quartz and prism $\langle a \rangle$ slip agrees with Schmid factors in category A quartz.

6.1.1.4. Boundary Trace Analysis

The boundary trace analysis was performed on over 200 quartz subgrain boundaries in the Qdd and Fdd. Slip systems were exclusively derived from about 100 identified subgrain boundaries assuming a tilt boundary model. In isolated cases, subgrain

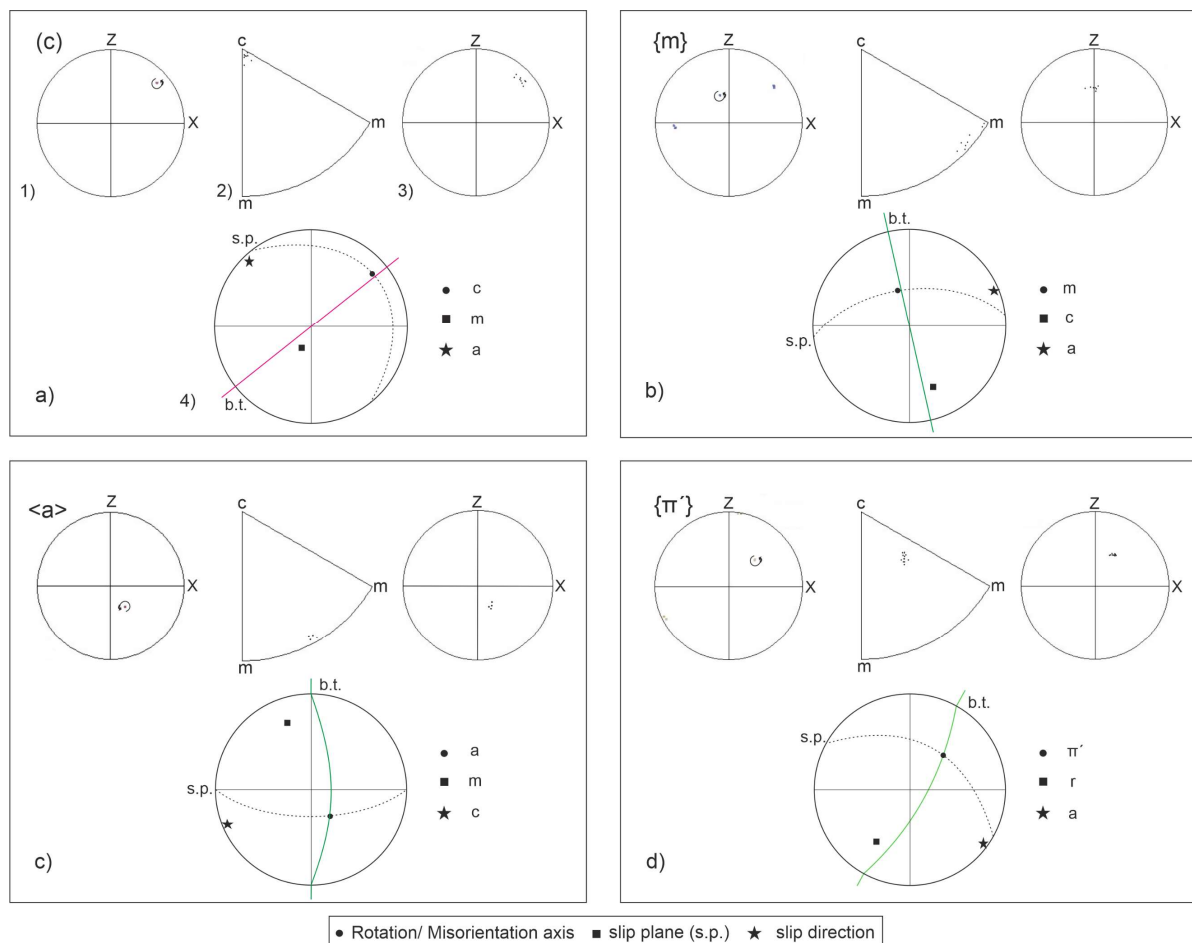


Fig. 29: Representative results of the boundary trace analysis: shown are rotation axis in pole figures (1), misorientation axis in inverse pole figures (2) and pole figures (3) and interpretation of subgrain boundary-slip system geometry (4) (b.t.: boundary trace, s.p.: slip plane).

boundaries were assigned to twist boundaries where the analysis was in accordance with the proposed model of Lloyd (2004) (Appendix Table 3). The results refer to category A, B and C quartz and are summarized for all domains. It should be noted that results of category A and B quartz are underrepresented due to a predominance of category C.

The boundary trace analysis yields multiple slip systems in quartz in the Fdd and Qdd and in all categories A, B and C (Table 5, Fig. 29, Appendix Table 3). The following slip systems were identified: *i.* rhomb slip of {r}, {z}, { π } and { π' } planes in <a> direction; *ii.* prism slip in <a>, <a+c> and [c] directions; *iii.* {a}[c] slip; *iv.* (c)<a> slip. Rhomb slip systems are most frequently detected with slip on positive {r} rhomb planes being most common (Table 5). Slip systems associated with prism planes are the second most detected slip systems. In category B and C no preference can be determined between prism slip in <a> and [c]

Table 5: Number of detected slip systems per domain and category.

Domain	Qdd			Fdd			total		
	A	B	C	A	B	C	A	B	C
{r}<a>	1	1	11	1	5	6	2	6	17
{z}<a>	1	1	5	2	2	6	3	3	11
{ π >a>	-	-	7	-	-	1	-	-	8
{ π' >a>	1	-	4	4	2	4	5	2	8
total rhomb	3	2	27	7	9	17	10	11	44
{m}<a>	-	2	7	4	2	3	4	4	10
{m}[c]	-	-	6	-	2	7	-	2	13
{m}<a+c>	-	-	-	-	1	1	-	1	1
total prism	-	2	13	4	5	11	4	7	24
{a}[c]	-	2	4	-	2	5	-	4	9
(c)<a>	1	1	2	2	-	4	3	1	6
total A, B, C	4	7	46	13	16	37	17	23	83
total		57			66			123	

directions. In category A only prism<a> slip was detected. Basal<a> and {a}[c] are least detected. The former occurs in all categories whereas the latter was only found in category B and C.

A further result from the boundary trace analysis is the unsuitable orientation of many slip planes at a high angle to the foliation (Fig. 29a).

6.1.1.5. Dauphiné Twinning

Dauphiné twinning is extensive in the investigated quartz. Therefore, most striking features are described in this section.

Dauphiné twins occur in all subdomains of the quartz and feldspar dominated domains and in all categories A, B and C (Figs. 21, 30). The appearance is often patchy and twin

boundaries are highly irregular and lobate (Fig. 30). Dauphiné twinning

causes a switch of negative and positive rhomb planes, z {01-11}

and r {10-11}, respectively (e.g., Menegon et al., 2011a; Tullis, 1970).

In the investigated quartz no dominance of r or z twin types is detected (in EBSD maps are grains

with purple colours r-types, and greenish/ yellow grains are z-types,

Fig. 30). Internal strain and the occurrence of subgrain boundaries

appears to a similar extend in all twin types (Fig. 30a, b). Subgrain

boundaries crossing and terminating (arrow) at Dauphiné twin boundaries.

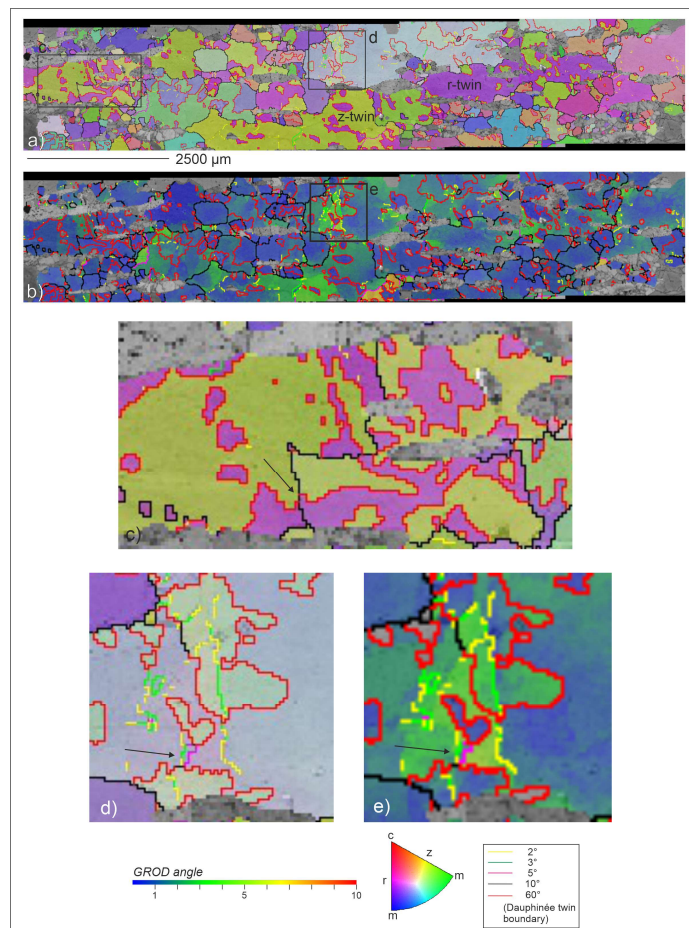


Fig. 30: Dauphiné twins: a, b) same EBSD map in inverse pole figure colour coding (a) and GROD angle colour coding (b); note r-twins display purple colours and z-twins greenish-yellow colours (see also legend); c-e) enlarged areas of a) and b) (marked with rectangles); c) Dauphiné twin boundaries crossing grain boundaries (arrow); d, e) subgrain boundaries crossing and terminating (arrow) at Dauphiné twin boundaries.

boundaries are observed to cross but also to terminate at twin boundaries (Fig. 30d, e). Furthermore, some twin boundaries cross high angle ($>10^\circ$) grain boundaries (Fig. 30c).

6.1.2. Feldspar

6.1.2.1. CPO

Alkali feldspar and plagioclase show similar orientation distributions in D1 A, D2, D3 and D4 (Figs. 31, 32). Alkali feldspar displays (010) planes parallel to subparallel to the foliation with maxima around Z. [100] directions scatter around the foliation plane with some maxima close to X. (001) planes and [001] directions show weak girdle distributions oblique to YZ and XZ planes. Maxima of (001) plane poles lie around Z while [001] directions display further maxima close to X. The described pattern is best pronounced in D3 with strongest maxima for (010) planes poles of 10.57 mud in the plagioclase dominated domain. In D1 aggregates and D4 this pattern becomes diffuse with weakest (010) maxima of 5.87 mud in D4.

Plagioclase shows similar orientation distributions for (010) planes and [100] directions as alkali feldspars. (001) planes and [001] directions show a largely random distribution. The most striking pattern of plagioclase CPOs is observed for (021) planes with poles forming girdle distributions in the YZ plane (D3/ D4) or cluster around Z (D1 A). A possible slip direction to the (021) plane is [1-12] (Montardi and Mainprice, 1987). [1-12] directions mostly display a random distribution, but single maxima point in X direction. Strongest maxima for (010) and [021] of ~ 11 mud occur in the plagioclase dominated domain of D3. Weakest textures are observed in D1 A and D4.

For both feldspars, the orientation distribution differs in D1 L and CPOs are strongest compared to all other domains with maxima up ~ 15 and 26 mud for alkali feldspar and plagioclase, respectively. Alkali feldspar (010) plane poles cluster around Y with few poles extending towards the periphery thereby forming a weak girdle. (001) plane poles and

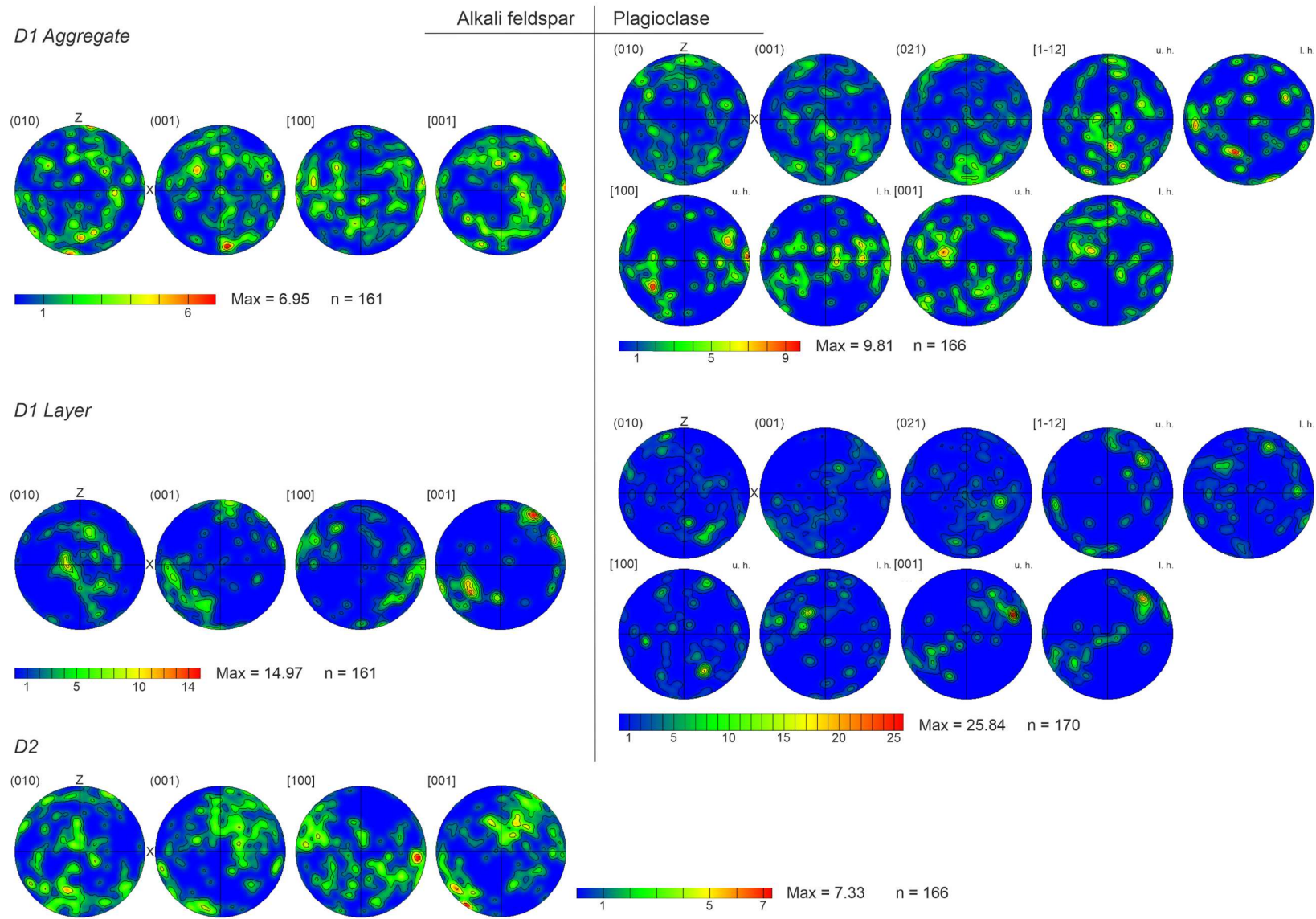


Fig. 31: Feldspar CPO in the Qdd.

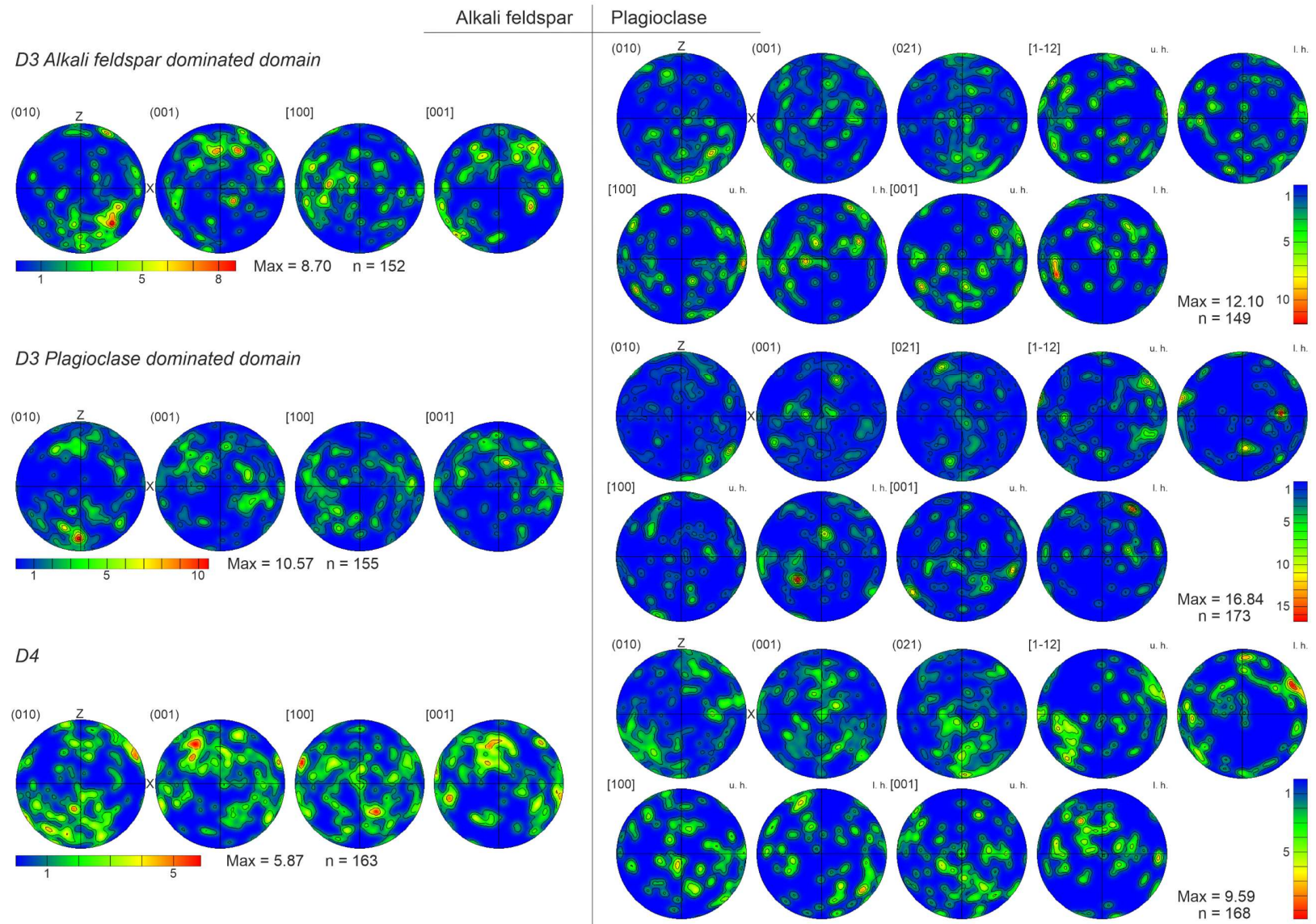


Fig. 32: Feldspar CPO in the Fdd.

[001] directions scatter preferentially in the periphery between X and Z. Plagioclase shows similar patterns as alkali feldspar. (010) plane poles reveal a girdle distribution, too, but maxima are shifted towards the periphery and around Z. (001) plane poles form a girdle perpendicular to (010) girdle distributions with maxima close to X. These are concordant with maxima of [001] directions which display strongest maxima of ~ 25 mud. (021) plane poles are no longer aligned in a girdle distribution but appear randomly distributed. [100] and [1-12] directions display no recognizable pattern.

6.1.2.2. Misorientation Analysis

The misorientation analysis of feldspar is based on processed EBSD maps presented in Appendix Figs. 3 and 4.

Misorientation Angle Distribution

Correlated misorientation angle distributions of alkali feldspar and plagioclase display increased frequencies for angles $2\text{--}10^\circ$ and $170\text{--}180^\circ$ (Fig. 33). The former can be assigned to subgrain boundaries. However, GROD maps show minor internal misorientation of feldspars (Fig. 34d, e). High frequencies around angles of $170\text{--}180^\circ$ are related to twinning operations (see next section). In all subdomains but D4 alkali feldspar shows a higher frequency of misorientation angles $<10^\circ$ whereas plagioclase reveals a greater fraction of angles between 170 and 180° . The smallest fraction of angles $<10^\circ$ is detected in D1 layers and D4. Both feldspars further show an increase of misorientation angles between 10 and $\sim 30^\circ$ compared to a random distribution. This is most evident for D2 alkali feldspars. In D2 misorientation angles between 10 and 20° often correlate with grain boundaries perpendicular to the foliation in lenticular alkali feldspars (Fig. 34a, b). In places low angle grain boundaries are observed to pass into high angle grain boundaries resulting in adjacent grains of similar orientation. Similar features are also observed in lentil shaped feldspars in the Fdd (Fig. 34c).

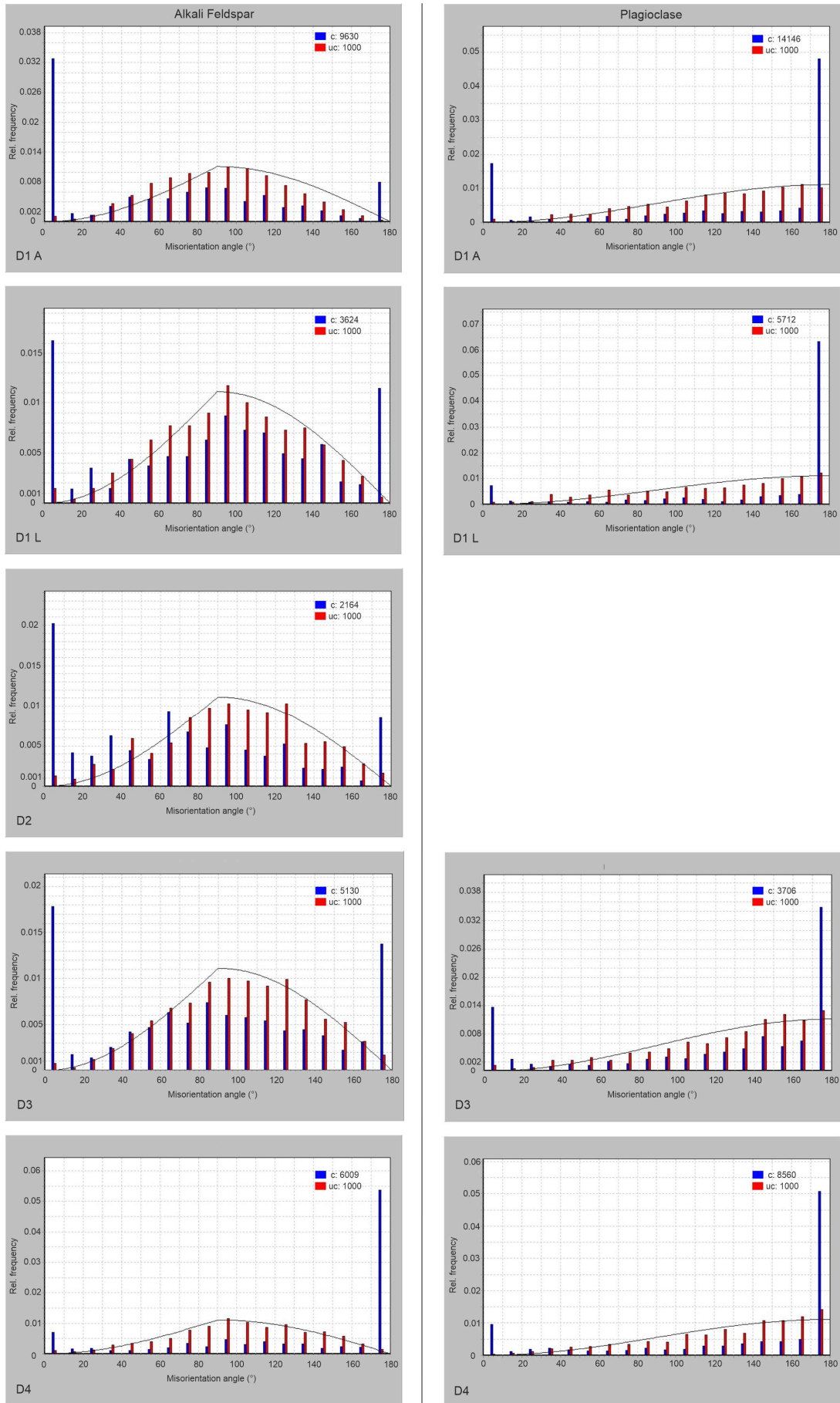


Fig. 33: Misorientation angle distributions of alkali feldspar (left row) and plagioclase (right row) (solid lines represent theoretical random distributions; c: correlated data points, uc: uncorrelated data points).

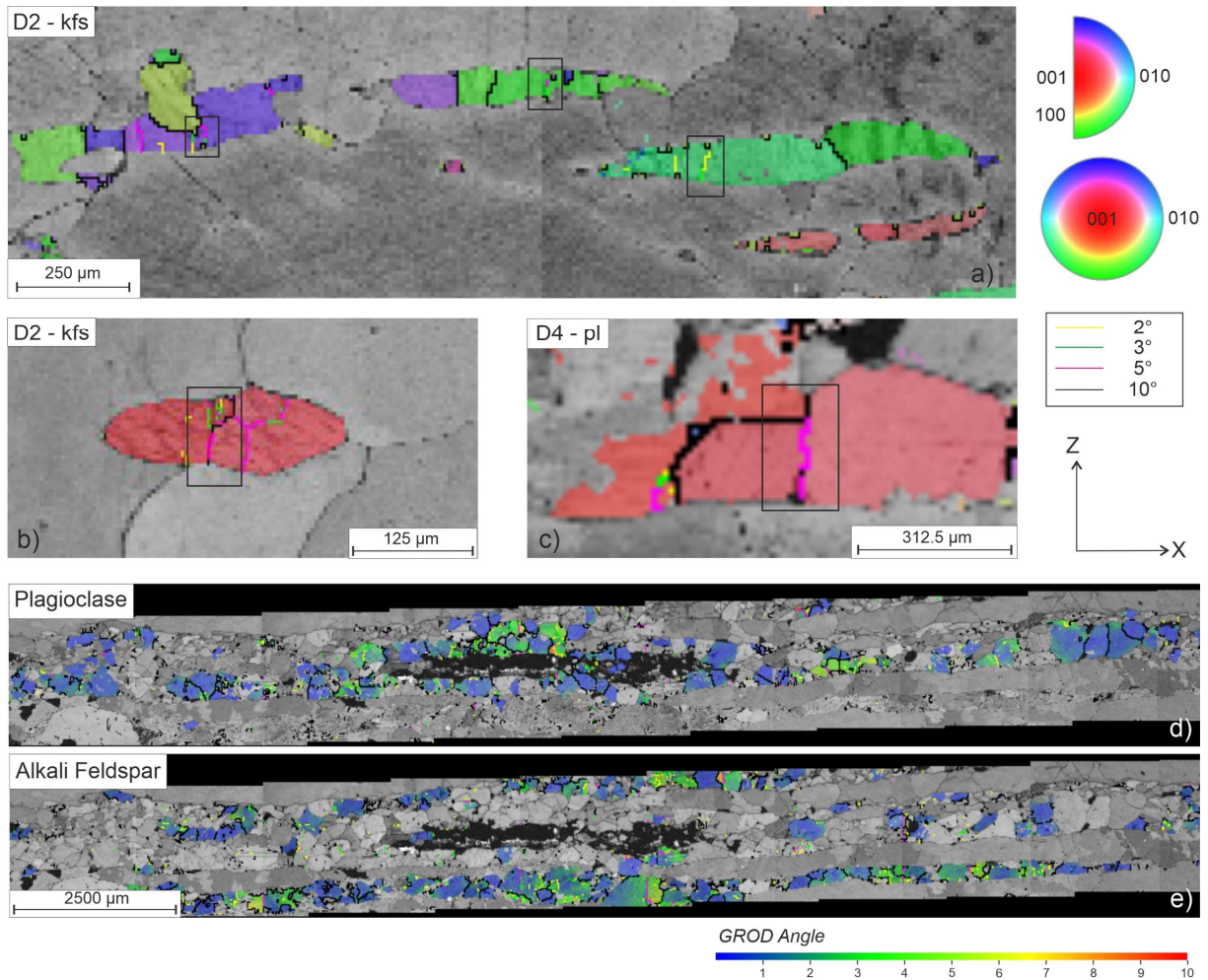


Fig. 34: Subgrain boundaries and internal misorientation of feldspars: a-c) EBSD map sections showing subgrain boundaries in lentil shaped feldspars of D2 (a, b) and in D4 (c) (for further explanation see text); d-e) EBSD GROD map of plagioclase (d) and alkali feldspar (e) in D3.

Misorientation Axis Distribution

The misorientation axis distribution for misorientation angles 2–10° of alkali feldspar shows similar distributions in crystal coordinates for D1 L, D2 and D3 (Fig. 35). Misorientation axes cluster mainly around directions of [201] and [-20-1] with the strongest maximum of 4.61 mud in D3. Weak maxima are also developed in D1 L around [001] and close to [021]. In D1 A and D4 misorientation axes are randomly distributed. In sample coordinates misorientation axes of alkali feldspar in D1 A, D3 and D4 show peripheral maxima between X and Z (~12 mud). In D1 L misorientation axes scatter around the foliation plane. Misorientation axes in D2 form an incomplete girdle distribution along the YZ plane.

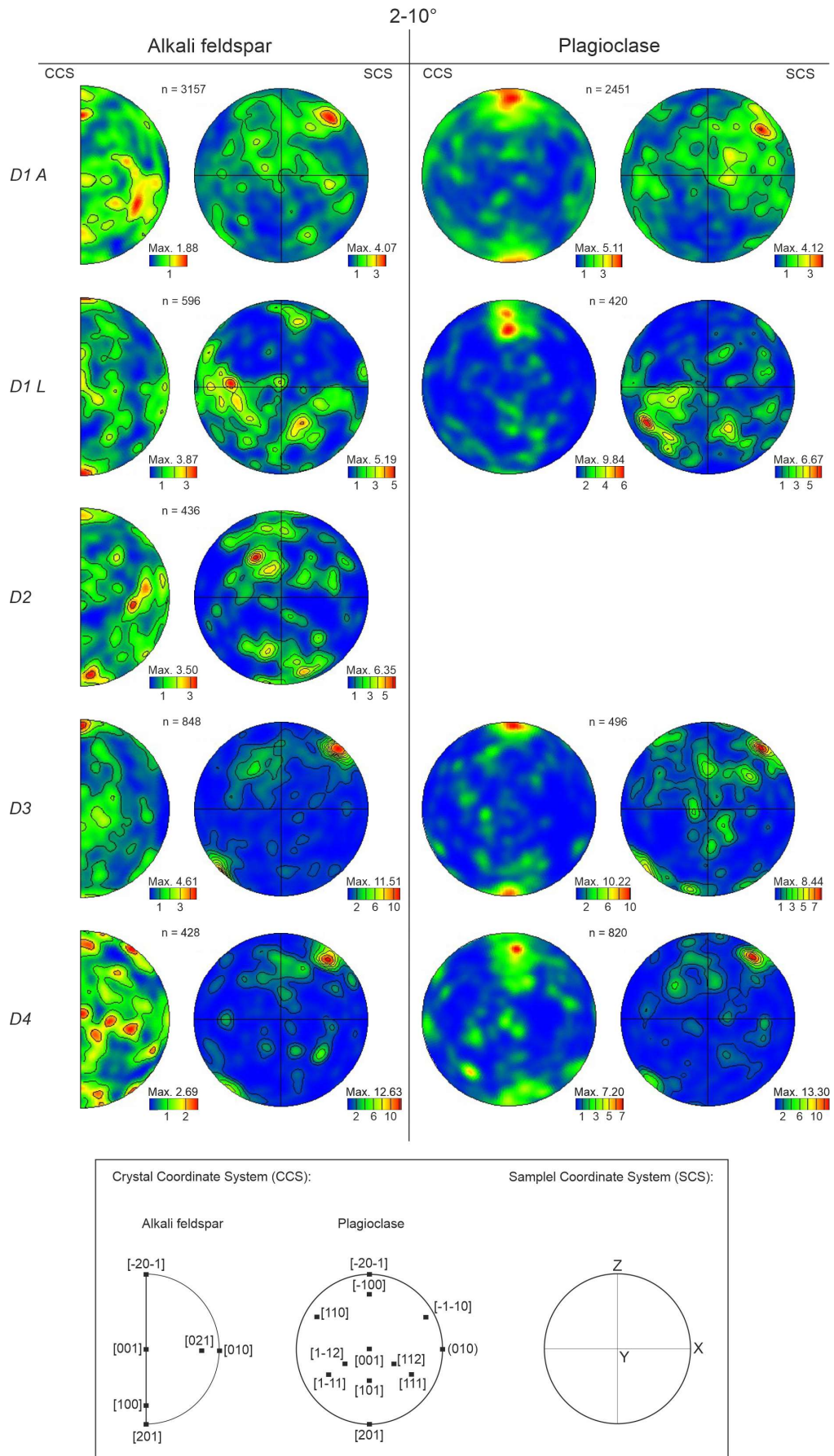


Fig. 35: Feldspar misorientation axis distributions for misorientation angles 2-10°.

Misorientation axes for misorientation angles 2–10° in plagioclase show in crystal coordinates pronounced maxima around [-20-1] and [-100] and in [201] direction. A strongest maximum occurs in D3 with ~10 mud. In sample coordinates misorientation axes are similarly distributed with equal intense maxima as is observed for alkali feldspar. Misorientation axis distributions for angles between 10–170° and 170–180° display coinciding maxima in crystal coordinates around [001], [201] and [-20-1] for both feldspars and further around the plane normal of (010) for plagioclase (Fig. 36). High angle rotations (>160°) around [001] and (010) can be assigned to Carlsbad and Albite twinning (Jiang et al., 2000; Smith, 1974). Maxima around [201] and [-201] might result from combined twinning operations. Apart from twinning related maxima, misorientation axis distributions for angles 10–170° are random. In alkali feldspar the region around [010] is largely free of misorientation axes which can be assigned to symmetrical

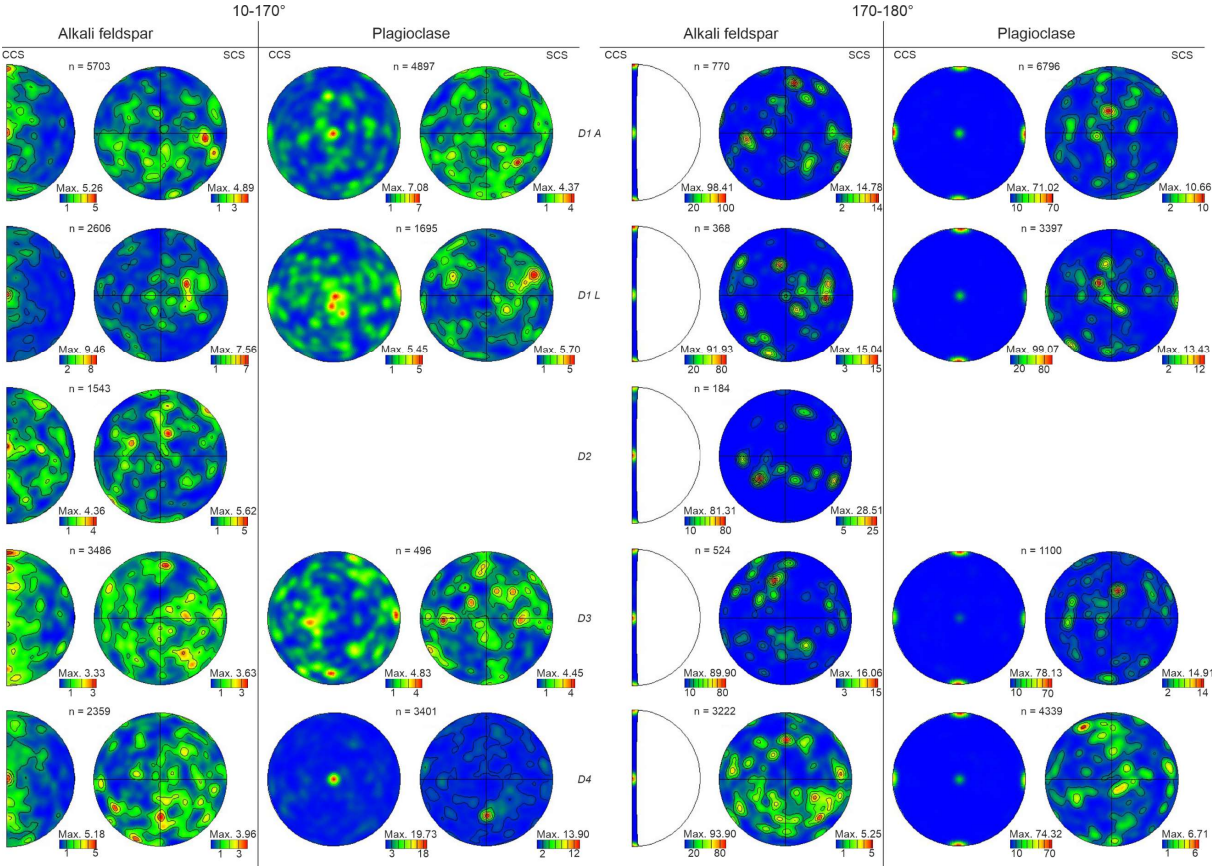


Fig. 36: Feldspar misorientation axis distributions for misorientation angles 10-170° and 170-180° (legend see Fig. 35; white areas in alkali feldspar inverse pole figures are forbidden regions for misorientation angles 170-180°).

restrictions for high misorientation angles (e.g., Wheeler et al., 2001). In sample coordinates misorientation axes display pronounced maxima which are related to twin boundaries. The distribution is random for angles 10–170° and 170–180°.

6.1.2.3. Boundary Trace Analysis

For the boundary trace analysis in alkali feldspar and plagioclase ~150 subgrain boundaries were analysed. For more than 50 subgrain boundaries per feldspar interpretable slip systems could be determined assuming a tilt boundary model (Table 6, Appendix Table 4, 5, Fig. 37).

For alkali feldspar the following slip system were identified (from most frequent to less frequent,) (Table 6, Fig. 37): *i.* (1-1-1)[110] and (11-1)[1-10], *ii.* (001) in [110] and [1-10], *iii.* (010) in [101] and [201], *iv.* (021)[1-12], *v.* (110)[1-12], *vi.* (010)[100], *vii.* (10-1) in [111] and [1-11], *viii.* (20-1) in [112] and [1-12], and *ix.* (010)[001], (1-20)[001], (13-1)[-112], (20-1)[102] and (11-1)[101].

Slip systems detected for plagioclase are the following (from most frequent to less frequent) (Table 6, Fig.37): *a.* (021)[1-12], *b.* (010) in [001], *c.* (010) in [101] and [201], *d.* (10-1) in [111] and [1-11], *e.* (13-1)[-112], and *f.* (010)[100], (20-1) in [112] and [1-12], (110)[1-12], (11-1)[1-10], (1-1-1)[110], (001) in [110] and [1-10].

Most slip systems are detected in combination with several possible misorientation axes (Appendix Table 4, 5). For most common slip systems a dominance of specific misorientation axes could be determined: [001] for (010) in [101] and [201]; [201] and [-20-1] for (021)[1-12] and (010)[001]; [101] for (1-1-1)[110] and (11-1)[110]. The spread of rotation axes is schematically illustrated in inverse pole figures in Fig. 38 for frequent slip systems identified in alkali feldspar and plagioclase in this study. These results are largely consistent with maxima in misorientation axis distributions for angles 2–10° (Fig. 35).

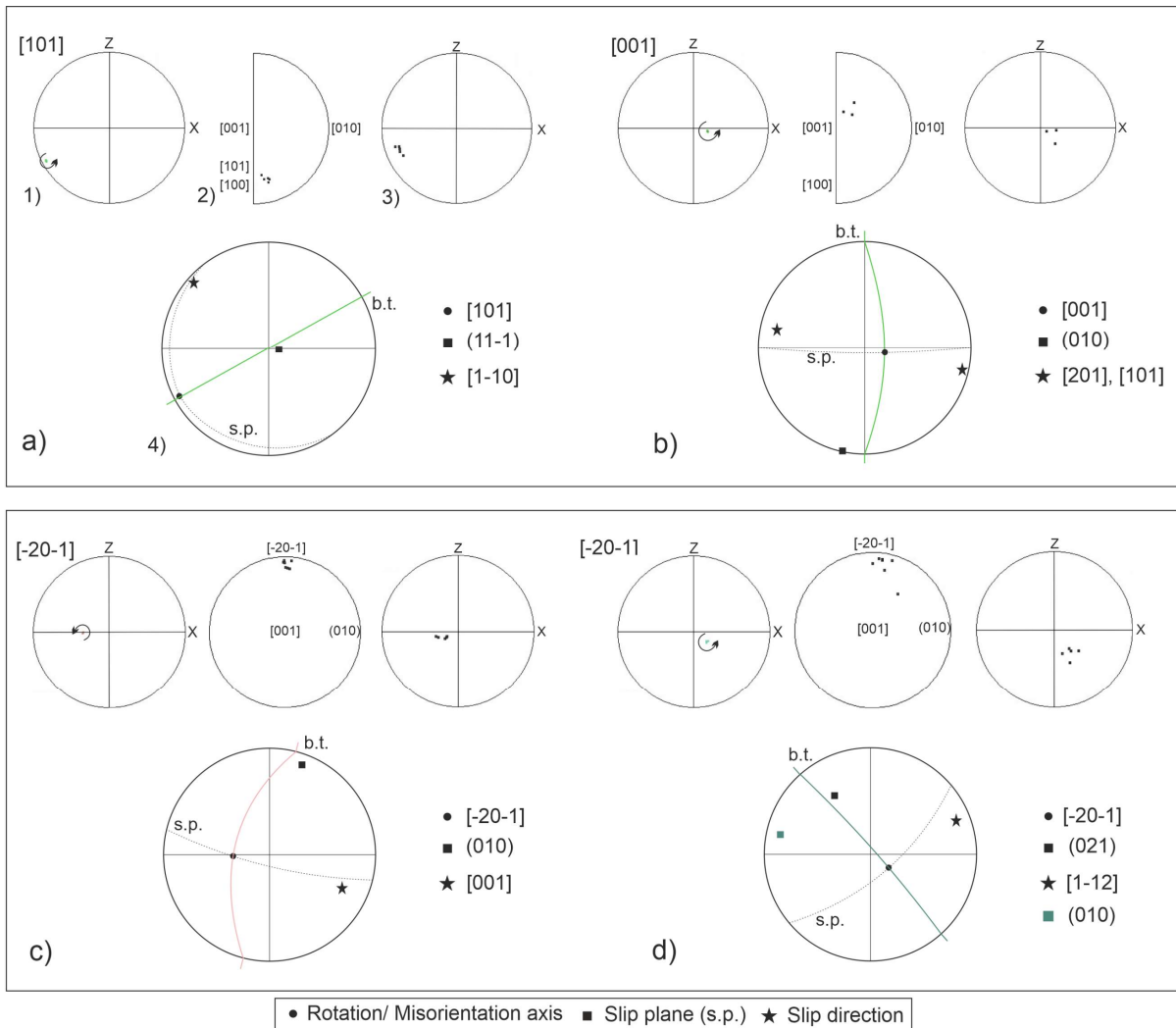


Fig. 37: Slip system interpretation of frequently detected slip systems in alkali feldspar (a-b) and plagioclase (c-d): Shown are rotation axis in pole figures (1), misorientation axis in inverse pole figures (2) and pole figures (3) and interpretation of subgrain boundary-slip system geometry (4) (b.t.: boundary trace, s.p.: slip plane); in d) the pole to the (010) plane is shown additionally in the interpretation pole figure.

A further finding of the boundary trace analysis is that many slip planes are at high angle to the foliation plane (Fig. 37a). Corresponding misorientation axes display peripheral accumulations in pole figures. This is consistent with misorientation axis distributions for small angles (2–10°) (Fig. 35). Similar observations were made for quartz and this will be discussed for both, quartz and feldspar, in section 6.2.1.4. Nevertheless, several slip planes are oriented in suitable orientation for slip subparallel to the foliation plane (Fig. 37b-d, Appendix Tables 4, 5). For alkali feldspar this is valid for different slip systems whereas for plagioclase a reasonable orientation is mostly detected for slip systems including slip on (010). Moreover, the (010) plane was often detected perpendicular to the foliation in

cases of identified $(021)[1-12]$ slip (Fig. 37d; Appendix Tables 4, 5).

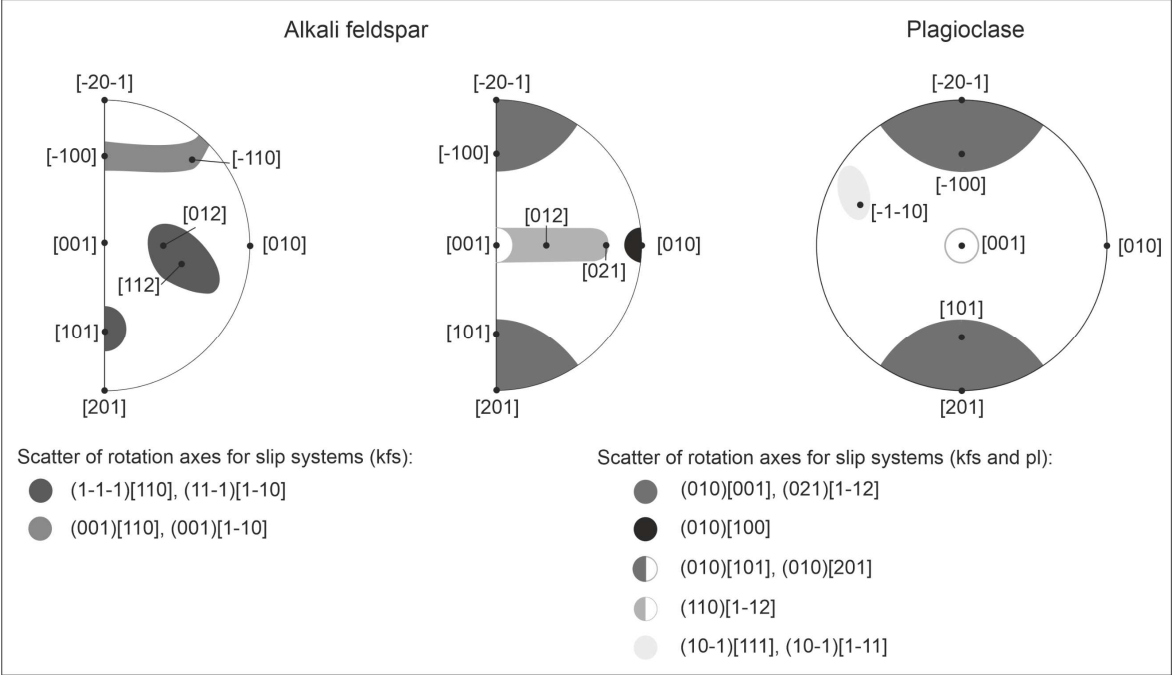


Fig. 38: Rotation axis distribution and corresponding slip systems as determined in this study.

Table 6: Detected slip systems in alkali feldspar and plagioclase.

Feldspar		Alkali feldspar						Plagioclase				
Domain		D1 A	D1 L	D2	D3	D4	total	D1 A	D1 L	D3	D4	total
Dominance	Slip system ¹											
dominant	(010)[001]	-	-	-	1	2	3	2	4	2	4	12
secondary	(010)[100]	0	1	1	2	1	5	1	-	1	1	3
	(010)[101], [201]	2	1	-	2	2	7	3	3	1	2	9
	(001)[100]	2	2	-	1	-	5	-	-	-	-	-
	(001)[110], [1-10]	1	1	4	-	2	8	-	-	-	1	1
	(1-1-1)[110], (11-1)[1-10]	3	1	2	3	-	9	-	2	-	-	2
	(10-1)[111], [1-11]	1	-	2	1	-	4	5	-	1	-	6
tentative	(11-1)[112]	-	-	-	1	-	1	-	-	-	-	-
	(110)[1-12]	4	1	-	-	2	7	1	-	1	-	2
Further rep.	(1-20)[001]	-	1	-	-	1	2	-	1	-	-	1
	(20-1)[102]	-	1	-	-	1	1	-	-	-	-	-
	(13-1)[-112]	-	1	-	-	-	1	3	-	1	-	4
	(20-1)[112], [1-12]	2	1	1	-	-	4	1	-	-	2	3
	(021)[1-12]	-	1	3	1	2	7	3	1	4	3	12
	(11-1)[101]	-	-	1	-	-	1	-	-	-	-	-
total		15	12	14	12	13	66	19	11	11	13	55

¹ Classification of slip system after dominance as reported by Kruse et al. (2001); Further reported (further rep.) are detected slip systems listed by Stünitz et al. (2003).

6.2. Discussion

In this chapter EBSD results are discussed with respect to deformation mechanisms including microstructural observations described in chapter 3.

6.2.1. Quartz

6.2.1.1. Deformation Mechanisms

Quartz microstructures yield evidence for deformation under high temperature conditions in both, the Qdd and Fdd. Subgrain boundaries associated with undulose extinction, the presence of misorientation angles $<10^\circ$, though minor, and a CPO are indicative for intracrystalline deformation by dislocation creep (Passchier and Trouw, 2005). Undulose extinction is often expressed by rectangular subgrains forming chessboard patterns (Fig. 9k, l) which are associated with combined basal and prism slip in the stability field of high quartz ($\sim <650^\circ\text{C}$) (Kruhl, 1996; Mainprice et al., 1986). Ribbons with straight grain boundaries (D4), interlobate grain shapes (D1, D2), seriate (D2) to inequigranular (D1) frameworks, dissection and pinning microstructures, and highly curved grain boundaries suggest dynamic recrystallization by GBM typical for high temperature conditions (Fig. 9) (Hippertt et al., 2001; Jessel, 1987; Stipp et al., 2002b; Urai et al., 1986). High temperature GBM in combination with diffusion, fast recovery and subsequent annealing might account for low internal misorientation of quartz (e.g., Heilbronner and Tullis, 2002; Urai et al., 1986). Subgrain rotation is assumed to additionally contribute to recrystallization as inferred from a decreasing transition from 2° – 10° misorientation angles and the occurrence of angles between 10 and 20° (Fig. 22) (e.g., Neumann, 2000; Passchier and Trouw, 2005). However, observed microstructures are dominated by GBM characteristics implying a minor role of SGR. The lack of misorientation angles between 10 and 20° in D1 (Fig. 22) might result from displacement of these boundaries by high angle boundaries due to unrestricted GBM (e.g., Stipp et al.,

2002a). This is supported by the increase of large misorientation angles in D1 (Fig. 22). Deformation by diffusion creep likely contributed to deformation at temperatures >800 °C in the investigated samples, but dislocation creep is dominant as inferred from microstructures and CPOs (e.g., Passchier and Trouw; Stipp et al., 2002b). Smooth quartz feldspar phase boundaries in all domains are indicative for diffusion assisted phase boundary migration (Fig. 11) (Gower and Simpson, 1992). In matrix quartz this is suggested to be the dominant deformation mechanisms. Dominant deformation by diffusion could also account for a random CPO because the development of a CPO is generally attributed to dislocation creep (Passchier and Trouw, 2005).

6.2.1.2. Dauphiné Twinning

Dauphiné twinning is a common feature of quartz from all domains as demonstrated by frequent 60° misorientation angles and related rotation around quartz c-axis (Fig. 22, 25b, 30) (e.g., Frondel, 1962). Dauphiné twinning can be a primary feature during crystal growth (Frondel, 1962), is associated with the α - β transition of quartz as inversion twins (e.g., Piazzolo et al., 2005) or can be induced by mechanical twinning in response to stress exposure (e.g. Lloyd, 2004; Menegon et al., 2011a; Tullis, 1970). The latter is considered as a process to reduce the stiffness of a mineral by switching stiff negative rhomb {z} planes to soft positive rhomb {r} planes parallel to the compression axis (e.g., Menegon et al., 2011a; Tullis, 1970;). Mechanical twinning is a possible source for Dauphiné twins in the investigated samples. This is inferred from interrupted subgrain boundaries along Dauphiné twin boundaries (Fig. 30e). Furthermore, twin boundaries reveal similar interlobate geometries as grain boundaries (Fig. 30) suggesting migration of twin boundaries. Migration of Dauphiné twin boundaries was observed to correlate with grain boundary migration by Piazzolo et al. (2005). Furthermore, some twin boundaries continue into neighbouring grains (Fig. 30c) which was stated in the paper of Heidelbach

et al. (2000) as indication for dynamic recrystallization of a twinned grain. However, it is not evident that one twin type (r or z) is more deformed than the other which would point to mechanical twinning to make a grain more deformable (Menegon et al., 2011a). Diffusion, fast recovery and grain boundary migration most likely obliterated possible indicators. Furthermore, it could be shown that some twinning reverts after stress is released (Wenk et al., 2007). Additional twinning during the α - β transition during cooling associated with especially high mobility of Dauphiné twin boundaries (Barber and Wenk, 1991) might further modify the imprint of mechanical twinning during deformation of investigated samples. This is supported by the occurrence of Dauphiné twins in quartz of all orientations and not only in grains suitably oriented for mechanical twinning (e.g., Menegon et al., 2011a; Minor et al., 2018). This could explain why some subgrain boundaries cross twin boundaries (Fig. 30e). The origin and evolution of Dauphiné twinning in quartz of the investigated samples appears complex, which to unravel is beyond the scope of this work.

6.2.1.3. Intracrystalline Slip

The cross-girdle distribution of type II in 2997 ribbons is indicative for combined basal, rhomb and prism slip in $\langle a \rangle$ direction during coaxial deformation (Fig. 20) (e.g., Schmid and Casey, 1986; Stipp et al., 2002b). Rhomb slip is also inferred from the occurrence of one of the positive $\{r\}$ plane poles around Z in all domains. Peripheral c-axis maxima partly overlapping with $\langle a \rangle$ and $\{m\}$ poles suggest combined basal and prism slip in $[c]$ and $\langle a \rangle$ directions in all domains (except matrix quartz) (e.g., Little et al., 2013). This is consistent with poles of combined $\langle a-c \rangle$ directions around X (Qdd and D3) and agrees with chessboard extinction. The latter is associated with combined basal and prism slip (Kruhl, 1996) Type II cross-girdles are further indicative for constrictional strain (Fig. 2c) (Schmid and Casey, 1986). However, in YZ section, ribbons are elongated (Fig. 7c) and

quartz c-axis opening angles are large ($\sim 100^\circ$) suggesting constrictional to plane strain (Schmid and Casey, 1986).

Similar CPO patterns as in D3 and the Qdd are also recorded from studies investigating quartz deformation under comparable high T conditions deforming by dislocation creep accommodated GBM recrystallization. Cavalcante et al. (2018) reported quite similar CPOs for quartz ribbons from the Três Rios region, SE Brazil. They suggested the patterns to result from diffusive processes associated with GBM recrystallization and subsequent grain growth. Alternatively, the authors considered activity of multiple slip systems of combined rhomb<a> and prism [c]. Little et al. (2013) analyzed quartz CPOs in eclogite-bearing migmatites deformed in the presence of melt at $T > 650^\circ$. Quartz CPOs resembling textures in the present study can be attributed to their *transitional to C-slip* CPOs. The authors interpret their pattern to indicate simultaneous activity of basal<a>, prism[c] and prism<a> slip systems. Martelat et al. (1999) reported for naturally deformed high-grade quartzo-feldspathic rocks from southern Madagascar comparable c-axis patterns for quartz ribbons (D3, D4) and conclude prism[c] slip. Augenstein and Burg (2011) investigated deformed and annealed quartzites from the French Massif Central and interpreted similar quartz textures as result of a combination of simple shear and constrictional deformation with activity of multiple slip systems basal, rhomb and prism <a> slip.

Schmid factor maps, misorientation axis distributions and results of the boundary trace analysis imply activity of multiple active slip systems. Schmid factor maps show that quartz grains are suitably oriented for prism<a> (category A), prism[c] (category B, C), basal<a> (category C) and rhomb<a> slip (category C) (Fig. 27). The repetitive pattern of misorientation axes accumulated around c, a, and between c and a quartz directions suggests a dominance of prism slip in combined <a+c> directions (Figs. 24c, d, 28). The

boundary trace analysis indicates dominant rhomb and subordinate prism slip in most quartz categories. Activity of multiple active slip systems is common in quartz deformed at high temperatures (e.g., Kruhl, 1996; Stipp et al., 2002b). Rhomb slip was probably promoted by mechanical Dauphiné twinning in the investigated samples (e.g., Menegon et al., 2011b). Prism slip becomes important at temperatures around ~ 500 °C and prism[c] slip is reported at temperatures >630 °C (e.g., Mainprice et al., 1986; Stipp et al., 2002b). Thus, multiple active slip systems including prism[c] slip at deformation temperatures around 800°C are consistent for the deformation of quartz in the investigated samples.

6.2.1.4. Modification of the Deformation Record

Schmid factor maps (Fig. 27) reveal high Schmid factors for basal<a> and prism[c] slip in category C quartz and high Schmid factors for prism[c] slip in category B. In category A quartz prism<a> slip alone reveals high Schmid factors. Rhomb<a> slip shows moderate Schmid factors in quartz of all categories. This observation conflicts with the frequency of observed slip systems, where rhomb slip systems are most common in all categories (Table 5). Recovery during annealing could modify records of active slip systems during deformation. This is inferred from unsuitable orientation of most slip planes at high angle to the foliation plane (Fig. 29a, Appendix Table 3) and low angle ($2-10^\circ$) misorientation axis distributions in sample coordinates (Fig. 24). The latter display misorientation axes accumulated at the periphery around Z (D1, D2, D3). Slip planes in suitable orientation for easy slip are commonly subparallel to the foliation plane and display misorientation axes (associated with tilt boundaries) around the kinematic vorticity axis Y in high strain zones (e.g., Kruse et al., 2001; Menegon et al., 2013; Reddy and Buchan, 2005). Augenstein and Burg (2011) reported that annealing can lead to activation of previously inactive slip systems and reactivation of slip systems. The authors investigated quartz deformed under

greenschist-ambhibolite facies conditions which annealed in the vicinity of a pluton intrusion to temperatures above 650 °C. They argued that modification of slip systems was due intergranular stresses related with a volume increase during α - β transition of quartz around 650 °C. Quartz investigated in this study display abundant Dauphiné twinning. In section 6.2.1.2. it was suggested that some twinning was induced by the α - β transition during cooling. Hence, α - β transition during cooling could cause intergranular stresses and thereby modifying the slip system record. However, low angle (2–10°) misorientation axes of feldspars in D1 A, D3 and D3 display similar patterns in sample coordinates as quartz in D1 and D2 (compare Figs. 24a and 35). This indicates that modification of the slip system record in quartz cannot be exclusively attributed to Dauphiné twinning, but that a change in the stress field during annealing affected both, quartz and feldspars, thereby possibly activating slip systems with slip planes at high angle to the foliation plane. In the Fdd the misorientation distribution pattern (sample coordinates) of quartz displays misorientation axes aligned to the YZ plane (Fig. 24b). A similar pattern occurs in lenticular D2 feldspar (Fig. 35). Both, quartz ribbons and alkali feldspar in D2 occur in foliation parallel layers of few grains in width and are restricted by surrounding feldspar matrix and quartz, respectively (Figs. 7d, e, 10k, l). Coarsening of feldspar matrix and D2 quartz during annealing could exert stresses on foliation parallel quartz ribbons and D2 alkali feldspars, respectively, thereby producing a common misorientation axis distribution.

Subgrain boundaries presenting slip planes subparallel to the foliation plane and with misorientation axes oriented around Y are scarce in quartz (Appendix Table 3). Therefore, dominant slip systems cannot be deduced from boundary trace analysis. Nevertheless, multiple active slip systems with dominant prism slip as indicated by the repetitive

pattern of misorientation axis distributions are consistent with quartz CPOs and agree with high temperature deformation.

6.2.1.5. CPOs and Selective Coarsening

Quartz CPOs differ between ribbons in the Fdd, 2997 ribbons and D1/ D2 (Fig. 20). However, common features in CPOs and similar deformation microstructures suggest similar intracrystalline deformation. Furthermore, misorientation axis distribution patterns and boundary trace analysis yield equivalent results though the deformation record is probably partly obliterated during annealing. Striking differences between individual domains are quartz modal content and grain size (Fig. 7, Table 4). CPOs become pronounced with increasing modal content and grain size and are strongest in D1 where quartz is the major phase and deformation can evolve unrestricted. Thus, it is inferred that the CPO development from the Fdd towards D1 is determined by unrestricted grain growth. Microstructures are indicative for deformation by GBM recrystallization which produces an increase in grain size (e.g., Hirth and Tullis, 1992; Stipp et al., 2010; Platt and Behr, 2011). Examination of quartz category A, B and C shows that category C reveals largest grain sizes in all domains (Table 4). Furthermore, c-axis orientation of category C quartz is identical with CPOs in D1 and D2 where quartz is almost exclusively represented by category C quartz. Thus, category C quartz coarsens selectively at the expense of category A and B quartz. It is suggested that selective coarsening of category C quartz is completed in D1 and D2 where quartz forms an interconnected framework. In quartz ribbons of the Fdd selective coarsening of category C is incomplete as reflected by CPO pattern. Selective coarsening might be inhibited by restricted growth in Z direction due to limited connectivity. 2997 ribbons display smallest ribbon grain sizes (Table 4) and coarsening is suggested to be negligible in this domain. Thus, CPOs in this domain might represent an initial stage of deformation before coarsening displaying multiple active slip

systems. Matrix quartz is excluded from this consideration as quartz grains are weakly connected and coarsening by GBM recrystallization requires a gradient in strain energy between adjacent grains.

Selective growth is observed in several studies to occur during dynamic (e.g., Heilbronner and Tullis, 2006; Muto et al., 2011) and static recrystallization (e.g., Barnhoorn et al., 2005; Stöckhert and Duyster, 1999). In the dynamic case GBM recrystallization leads to consumption of grains with high dislocation density to reduce strain energy (e.g., Urai et al., 1986). Several studies reported that grains with soft orientation for specific slip systems grow at the expense of grains with hard orientation (Heilbronner and Tullis, 2006; Muto et al., 2011; Neumann, 2000; Stöckhert and Duyster, 1999). This is because grains with hard orientation accumulate strain which cannot be removed due to impeded crystal slip. In this study a difference in strain energy cannot be inferred between quartz of different categories. GROD maps display similar low internal misorientation of all quartz grains and subgrain boundaries occur in all categories (Figs. 21, 23, 27). Possible differences are most likely erased during annealing. However, Schmid factor maps and CPOs in D1 and D2 suggest combined slip of prism, basal and rhomb planes in $\langle a \rangle$ and $[c]$ directions (Figs. 20, 27). In category A and B quartz high Schmid factors are only indicated for prism $\langle a \rangle$ and prism $[c]$ slip, respectively. Thus, in category C quartz multiple slip systems are active. Grains that deform by multiple slip systems store higher strain energies than grains that deform by a single dominant slip system (Kamb, 1972; Nicolas and Poirier, 1976). Stipp et al. (2002b) proposed that at high temperatures high internal strain energy may contribute to higher grain boundary mobility. Therefore, soft orientation for multiple slip systems and resulting high grain boundary mobility may cause selective growth of category C quartz. Mechanical Dauphiné twinning probably

contributed to the activity of multiple active slip systems as the {r} rhomb planes are aligned parallel to the foliation plane (Fig. 20).

Selective coarsening during static conditions can further contribute to a modification in CPOs (e.g., Stöckhert and Duyster, 1999). The lack of highly amoeboid grain shapes, low internal misorientation, low abundance of misorientation angles $<10^\circ$, partly straightened grain boundaries as well as the occurrence of equilibrated triple junction angles of 120° infer that deformation microstructures were modified during post-deformational annealing (Fig. 9) (e.g., Passchier and Trouw, 2005). However, low internal misorientation can also result from high temperature deformation by dynamic GBM recrystallization, contemporaneous diffusion and fast recovery, all process which act to lower the internal strain energy (e.g., Passchier and Trouw, 2005). Piazzolo et al. (2006) found in experimentally deformed-than-annealed synthetic rocksalt that at high temperatures (their GBM 2) annealing is characterized by nucleation and growth of strain free grains. Heilbronner and Tullis (2002) further investigated the effect of static annealing on experimentally deformed quartzites. They found that annealing subsequent to high temperature dynamic GBM recrystallization (their regime 3) results in the least grain size increase compared to lower temperature/ high stress deformation (their regime 1 and 2). The authors explained this effect by largest recrystallized grain sizes and lowest stored strain energy in their regime 3 because these factors influence nucleation (see also Humphreys and Hatherly, 1995). Therefore, Heilbronner and Tullis (2002) interpreted that final microstructures result probably entirely from growth of pre-existing grains. In this study, deformation temperatures are very high ($\sim 800^\circ\text{C}$) and grain sizes very large supporting low stresses, fast diffusion and recovery, and high grain boundary mobility (e.g., Piazzolo et al., 2006) all of which likely resulted in low stored strain energy after deformation. Furthermore, nucleation of strain free grains is not

evident. Therefore, it is interpreted that annealing did not contribute to selective coarsening of category C quartz and that CPOs in D1 and D2 represent preserved deformation textures.

6.2.2. Feldspar

6.2.2.1. Deformation Mechanisms

Both feldspars show in the Fdd and Qdd evidence for intracrystalline deformation by dislocation creep as undulatory extinction, subgrain boundaries and in plagioclase bended twin lamellae and deformation twins (Fig. 10) (e.g., Passchier and Trouw, 2005). Irregular grain shapes with interlobate grain boundaries, dissection and pinning microstructures, left-over grains, and a CPO are indicative for dislocation creep accommodated by GBM recrystallization (Figs. 10, 31, 32) (e.g., Jessel, 1987; Lister et al., 1978; Passchier and Trouw, 2005; Urai et al., 1986). Microstructures of alkali feldspar in D2 show some differences to other domains suggesting different deformation behaviour: alkali feldspar often shows lenticular aggregates of one grain in width and grain and subgrain boundaries perpendicular to the foliation (Fig. 34a, b). In places, the latter is observed to pass in high angle grain boundaries ($>10^\circ$) (Fig. 34a, b). Furthermore, adjacent grains in these aggregates often reveal similar orientations. The misorientation angle distribution in D2 shows a high abundance of angles between 10 and 20° for correlated data pairs which deviates from the uncorrelated distribution (Fig. 33). This is indicative for inheritance of microstructures by SGR where the misorientation of low angle boundaries ($<10^\circ$) progressively increases to high misorientation angles ($>10^\circ$) (Wheeler et al., 2001). The transition from low to high angle boundaries and similar orientation of neighbouring grains support this explanation for alkali feldspar in D2. SGR in feldspar is suggested to be promoted by constriction by quartz because indicative

features are most pronounced in feldspars surrounded by quartz, e.g., also in constricted feldspar layers in the Fdd (Fig. 34c).

Smoothly curved, protruding and bulging phase boundaries between both feldspars and between quartz and feldspar are indicative for diffusional processes during deformation (Fig. 11) (e.g., Gower and Simpson, 1992; Menegon et al., 2013). Furthermore, especially in D2 alkali feldspar boundaries often form cusps parallel but also perpendicular to the foliation (Fig. 11f). Such microstructures are a common feature in granulite facies rocks (e.g., Martelat et al., 1999) and are interpreted by Gower and Simpson (1992) as diffusion assisted phase boundary migration. Diffusion is also inferred from films and bands of one feldspar phase and/ or quartz along grain boundaries of the other feldspar and by interstitial occurrence of both (Fig. 10b, c). The former is often observed in alkali feldspar where plagioclase builds the film/ band phase. Similar microstructures were reported by Franek et al. (2011; their Fig. 10b) and interpreted to result from chemically driven recrystallization of perthitic alkali feldspar and redistribution of plagioclase probably via grain boundary diffusion. However, in this study no relictic prophyroclasts of perthites are found and plagioclase composition reveals similar An-contents in all subdomains of the Fdd (Table 1). Therefore, chemically driven recrystallization is suggested to be of minor importance in the investigated samples.

6.2.2.2. Intracrystalline Slip

Both feldspars, alkali feldspar and plagioclase, show in all subdomains of the Qdd and Fdd a CPO (Figs. 31, 32). In D1 A, D2 and in the Fdd the CPO patterns are similar and infer slip of (010) in [100] for alkali feldspar and for plagioclase (010) slip in [100] and [001]. Plagioclase CPOs are further indicative for (021)[1-12] slip. The boundary trace analysis supports these slip systems (Table 6, Fig. 37). The (010) plane is the most common slip plane observed in experimentally and naturally deformed feldspars (e.g., Kruse et al.,

2001; Marshall and McLaren, 1977b; Martelat et al., 1999; Schulmann et al., 1996; Svahnberg and Piazzolo, 2010; Willaime et al., 1979). (010) slip in [001], [100], [201] and [101] was reported in several studies (e.g., Kruse et al., 2001, references therein; Martelat et al., 1999). Slip of (021)[1-12] is common in plagioclase in this study but rarely reported in other studies (e.g., Montardi and Mainprice, 1987; Svahnberg and Piazzolo, 2010). Svahnberg and Piazzolo (2010) detected (021)[1-12] in plagioclase from sheared anorthosite-leucogabbros at amphibolite to granulite facies. They found this slip system in plagioclase of hard orientation for (010)[001] slip and suggested (021)[1-12] to represent healed microfractures thereby following Kruse et al. (2001) that grains in hard orientation for the former slip system respond by fracturing. In this study (021)[1-12] is often observed in grains unsuitably oriented for slip on (010) (Fig. 37d, Appendix Tables 4, 5). Stünitz et al. (2003) investigated dislocation generation in experimentally deformed plagioclase and found that fracturing is a common precursor of dislocations and accompanies crystal plastic deformation in plagioclase even at temperatures as high as 700–900°C (references therein). Moreover, dry mineral assemblages are much stronger than water-bearing rocks which promotes fracturing (e.g., Rybacki and Dresen, 2004; Menegon et al., 2011b). The Sri Lankan granulites are suggested dry as inferred from the lack of OH-bearing mineral phases and low OH contents in quartz (preliminary investigations, not presented in this study). Therefore, it is concluded that the (021)[1-12] slip system results from dislocation generating fractures in plagioclase unsuitably oriented for slip on the (010) plane.

In D1 L the CPO differs from other subdomains (Fig. 31). For alkali feldspar the CPO is indicative for slip of (001)[100] resulting in a shift of (010) plane poles towards Y. Poles to (001) planes scatter also in other subdomains around Z and (001)[100] slip systems were further detected in D1 A and D3 via boundary trace analysis (Table 6). (001)[100]

is reported in other studies as subordinate slip systems for plagioclase and alkali feldspar (e.g., Kruse et al., 2001, references therein; Martelat et al., 1999). For alkali feldspar in D1 L it is suggested that (001)[100] slip dominated over (010) slip causing different CPOs. Plagioclase CPOs in D1 L show no longer a girdle distribution of (021) plane poles parallel to the YZ plane. The lack of a preferred orientation for (021)[1-12] slip implies less fracturing in plagioclase of D1 L following the above argumentation. Less fracturing and a stronger CPO in D1 L are indicative for pronounced crystal plastic deformation and, hence could imply that plagioclase in D1 L is weaker than in other subdomains. A possible explanation for weak plagioclase could be the lowest measured An-contents in D1 L (Table 1). Rybacki and Dresen (2004) established deformation mechanism maps for feldspar rocks based on published constitutive laws and stated that anorthite aggregates are strongest. Thus, lowest An-contents at same deformation conditions could result in weak plagioclase in D1 L compared to other subdomains.

The boundary trace analysis reveals for both feldspars further slip systems in all subdomains (Table 6, Appendix Tables 4, 5). In plagioclase (010)[001] and (021)[1-12] are dominant and correlate with observed CPOs. Therefore, remaining slip systems are interpreted to be subordinate. For alkali feldspar further (001) in [110] and [-110], (1-1-1)[110], (11-1)[1-10] and (021)[1-12] slip systems are frequently detected (Table 6). Activity of multiple slip systems might account for weaker CPOs compared to plagioclase (Fig. 31, 32). Furthermore, (021)[1-12] could indicate fracturing in alkali feldspar equivalent to plagioclase. However, the lack of pronounced distribution pattern for the (021) plane in pole figures suggest that fracturing was less important in alkali feldspar compared to plagioclase.

Results of the boundary trace analysis yield abundant slip planes at high angle to the foliation plane (Fig. 37a, Appendix Tables 4, 5). Furthermore, low angle misorientation

axes ($2-10^\circ$) display peripheral maxima around Z in sample coordinates (Fig. 35). Similar features are also detected in quartz and possible explanations were discussed in section 6.2.1.4. For quartz it was concluded that the deformation record was modified during annealing. This is also suggested for feldspars. However, in plagioclase the (010) slip plane was frequently detected subparallel to the foliation plane (Appendix Table 5, Fig. 37c). Furthermore, the high frequency of (010) and (021) slip planes is consistent with CPOs (Figs. 31, 32). Therefore, it is concluded that in plagioclase subgrain boundaries formed during deformation are partly preserved. This might also apply to alkali feldspar but is difficult to demonstrate because a preferred foliation parallel orientation is not evident for specific slip planes (Appendix Table 4).

6.2.2.3. Slip systems and Misorientation Axes

The boundary trace analysis yields in most cases several possible misorientation axes for a specific slip system (Appendix Tables, 4, 5). For the most common slip systems a dominance of specific misorientation axes could be determined (Fig. 38). For instance, [100] and [-100] are frequently identified as misorientation axes for (010)[001] and (021)[1-12] (Fig. 38, Appendix Table 4, 5). This is consistent with results of Svahnberg and Piazzolo (2010) and Kruse et al. (2001). However, there is no consistency in literature for individual misorientation axes defined for specific slip systems. For instance, Kruse et al. (2001) discussed [-110] as possible rotation axis for either (001)[100] or (001)<110>. Menegon et al. (2013) further interpret [010] as possible rotation axis for the same slip system (001)[110] as discussed by Kruse et al. (2001). Moreover, Kruse et al. (2001) stated that for lower crystal symmetry (lower than orthorhombic) for tilt boundaries the angle between rotation axes and Burgers vectors may vary between 60° and 120° . Consequentially, there might be a variation in misorientation/ rotation axes for specific slip systems. Based on the large data set in this study a model is proposed for the spread

of rotation axes in inverse pole figures and relating slip systems (Fig. 38). This model is equivalent to that of quartz (Fig. 24d) (Neumann, 2000) and could serve as template for future work on misorientation axis distributions in feldspars.

6.2.2.4. Differences in CPO Intensity between Subdomains

The observed CPOs are weakest in D1 A and D4 for both feldspars (Figs. 31, 32). In D4 weak textures can be attributed to the polyphase composition including matrix quartz. Impure phase assemblages are commonly observed to display weak CPOs because abundant second phases inhibit dislocation creep accommodated by GBM by pinning and rather promote deformation mechanisms such as mass transfer processes and grain boundary sliding, both which do not produce a CPO (e.g., Herwegh and Berger, 2004; Linckens et al., 2011). In D4 both feldspars and quartz occur isolated as interstitials and display smoothly curved phase boundaries (Figs. 10b, c, 11d). These features are indicative for diffusional processes (Franek et al., 2011; Gower and Simpson, 1992; Menegon et al., 2013). In D1 A, D1 L and D3 feldspar assemblages are largely free of quartz and display stronger CPOs compared to D4. Feldspars are less restricted by quartz and can deform by dislocation creep.

Moderate textures in D1 A can be attributed to the predominance of quartz in the Qdd (Fig. 7a). The latter is generally weaker than feldspar although the strength contrast between quartz and feldspar is supposed to be small at high temperatures (e.g., Passchier and Trouw, 2005). Nevertheless, quartz microstructures, grain size and CPO infer strong deformation whereas feldspar aggregates display lenticular shapes with locally developed pinch and swell structures implying that quartz is the weaker phase (Figs. 7a, 11a) (e.g., Fossen, 2016; Gardner et al., 2016). Thus, quartz probably accommodated more strain than feldspar in D1. In the Fdd quartz is less abundant and feldspar can accommodate more strain resulting in stronger CPOs of feldspars in the Fdd compared to

the Qdd. D1 L constitutes a special case because feldspar CPOs are strongest, and the layer is not constricted by quartz to lentil shapes or pinch and swell structures (Fig. 7a). The strong plagioclase CPO in D1 L was already discussed and suggested to result from a lower strength of An-poor plagioclase. The predominance of plagioclase in D1 L and lower strength should also result in a lower strength contrast between quartz and the layer thereby equally distributing strain between quartz and feldspar. This could favour a stronger plagioclase CPO in D1 L compared to D1 A which also affects alkali feldspar displaying strongest CPOs in D1 L.

6.2.2.5. Differences between Alkali Feldspar and Plagioclase

Alkali feldspar shows a greater variation in slip systems than plagioclase and this correlates with a weaker CPO of the former in all subdomains (Figs. 31, 32, Table 6). It appears that in alkali feldspar slip on multiple slip systems is easier facilitated than in plagioclase. So far, investigation of naturally and experimentally deformed feldspars did not reveal systematic differences between the crystal plastic deformation of alkali feldspar and plagioclase (for review see Tullis, 1983, 2002). Furthermore, studies with comparable high-grade microstructures are scarce (e.g., Eglydio-Silva et al., 2002; Gower and Simpson, 1993; Martelat et al., 1999) and lack the comparison of two feldspars deformed under same conditions. Nevertheless, in a review paper Tullis (1982) pointed that some studies on naturally deformed feldspars indicate that plagioclase remains brittle or undeformed at conditions where alkali feldspar shows slip or recrystallization (references therein). The author argued this could be due to a lower disordering temperature of Al-Si order in alkali feldspar because "disordering may be necessary for substantial slip and recovery". Furthermore, alkali feldspar shows more features of dynamic recrystallization by GBM as indicated by interlobate frameworks compared to polygonal aggregates of plagioclase. Stipp et al. (2002b) argued for quartz that grains

deforming by multiple slip systems probably build up higher strain energy (references therein) which is a driving force for grain boundary migration (Urai et al., 1986). Therefore, in alkali feldspar a greater ease of slip might enhance the activity of multiple slip systems resulting in a higher stored strain energy and provide the driving force for GBM recrystallization. Tullis and Yund (1985) divided the dislocation creep regime into dynamic recovery accommodated and dynamic recrystallization accommodated regimes. Based on their findings they concluded that recovery accommodated dislocation creep is difficult in feldspars because it involves diffusion for dislocations to climb. However, at high temperatures diffusion is faster and recovery becomes possible which is indicated in this study by subgrain boundaries and misorientation angles $<10^\circ$. Therefore, the deformation of alkali feldspar could be described as recovery and recrystallization accommodated while microstructures in plagioclase point to a dominance of recovery as accommodation mechanism. Different microstructures could also result from different annealing behaviour. This will be discussed in chapter 7 and 8.

7. Modal Content, Grain Size, Shape and Connectivity

7.1. Results

7.1.1. Quartz

7.1.1.1. Grain Size, Modal Content and Connectivity

In the Qdd quartz reveals largest grain sizes with area weighted mean grain sizes of ~13 mm in D1 and D0 (Table 7). D2 quartz shows a mean grain size smaller by one order of magnitude of 2.4 mm. In the Fdd mean ribbon grain sizes range between 6.5 mm in D3 and 3.8 mm in D4. Matrix quartz reveals smallest mean grain sizes of 257 and 338 μm in D3 and D4, respectively. Grain size distributions of D1/ D0 are polymodal (Fig. 39). In D2 the grain size distribution is skewed to smaller grain sizes. Grain size distributions of ribbons in the Fdd are also polymodal but significantly skewed to left. This is better pronounced for D4 ribbons whereas D3 ribbons display several striking peaks for large grain sizes. The grain size distribution of matrix quartz is shifted to smaller grain sizes and peaks at 200 and 250 μm in D3 and D4, respectively. In D3 a further pronounced peak lies around 500 μm and in D4 several minor peaks occur at larger grain sizes.

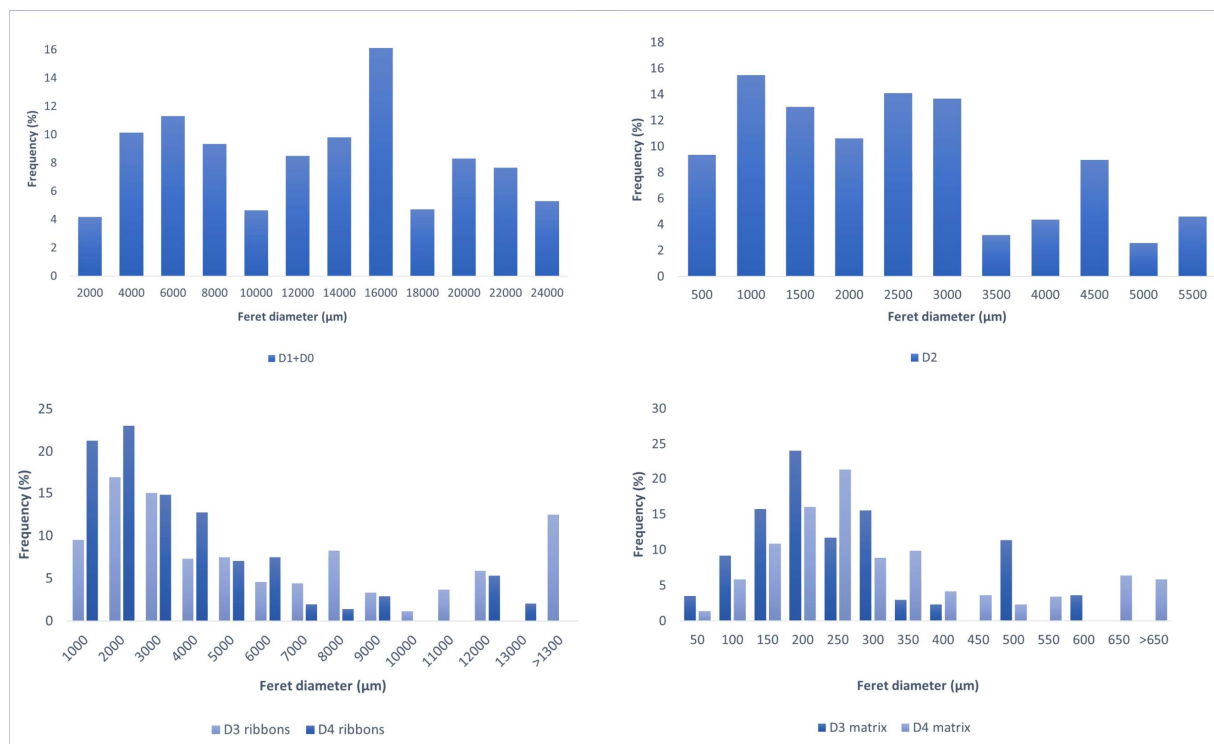


Fig. 39: Quartz grain size distributions.

The grain size development of quartz from matrix to D1 correlates in general with quartz volume fraction and connectivity (C_k and contact frequencies) (Fig. 40, Table 7).

Between matrix quartz and D2 the grain size increase is mainly determined by the volume fraction (note the large gap between D2 and matrix in Fig. 40a) and to a lesser extent by connectivity (Fig. 40b, c). On

the contrary, between D2 and D1 the controlling factor for the grain size development is the connectivity and is best pronounced by the number of neighbouring grains expressed by C_k (Fig. 40b). For D1 and D0 the results

show a stable grain size between ~10 and 15 mm in average which does not significantly develop with volume fraction nor connectivity.

The grain size development of quartz ribbons in the Fdd differs from other domains (Fig. 40). Quartz ribbons increase in size with volume fraction but decrease with connectivity (Fig. 41). Matrix quartz grain size correlates positively with volume fraction and connectivity (Fig. 42). In D3 quartz is less abundant in the matrix resulting in a lower

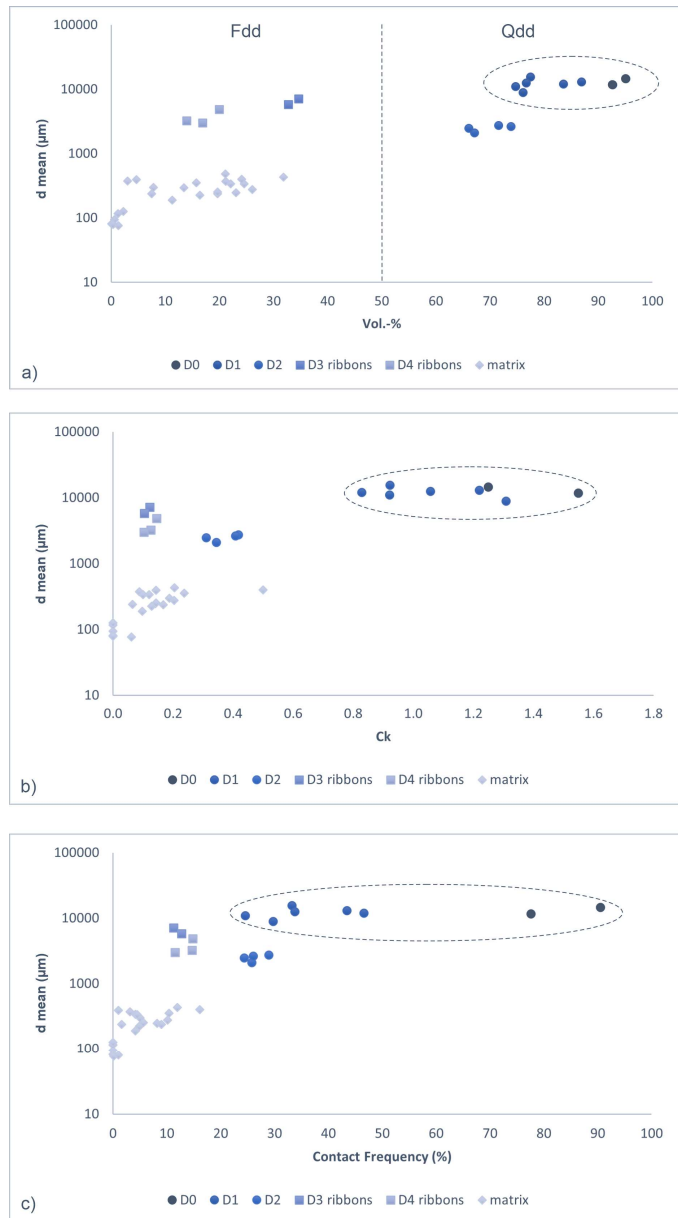


Fig. 40: Quartz grain size relations with modal content (a), and connectivity (b, c); note stable grain size in D1 and D0 (dashed circle) (grain size in logarithmic scale).

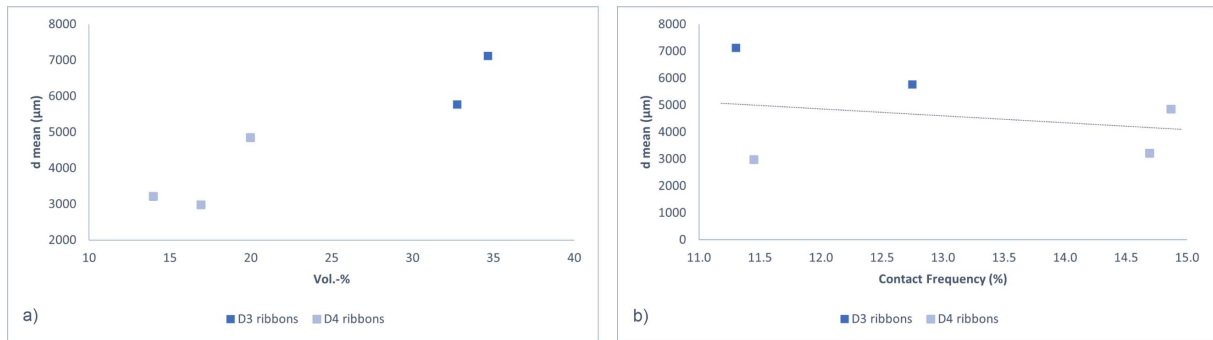


Fig. 41: Quartz ribbon grain size relations: a) increase of grain size with modal content; b) indicated (line) decrease with contact frequency.

connectivity and smaller grain sizes compared to D4 (Fig. 42, Table 7). Furthermore, in D3 matrix the development of grain size with volume fraction and connectivity is not as distinct as in D4 because in the former large, isolated grains occur which bias the correlation (Fig. 42d).

In the Fdd grain sizes of ribbons and matrix quartz correlate with the partition of quartz into matrix and ribbons (Fig. 43, Table 7). In D3 most quartz partitions into ribbons of coarse grain size (mean grain size 6.5 mm) (Fig. 43a). In the matrix quartz is depleted (Fig. 43c) and mean grain sizes are in average $\sim 250 \mu\text{m}$. In D4 ribbon quartz content is

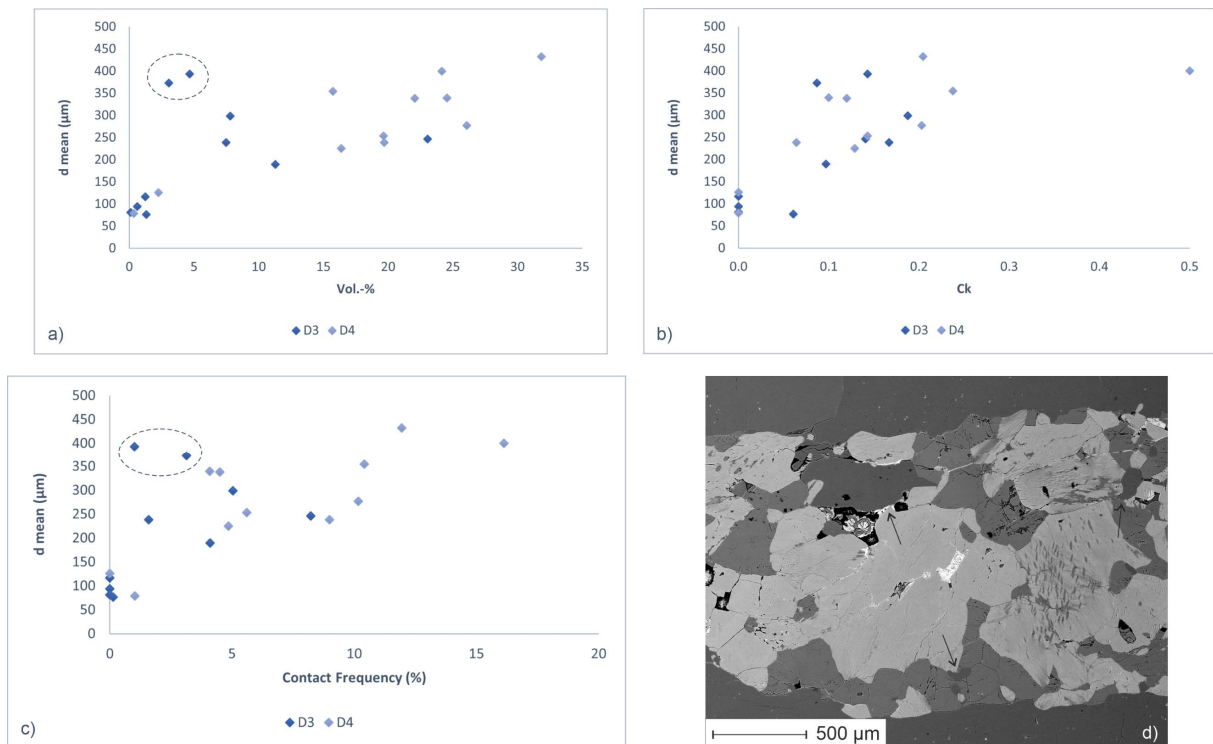


Fig. 42: Matrix quartz grain size relations: dashed circles in a) and b) refer to subdomains in D3 in which large, isolated grains bias the area weighted grain size to larger values; d) (BSE image) black arrows point to large and small quartz grains in a quartz poor domain of D3.

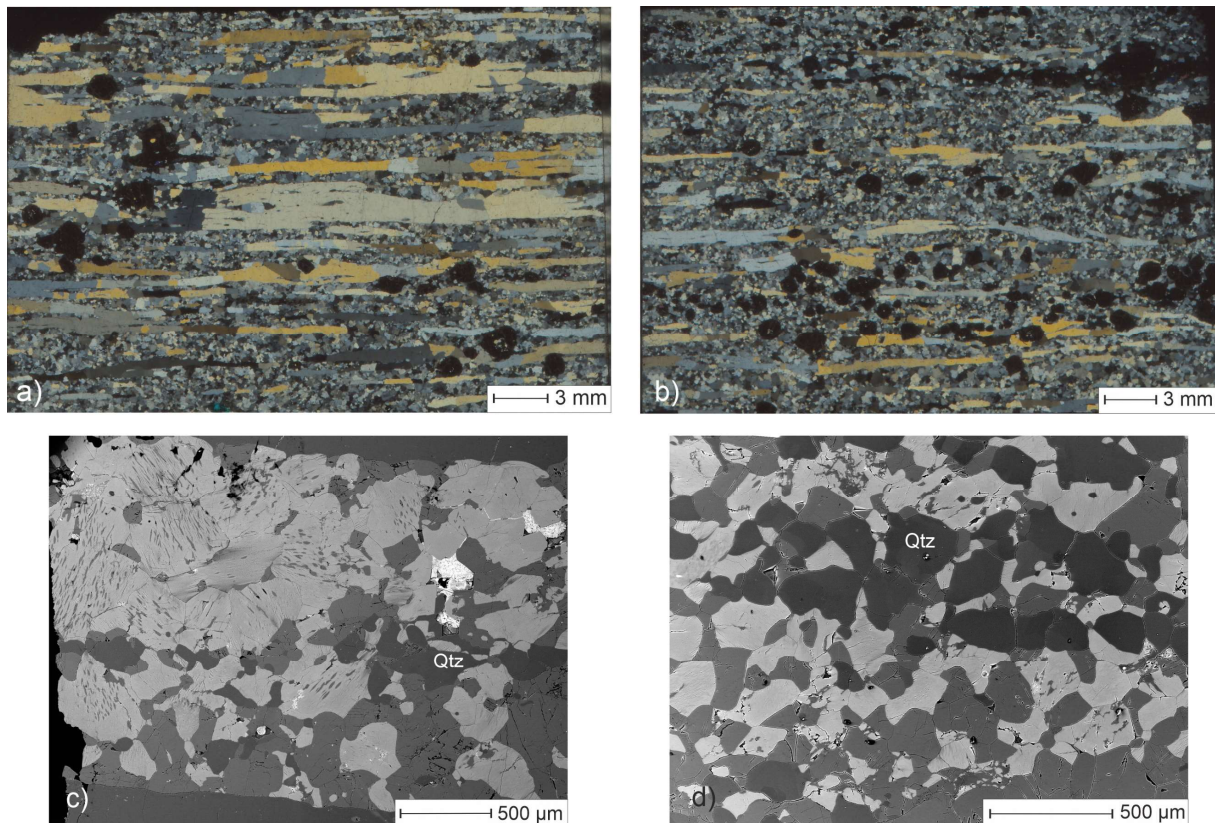


Figure 43: Quartz partition into ribbons and matrix in the Fdd (a, b: thin section scans recorded with polarization filter; c, e: BSE images): a, c) ribbons (a) and matrix quartz (c) in D3; b, d) ribbons (b) and matrix quartz (d) in D4.

decreased and so is the mean ribbon size (3.8 mm) (Fig. 43b). Matrix quartz is more abundant with larger grain sizes of $\sim 340 \mu\text{m}$ (Fig. 43d).

In summary, the results show that in the Fdd grain size increase is best related with modal content of quartz whereas in the Qdd in D2 and between D2 and D1 the grain size increase correlates stronger with the connectivity. This becomes evident in the relation of C_k and contact frequency with volume fraction of quartz (Fig. 44 a, b). In the Fdd the connectivity of matrix quartz increases up to a quartz volume fraction of about 10 %. Above this value no significant change in connectivity occurs neither for matrix quartz nor for ribbons. In the Qdd, where quartz constitutes the major component ($>50 \text{ Vol.-%}$), the connectivity increases considerably with volume fraction. This relation is also expressed in the Zener plot (Fig. 44c). In the Zener plot the connectivity of quartz in the Qdd is replaced by the Zener parameter defined by the aggregate size and volume fraction of feldspar aggregates (Appendix Table 6). The results show an increase of quartz grain size D with Z between

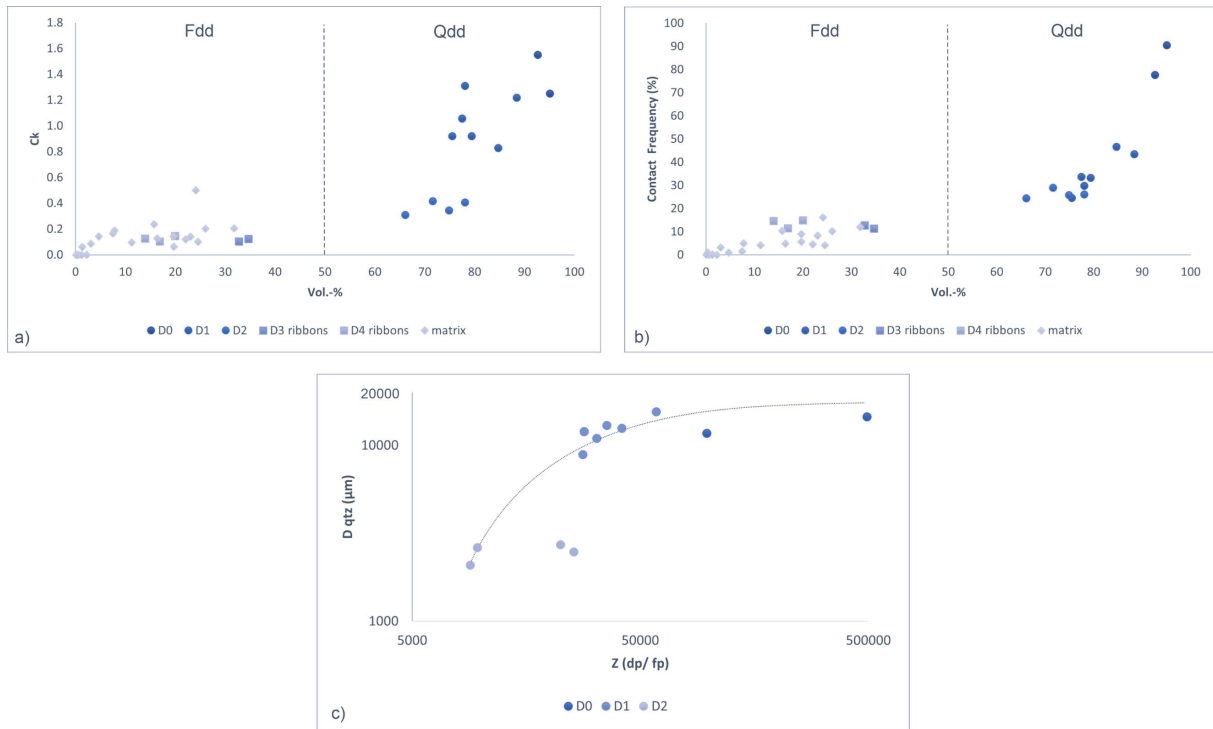


Figure 44: Quartz connectivity and Zener plot: a, b) development of connectivity C_k (a) and contact frequency (b) with modal content; c) Zener plot for quartz in the Qdd.

D2 and D1. In D1 the grain size increase attenuates and levels out towards D0. This is consistent with relations of quartz grain size with C_k and contact frequency and modal content (Fig. 40).

7.1.1.2. Shape Descriptors

In D1 and D0 Paris factor and Ω' display highest average values of $\sim 30\%$ (Paris factor and Ω') to 40% (Paris factor, D1) indicating most indented grain shapes and smoothest grain boundaries, respectively (Table 7). Paris factor and Ω' decrease over D2, D3 and D4 ribbons and are smallest in matrix quartz. In the latter, the average Paris factor is smallest in the matrix of D3 ($\sim 2\%$) whereas in D4 quartz grains reveal most angular grains as indicated by Ω' of 8.7% (Table 7). The development of Paris factor and Ω' shows a general trend from matrix quartz to D1/ D0 and increases with grain size, modal content, and connectivity (Table 7, Fig. 45, only shown for grain size and C_k). Within single domains there is a deviation from this overall development. In D1 and D0 there is a large scatter in data which show no correlation with grain size, modal content or connectivity (Fig. 45,

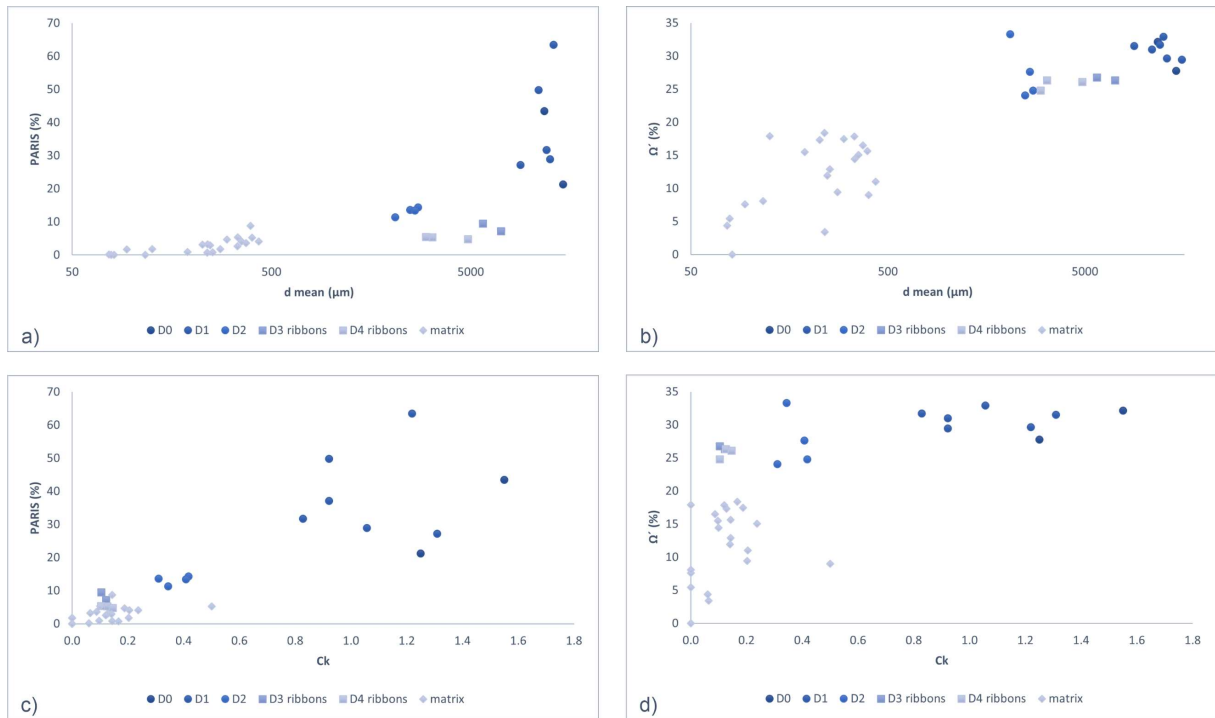


Figure 45: Paris factor and angularity (Ω') relations: a, b) relations with grain size (logarithmic scale); c, d) relations with connectivity (C_k).

Table 7). Quartz ribbons in D3 and D4 reveal a decrease of Paris factor and Ω' with increasing connectivity (Fig. 46). This refers to the polycrystalline nature of D4 ribbons. Fig. 46b shows that polycrystalline ribbons consist of small grains with straight boundaries and sharp edges (high angularity) whereas coarse-grained ribbons display smoothly curved or serrated grain boundaries. The development of Ω' in matrix quartz

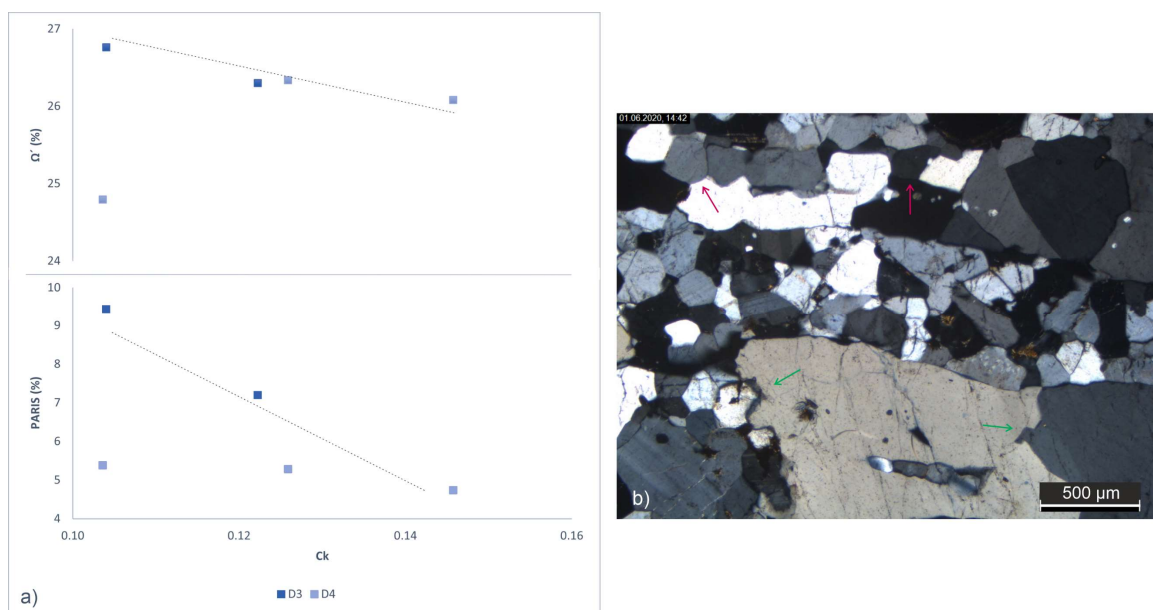


Fig. 46: Paris factor and angularity in quartz ribbons: a) decreasing Paris factor and Ω' with C_k ; b) (microscopic image with crossed polarizers) red arrows point to angular grains with straight boundaries in polycrystalline ribbons; green arrows indicate indented grain shapes and curved boundaries in coarse ribbons.

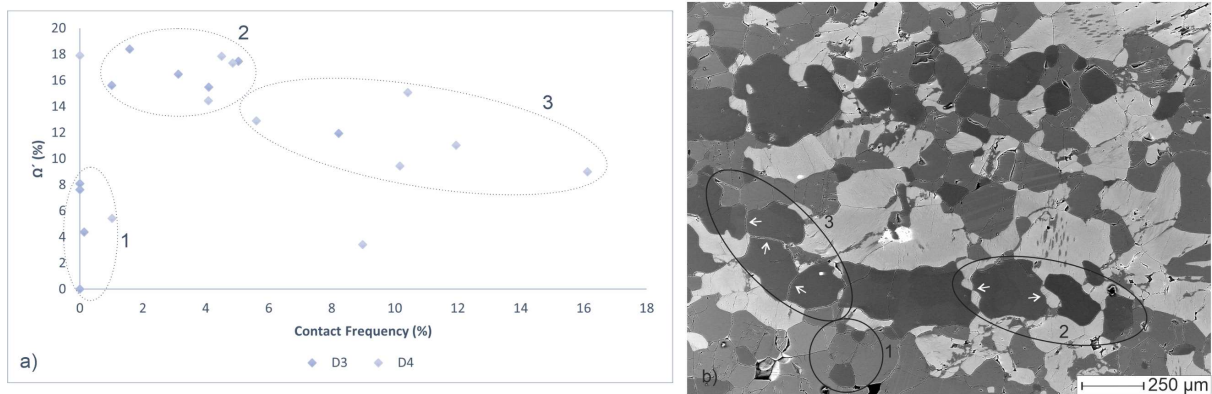


Fig. 47: Angularity in matrix quartz: a) three cluster of matrix quartz displaying different angularity; b) (BSE image): white arrows point to curved and straight boundaries in cluster 3 and 2, respectively.

shows a negative correlation with volume fraction and connectivity. In Fig. 47 this is demonstrated in exemplary fashion for the Ω' -contact frequency relation and displays three cluster of quartz grains with distinct angularity and contact frequency. The first cluster is characterized by largely isolated and highly angular grains. These grains often occur at junctions of three or four grains of feldspar (Fig. 47b). The second cluster is defined by grains with larger grain size but low connectivity. These grains occur between feldspars and form smoothly curved phase boundaries with feldspars. The third cluster has highest contact frequencies of like-like boundaries and displays straight grain boundaries between neighbouring quartz grains resulting in low values of Ω' .

Most elongated grain shapes are detected for D3 and D4 ribbons which display highest aspect ratios >3 (Table 7). The aspect ratio decreases over D2, D1/ D0 and is smallest for matrix quartz with an average of 1.7–1.8. For coarse-grained quartz (D3/ D4 ribbons and Qdd) the aspect ratio can be related with the connectivity and is decreasing with increasing connectivity (Fig. 48a, b). Furthermore, the aspect ratio reveals a positive relation with grain size for D2 and Fdd ribbons and further a correlation with volume fraction for D3/ D4 ribbons (Fig. 48c, d). Matrix quartz shows no development of aspect ratio.

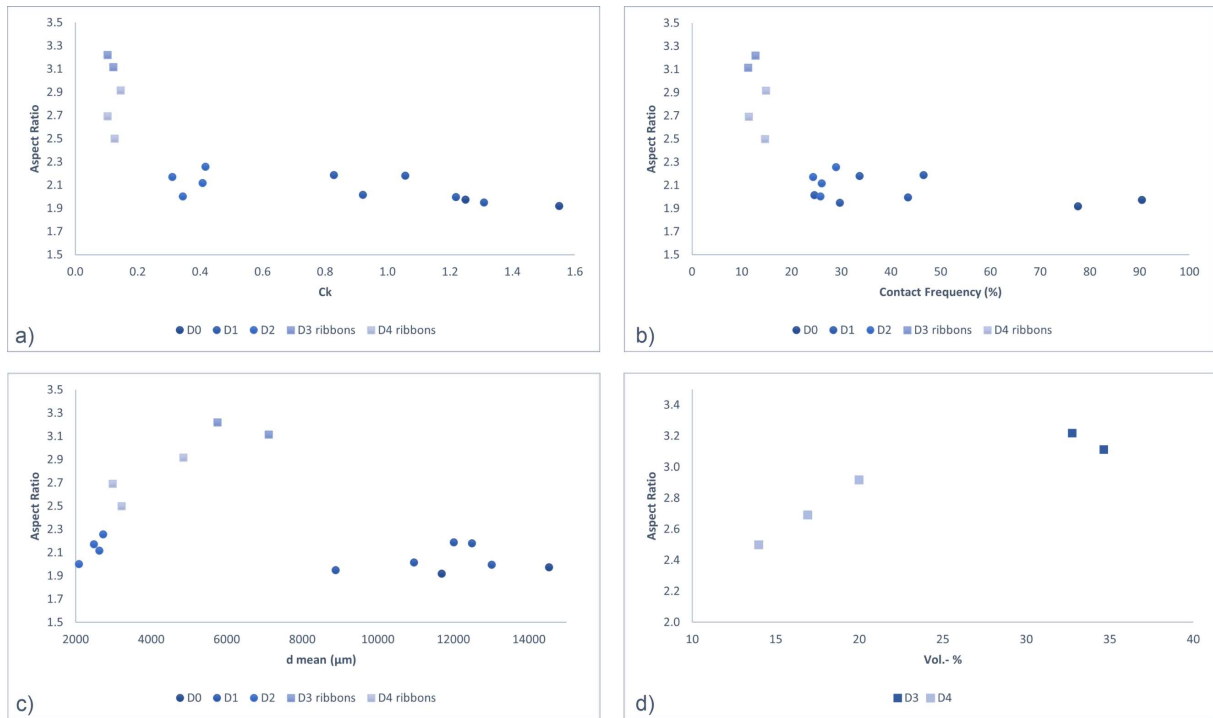


Fig. 48: Aspect ratio development of quartz in the Qdd and Fdd: relation with C_k (a), contact frequency (b) and grain size (c); d) relation with modal content for quartz ribbons.

Table 7: Modal content, grain size, shape and connectivity of quartz in the Qdd and Fdd.

Domain/ sample	n	Vol.-%	d (μm) ^a	PARIS (%)	Ω' (%)	AR ^b	C_k	CF ^c (%)
Quartz dominated domain (Qdd)								
D0								
25313	58	95.1	14535	21.3	27.8	2.0	1.3	90.5
25314	45	92.6	11694	43.4	32.1	1.9	1.6	77.6
<i>mean/ total</i>	<i>103</i>	<i>93.9</i>	<i>12723</i>	<i>30.7</i>	<i>30.0</i>	<i>2.0</i>	<i>1.4</i>	<i>84.0</i>
D1								
2997-1n	69	79.4	15537	37.1	29.5	7.5	0.9	33.2
2997-5	94	77.5	12496	28.9	32.9	2.2	1.1	33.7
2997-6	25	88.4	13016	63.4	29.6	2.0	1.2	43.4
2997-2	40	75.5	10960	49.8	31.0	2.0	0.9	24.6
2997-3D1	90	84.7	12010	31.7	31.7	2.2	0.8	46.6
29974D1	57	78.1	8886	27.2	31.5	1.9	1.3	29.7
<i>mean/ total</i>	<i>375</i>	<i>80.6</i>	<i>12711</i>	<i>39.2</i>	<i>31.5</i>	<i>2.1</i>	<i>1.0</i>	<i>35.2</i>
D2								
2997-6	547	74.9	2088	11.3	33.3	2.0	0.3	25.8
2997-D2.3	139	71.6	2725	14.3	24.8	2.3	0.4	28.9
2997-D2.5	301	66.1	2484	13.6	24.1	2.2	0.3	24.4
29972n	264	78.1	2626	13.4	27.6	2.1	0.4	26.1
<i>mean/ total</i>	<i>1251</i>	<i>72.7</i>	<i>2445</i>	<i>12.7</i>	<i>27.5</i>	<i>2.1</i>	<i>0.4</i>	<i>26.3</i>

Domain/ sample	n	Vol.-%	d (μm) ^a	PARIS (%)	Ω' (%)	AR ^b	C _k	CF ^c (%)
Feldspar dominated domain (Fdd)								
D3 ribbons								
30545	455	34.7	7113	7.2	26.3	3.1	0.1	11.3
30545n	428	32.8	5757	9.4	26.8	3.2	0.1	12.7
<i>mean/ total</i>	<i>883</i>	<i>33.7</i>	<i>6470</i>	<i>8.3</i>	<i>26.5</i>	<i>3.2</i>	<i>0.1</i>	<i>12.0</i>
D4 ribbons								
30544	423	14.0	3214	5.3	26.3	2.5	0.1	14.7
30546	403	16.9	2980	5.4	24.8	2.7	0.1	11.5
30546n	452	20.0	4850	4.7	26.1	2.9	0.1	14.9
<i>mean/ total</i>	<i>1278</i>	<i>17.0</i>	<i>3842</i>	<i>5.1</i>	<i>25.7</i>	<i>2.7</i>	<i>0.1</i>	<i>13.7</i>
D3 matrix								
Map7	3	0.6	94	1.6	7.6	1.7	0.0	0.0
SE1	64	23.1	246	2.9	11.9	1.7	0.1	8.2
SE9	48	7.8	299	4.7	17.5	1.8	0.2	5.0
SE12	3	0.1	81	0	0.0	1.2	0.0	0.0
SE14	17	4.7	393	8.8	15.6	2.0	0.1	1.0
Map6	33	1.3	77	0.1	4.4	1.8	0.1	0.1
SE1n	23	3.1	371	3.6	16.5	2.0	0.1	3.1
SE2	33	1.2	116	0	8.1	1.9	0.0	0.0
SE4	91	11.3	189	0.9	15.5	1.8	0.1	4.1
SE5	12	7.5	238	0.7	18.4	1.6	0.2	1.6
<i>mean/ total</i>	<i>327</i>	<i>6.1</i>	<i>257</i>	<i>2.3</i>	<i>13.0</i>	<i>1.8</i>	<i>0.1</i>	<i>2.3</i>
D4 matrix								
Map1	76	19.7	239	3.2	3.4	1.7	0.1	9.0
Map2	137	31.8	433	4.1	11.0	1.7	0.2	11.9
Map3	74	26.1	277	1.8	9.4	1.7	0.2	10.2
SE3	69	16.4	225	3.1	17.3	1.8	0.1	4.9
SE2	50	24.6	339	5.3	14.4	1.8	0.1	4.1
SE7	76	22.1	338	2.6	17.8	1.7	0.1	4.5
SE8	64	19.7	254	0.8	12.9	1.6	0.1	5.6
SE9	21	2.2	126	1.8	17.9	2.7	0.0	0.0
SE11	59	15.7	354	4.1	15.1	1.8	0.2	10.4
Map8	12	0.3	79	0	5.4	1.7	0.0	1.0
Map9	40	24.1	400	5.3	9.0	1.8	0.5	16.1
<i>mean/ total</i>	<i>733</i>	<i>19.2</i>	<i>338</i>	<i>3.1</i>	<i>8.7</i>	<i>1.7</i>	<i>0.2</i>	<i>7.1</i>

^a area weighted mean grain size

^b AR: aspect ratio

^c CF: Contact Frequency.

7.1.2. Feldspar

Grain size, shape, modal content, and connectivity are only described for feldspars in D2 and the Fdd. Feldspars in D1 of the Qdd are highly weathered which inhibits a reliable detection of grain size and shape.

7.1.2.1. Grain Size, Modal Content and Connectivity

Area weighted mean grain sizes of feldspar in the Fdd are largest in D3 for both feldspars, alkali feldspar and plagioclase (Table 9). Mean grain sizes in D3 are 465 μm and 394 μm for alkali feldspar and plagioclase, respectively. In D4 mean grain sizes are in the same range of around 320 μm for both feldspars. Alkali feldspar in D2 shows a mean grain size of ~ 400 μm (Table 8). Grain size distributions are skewed to smaller grain sizes for all feldspars in the Fdd and D2 (Fig. 49). In the Fdd grain size distributions are polymodal and shifted to smaller grain sizes for both feldspars in D4 (Fig. 49a, b). Both feldspars show a pronounced accumulation of grain sizes between around 100 and 500 μm with peaks around 250 and 300 μm for plagioclase and alkali feldspar, respectively. Further, both feldspars show minor frequent grain sizes between 500–700 μm (alkali feldspar)

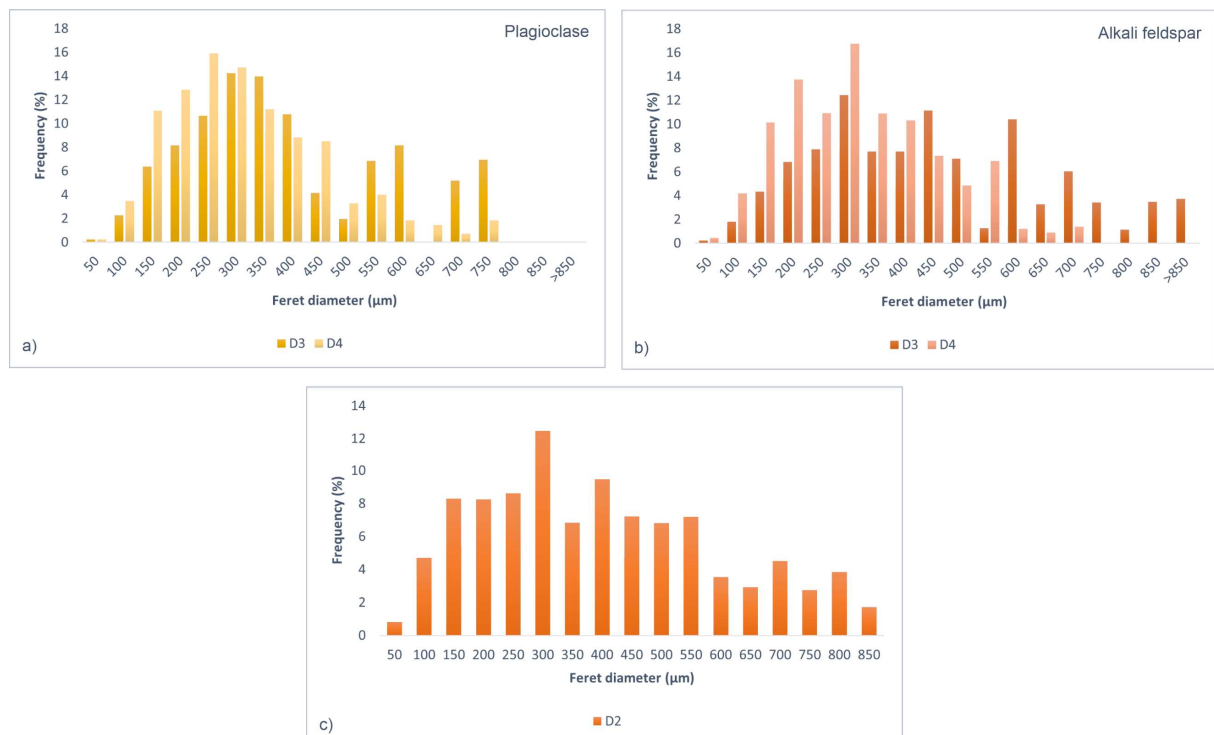


Fig. 49: Grain size distributions of feldspar in the Fdd (a, b) and D2 (c).

and 500–750 μm (plagioclase). The grain size distribution of plagioclase is less disrupted by protruding peaks and the increase and decrease of grain size frequencies towards and away from the maximum are more continuous compared to alkali feldspar. In D3 grain size distributions are polymodal, too, but slightly shifted to larger grain sizes for both feldspars (Fig. 49a, b). For plagioclase, the shape is similar to D4, but larger grain sizes are more frequent. The same is observed for alkali feldspar but the distribution is significantly broader with maximum grain sizes $>850 \mu\text{m}$. The grain size distribution in D2 is similar to that of alkali feldspar in the Fdd (Fig. 49b, c). The distribution is shifted to smaller grain sizes and peaks at 300 μm . Furthermore, small grains $<300 \mu\text{m}$ are more abundant and the distribution is less broad compared to D3 with maximum grain sizes around 850 μm . For single subdomains in the Fdd both feldspars show a positive correlation of grain size with modal content and connectivity (Fig. 50, Table 9). Plagioclase shows two groups of grain size cluster (Fig. 50a). For a volume fraction $<50 \text{ Vol.-%}$ and low connectivity mean grain sizes scatter between ~ 200 and 300 μm . With increasing volume fraction $>50 \text{ Vol.-%}$ and connectivity grain sizes scatter between ~ 400 and 500 μm and show no further development. In D2 the development of grain size is comparable to the Fdd despite some scatter and shows an increase with modal content and connectivity (Fig. 51). One subdomain (Map 9) shows striking differences in connectivity and grain size (Fig. 51e, Table 8). In Map 9 alkali feldspar is clustered to an aggregate resulting in high connectivity and grain size. This differs from most other subdomains in D2 (Fig. 51d,) where alkali feldspar is more dispersed within the quartz matrix resulting in low connectivity and small grain size (Table 8).

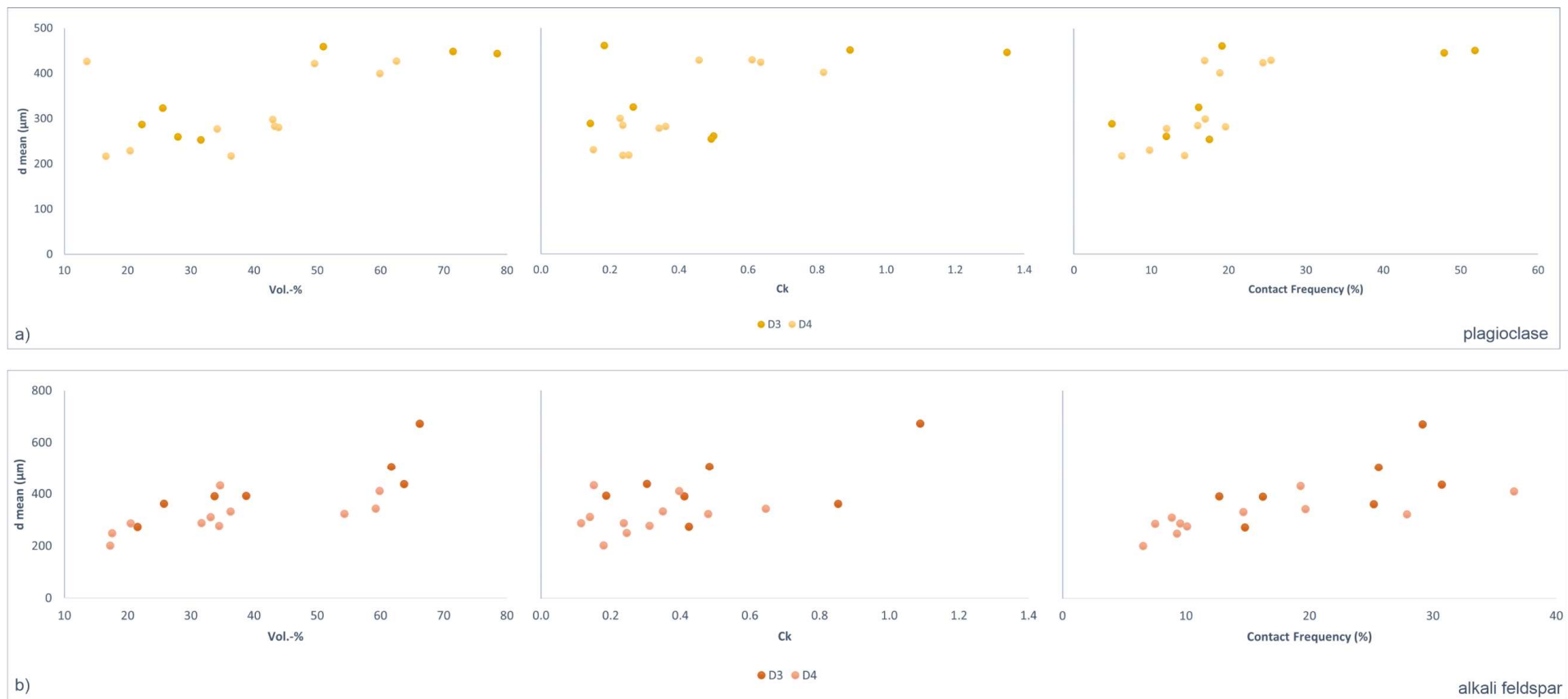


Fig. 50: Feldspar grain size relations in the Fdd: a) relations for plagioclase; b) relations for alkali feldspar.

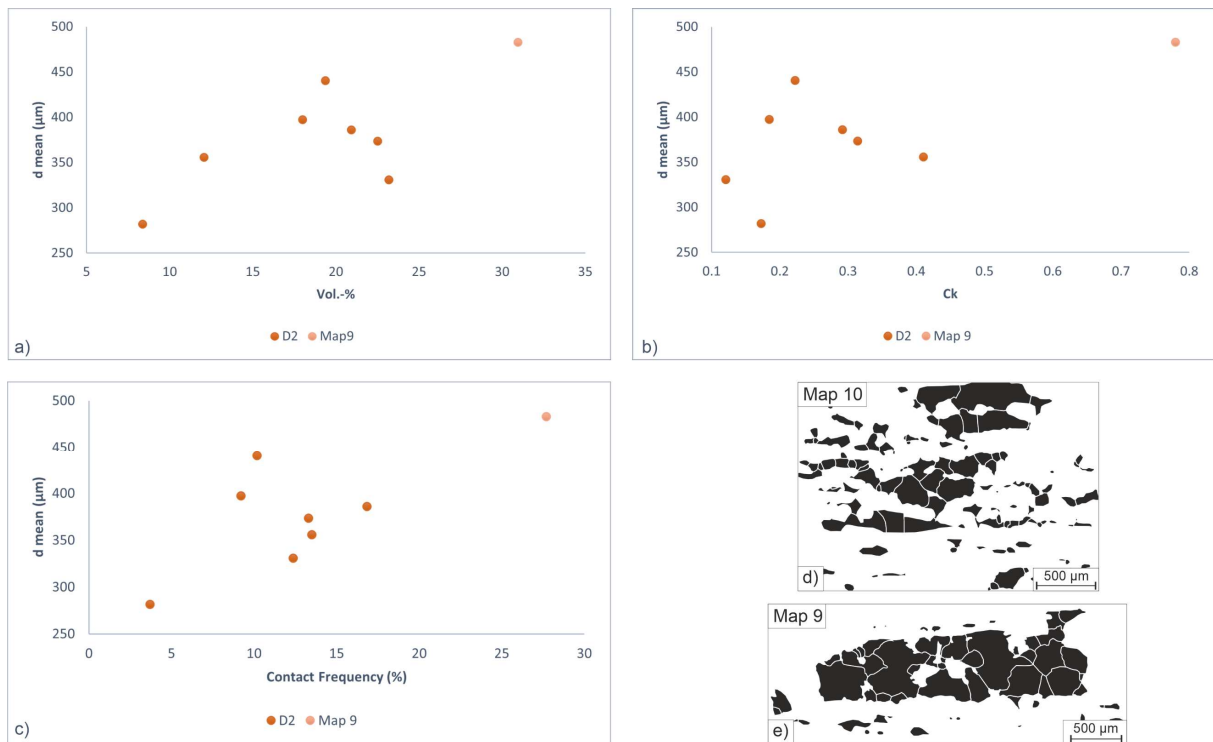


Fig. 51: Grain size relations of alkali feldspar in D2; d, e) grain maps of D2 subdomains after image processing).

7.1.2.2. Shape Descriptors

Most irregular shapes are detected for alkali feldspar in D3 with highest average Paris factor of ~8 % (Table 9). The Paris factor decreases towards D4 and is lowest in D2 with a mean value of ~3 % (Table 8). The mean Paris factor of plagioclase is about 6 % in both, D3 and D4. For single subdomains of alkali feldspar in the Fdd an increase of Paris factor is detected with grain size, modal content, and connectivity (Fig. 52a, b). For plagioclase in D4 an increase of Paris factor is indicated with connectivity but a decrease in D3 (Fig. 52c), but this development is not striking. Nevertheless, this trend can be explained in the following manner: Fig. 52d shows that smallest plagioclase grains hardly reveal indented grain shapes. Such grains often occur isolated within an alkali feldspar assemblage or have only few neighbours and, hence, have a low connectivity. Larger plagioclase grains in Fig. 52d have more neighbours resulting in a higher connectivity. But abundant phase boundaries with alkali feldspar (and quartz) are smoothly curved and form indentations into plagioclase resulting in higher Paris factors (Figs. 52c, d). In D3 more pure layers of

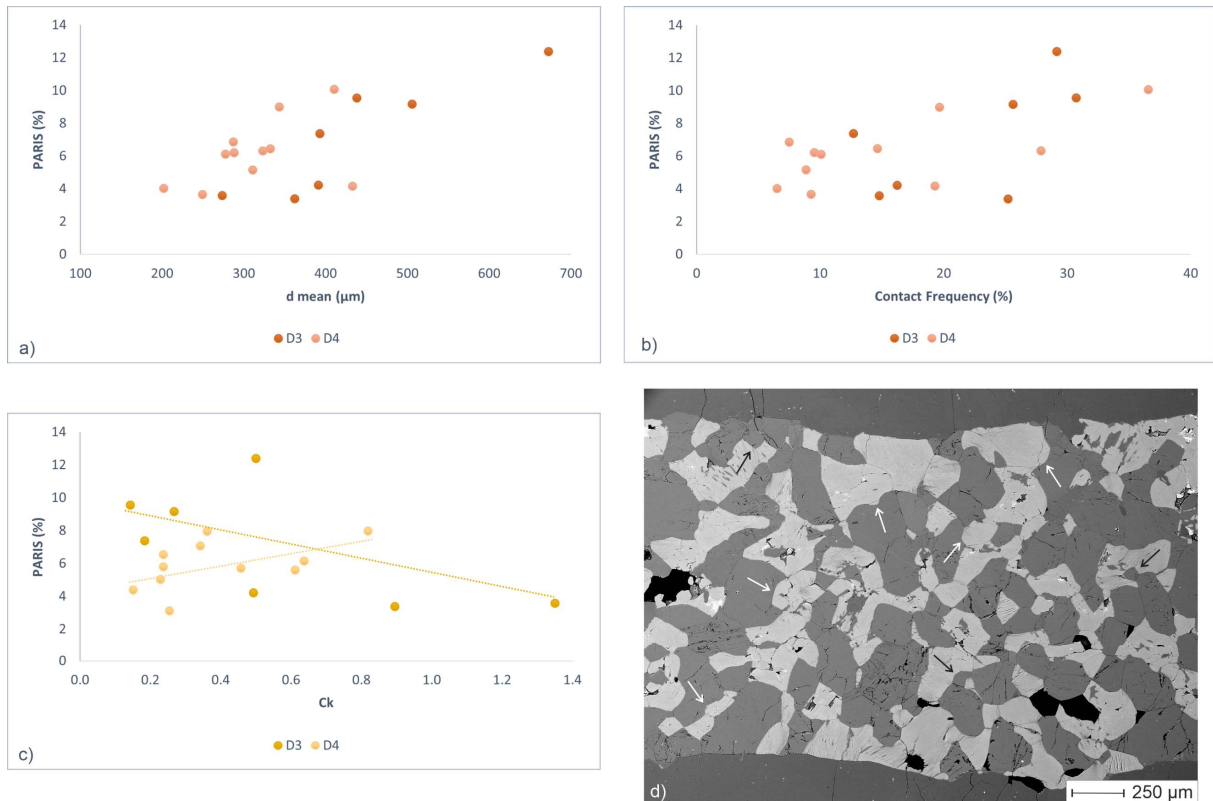


Fig. 52: Paris factor development of feldspars in the Fdd; a, b) alkali feldspar relation with grain size (a) and contact frequency (b); c) plagioclase relation with C_k ; d) (BSE image): white arrows point to indentations of plagioclase by alkali feldspar and black arrows point to small plagioclase grains without indentations (for further explanation see text).

alkali feldspar and plagioclase occur (Fig. 56c, d). The connectivity is highest in these pure layers, smoothly curved phase boundaries lack, and plagioclase displays straight grain boundaries resulting in lower Paris factors (Fig. 56c).

In single subdomains of D2 Map 9 displays by far the highest Paris factor of 7.3 % which is in the range of alkali feldspar in the Fdd (Tables 8, 9, Fig. 53). The remaining subdomains in D2 reveal average Paris factors ranging between ~ 1 and 3%. Furthermore, Map 9 reveals the highest connectivity in D2. The relation with contact

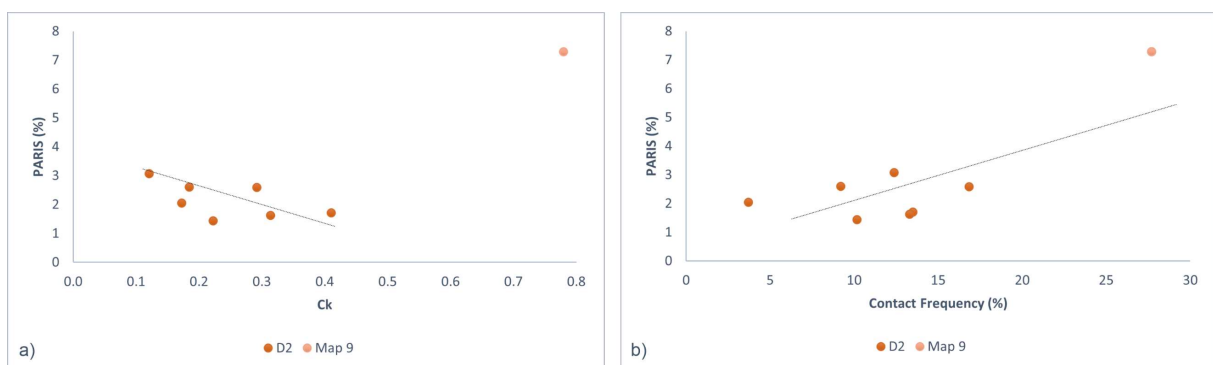


Fig. 53: Paris factor development of alkali feldspar in D2.

frequency shows an increase of Paris factor including Map 9 (Fig. 53b). On the contrary, a relation with C_k reveals a decrease of Paris factor (excluding Map 9) (Fig. 53a). In Fig. 54 this development is explained in exemplary fashion for Map 2 and 10. In Map 2 most alkali feldspar is clustered into an aggregate (Fig. 54a). Within this aggregate alkali feldspars have abundant neighbouring grains (Fig. 54c) with moderate indentations and low Paris

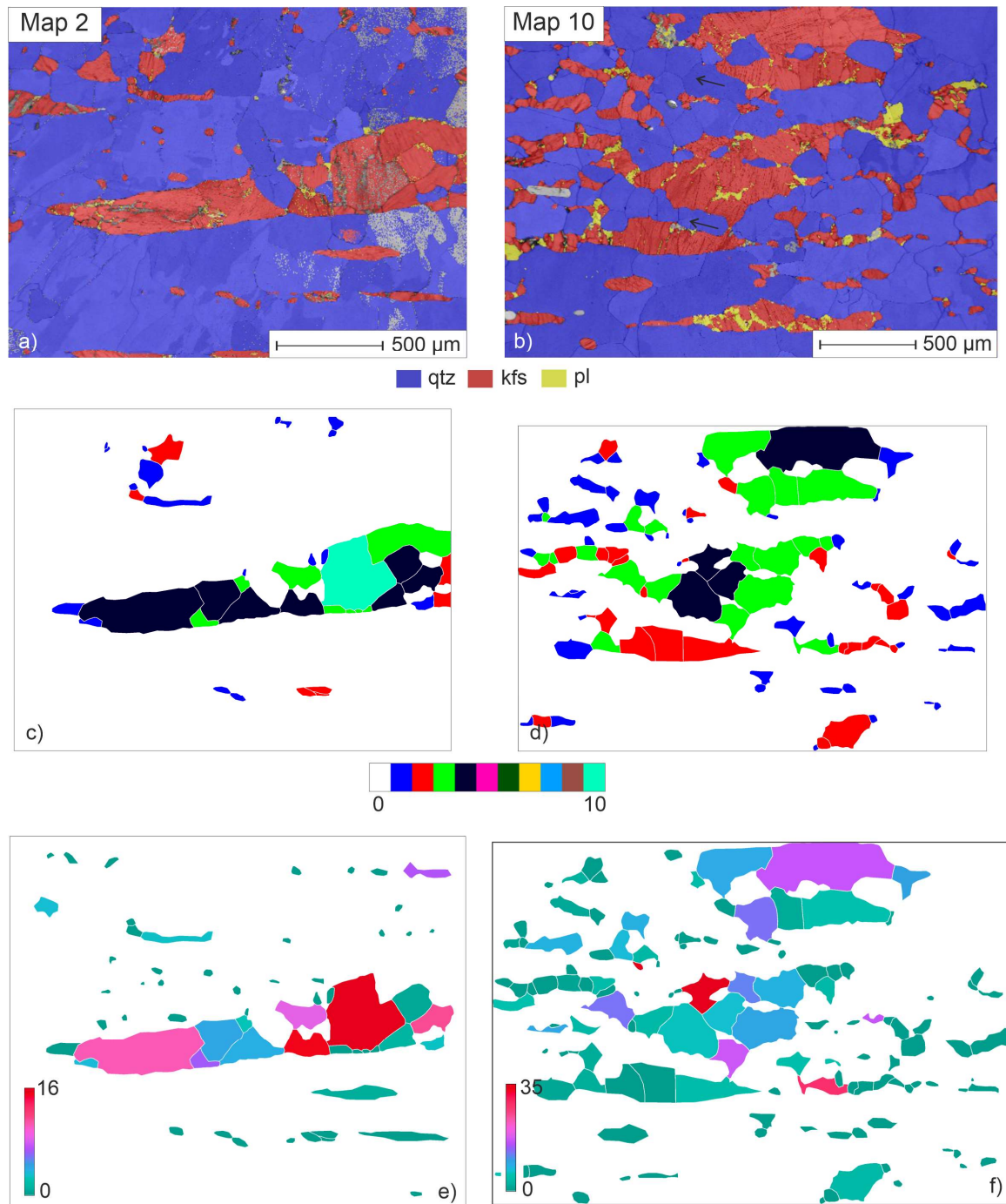


Fig. 54: Paris factor and C_k in Map 2 and Map 10: a, b) EBSD maps in phase colour coding; black arrows in b) point to small sized quartz; c, d): the same section colour coded with respect to the number of neighbours (grains with 0 neighbours are not outlined); e, f): the same section colour coded with respect to the Paris factor of individual grains (for bulk C_k and Paris factor see Table 8; for further explanation see text).

factors (Fig. 54e). In Map 10 alkali feldspar is dispersed within the quartz matrix (Fig. 54b). Most grains have only one or two neighbours (Fig. 54d). This results in a low bulk connectivity (Table 8). The strong dispersion of alkali feldspar inhibits quartz grain growth and small quartz grains form smoothly curved phase boundaries with alkali feldspar (Fig. 54b). Smoothly curved phase boundaries form indentations into feldspar grains which results in higher Paris factors (Fig. 54f).

Alkali feldspars in D2 are most angular with a mean value for Ω' of 12.2 % (Table 8). Highest mean values and least angularity is detected for plagioclase in D3 Ω' of 17 % (Table 9). Alkali feldspar and plagioclase in the Fdd show no distinct development of angularity. In D2 an increase of Ω' is indicated with grain size, modal content, and connectivity (Fig. 55, only shown for contact frequency) and highest values are in the range of feldspars in the Fdd (Tables 8, 9).

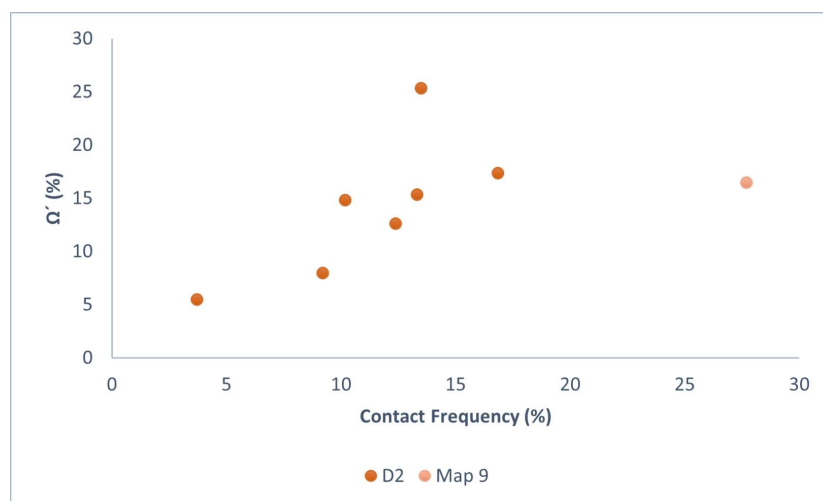


Figure 55: Angularity-contact frequency relation in D2.

Mean aspect ratios of feldspars in the Fdd range between 1.8 and 1.9 (Table 9). D2 feldspars are more elongated with an average aspect ratio of 2.4 (Table 8). Alkali feldspar in the Fdd shows no development of aspect ratios for single subdomains. Plagioclase in the Fdd shows a decrease of aspect ratio with grain size, modal content, and connectivity (Fig. 56, shown for grain size and contact frequency). A clustering of aspect ratios is

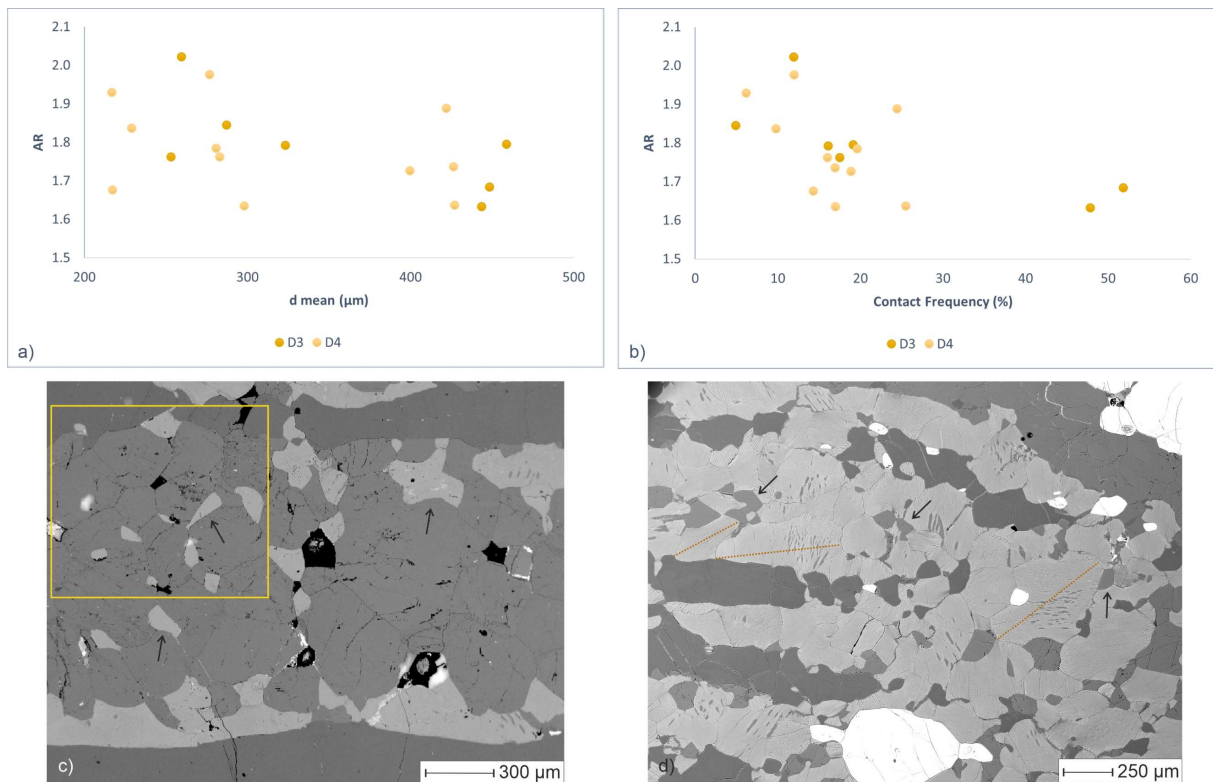


Fig. 56: Aspect ratio of plagioclase in the Fdd (c, d: BSE images): a, b) relations with grain size (a) and contact frequency (b); c) yellow rectangle highlights polygonal framework of plagioclase; black arrows point to interstitial and elongated alkali feldspar; d) alkali feldspar rich domain in D3; yellow lines trace high aspect ratios of alkali feldspar; black arrows point to interstitial plagioclase with high aspect ratios.

evident in relation with grain size which correspond to grain size cluster in Fig. 50a. Alkali feldspars in D2 show a decrease of aspect ratios with modal content and connectivity (Fig. 57b, c). Map 9 reveals lowest average aspect ratio of 1.9 which is in the range of values in the Fdd (Table 8, 9). For the relation of aspect ratio with grain size a general decrease is evident (Fig. 57a). However, the data form cluster which can be explained in exemplary fashion in Fig. 57d. Cluster 1 refers to isolated small grains which are included in quartz and strongly elongated. Cluster 2 contains feldspar aggregates of only a few grains in which small grains have low aspect ratios and large grains are elongated. Cluster 3 is defined by largest grain sizes and highest connectivity in D2. These grains form aggregates similar to that in Map 9 and reveal smallest aspect ratios.

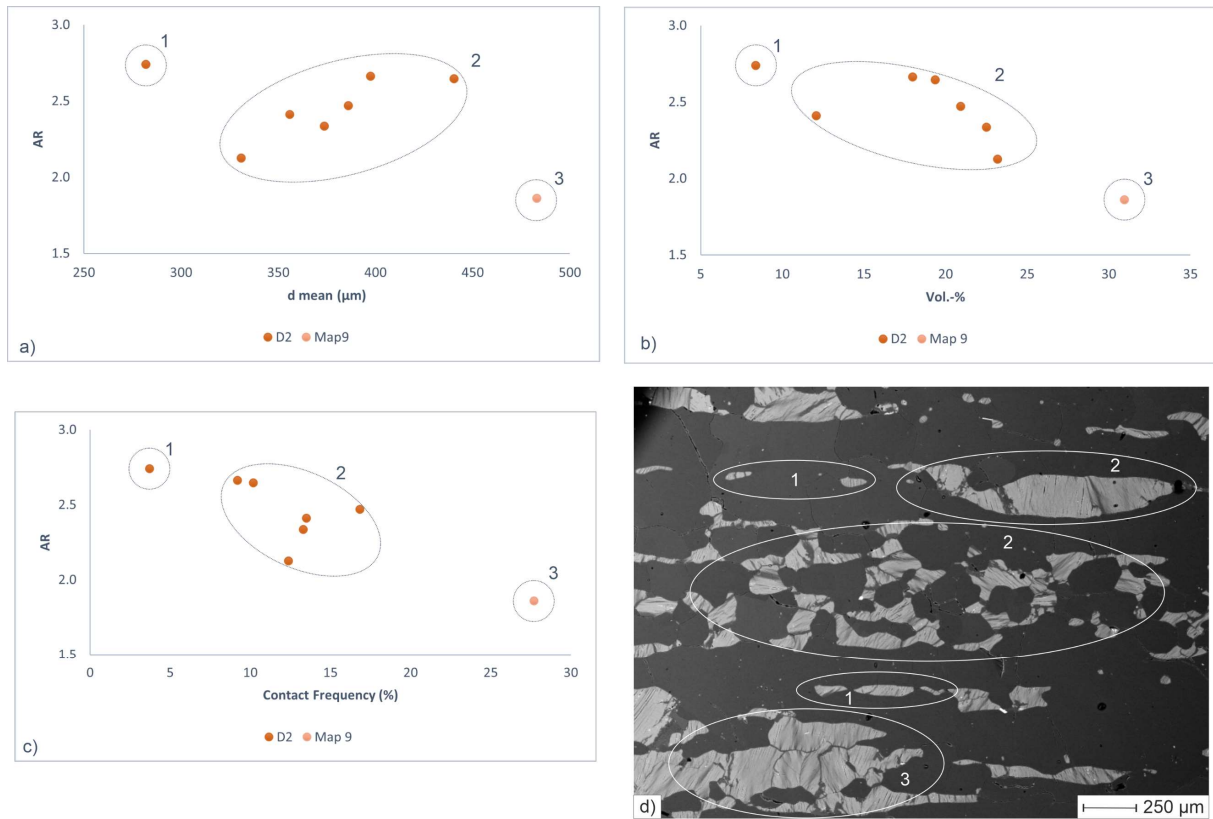


Fig. 57: Aspect ratio of alkali feldspar in D2 (d: BSE image; for explanation see text).

Table 8: Modal content, grain size, shape and connectivity of alkali feldspar in D2.

Sample/ Domain	n	Vol.-%	d (μm) ^a	PARIS (%)	AR ^b	Ω' (%)	Ck	CF (%) ^c
D2								
29972n - Map2	59	12	356	1.7	2.4	8.5	0.3	12.3
29972n- Map3	29	8	282	2.0	2.7	5.5	0.2	3.7
29972n - Map7	76	18	397	2.6	2.7	8.0	0.2	9.2
29972n - Map9	59	31	483	7.3	1.9	16.5	0.8	27.7
29972n - Map10	119	23	331	2.3	2.1	12.6	0.1	12.9
29976 - SE41	87	19	440	1.4	2.6	14.8	0.2	10.2
29976 - Se42	86	23	374	1.6	2.3	15.3	0.3	13.3
29976 - SE 43	95	21	386	2.6	2.5	17.4	0.3	16.8
<i>mean/ total</i>	<i>610</i>	<i>20</i>	<i>399</i>	<i>2.7</i>	<i>2.4</i>	<i>12.2</i>	<i>0.3</i>	<i>13.3</i>

^a area weighted mean grain size

^b AR: aspect ratio

^c CF: Contact Frequency measured as percentage of like-like boundaries.

Table 9: Modal content, grain size, shape and connectivity of Feldspar in the Fdd.

Sample/ Domain	n		Vol.-%		d (μm) ^a		PARIS (%)		AR ^b		Ω' (%)		C _k		CF (%) ^c	
	kfs	pl	kfs	pl	kfs	pl	kfs	pl	kfs	pl	kfs	pl	kfs	pl	kfs	pl
D3																
30545 - Map7	33	39	66	28	673	260	12.4	5.5	2.0	2.0	13.0	11.7	1.1	0.5	29.2	11.9
30545 - SE1	52	76	34	32	391	253	4.2	4.0	1.8	1.8	19.7	19.1	0.4	0.5	16.2	17.5
30545 - SE9	95	96	62	26	506	323	9.2	6.5	1.8	1.8	21.6	19.1	0.5	0.3	25.6	16.1
30545 - SE12	35	39	26	71	362	448	3.4	4.0	1.7	1.7	17.5	19.2	0.9	0.9	25.2	51.8
30545 - SE14	109	88	39	51	393	459	7.4	7.8	1.8	1.8	17.6	22.8	0.2	0.2	12.7	19.1
30545n - Map6	54	49	64	22	438	287	9.5	7.9	1.9	1.8	14.1	12.3	0.3	0.1	30.7	4.9
30545n - SE3	33	41	22	78	273	444	3.6	3.4	2.0	1.6	8.4	10.7	0.4	1.4	14.8	47.8
<i>mean/ total</i>	<i>411</i>	<i>428</i>	<i>45</i>	<i>44</i>	<i>465</i>	<i>394</i>	<i>8.1</i>	<i>5.9</i>	<i>1.8</i>	<i>1.8</i>	<i>12.8</i>	<i>17.0</i>	<i>0.5</i>	<i>0.5</i>	<i>22.1</i>	<i>24.2</i>
D4																
30544 - Map1	73	38	54	17	323	217	6.3	5.8	1.7	1.9	12.0	11.8	0.5	0.2	27.9	6.2
30544 - Map2	237	132	35	20	433	229	4.2	4.4	1.9	1.8	14.2	12.0	0.2	0.2	19.3	9.8
30544 - Map3	58	56	18	50	249	422	3.7	6.2	1.8	1.9	13.2	14.7	0.2	0.6	9.3	24.4
30544 - SE3	50	72	17	63	202	427	4.0	5.6	1.8	1.6	17.3	21.4	0.2	0.6	6.5	25.5
30546 - SE2	61	85	21	44	287	281	6.9	8.0	2.0	1.8	14.8	15.2	0.2	0.4	7.5	19.6
30546 - SE7	134	114	32	43	288	298	6.2	5.0	1.9	1.6	18.3	21.0	0.1	0.2	9.5	17.0
30546 - SE8	107	116	33	43	311	283	5.2	6.5	1.9	1.8	16.7	19.1	0.1	0.2	8.9	16.0
30546 - SE9	29	40	59	36	343	217	9.0	3.1	1.9	1.7	21.3	16.4	0.6	0.3	19.7	14.3
30546 - SE11	110	59	60	14	411	426	10.1	5.7	1.8	1.7	17.1	14.4	0.4	0.5	36.6	16.9
30546n - Map8	46	35	34	60	277	399	6.1	8.0	2.0	1.7	10.0	10.6	0.3	0.8	10.1	18.9
30546n - Map9	81	80	36	34	332	277	6.4	7.1	1.9	2.0	13.2	12.9	0.4	0.3	14.7	12.0
<i>mean/ total</i>	<i>986</i>	<i>827</i>	<i>36</i>	<i>38</i>	<i>322</i>	<i>321</i>	<i>5.9</i>	<i>6.3</i>	<i>1.9</i>	<i>1.8</i>	<i>15.8</i>	<i>15.5</i>	<i>0.3</i>	<i>0.4</i>	<i>15.4</i>	<i>16.4</i>

^a area weighted mean grain size

^b AR: aspect ratio

^c CF: Contact Frequency measured as percentage of like-like boundaries.

7.2. Discussion

7.2.1. Challenges in Analysing Grain Size, Shape and Connectivity

The analysis of grain size, shape and connectivity in the Sri Lankan samples was a challenging endeavour. The main reason for this is the tremendous difference in grain size between quartz in different domains ranging from $\sim 100 \mu\text{m}$ up to centimetre sized grains. These differences made it difficult to find an appropriate method for the analysis of grain sizes in all domains to ensure a comparability of data (e.g., Berger et al., 2011). For instance, the two-dimensional grain size analysis is not ideal for millimetre to centimetre sized quartz in D1 and D0 for several reasons: 1) large grain sizes result in a reduced number of grains per thin section (<100 grains); 2) large and irregularly shaped grains can be dissected into multiple fragments which increase the number of apparent grains in thin section and reduce the true grain size. To minimize this effect area weighted mean grain sizes were calculated (Berger et al., 2011; Heilbronner and Bruhn, 1998). However, due to the large grain size and small number of grains in D1/ D0 the error is still expected to be large, and therefore the results are treated with reservations.

The selection of appropriate feldspar subdomains in the Fdd was challenging as well because of the inhomogeneity of the three-phase matrix. Moreover, in D3 an increase in quartz ribbons results in narrow matrix domains which contain only few grains. However, the homogeneity of subdomains with respect to phase distribution was preferred over the number of grains because the former determines grain size and shape.

7.2.2. Quartz

7.2.2.1. Grain Size, Shape and Deformation Mechanisms

Grain size distributions and shape descriptors reflect deformation mechanisms and connectivity in the investigated samples. In matrix quartz grain sizes are small due to low connectivity resulting in grain size distributions skewed to smaller grain sizes (Figs. 39,

42). The connectivity further governs the dominant deformation mechanism in matrix quartz. This becomes evident in the development of angularity (Fig. 47). Isolated (non-interstitial) grains (Fig. 58a) display smoothly curved phase boundaries with feldspar resulting in low angularity (high Ω') (group 2 in Fig. 47). Smoothly curved phase boundaries are indicative for diffusion assisted phase boundary migration (Gower and Simpson, 1992). With increasing connectivity ribbon forming processes are initiated (Fig. 58b, Fig. 9c, d). These incipient ribbons are characterized by straight boundaries and high angularity (group 3 in Figs. 47). Incipient ribbon formation was suggested by Hippertt et al. (2001) to result from crystal plastic deformation of scattered matrix grains by migration of grain boundaries. In this study GBM recrystallization between coalescing grains is suggested to cause grain coarsening. This is further suggested by large grain sizes of category C quartz in the matrix (chapter 6, Table 4). Polymodal grain size distributions in matrix quartz reflect abundant weakly connected grains deforming by diffusion assisted phase boundary migration and initiation of grain growth by GBM recrystallization in incipient ribbons (Figs., 39, 58a, b).

Increasing quartz content and connectivity enables ribbon formation and GBM recrystallization in D4 and D3 (Fig. 58c, d) as inferred from increasing grain sizes, aspect ratios, Paris factors and depletion of matrix quartz in D3 (Table 7, Fig. 43). In D4 the quartz content is low resulting in ribbon formation into narrow layers which are restricted to grow in Z direction (Fig. 58c). This probably impedes further coarsening of grains in suitable orientation (category C quartz) resulting in polycrystalline ribbons with high connectivity and polygonal shapes (low Paris factor and Ω') (Fig. 46). Impeded selective coarsening might further preserve minor SGR recrystallization which is inferred from misorientation angles between 10–20° (Fig. 22) and is also suggested in matrix quartz (Fig. 58b). During high temperature deformation unrestricted migration of grain

boundaries can eliminate low angle grain boundaries produced by SGR recrystallization (Stipp et al., 2010). Thus, restricted GBM recrystallization might preserve these low angle boundaries and associated small grains in polycrystalline ribbons. Straight grain

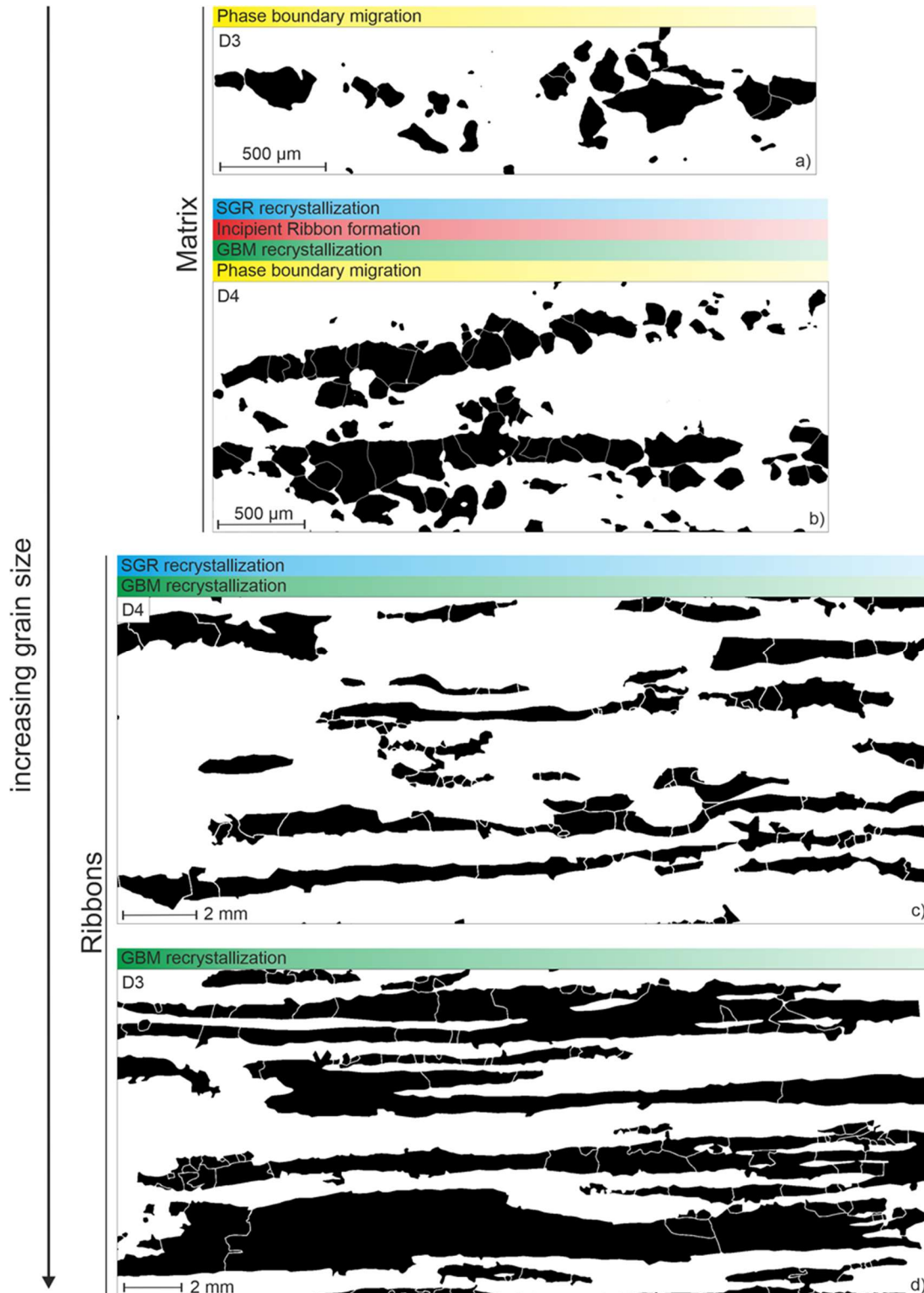


Fig. 58: Interpretation of dominant apparent deformation mechanisms of quartz in the Fdd (sections of grain maps after image processing of thin section scans; colour bars highlight most apparent deformation mechanism); a) D3 matrix; b) D4 matrix; c) D4 ribbons; d) D3 ribbons (for explanation, see text.).

boundaries and polygonal shapes of small grains in polycrystalline ribbons might further result from static recrystallization during annealing. The polycrystalline nature of D4 ribbons is reflected in the grain size distribution which is skewed to small grain sizes and displays only few large and strongly elongated grains (Fig. 39). In D3 quartz modal content increases. This comes along with increasing ribbon proportion, higher Paris factors, Ω' and increasing ribbon size indicating coarsening by GBM recrystallization (Fig. 58d). Selective coarsening further produces monocrystalline ribbons with low connectivity (Figs. 41, 46). Furthermore, the matrix is depleted by quartz. This suggests that in D3 lateral coalescence of quartz to ribbons is largely completed as most quartz is accumulated in layers. Progressed selective coarsening by GBM recrystallization is illustrated in polymodal grain size distributions which are shifted to larger grain sizes and are broader than in D4 (Fig. 39).

In the Qdd quartz is the dominant phase (>50 Vol.-%) and forms an interconnected framework in all directions (Fig. 59). This comes along with an increase in connectivity. GBM recrystallization proceeds in all directions resulting in higher Paris factors and lower angularity (Fig. 45). However, in D2 abundant feldspar still causes restricted GBM recrystallization. Quartz restricted by feldspar into layers develops ribbon shapes with high aspect ratios (red grains in Fig. 59a). The ribbon shape development is illustrated in Fig. 48a and shows that with increasing connectivity quartz is less restricted to grow in Z direction resulting in decreasing aspect ratios from D4 to D1/ D0. In D2, abundant feldspar further exerts a pinning effect which keeps many grains to small sizes (Herwegh and Berger, 2004) and probably preserves evidence for other deformation mechanisms by restricted GBM recrystallization (Stipp et al., 2010). Small grain sizes due to second phase pinning was reported to promote a change in deformation mechanism (e.g., Kilian et al., 2011; Linckens et al., 2011). In D2 second phase pinning is suggested to reflect

preservation of microstructures as ribbon formation, SGR recrystallization and phase boundary migration by restricted GBM recrystallization (Fig. 59a). The broad and polymodal grain size distribution of D2 illustrates the pinning effect and variation in deformation microstructures (Fig. 39). The shift to smaller grain sizes further demonstrates abundant pinning by feldspar.

In D1 and D0 the connectivity is greatest resulting in unrestricted GBM recrystallization (Fig. 59b, c). This is accompanied by most indented grain shapes (high Paris factor and Ω' , Table 7), largest grain sizes and complete selective coarsening of category C quartz (chapter 6). A polymodal grain size distribution results most likely from the sectioning effect in these domains. However, abundant largest grain sizes demonstrate the ceasing pinning effect and dominance of GBM recrystallization.

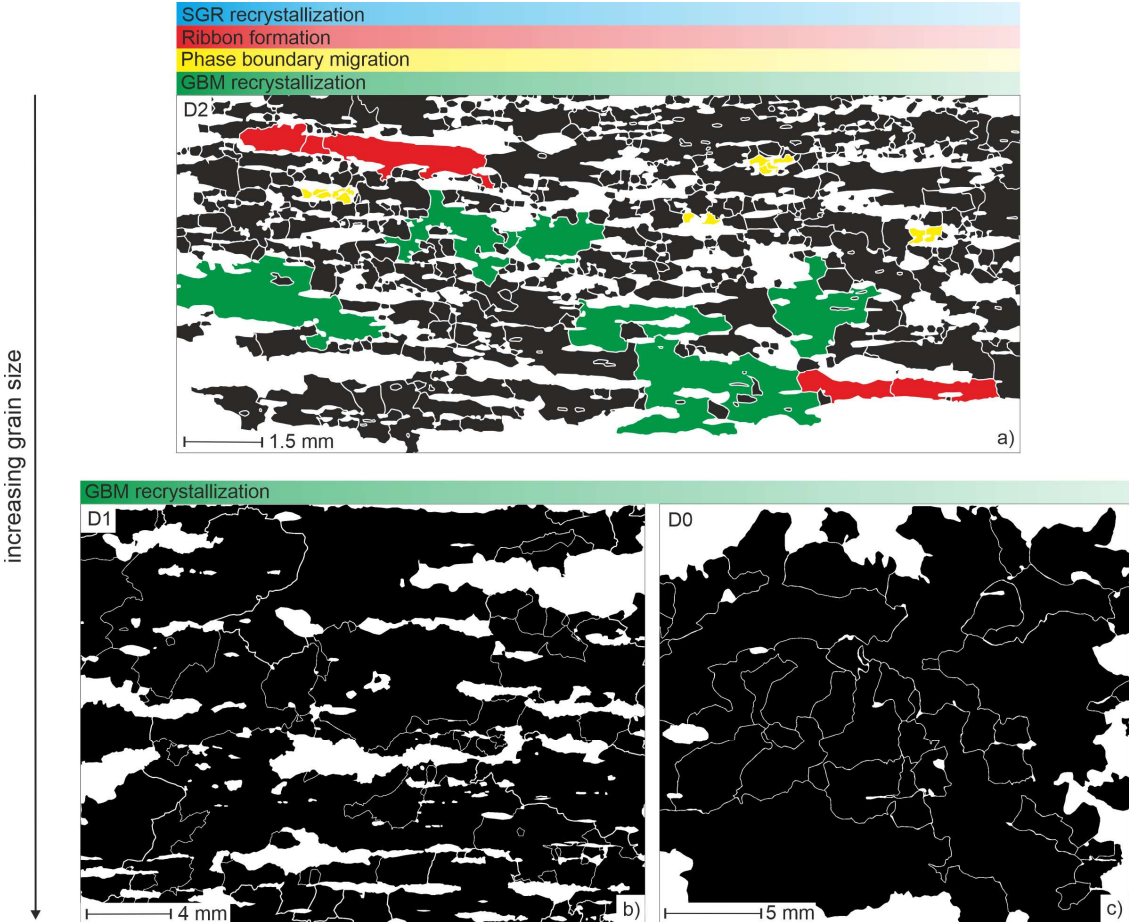


Fig. 59: Interpretation of dominant apparent deformation mechanisms of quartz in the Qdd (sections of grain maps after image processing of thin section scans; colour bars highlight most apparent deformation mechanism); a) D2; individual grains are highlighted with respect to apparent microstructure and deformation mechanism; colours refer to deformation mechanisms in colour bars (SGR recrystallization is suggested but cannot unequivocally be assigned to specific grains in this image section); b) D1; c) D0 (for further details, see text.).

7.2.2.2. Control on Grain Size Development

Quartz grain size increase is related with modal content and connectivity (Fig. 40). In the Fdd quartz constitutes a minor component with <50 Vol.-%. The grain size development depends on the bulk content of quartz and is well illustrated in the partition of quartz into matrix and ribbons (Fig. 43). With increasing bulk content of quartz more ribbons develop which reveal coarser grain sizes than matrix quartz. The grain size increase between matrix and ribbons is also a consequence of increasing connectivity because GBM recrystallization is only possible between adjacent grains. However, this is not indicated by parameters C_k and contact frequency. This is because of quartz restriction into layers and inhibited connection in Z-direction. Consequently, quartz displays neighbouring grains only within ribbon layers parallel to the foliation. Thus, in polycrystalline ribbons, which display smaller grain sizes, the connectivity is greater compared to coarse-grained and partly monocrystalline ribbons in D3 (Figs. 41b, 46b). Therefore, in the Fdd grain size development of quartz is termed as *modal content controlled* (Fig. 60a). In the Qdd quartz constitutes the major phase with >50 Vol.-%. Grain size development between D2 and D1/ D0 reveals a strong correlation with connectivity (Fig. 40b, c). Thus, the grain size development can be described as *connectivity controlled* (Fig. 60b). Furthermore, the modified application of the Zener parameter shows an increase of quartz grain size with increasing Z (Fig. 60c). This development is consistent with the Zener trend in Herwegh and Berger (2004). Moreover, the Zener trend observed in this study agrees with grain size- C_k relations (Fig. 40b). Therefore, the grain size development between D2 and D1/ D0 can additionally be referred to as *second phase controlled* (Fig. 60c). In D1/ D0 the Zener trend infers a grain size stabilization. This is also indicated by comparable mean grain sizes for individual domains in D1 and D0 (Table 7). Furthermore, no development of grain size with connectivity or modal content is indicated (Fig. 40). According to

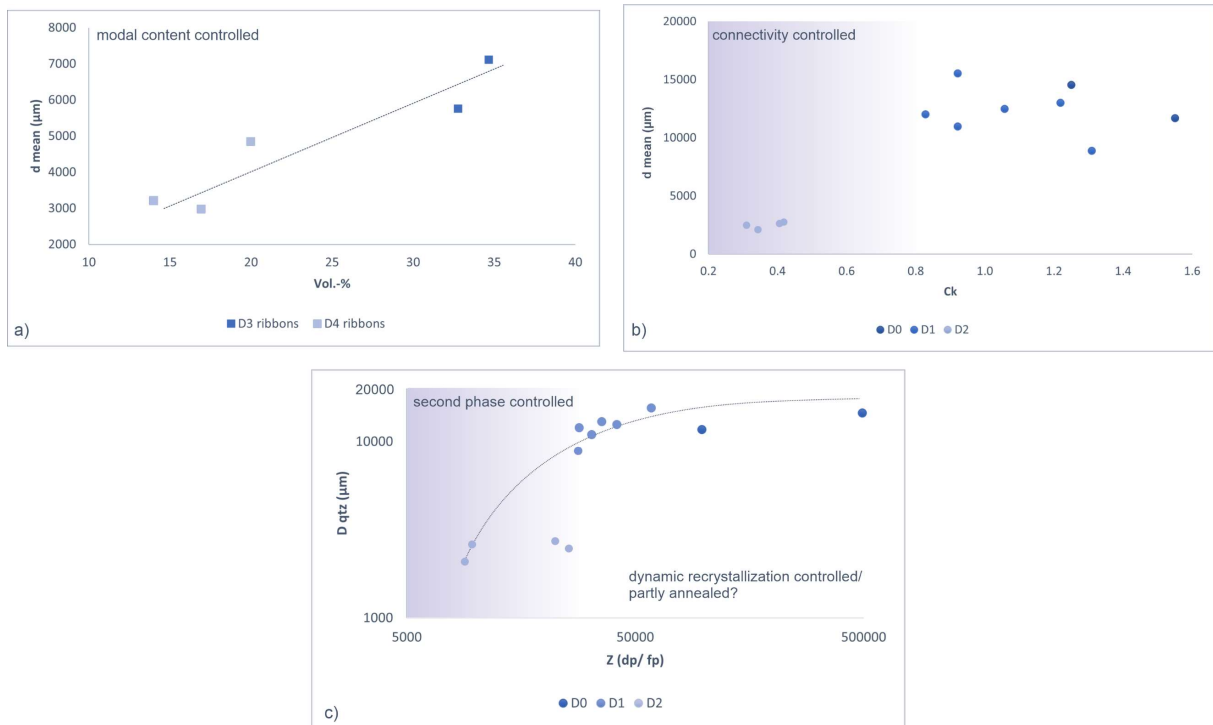


Figure 60: Control on grain size development: a) modal content control of quartz (ribbons) in the Fdd; b) connectivity control of quartz between D2 and D1; c) Zener plot for quartz in the Qdd (for further explanation see text).

Herwegh and Berger (2004) a flattened Zener trend in deformed aggregates indicates grain size stabilization by dynamic recrystallization. At this stage, the second phase content is too low to effectively pin grain boundaries. Grain size stabilization in dynamically recrystallized aggregates results from a balance of grain size reducing and grain size increasing mechanisms (Herwegh and Berger, 2004; references therein). During GBM recrystallization grain growth and grain size reduction are driven by local differences in strain energy. At a progressed stage stable grain sizes are achieved when grains growing at one side may be consumed at another side (Platt and Behr, 2011). The sectioning effect in D1/ D0 might wipe out further grain size increase during annealing. However, grain growth during annealing can also be impeded by stabilization of grain boundaries. Kruhl and Peternell (2002) investigated grain boundary stabilization of dynamically recrystallized quartz. They found that at high temperatures grain boundary stabilization is crystallographically controlled and that stabilized grain boundaries are stable against subsequent annealing. Indicative features are serrated grain boundaries

and perpendicular c-axes of adjacent grains. In this study serrated quartz grain boundaries are common (Fig. 9b, g) and quartz c-axes are perpendicular to each other in D1 (Fig. 20). This suggests that quartz grain boundaries are stabilized in D1. Furthermore, in chapter 6 it was concluded that selective coarsening of category C quartz was achieved in response to dynamic GBM recrystallization. Therefore, the grain size development in D1/ D0 is conditionally proposed to be *dynamic recrystallization controlled* (Fig.60c). More adequate grain size estimations are required in D1 and D0 to confirm this interpretation.

7.2.2.3. Modified Zener Parameter Application

Outliers of D2 subdomains in the Zener trend point to restrictions in the modified application (Fig. 60c). These outliers refer to inhomogeneous distribution of feldspar aggregates in D2 affecting quartz grain size (e.g., Fig. 54). The Zener parameter as investigated by Herwegh and Berger (2004) refers to a homogeneous distribution of second phase particles. According to the authors coarsening of the second phase (d_p) results in a decrease of their number fraction per unit area. Furthermore, the interparticle distance decreases and allows the major phase to grow (see also Herwegh et al., 2011). An inhomogeneous feldspar distribution in D2 does not meet these criteria completely and results in outliers within the Zener trend. The selection of homogeneous domains in D2 is difficult because it requires a smaller domain size. This in turn reduces the number of quartz grains and impedes reliable grain size estimations. Nevertheless, in D1 feldspar is clustered to coarser aggregates resulting in an increased distance between these aggregates which allows quartz to grow and fits into the Zener trend. The growth of quartz with increasing aggregate size and aggregate distance resembles coupled grain coarsening where matrix and second phase grains grow (e.g., Herwegh et al., 2005, references therein). However, aggregate size and distance in D1 is most likely the result

of feldspar distribution before deformation. Therefore, the development of aggregates from D2 to D1/ D1 cannot be referred to aggregate growth in the sense of grain growth. Furthermore, quartz in D1/ D0 requires a more robust method for adequate grain size estimation. Nevertheless, in this study it is concluded that the modified application of the Zener parameter delivers reasonable results for the grain size development of quartz.

7.2.3. Feldspar

Polymodal grain size distributions of feldspars in the Fdd represent grain sizes in a polyphase aggregate (Heilbronner and Bruhn, 1998). The broad peak between ~100 and 500 μm in D3 and D4 (Fig. 49a, b) can be assigned to abundant polyphase layers in the Fdd which consist of at least two feldspars and more (D4) or less quartz (D3). Protruding peaks at larger grain sizes can be assigned to layers where one feldspar is dominant. The shift to larger grain sizes in D3 correlates further with a reduced quartz contribution to the matrix (Fig. 43) and illustrates a more unimpeded grain size and shape development due to a reduced pinning effect (Herwegh and Berger, 2004).

Grain size distributions of plagioclase display two distinct groupings in D3 and D4 (Fig. 49a). These groupings can be assigned to plagioclase poor domains (<50 Vol.-%) with low connectivity and small grain sizes (~200–300 μm) and plagioclase rich domains (>50 Vol.-%) with higher connectivity and larger grain sizes (~400–500 μm) (Fig. 50a). The narrow width of the second grouping is indicative for normal grain growth during static conditions at which the average grain size increases while grain size and shape maintain a narrow distribution (e.g., Atkinson, 1988; Evans et al., 2001). A narrow distribution of plagioclase shape is inferred from the lack of a pronounced evolution of Paris factor and Ω' and clustering of aspect ratio at large grain sizes (Figs. 52c, 56a, Table 9). Furthermore, Paris factors (weakly pronounced in D3) and aspect ratios decrease with increasing grain size and connectivity reflecting the tendency of plagioclase to develop

polygonal frameworks in pure domains (Figs. 52c, 56). These microstructures indicate static fabrics which probably developed during annealing (e.g., Barnhoorn et al., 2005; Heilbronner and Tullis, 2002). Results of chapter 6 show that plagioclase reveals a pronounced CPO and microstructures described in chapter 3 yield evidence for crystal plastic deformation accommodated by GBM recrystallization. Therefore, it is proposed that dynamic recrystallization microstructures are modified during annealing. This statement will be verified in chapter 8. In polyphase domains plagioclase displays high aspect ratios and Paris factors where plagioclase forms smooth phase boundaries with alkali feldspar and quartz (Figs. 52d, 56d). These are attributed to diffusion creep accommodated by phase boundary migration (Gower and Simpson, 1992). These deformation microstructures are likely preserved due to inhibited growth by abundant phase boundaries to alkali feldspar and quartz.

Alkali feldspar in the Fdd shows a greater spread in grain sizes in both, D4 and D3, and grain size distributions reveal complex polymodal distributions. Complex and broad grain size distributions are indicative for GBM recrystallization (Berger et al., 2011, references therein; Stipp et al., 2002a). Furthermore, mean grain sizes of alkali feldspar increase with modal content and connectivity. An increased connectivity comes along with a reduced pinning effect of alkali feldspar by plagioclase and/ or quartz. Furthermore, the Paris factor increases with grain size, modal content and connectivity indicating the development of irregular grain shapes. A grain size increase accompanied by the development of irregular shapes support microstructural observations indicating recrystallization by GBM (e.g., Passchier and Trouw, 2005; Stipp et al., 2002b; Urai et al., 1986). In D4, the Paris factor of alkali feldspar is in the same range as for plagioclase (Table 9). Microstructural observations show same smooth phase boundaries as for plagioclase (Fig. 52d). Therefore, it is concluded that the lobateness of less connected

grains in D4 results from diffusion assisted phase boundary migration just as suggested for plagioclase. In conclusion, results of alkali feldspar show that deformation microstructures are preserved.

In alkali feldspar of D2 the broad grain size distribution reflects the occurrence of feldspar as isolated grains and in aggregates of variable connectivity (Figs. 49c, 51d, e, 54). Grain size and shape development of alkali feldspar is complex in D2. This is due to the interdependence of quartz and feldspar. A low connectivity of feldspar is equivalent to a high degree of dispersion and high dispersion of feldspar results in low connectivity of quartz. In D2 a low connectivity of feldspar can result in two scenarios (Fig. 61a, b): 1) in the first scenario feldspar connectivity is lowest and feldspar is included in large quartz grains which accomplished sufficient coarsening to overcome second phase pinning (GBM regime II in Stipp et al., 2002b). In this scenario most feldspars develop elongated shapes parallel to the foliation (cluster 1 in Fig. 57, Fig. 61a); 2) in the second scenario, feldspar connectivity is intermediate and causes sufficient pinning thereby preventing quartz coarsening. In this scenario quartz and feldspar build an individual domain in which microstructures are dominated by diffusion assisted phase boundary migration as indicated by high Paris factors and smooth phase boundaries (cluster 2 in Fig. 57; Map 10 in Fig. 54, Fig. 61b). At high connectivity of alkali feldspar there are again two distinct scenarios which depend on the modal content of feldspar (Fig. 61c, d): 3) at lower modal content but sufficient connectivity alkali feldspar forms elongated cluster (cluster 3 in Fig. 57; Map 2 in Fig. 54, Fig. 61c). These cluster resemble ribbon shapes in which grain boundaries are straight and often at a high angle to the foliation. This might explain highest angularity of alkali feldspar in D2 (lowest Ω') compared to feldspars in the Fdd; 4) higher connectivity and modal content further enable the cluster size to increase in which shape and grain sizes resemble those of alkali feldspar in D3 (Map 9; Table 8, Fig.

61d). In case (3) and (4), microstructures and shapes are indicative for dominant GBM recrystallization. In case (1) and (2) GBM is probably impeded by low connectivity and deformation is governed by diffusion assisted phase boundary migration. In all cases SGR recrystallization is additionally suggested to contribute to deformation as indicated by abundant misorientation angles 10–20° (chapter 6, Fig. 33).

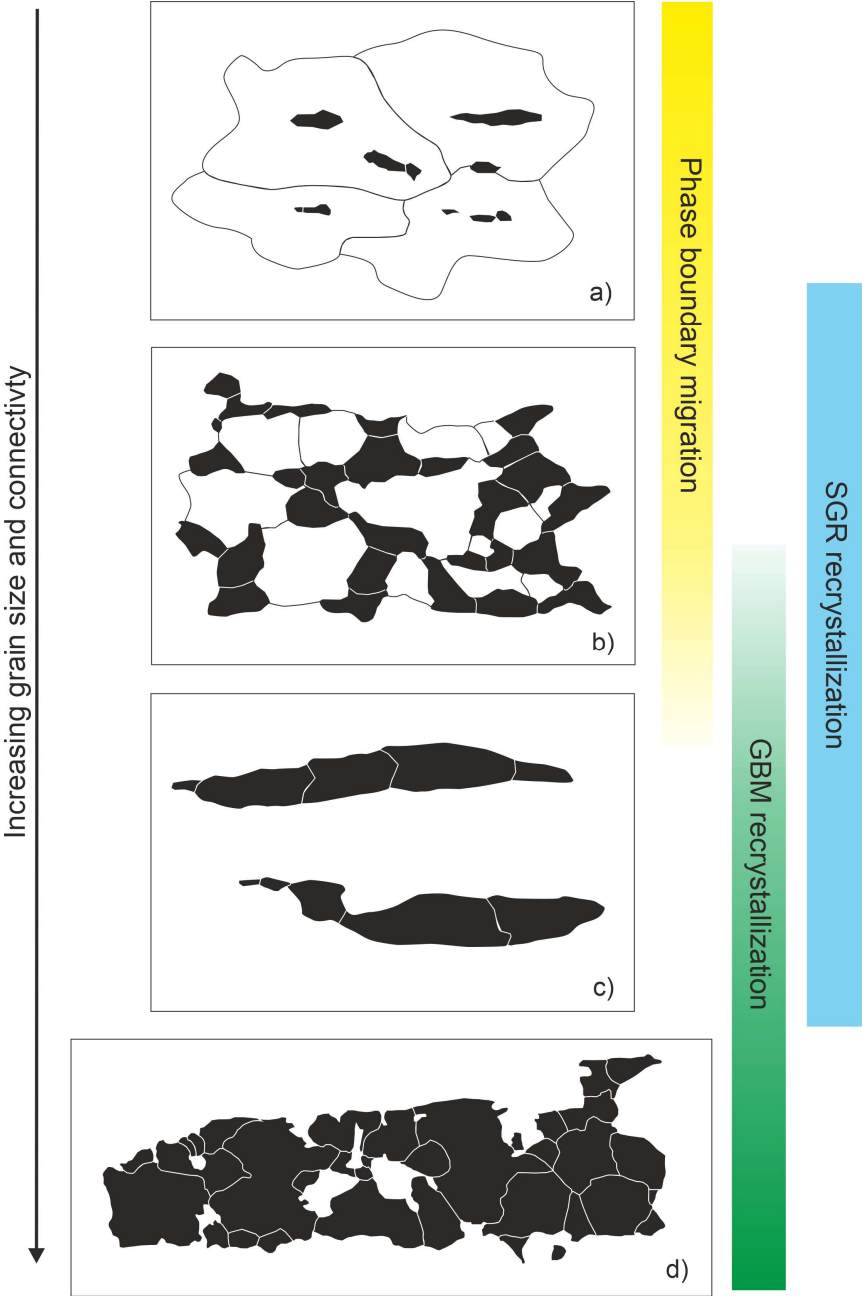


Fig. 61: Interpretation of microstructures and deformation mechanisms in D2 (white grains in a) and b) are quartz; for explanation see text).

8. Curvature and Dihedral Angle Analysis

In this part curvature and dihedral angle analysis is performed on like-like grain boundaries of quartz and feldspar in the Sri Lankan samples and on *test quartz*. Test quartz samples constitute of deformed and equilibrated quartz aggregates (Fig. 62). Deformed test quartz is characterized by highly amoeboid grain boundaries resulting from GBM recrystallization (Fig. 62a). Equilibrated quartz consists of a polygonal framework with straight grain boundaries and equilibrated dihedral angles of 120° (Fig. 62b). Results of curvature and dihedral angle analysis of deformed and equilibrated test quartz are used as endmember microstructures formed by deformation by GBM recrystallization and equilibration, respectively. Results of Sri Lankan quartz and feldspar serve to determine the application to polyphase aggregates and to interpret deformation and annealing microstructures.

Results of D1 and D0 are summarized due to similarities. Results of matrix quartz are summarized because isolated quartz in D3 does not have like-like grain boundaries. Results of dihedral angle measurements in D3 and D4 ribbons are additionally given as summary due to a small data set.

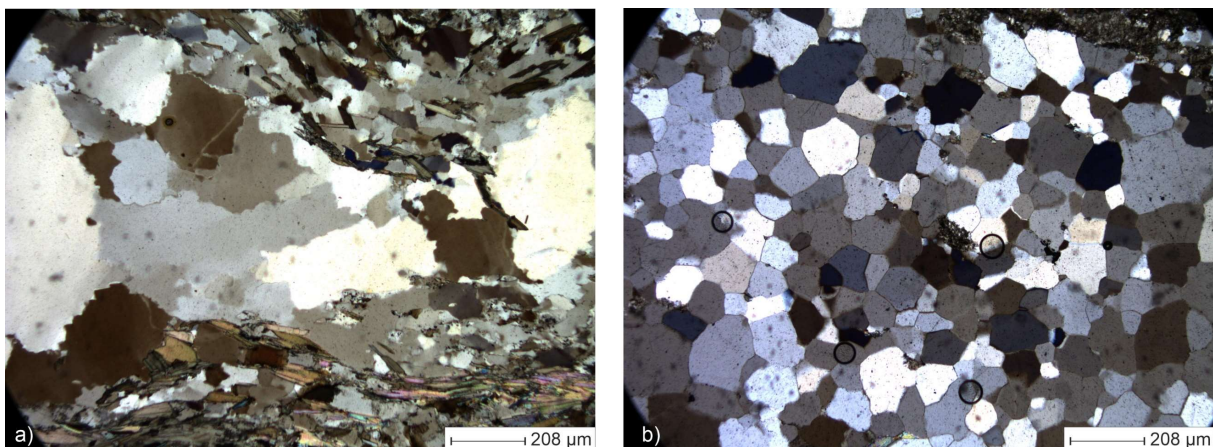


Fig. 62: Test quartz (microscopic images with crossed polarizers): a) deformed; b) equilibrated.

8.1. Results

8.1.1. Equilibrated and Deformed Quartz

Like-like grain boundaries of equilibrated quartz yield a value for C_s of 86 % (Table 10). The curvature for single boundaries ranges between 0 and $0.0236 \mu\text{m}^{-1}$. The frequency distribution of curvature is skewed to smallest values of $<0.004 \mu\text{m}^{-1}$ (Fig. 63a). Deformed quartz grain boundaries yield a C_s of 0 %. The values of curvature are greater by two orders of magnitude compared to equilibrated quartz and range between 0.0043 and $0.1041 \mu\text{m}^{-1}$. The frequency distribution is unimodal and slightly skewed to smaller values (Fig. 63b). The peak is broad ranging between curvatures of 0.0200 and $0.0500 \mu\text{m}^{-1}$.

Dihedral angles of equilibrated quartz reveal a T_{j120} of 37.3 % and T_{j90} of 13.3 %. The frequency distribution is unimodal approaching a Gaussian shape with a peak between 110° and 130° (Fig. 63c). The distribution reveals a minor second peak for angles between 170 and 180° . Deformed quartz reveals a smaller value of T_{j120} of 20.5 % and a higher fraction of 90° angles with T_{j90} of 19.2 %. The frequency distribution of measured angles

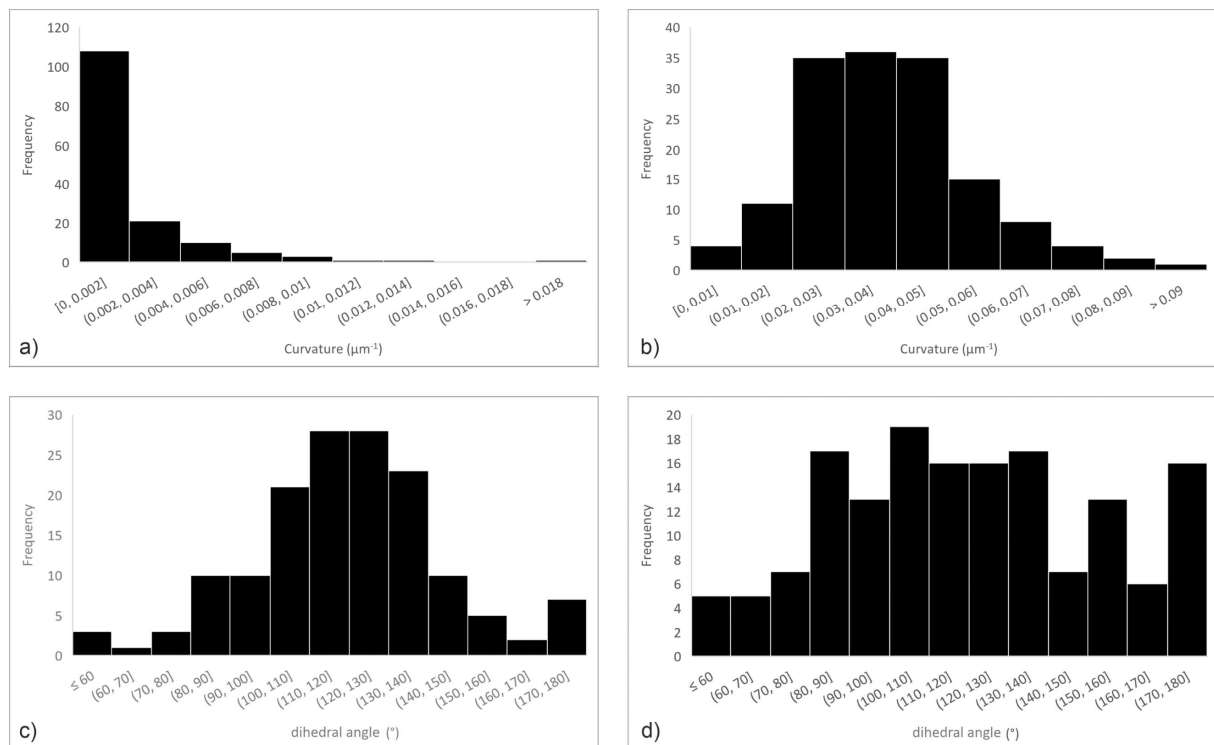


Fig. 63: Frequency distributions of Curvature and dihedral angles in equilibrated (a, c) and deformed (b, d) test quartz.

is polymodal with a major maximum at angles between 100 and 110° (Fig. 63d). Further maxima lie at angle classes of 80–90°, 150–160°, and 170–180°.

Table 10: Results of Curvature and Dihedral Angle Analysis.

Sample	Curvature				Dihedral Angle				
	n _{tot} ^a	n _s ^b	C _s (%)	Max (μm ⁻¹)	n _{tot} ^a	n ₁₂₀ ^c	T _{j120} (%)	n ₉₀ ^c	T _{j90} (%)
Test qtz									
equilib. ^d	150	129	86.0	0.024	150	56	37.3	20	13.3
deformed	150	0	0.0	0.104	156	32	20.5	30	19.2
Sri Lanka									
Qtz									
D1+D0	300	54	18.0	0.039	300	108	36.0	43	14.3
D2	150	52	34.7	0.067	150	72	48.0	22	14.7
D3 rb ^d	150	31	20.7	0.036	90	39	43.3	9	10.0
D4 rb ^d	150	45	30.0	0.038	108	34	31.5	14	13.0
matrix	150	71	47.3	0.053	141	52	36.9	15	10.6
D3+D4 rb ^d					198	73	36.9	23	11.6
Fsp									
D3									
kfs	150	48	32.0	0.046	153	64	41.8	22	14.4
pl	150	51	34.0	0.063	99	53	53.5	7	7.1
D4									
kfs	150	64	42.7	0.094	150	33	22.0	34	22.7
pl	150	97	64.7	0.025	150	62	41.3	19	12.7
D2									
kfs	150	67	44.7	0.032	150	46	30.7	24	16.0

^a total number of analyzed grain boundaries and dihedral angles

^b number of analyzed grain boundaries with a curvature <0.004 cm⁻¹

^c total number of analyzed dihedral angles with values of 120° ± 10° (n₁₂₀) and 90° ± 10° (n₉₀)

^d equilib.: equilibrated; rb: ribbons.

8.1.2. Sri Lanka Samples

8.1.2.1. Quartz

The curvature of like-like boundaries is smallest for matrix and D2 quartz with C_s of 47.3 and 34.7 %, respectively (Table 10). The curvature increases towards ribbons in the Fdd with D4 ribbons displaying more straight grain boundaries (C_s of 30 %) than D3 ribbons (C_s of 20.7 %). Quartz in D1/ D0 reveal the highest curvature with C_s of 18 %. The data of C_s are consistent with frequency distributions (Fig. 64). For matrix, D2 and D4 the distributions are skewed towards smallest curvatures. Matrix quartz reveals the most

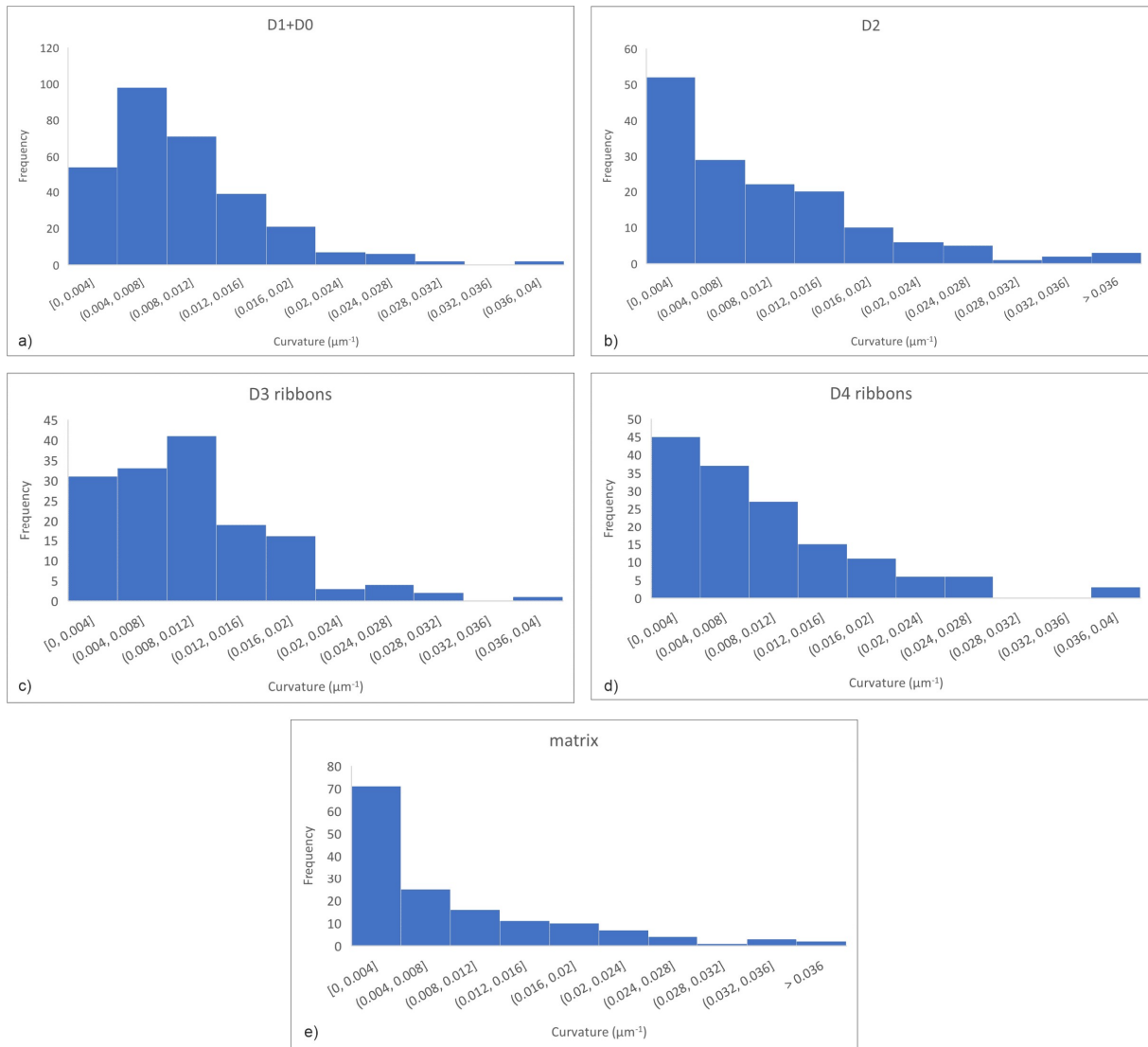


Fig. 64: Frequency distributions of quartz curvature.

pronounced peak for grain boundaries with curvatures $<0.004 \mu\text{m}^{-1}$. Frequency distributions of D3 and D1/ D0 quartz are asymmetrically unimodal and skewed to smaller curvature with a peak around $0.004\text{--}0.008 \mu\text{m}^{-1}$ in D1/ D0 and $0.008\text{--}0.012 \mu\text{m}^{-1}$ for D3 ribbons. The maximum curvature is comparable in D1/ D0 and D3/ D4 ribbons and ranges between 0.036 and $0.039 \mu\text{m}^{-1}$. In D2 and matrix higher maximum values of 0.067 and $0.053 \mu\text{m}^{-1}$ are detected, respectively.

Dihedral angles reveal the highest fraction for T_{j120} of 48 % in D2 quartz (Table 10). Quartz in D1/ D0, ribbons (D3+D4) and matrix yield similar values of T_{j120} around ~ 36 %. T_{j90} scatters around ~ 14 % in D1/ D0 and D2 and is lower in ribbons and matrix with 11.6

and 10.6 %, respectively. An individual description of Fdd ribbons shows that T_{j90} is slightly lower in D3 (10 %) compared to D4 (13 %). Moreover, D3 ribbons reveal a significantly higher fraction of 120° angles with T_{j120} of 43.3 % compared to 31.5 % in D4. Frequency distributions of dihedral angles show a maximum around 120° angles for D1, D2, matrix and quartz ribbons (D3-D4) (Fig. 65). The sharpest peak is developed for D2 ribbons. Furthermore, in D2 a second minor peak is observed at 90° . In D1/ D0 the peak is significantly broader than in D2. Ribbons (D3+D4) and matrix quartz reveal asymmetric distributions. The latter further shows the highest frequency of low and high dihedral angles and a further minor peak for angles between 170 and 180° . Individual distributions of quartz ribbons are nearly unimodal and symmetric with a pronounced peak around

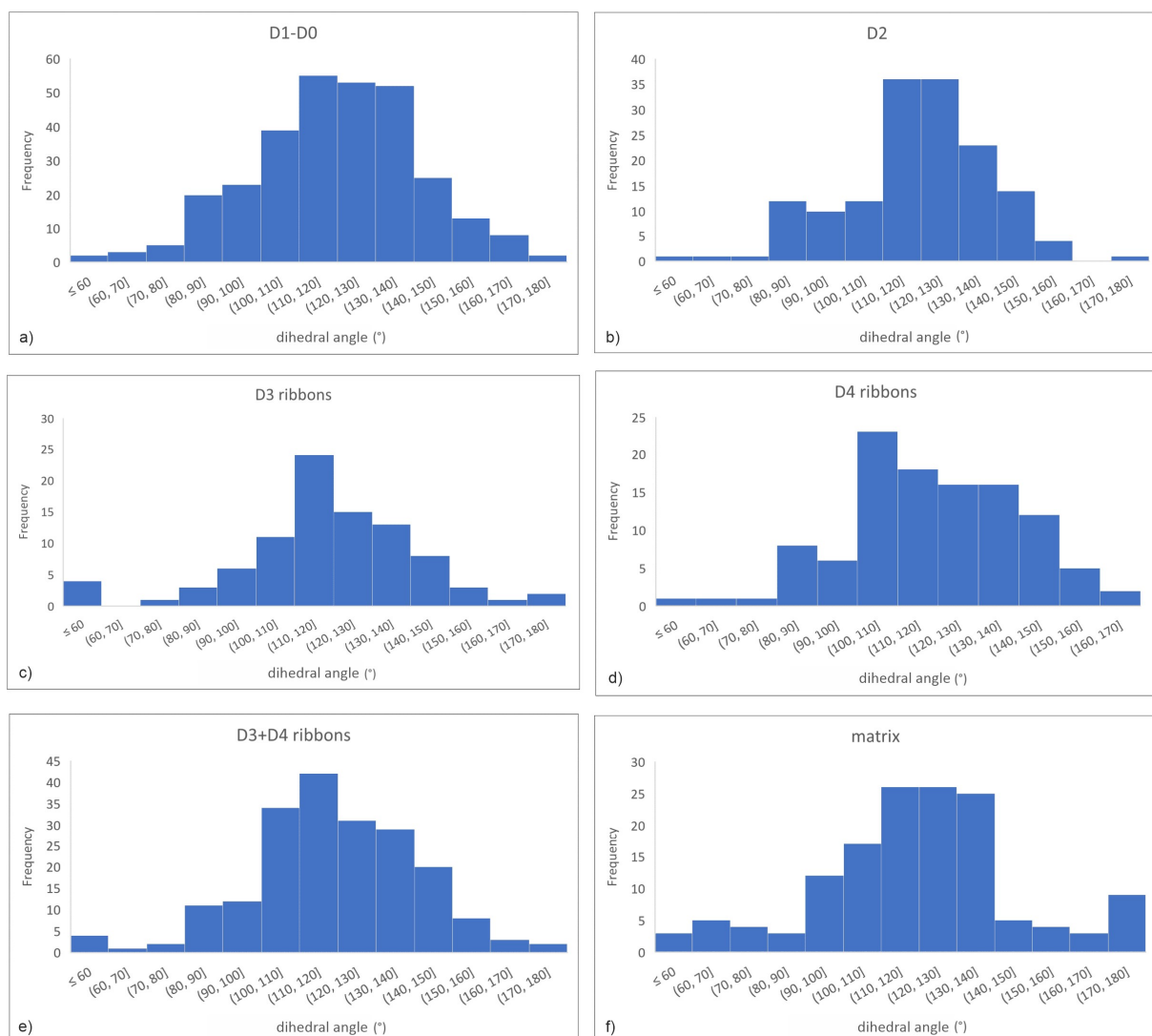


Fig. 65: Frequency distributions of quartz dihedral angles.

120° for D3. The distribution of D4 ribbons is asymmetric. The peak lies at 100–110° and angles between 110 and 150° are more abundant than angles <100°.

8.1.2.2. Feldspar

Like-like grain boundaries of feldspar in D3 display C_s of 34 % and 32 % for plagioclase and alkali feldspar, respectively (Table 10). In D4 C_s increases to 64.7 % for plagioclase and 42.7 % for alkali feldspar. Thus, the fraction of straight grain boundaries is greater in D4 and plagioclase reveals straighter grain boundaries than alkali feldspar in both domains. Alkali feldspar in D2 reveals a C_s of 44.7 %. The frequency distribution is skewed to smallest curvature for all feldspars (Fig. 66). In D4 the distribution of plagioclase curvature decreases abruptly for values greater 0.004 μm^{-1} and displays the smallest

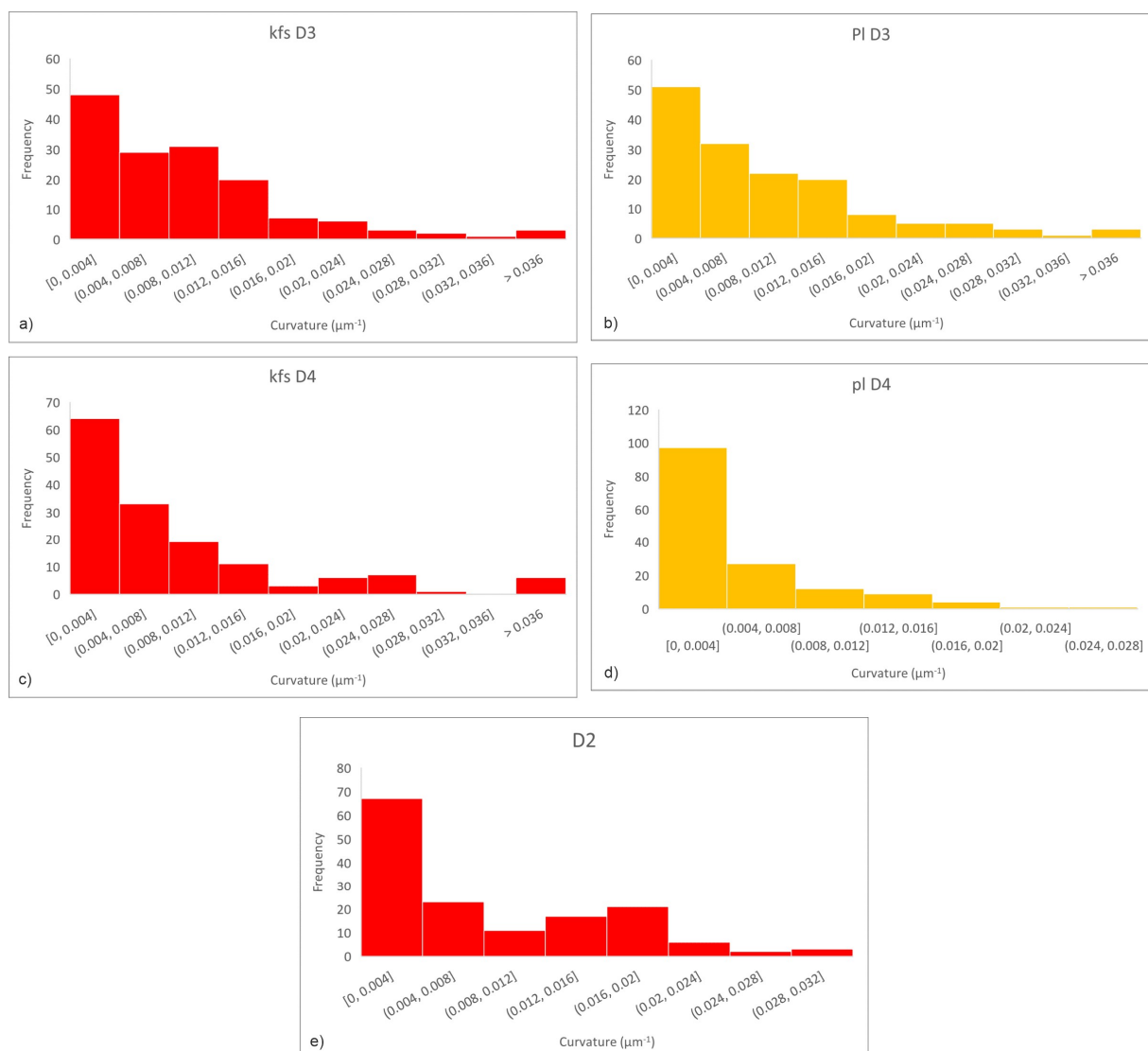


Fig. 66: Frequency distribution of feldspar curvature.

maximum curvature of $0.025 \mu\text{m}^{-1}$ of all feldspars. For plagioclase in D3 the decrease towards greater curvature is more continuous and the distribution is broader with a maximum curvature of $0.063 \mu\text{m}^{-1}$. All alkali feldspars (D3, D4, D2) reveal a less continuous decrease towards curvature $>0.004 \mu\text{m}^{-1}$ and show minor peaks at greater curvature. The maximum curvature of alkali feldspars is greatest in D4 with $0.094 \mu\text{m}^{-1}$. In D3 the maximum value is 0.046 and in D2 $0.032 \mu\text{m}^{-1}$. The latter results in a narrower frequency distribution compared to other alkali feldspars.

Dihedral angles of feldspar in the Fdd reveal a greater fraction 120° angles for plagioclase than for alkali feldspar in both domains, D3 and D4. In D3 T_{j120} is 53.5% for plagioclase and 41.8% for alkali feldspar (Table 10). In D4 T_{j120} is 41.3% and 22% for plagioclase and alkali feldspar, respectively. Alkali feldspar in D2 reveals a value of $T_{j120}=30.7\%$. T_{j90} is in both, D3 and D4, smaller for plagioclase than for alkali feldspar but for both feldspars higher in D4. In D3 T_{j90} is 14.4 and 7.1% and in D4 22.7 and 12.7% for alkali feldspar and plagioclase, respectively. In D2 T_{j90} yields a value of 16% . Frequency distributions of dihedral angles in D3 are asymmetrically unimodal for both feldspars with a peak at angles between 110° and 120° (Fig. 67). However, plagioclase reveals a sharper peak. In D4 the frequency distribution is polymodal for alkali feldspar and bimodal for plagioclase. For alkali feldspar peaks are developed at angle classes of $80-90^\circ$, $110-110^\circ$, $130-140^\circ$, and $160-170^\circ$. The distribution of dihedral angles for plagioclase peaks at angles between 120 and 130° and a minor maximum is developed for angles between $150-160^\circ$. Alkali feldspar in D2 displays a polymodal distribution with a pronounced peak at $110-120^\circ$. The frequency of measured angles decreases steadily towards both sides and is interrupted by further peaks at angles classes of $80-90^\circ$ and $170-180^\circ$.

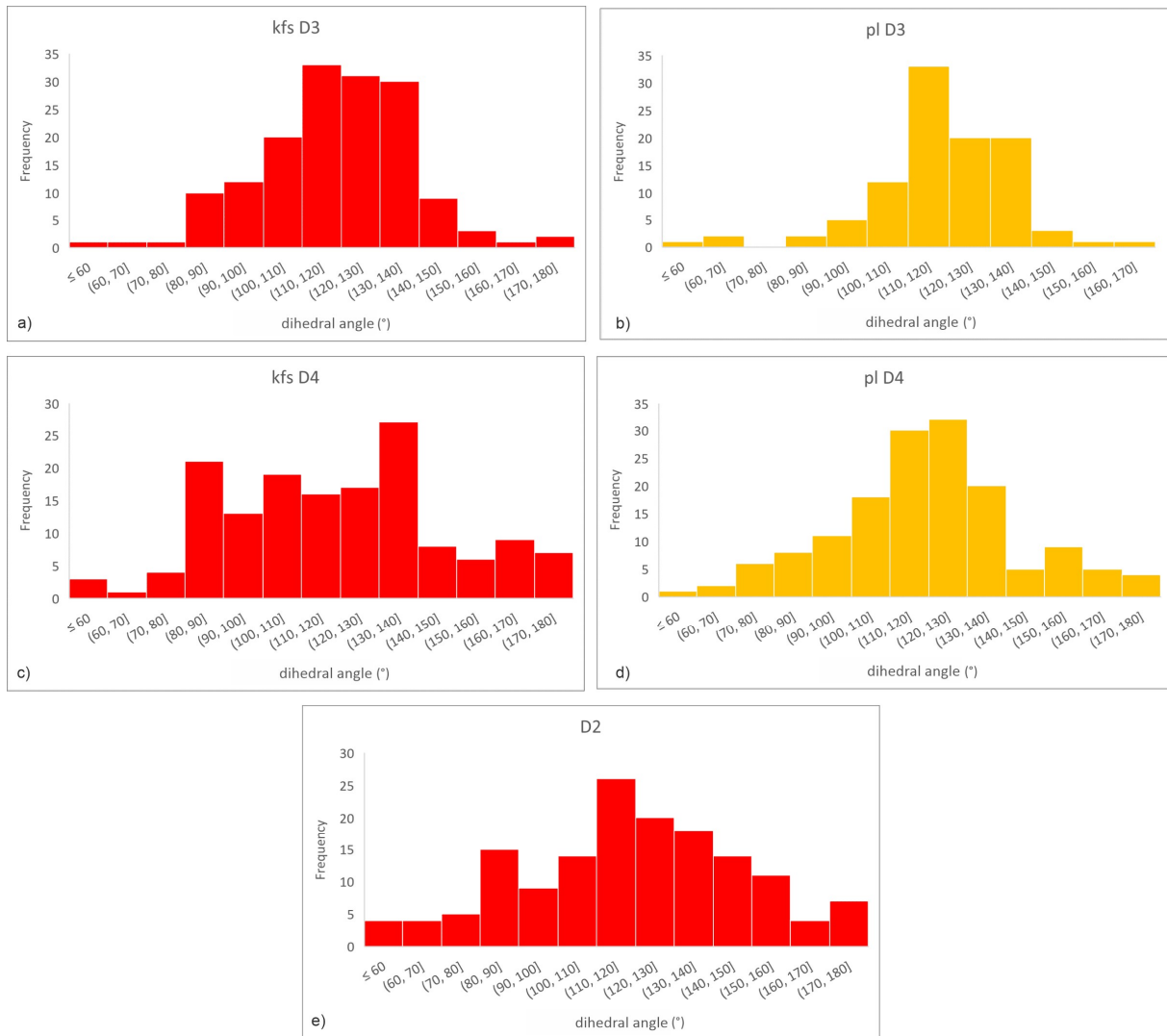


Fig. 67: Frequency distribution of feldspar dihedral angles.

8.1.2.3. Cumulative Frequency Curves of Dihedral Angles

Figure 68 shows cumulative frequency curves of dihedral angles as calculated by Elliott et al. (1997) and for the investigated samples including test quartz. A comparison of test quartz with the curves of Elliott et al. (1997) shows corresponding differences between equilibrated and unequilibrated/ deformed curves with the latter revealing more lower and higher angles than in equilibrated textures. However, intersection of equilibrated and unequilibrated curves is at 120° in the curves of Elliott et al. (1997) (Fig. 68a) while in test quartz curves intersect at 110° (Fig. 68b). Furthermore, the cumulative frequency of 120° angles is at 50 % in Elliott et al. (1997) and ranges between 60 and 70% for test quartz. Cumulative frequency curves of quartz in the Sri Lankan samples are similar in all

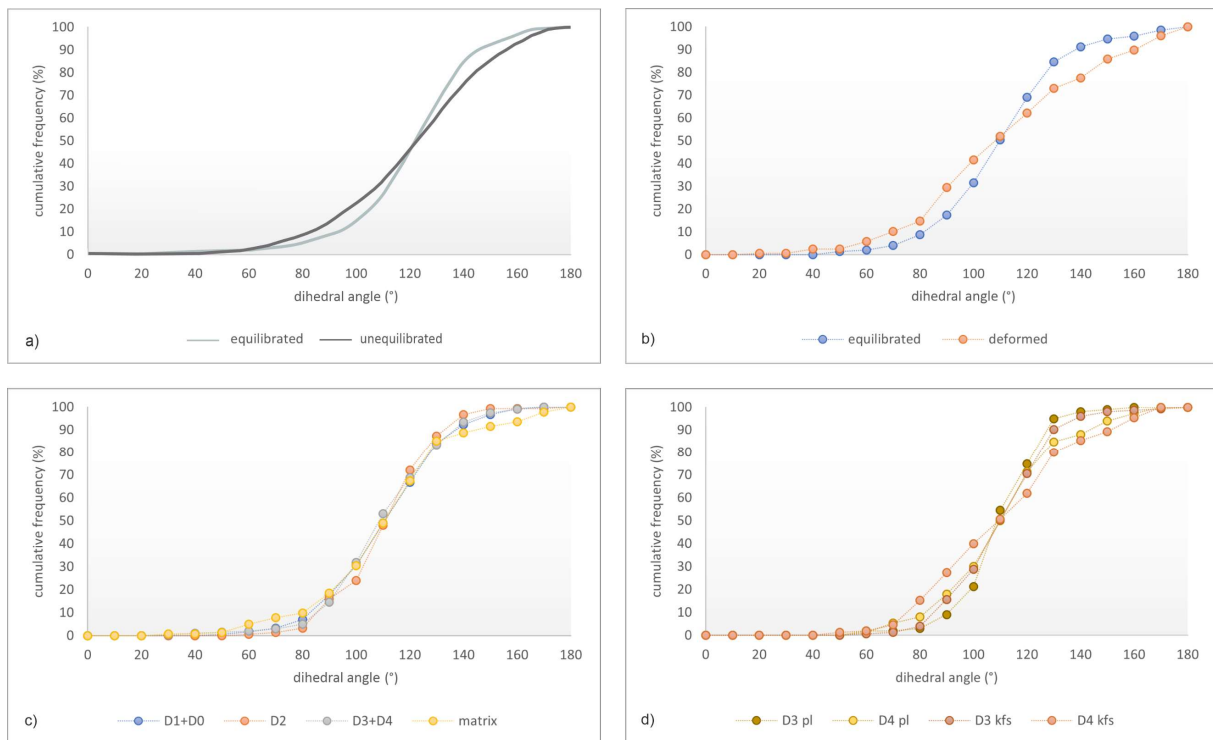


Fig. 68: Cumulative frequency curves of dihedral angles: a) curves for equilibrated and unequilibrated textures determined by Elliott et al. (1997) (redrawn); b) frequency curves of test quartz; c, d) frequency curves of Sri Lanka quartz (c) and feldspar (d).

domains and are closer in shape to the curves of the equilibrated case (Fig. 68c). The strongest deviation is observed for matrix quartz while D2 quartz exhibits the steepest curve between 80 and 140°. The latter is even steeper than for equilibrated test quartz which agrees with the results of Tj_{120} .

Sri Lankan feldspars display for both feldspars the steepest curves in D3 (Fig. 68d). Plagioclase in D3 reveals the best pronounced s-shape with even a steeper segment between 80 and 130° than equilibrated test quartz. This is consistent with a higher value of Tj_{120} for D3 plagioclase than for equilibrated test quartz (Table 10). Furthermore, the curves are steeper for plagioclase than for alkali feldspar in both domains.

8.2. Discussion

8.2.1. Comparison with Microstructures

A comparison of equilibrated and deformed test quartz reveals clear differences for curvature and dihedral angles. Frequency distributions display distinct features for equilibrated and deformed quartz. Further, the parameters C_s and T_{j120} differ significantly for both tested quartz samples, while the difference in T_{j90} is apparent but less pronounced.

The analysis of curvature and dihedral angles in Sri Lankan quartz and feldspar delivers reasonable results. The curvature of like-like boundaries shows for instance for D1/ D0 quartz the smallest value for C_s of 18 %. This agrees with highest Paris factors in these domains (chapter 7, Table 7) and demonstrates interlobate aggregate shapes. Moreover, the similar nature of like-like boundaries in D3 and D1/ D0 is well expressed using C_s and the frequency distribution of measured curvatures (Fig. 64a, c, Table 10). This similar nature is not evident using shape factors as aspect ratio, Paris factor or angularity which indicate huge differences between D3 ribbons and D1/ D0 quartz (chapter 7, Table 7). Thus, the curvature can demonstrate common features of grain boundaries independent of the bulk grain shape.

For feldspars in the Fdd the measure of curvature shows more straight like-like boundaries for plagioclase than for alkali feldspar (Fig. 66, Table 10). This underpins results of the shape analysis in chapter 7 that plagioclase tends to develop polygonal frameworks while alkali feldspar forms interlobate shapes. Nevertheless, the results show also that the method of analysing curvature is not trivial. For instance, in D2 quartz C_s and the frequency distribution of measured curvature indicate a high fraction of straight grain boundaries despite comparatively high Paris factors (Table 10, chapter 7, Table 7). This can be explained by the high abundance of small grains and a tendency to

form ribbon shapes where most grain boundaries are straight (Fig. 59a). A high curvature of individual grain boundaries of large grains in D2 is best inferred from the maximum curvature which reveals the highest value of all analyzed quartz (Table 10).

The analysis of dihedral angles also delivers comprehensible results for quartz and feldspar in the investigated samples. In D2, for example, T_{j120} and the frequency distribution reveal the greatest fraction of 120° angles which can be deduced from the abundance of small sized quartz aggregates forming polygonal frameworks (Fig. 9a). In other quartz domains polygonal aggregates lack which is consistent with decreasing T_{j120} and broadening peaks in frequency distributions (Fig. 65). In D3 ribbons T_{j120} and the frequency distribution indicate the second most fraction of 120° dihedral angles. However, no distinct differences between D3 ribbons and other domains (D4, matrix, D1/D0) are evident from microscopic observations. Furthermore, in D3 fewer dihedral angles are available reducing the number of measured angles to 90. Riegger and Van Vlack (1960) reported that the measurement of 100 dihedral angles gives an accuracy of $\pm 4^\circ$. Therefore, in D3, and also in D4 ($n=108$), the error is larger compared to other domains of at least 141 measurements (Table 10). The summary of D3 and D4 however gives a similar T_{j120} value and frequency distribution to D1/D0 and matrix quartz. The results are consistent with less equilibrated dihedral angles compared to D2 because of the lack of polygonal aggregates. The measure of dihedral angles is even more consistent for feldspars in the Fdd. For plagioclase high values for T_{j120} and narrow frequency distributions peaking at 120° agree with polygonal frameworks as indicated by low Paris factors (chapter 7). On the other hand, lower T_{j120} and peak broadening in frequency distributions of alkali feldspars (Fdd, D2) correspond to interlobate structures. However, in D4 n is 99 for plagioclase but more than half of the measured angles scatter around 120° . Considering a larger error for D4, plagioclase T_{j120} would still display a high value.

Dihedral 90° angles are not striking in frequency distributions of quartz. Tj_{90} is in the range of equilibrated quartz and in accordance with high values for Tj_{120} (Table 10). This could indicate a high degree of equilibration. Nevertheless, in D2 quartz the small peak around 90° infers a deviation from an equilibrated texture despite a high value of Tj_{120} and highlights the contribution of large grains with less equilibrated dihedral angles next to small-sized polygonal aggregates (Fig. 59a). In alkali feldspar of D4 and D2 frequency distributions display protruding peaks around 90° (Fig. 67c, e). Furthermore, Tj_{90} reveals highest values at lowest Tj_{120} in these domains (Table 10). In plagioclase a high value of Tj_{120} corresponds to low values of Tj_{90} . This suggests that a dihedral angle of 90° indeed could represent a feature of deformed rocks which was also observed in other studies (e.g., Lister and Dornsiepen, 1982; Little et al., 2013; Pennacchioni et al., 2010). However, these results serve as additional observation made in deformed rocks, but further work is needed on the development of 90° angles.

The presentation of dihedral angles in cumulative frequency curves is consistent with the results of Elliott et al (1997). The curves of equilibrated and deformed test quartz show similar features as those determined by Elliott et al. (1997) (Fig. 68a, b). However, the curves of test quartz are shifted to higher frequency of smaller and larger angles around 120° compared to the curves of Elliott et al. (1997). A possible reason could be that the authors measured angles on simulated textures whereas test quartz represent natural samples. Nevertheless, equivalent differences between equilibrated and unequilibrated/deformed curves in both cases demonstrate that selected test quartz in this study state good approximations for endmembers of equilibrated and deformed textures.

For Sri Lankan quartz and feldspar cumulative frequency curves display results consistent with frequency distributions and values of Tj_{120} for quartz and feldspar in all domains (including D2 feldspar which is not shown). However, frequency distributions

better illustrate striking features such as the peak around 90° angles for alkali feldspar in D4 and D3.

8.2.2. Curvature and Equilibration of Quartz Grain Boundaries

The measurement of curvature of quartz like-like boundaries in the investigated samples shows differences in C_s between the different subdomains despite a common deformation and annealing history. In section 7.2.2.2. serrated and curved quartz grain boundaries were discussed as equilibrated grain boundaries in low energy configurations which are controlled by crystallography. Kruhl and Peternell (2002) stated that such low energy configurations are stable against subsequent annealing as long as the material is not reformed. Thus, the reduction of surface energy by straightening grain boundaries is cancelled by the crystallographic control of achieving lowest energy states. Therefore, a low curvature is not a reliable indicator for equilibration in coarse-grained quartz with serrated grain boundary segments such as in D1/ D0 and D3. Voll (1969) pointed out that for deformation induced GBM the segment length increases with increasing temperature. Kruhl and Peternell (2002) further stated that curved grain boundaries from dynamically recrystallized quartz are never curved but consist of straight segments. In D1/ D0 and D3 grain boundaries are often serrated consisting of several straight segments (Fig. 9b, g, h). In D2, D4 and matrix serrated grain boundaries hardly occur. Hence, it is suggested that grain boundaries in the latter domains represent shortest straight segments in quartz deformed at high temperatures. Thus, in quartz deformed at high temperatures, the reliability of curvature to represent the degree of equilibration decreases with increasing grain boundary length. Furthermore, straight grain boundaries are common in ribbons formed during high temperature conditions (Hippertt et al., 2001). Nevertheless, highly curved grain boundaries are formed during dynamic GBM recrystallization and equilibrated serrated grain boundaries are still less curved than the former. This is

evident in striking differences between C_s and frequency distributions of deformed test quartz and quartz of D1/ D0 and D3 (Figs. 63a, 64a, c, Table 10). Therefore, in quartz deformed and annealed at high temperatures the estimation of equilibration based on curvature should only be made under careful consideration of microstructures.

8.2.3. Concluding Remarks

The analysis of curvature and dihedral angles can serve as useful tool to characterize like-like boundaries and to estimate equilibration in polyphase aggregates. Furthermore, the curvature of like-like boundaries gives additional information on shape characteristics which are not accessible when analyzing the bulk shape by means of Paris factor or angularity. The combination of parameters C_s , Tj_{120} and Tj_{90} with frequency distributions can describe adequately curvature and dihedral angles. Nevertheless, the estimation of equilibration should be made carefully. This involves consideration of driving forces of equilibration and a careful inspection of the surrounding framework. Furthermore, curvature and dihedral angles should be applied in combination because they represent independent measures (Elliott et al., 1997).

8.2.4. Equilibration of Quartz and Feldspar

Quartz is suggested to be partly equilibrated during post-deformational annealing. This is inferred from high values of Tj_{120} and frequency distributions which better resemble equilibrated test quartz. Considering aspects stated in section 8.2.2., the curvature further indicates partial equilibration as inferred from moderate values of C_s in D2, D4 and matrix. Frequency distributions in these domains are skewed to smallest curvature but maximum curvatures indicate still highly curved like-like boundaries, even in matrix quartz with the shortest grain boundaries. Frequency distributions of curvature in D3 and D1/ D0 show a high frequency of straight grain boundaries despite low values of C_s . Serrated and curved

grain boundaries might represent equilibrated grain boundaries and support equilibration of quartz. Partial equilibration of quartz is consistent with low internal misorientation (chapter 6).

For feldspars in the Fdd plagioclase reveals a high degree of equilibration as inferred from frequency distributions of curvature and dihedral angles similar to equilibrated quartz. Alkali feldspar reveals a lower degree of equilibration than plagioclase. This is indicated by abundant curved grain boundaries and irregular frequency distributions of dihedral angles in both, the Fdd and D2. Further, for both feldspars in the Fdd a higher degree of equilibration is interpreted for D3 compared to D4 and is indicated by dihedral angles in frequency distributions and cumulative frequency curves. This interpretation is made against a higher fraction of straight boundaries in D4 compared to D3 because the difference in frequency distribution of dihedral angles is more pronounced than that for curvature. In D2 the curvature and dihedral angles indicate equilibration intermediate between D3 and D4 alkali feldspar.

A high degree of equilibration for plagioclase is consistent with low Paris factors, low internal misorientation and decreasing aspect ratios in D3 (chapters 6, 7). The latter was also observed by Dresen et al. (1996) for increasing annealing temperature and duration of synthetic anorthite aggregates. For alkali feldspar a lower degree of equilibration based on curvature and dihedral angles is consistent with measured shape factors (chapter 7). The question arises whether the difference in equilibration between alkali feldspar and plagioclase is due to deformation or annealing. In section 6.2.2.5. it was discussed that in alkali feldspar dislocation creep might be accommodated by recovery and dynamic recrystallization (GBM) producing interlobate frameworks. For plagioclase it was suggested that the dominant accommodation mechanism was recovery and that dynamic recrystallization by GBM was of minor importance resulting in less disturbance of grain

fabrics. However, both feldspars show signs of dynamic GBM recrystallization and both feldspars show signs of equilibration (alkali feldspar in D3) though not to the same extent. Striking features of alkali feldspar aggregates are perthitic exsolution, abundant plagioclase films along alkali feldspar grain boundaries and plagioclase interstitials (Fig. 10b, c, g). The former was observed to pin migrating grain boundaries and the latter are often aligned to already curved alkali feldspar boundaries. This infers a development before or during deformation in the case of pinning exsolutions and syn- to postdeformational origin for plagioclase films. Therefore, during annealing, alkali feldspar boundaries were highly obstructed which was not the case for plagioclase to this extent. Obstacles exercise a drag force on boundaries and retard boundary migration (Evans et al., 2001). Thus, abundant plagioclase obstacles in alkali feldspar could impede equilibration of alkali feldspar. This could also explain less equilibrated microstructures in D4 of both feldspars because in this domain abundant quartz probably contributes to pinning by forming interstitials and films along feldspar boundaries (e.g., Figs. 8e, 11d). A different dynamic recrystallization behaviour between alkali feldspar and plagioclase, however, cannot be inferred due to equilibration of plagioclase microstructures.

9. Summary and Conclusion

Deformation of quartz-feldspar rocks from the Highland Complex of Sri Lanka occurred under dry conditions at minimum temperatures of 773 °C (two-feldspar thermometry) to 836 °C (TitaniQ thermometry) and is related to the D₂ deformation event.

Quartz deformed by dominant dislocation creep accommodated by GBM recrystallization (ribbons in D3, D4 and 2997, D1, D2) and minor SGR recrystallization. Diffusion assisted phase boundary migration was dominant in matrix quartz but contributed probably to deformation in all domains producing smoothly curved quartz-feldspar phase boundaries. Intracrystalline slip was accommodated by multiple active slip systems resulting in cross-girdle distributions in 2997 ribbons. Suitable orientation of category C quartz for combined prism[c], basal<a> and rhomb<a> slip resulted in high stored strain energy increasing grain boundary mobility. Rhomb<a> slip was probably promoted by mechanical Dauphiné twinning. Increased grain boundary mobility caused selective coarsening of category C quartz in all domains at the expense of category A and B quartz. The latter two reveal suitable orientation for limited slip systems resulting in lower stored strain energy and grain boundary mobility. Selective coarsening of category C quartz resulted in a strengthening of quartz crystallographic preferred orientation (CPO) from matrix quartz over ribbons in the Fdd towards D2 and D1. Random CPO in matrix quartz was probably promoted by diffusion accommodated crystal plastic deformation. Incomplete selective coarsening due to restriction into layers caused less pronounced and weak (D4) CPO pattern in ribbons of D4 and D3. Small grain sizes of 2997 ribbons suggest that coarsening was least effective in this domain preserving cross-girdle distributions. Selective coarsening of category C quartz is largely completed in D2 and D1 resulting in strong CPOs.

Selective coarsening and dominant deformation mechanisms were controlled by quartz connectivity. In the Fdd quartz connectivity was determined by the modal content. A low quartz content resulted in a weak connectivity of quartz favouring diffusion assisted phase boundary migration in the matrix. Increasing quartz content caused increasing connectivity which promoted ribbon formation and GBM recrystallization. Increasing quartz content in the Qdd resulted in a high connectivity and the formation of an interconnected framework. In D2 connectivity and dominant deformation mechanisms were determined by feldspar (second phase) content. Abundant feldspar caused restricted GBM recrystallization and preserved evidence for SGR recrystallization and ribbon formation. Pinning of quartz by feldspar kept numerous quartz grains small which deformed by diffusion assisted phase boundary migration. In quartz rich domains D1 and D0 feldspar pinning was negligible, and microstructures were controlled by dynamic recrystallization. A sustainable influence of annealing on grain size development is not evident in a Zener plot.

It is proposed that equilibration of quartz was already initiated during ceasing dynamic conditions by GBM recrystallization, recovery, and stabilization of grain boundaries. Progressive recovery during annealing probably (re)activated slip systems in response to changing stress fields resulting in slip planes and corresponding misorientation axes at high angle to the foliation plane. Further microstructural modification of quartz was restricted to equilibration of dihedral angles which indicate partial equilibration. The curvature of grain boundaries suggests partial equilibration. This conclusion is made considering the crystallographic control on grain boundary stabilization and characteristic straight grain boundaries in ribbons (Hippertt et al., 2001). Quartz CPOs in the Qdd reflect crystal slip during dynamic conditions, and it is suggested that annealing

did not sustainably modify the pattern. However, a modification of CPOs in the Fdd cannot be excluded.

The investigation of quartz microstructures in a sequence of quartz poor to quartz rich domains reveals a complete image of quartz deformation in polyphase rocks under lower crustal conditions. Investigation of quartz ribbons alone could lead to incorrect interpretation because selective coarsening is best evident when considering D1 and D2. Furthermore, the results show that microstructures developed at high temperatures by dynamic GBM recrystallization can be partially preserved during subsequent annealing as observed in other studies (e.g., Barnhoorn et al., 2005; Heilbronner and Tullis, 2002).

Alkali feldspar and plagioclase deformed by diffusion assisted phase boundary migration and by dislocation creep accommodated by GBM recrystallization and subordinate SGR recrystallization. Similar to quartz, the dominance of deformation mechanisms was governed by connectivity and modal content. In D2 and in the polyphase matrix of D4 low modal content and weak connectivity resulted in dominant phase boundary migration and smoothly curved phase boundaries between alkali feldspar, plagioclase and matrix quartz. Deformation by diffusion in D4 is attributed to weaken alkali feldspar and plagioclase CPOs. In D2 increasing content and connectivity are characterized by accumulation of alkali feldspar in lenticular polycrystalline aggregates in which GBM and SGR recrystallization became important. D2 aggregates with high connectivity display similar microstructures as alkali feldspar rich layers in D3 in which GBM was the dominant deformation mechanism.

Similar CPOs of both feldspars in D1 A, D2 (alkali feldspar) and the Fdd suggest similar deformation behaviour despite the lack of detailed grain size and shape analysis in the former. Intracrystalline slip of alkali feldspar was accommodated by multiple active slip systems resulting in moderate CPOs. Slip on (010) in [100] direction is proposed as

dominant slip system. In D1 L (001) in [100] is suggested to be dominant over (010)[100]. Plagioclase CPOs are stronger compared to alkali feldspar CPOs in all domains. This is probably due to dominant slip solely on the (010) plane. [100] and [001] are corresponding dominant slip directions. Furthermore, (021)[1-12] slip is pronounced in CPOs. It is suggested that this slip system was generated in healed fractures of grains with unsuitable orientation for (010) slip. Plagioclase CPOs are strongest in D1 L which is related with enhanced crystal plastic deformation of weak and An-poor plagioclase. This is supported by the lack of preferred orientation of (021).

CPOs of both feldspars correspond to deformation and were not altered during annealing. It is suggested that low internal misorientation was initiated during ceasing deformation by recovery and GBM recrystallization just as for quartz. Furthermore, the deformation record in subgrain boundaries was partly modified for the same reason as in quartz and is inferred from comparable low angle (2–10°) misorientation axis distributions and slip planes at high angle to the foliation. However, the boundary trace analysis reveals a spread in detected slip systems of alkali feldspar and compliance of dominant slip systems in plagioclase which agrees with CPOs. Therefore, it is concluded that some record is preserved. Equilibration of grain boundaries and dihedral angles was impeded in alkali feldspar by pinning exsolutions and plagioclase films along grain boundaries. The lack of obstacles along plagioclase grain boundaries in D3 enabled a high degree of equilibration resulting in polygonal frameworks with straight grain boundaries and abundant dihedral angles of 120°. In D4 and D2 (alkali feldspar) equilibration of both feldspars is less accomplished due to restriction of grain boundaries in a polyphase assemblage.

The investigation of feldspars in the Sri Lankan samples completes the scarce record of GBM recrystallization microstructures. Furthermore, results of the boundary trace analysis in this study provide a model for misorientation axis spread and corresponding

slip systems which can serve as template for future work. Deformation by dislocation creep supports rheology estimates of the lower crust which are based on dislocation creep flow laws for plagioclase (e.g., Bürgmann and Dresen, 2008). This is opposite to the statement of Rosenberg and Stünitz (2003) who proposed that lower crustal rheology for polyphase rocks is better approximated by diffusion creep flow laws. Crystal-plastic deformation microstructures and CPOs of feldspars in all domains show that quartz did not accommodate all strain but that it was partitioned between quartz and feldspars. This suggests a low strength contrast between feldspar and quartz which is even lower regarding An-poor plagioclase in D1 L.

10. Outlook

Conclusions regarding quartz microstructures in D1 and D0 were made with reservations due to limitations in two-dimensional analysis of microstructures. Millimetre to centimetre sized quartz require appropriate methods for grain size, shape, and connectivity estimations, ideally in three dimensions. Appropriate methods are Serial Sectioning or Computer Tomography.

The modified application of the Zener Parameter with respect to aggregate size instead of second phase grain size requires a larger data set to verify its application. In the case of coarse-grained quartz, this should ideally be performed on the basis of three-dimensional grain size estimations.

Dihedral angles of 90° appear to be a feature of deformation microstructures. The present study complemented the scarce record in deformed rocks. Further work is needed to confirm that 90° angles are characteristic features of deformed rocks. Furthermore, 90° angles should be investigated with respect to nature and cause and to deformation conditions and recrystallization mechanisms.

References

- Acosta, M. D., Watkins, J. M., Reed, M. H., Donovan, J. J., & DePaolo, D. J. (2020). Ti-in-quartz: Evaluating the role of kinetics in high temperature crystal growth experiments. *Geochimica et Cosmochimica Acta*, 281, 149-167.
- Ashley, K. T., Webb, L. E., Spear, F. S., & Thomas, J. B. (2013). P-T-D histories from quartz: A case study of the application of the TitaniQ thermobarometer to progressive fabric development in metapelites. *Geochemistry, Geophysics, Geosystems*, 14(9), 3821-3843.
- Ashley, K. T., Carlson, W. D., Law, R. D., & Tracy, R. J. (2014). Ti resetting in quartz during dynamic recrystallization: Mechanisms and significance. *American Mineralogist*, 99(10), 2025-2030.
- Ashley, K. T., & Law, R. D. (2015). Modeling prograde TiO₂ activity and its significance for Ti-in-quartz thermobarometry of pelitic metamorphic rocks. *Contributions to Mineralogy and Petrology*, 169(2), 23.
- Atkinson, H. V. (1988). Overview no. 65: Theories of normal grain growth in pure single phase systems. *Acta Metallurgica*, 36(3), 469-491.
- Augenstein, C., & Burg, J. P. (2011). Natural annealing of dynamically recrystallised quartzite fabrics: Example from the Cévennes, SE French Massif Central. *Journal of Structural Geology*, 33(3), 244-254.
- Augenstein, C., & Burg, J. P. (2011). Natural annealing of dynamically recrystallised quartzite fabrics: Example from the Cévennes, SE French Massif Central. *Journal of Structural Geology*, 33(3), 244-254.
- Barber, D. J., & Wenk, H. R. (1991). Dauphiné twinning in deformed quartzites: implications of an in situ TEM study of the α - β phase transformation. *Physics and Chemistry of Minerals*, 17(6), 492-502.
- Barnhoorn, A., Bystricky, M., Burlini, L., & Kunze, K. (2005). Post-deformational annealing of calcite rocks. *Tectonophysics*, 403(1-4), 167-191.
- Batanova, V. G., Sobolev, A. V., & Magnin, V. (2018). Trace element analysis by EPMA in geosciences: Detection limit, precision and accuracy. In *IOP Conference Series: Materials Science and Engineering* (Vol. 304, No. 1, p. 012001). IOP Publishing.
- Benisek, A., Kroll, H., & Cemic, L. (2004). New developments in two-feldspar thermometry. *American Mineralogist*, 89(10), 1496-1504.
- Benisek, A., Dachs, E., & Kroll, H. (2010). A ternary feldspar-mixing model based on calorimetric data: development and application. *Contributions to Mineralogy and Petrology*, 160(3), 327-337.
- Berger, A. R., & Jayasinghe, N. R. (1976). Precambrian structure and chronology in the Highland Series of Sri Lanka. *Precambrian Research*, 3(6), 559-576.
- Berger, A., Herwegh, M., Schwarz, J. O., & Putlitz, B. (2011). Quantitative analysis of crystal/grain sizes and their distributions in 2D and 3D. *Journal of Structural Geology*, 33(12), 1751-1763.
- Bestmann, M., & Prior, D. J. (2003). Intragranular dynamic recrystallization in naturally deformed calcite marble: diffusion accommodated grain boundary sliding as a result of subgrain rotation recrystallization. *Journal of Structural Geology*, 25(10), 1597-1613.
- Blacic, J. D. (1975). Plastic-deformation mechanisms in quartz: the effect of water. *Tectonophysics*, 27(3), 271-294.

- Bragg, W. H., Bragg, W. L. (1915). X-Rays and Crystal Structure. *G. Bell and Sons Ltd*, London.
- Braun, I., & Kriegsman, L. M. (2003). Proterozoic crustal evolution of southernmost India and Sri Lanka. *Geological Society, London, Special Publications*, 206(1), 169-202.
- Brocher, J. (2015, January). The BioVoxel image processing and analysis toolbox. In *European BioImage Analysis Symposium. Paris, France*.
- Brodhag, S. H., Herwegh, M., & Berger, A. (2011). Grain coarsening in polymineralic contact metamorphic carbonate rocks: The role of different physical interactions during coarsening. *Journal of structural geology*, 33(4), 698-712.
- Bürgmann, R., & Dresen, G. (2008). Rheology of the lower crust and upper mantle: Evidence from rock mechanics, geodesy, and field observations. *Annual Review of Earth and Planetary Sciences*, 36.
- Cavalcante, C., Lagoeiro, L., Fossen, H., Egydio-Silva, M., Morales, L. F., Ferreira, F., & Conte, T. (2018). Temperature constraints on microfabric patterns in quartzofeldspathic mylonites, Ribeira belt (SE Brazil). *Journal of Structural Geology*, 115, 243-262.
- Ceccato, A., Pennacchioni, G., Menegon, L., & Bestmann, M. (2017). Crystallographic control and texture inheritance during mylonitization of coarse grained quartz veins. *Lithos*, 290, 210-227.
- Cherniak, D. J., Watson, E. B., & Wark, D. A. (2007). Ti diffusion in quartz. *Chemical Geology*, 236(1-2), 65-74.
- Cherniak, D. J. (2010). Cation diffusion in feldspars. *Reviews in Mineralogy and Geochemistry*, 72(1), 691-733.
- Cooray, P. G. (1994). The Precambrian of Sri Lanka: a historical review. *Precambrian research*, 66(1-4), 3-18.
- Cross, A. J., Hirth, G., & Prior, D. J. (2017). Effects of secondary phases on crystallographic preferred orientations in mylonites. *Geology*, 45(10), 955-958.
- De Bresser, J. H. P., Peach, C. J., Reijs, J. P. J., & Spiers, C. J. (1998). On dynamic recrystallization during solid state flow: Effects of stress and temperature. *Geophysical Research Letters*, 25(18), 3457-3460.
- Dell'Angelo, L. N., & Tullis, J. (1986). A comparison of quartz c-axis preferred orientations in experimentally deformed aplites and quartzites. *Journal of structural geology*, 8(6), 683-692.
- De Maesschalck, A. A., Oen, I. S., Hebeda, E. H., Verschure, R. H., & Arps, C. E. S. (1990). Rubidium-strontium whole-rock ages of Kataragama and Pottuvil charnockites and East Vijayan gneiss: Indication of a 2 Ga metamorphism in the highlands of southeast Sri Lanka. *The Journal of Geology*, 98(5), 772-779.
- Dharmapriya, P. L., Malaviarachchi, S. P., Santosh, M., Tang, L., & Sajeev, K. (2015). Late-neoproterozoic ultrahigh-temperature metamorphism in the Highland Complex, Sri Lanka. *Precambrian Research*, 271, 311-333.
- Dharmapriya, P. L., Malaviarachchi, S. P. K., Sajeev, K., & Zhang, C. (2016). New LA-ICPMS U-Pb ages of detrital zircons from the Highland Complex: insights into late Cryogenian to early Cambrian (ca. 665–535 Ma) linkage between Sri Lanka and India. *International Geology Review*, 58(15), 1856-1883.

- Dharmapriya, P. L., Malaviarachchi, S. P., Kriegsman, L. M., Galli, A., Sajeev, K., & Zhang, C. (2017). New constraints on the P-T path of HT/UHT metapelites from the Highland Complex of Sri Lanka. *Geoscience Frontiers*, 8(6), 1405-1430.
- Dharmapriya, P. L., Malaviarachchi, S. P., Kriegsman, L. M., Galli, A., Dyck, B., Sajeev, K., ... & Pitawala, A. (2020). Symplectite growth in the presence of alkaline fluids: evidence from high-aluminous metasediments of the Highland Complex, Sri Lanka. *Mineralogy and Petrology*, 114(6), 515-538.
- Dresen, G., Wang, Z., & Bai, Q. (1996). Kinetics of grain growth in anorthite. *Tectonophysics*, 258(1-4), 251-262.
- Egydio-Silva, M., Vauchez, A., Bascou, J., & Hippertt, J. (2002). High-temperature deformation in the Neoproterozoic transpressional Ribeira belt, southeast Brazil. *Tectonophysics*, 352(1-2), 203-224.
- Elliott, M. T., Cheadle, M. J., & Jerram, D. A. (1997). On the identification of textural equilibrium in rocks using dihedral angle measurements. *Geology*, 25(4), 355-358.
- Evangelakakis, C., Kroll, H., & Voll, G. (1991). Exsolution and ordering structures in feldspars from high-grade metamorphic rocks in Sri Lanka. *The crystalline crust of Sri Lanka. I. Summary of research of the German-Sri Lankan Consortium. Geol Surv Dep of Sri Lanka, Prof Pap*, 5, 268-271.
- Evangelakakis, C., Kroll, H., Voll, G., Wenk, H. R., Meisheng, H., & Köpcke, J. (1993). Low-temperature coherent exsolution in alkali feldspars from high-grade metamorphic rocks of Sri Lanka. *Contributions to Mineralogy and Petrology*, 114(4), 519-532.
- Evans, B., Renner, J., & Hirth, G. (2001). A few remarks on the kinetics of static grain growth in rocks. *International Journal of Earth Sciences*, 90(1), 88-103.
- Faulhaber, S., & Raith, M. (1991). Geothermometry and geobarometry of high-grade rocks: a case study on garnet-pyroxene granulites in southern Sri Lanka. *Mineralogical Magazine*, 55(378), 33-56.
- Fossen, H. (2016). *Structural geology*. Cambridge University Press.
- Franěk, J., Schulmann, K., Lexa, O., Ulrich, S., Štípská, P., Haloda, J., & Týcová, P. (2011). Origin of felsic granulite microstructure by heterogeneous decomposition of alkali feldspar and extreme weakening of orogenic lower crust during the Variscan orogeny. *Journal of Metamorphic Geology*, 29(1), 103-130.
- Fron del, C. (1962). The system of mineralogy, 7th edn, vol III *Silica minerals*. Wiley, New York.
- Fuhrman, M. L., & Lindsley, D. H. (1988). Ternary-feldspar modeling and thermometry. *American mineralogist*, 73(3-4), 201-215.
- Gardner, R. L., Piazzolo, S., & Daczko, N. R. (2016). Shape of pinch and swell structures as a viscosity indicator: application to lower crustal polyphase rocks. *Journal of Structural Geology*, 88, 32-45.
- Ghent, E. D., & Stout, M. Z. (1984). TiO₂ activity in metamorphosed pelitic and basic rocks: principles and applications to metamorphism in southeastern Canadian Cordillera. *Contributions to Mineralogy and Petrology*, 86(3), 248-255.
- Gleason, G. C., Tullis, J., & Heidelbach, F. (1993). The role of dynamic recrystallization in the development of lattice preferred orientations in experimentally deformed quartz aggregates. *Journal of Structural Geology*, 15(9-10), 1145-1168.

- Gower, R. J., & Simpson, C. (1992). Phase boundary mobility in naturally deformed, high-grade quartzofeldspathic rocks: evidence for diffusional creep. *Journal of Structural Geology*, 14(3), 301-313.
- Griggs, D., & Bell, J. F. (1938). Experiments bearing on the orientation of quartz in deformed rocks. *Bulletin of the Geological Society of America*, 49(11), 1723-1746.
- Grove, T. L., Baker, M. B., & Kinzler, R. J. (1984). Coupled CaAl-NaSi diffusion in plagioclase feldspar: experiments and applications to cooling rate speedometry. *Geochimica et cosmochimica Acta*, 48(10), 2113-2121.
- Grujic, D., Stipp, M., & Wooden, J. L. (2011). Thermometry of quartz mylonites: Importance of dynamic recrystallization on Ti-in-quartz reequilibration. *Geochemistry, Geophysics, Geosystems*, 12(6).
- Halfpenny, A. (2010). Some important practical issues for the collection and manipulation of Electron Backscatter Diffraction (EBSD) data from geological samples. *Journal of the Virtual Explorer*, 35.
- Handy, M. R. (1994). Flow laws for rocks containing two non-linear viscous phases: a phenomenological approach. *Journal of Structural Geology*, 16(3), 287-301.
- He, X. F., Santosh, M., Tsunogae, T., & Malaviarachchi, S. P. (2016a). Early to late Neoproterozoic magmatism and magma mixing-mingling in Sri Lanka: implications for convergent margin processes during Gondwana assembly. *Gondwana Research*, 32, 151-180.
- He, X. F., Santosh, M., Tsunogae, T., Malaviarachchi, S. P., & Dharmapriya, P. L. (2016b). Neoproterozoic arc accretion along the 'eastern suture' in Sri Lanka during Gondwana assembly. *Precambrian Research*, 279, 57-80.
- Heidelberg, F., Kunze, K., & Wenk, H. R. (2000). Texture analysis of a recrystallized quartzite using electron diffraction in the scanning electron microscope. *Journal of Structural Geology*, 22(1), 91-104.
- Heilbronner, R., & Bruhn, D. (1998). The influence of three-dimensional grain size distributions on the rheology of polyphase rocks. *Journal of Structural Geology*, 20(6), 695-705.
- Heilbronner, R., & Tullis, J. (2002). The effect of static annealing on microstructures and crystallographic preferred orientations of quartzites experimentally deformed in axial compression and shear. *Geological Society, London, Special Publications*, 200(1), 191-218.
- Heilbronner, R., & Tullis, J. (2006). Evolution of c axis pole figures and grain size during dynamic recrystallization: Results from experimentally sheared quartzite. *Journal of Geophysical Research: Solid Earth*, 111(B10).
- Heilbronner, R., & Barrett, S. (2013). *Image analysis in Earth Sciences: microstructures and textures of earth materials* (Vol. 129). Springer Science & Business Media.
- Herwegh, M., & Berger, A. (2004). Deformation mechanisms in second-phase affected microstructures and their energy balance. *Journal of structural geology*, 26(8), 1483-1498.
- Herwegh, M., Berger, A., & Ebert, A. (2005). Grain coarsening maps: a new tool to predict microfabric evolution of polymineralic rocks. *Geology*, 33(10), 801-804.
- Herwegh, M., Berger, A., Ebert, A., & Brodhag, S. (2008). Discrimination of annealed and dynamic fabrics: consequences for strain localization and deformation episodes of large-scale shear zones. *Earth and planetary science letters*, 276(1-2), 52-61.

- Herwegh, M., Linckens, J., Ebert, A., Berger, A., & Brodhag, S. H. (2011). The role of second phases for controlling microstructural evolution in polymineralic rocks: A review. *Journal of Structural Geology*, 33(12), 1728-1750.
- Hippertt, J., Rocha, A., Lana, C., Egydio-Silva, M., & Takeshita, T. (2001). Quartz plastic segregation and ribbon development in high-grade striped gneisses. *Journal of Structural Geology*, 23(1), 67-80.
- Hirth, G., & Tullis, J. A. N. (1992). Dislocation creep regimes in quartz aggregates. *Journal of structural geology*, 14(2), 145-159.
- Hobbs, B. E. (1985). The geological significance of microfabric analysis. *Preferred Orientation in Deformed Metals and Rocks: An Introduction to Modern Texture Analysis*.
- Hokada, T. (2001). Feldspar thermometry in ultrahigh-temperature metamorphic rocks: Evidence of crustal metamorphism attaining ~ 1100 C in the Archean Napier Complex, East Antarctica. *American Mineralogist*, 86(7-8), 932-938.
- Hözl, S. (1991). Geochronology of the Sri Lankan basement. *Summary of Research of the German-Sri Lankan Consortium*, 237-257.
- Hözl, S., Hofmann, A. W., Todt, W., & Köhler, H. (1994). U-Pb geochronology of the Sri Lankan basement. *Precambrian Research*, 66(1-4), 123-149.
- Huang, R., & Audétat, A. (2012). The titanium-in-quartz (TitaniQ) thermobarometer: A critical examination and re-calibration. *Geochimica et Cosmochimica Acta*, 84, 75-89.
- Humphreys, F. J., & Heatherly, M. (1995). *Recrystallization and Related Phenomena*, Bergama, Turkey.
- Hunter, R. H. (1987). Textural equilibrium in layered igneous rocks. In *Origins of igneous layering* (pp. 473-503). Springer, Dordrecht.
- Hunter, N. J., Hasalová, P., Weinberg, R. F., & Wilson, C. J. (2016). Fabric controls on strain accommodation in naturally deformed mylonites: The influence of interconnected micaceous layers. *Journal of Structural Geology*, 83, 180-193.
- Hunter, N. J., Weinberg, R. F., Wilson, C. J. L., Luzin, V., & Misra, S. (2019). Quartz deformation across interlayered monomineralic and polymineralic rocks: A comparative analysis. *Journal of Structural Geology*, 119, 118-134.
- Jayawardena, D. D. S., & Carswell, D. A. (1976). The geochemistry of 'charnockites' and their constituent ferromagnesian minerals from the Precambrian of south-east Sri Lanka (Ceylon). *Mineralogical Magazine*, 40(314), 541-554.
- Jessell, M. W. (1987). Grain-boundary migration microstructures in a naturally deformed quartzite. *Journal of Structural Geology*, 9(8), 1007-1014.
- Jiang, Z., Prior, D. J., & Wheeler, J. (2000). Albite crystallographic preferred orientation and grain misorientation distribution in a low-grade mylonite: implications for granular flow. *Journal of Structural Geology*, 22(11-12), 1663-1674.
- Jiao, S., & Guo, J. (2011). Application of the two-feldspar geothermometer to ultrahigh-temperature (UHT) rocks in the Khondalite belt, North China craton and its implications. *American Mineralogist*, 96(2-3), 250-260.

- Kamb, B. (1972). Experimental recrystallization of ice under stress. *Washington DC American Geophysical Union Geophysical Monograph Series*, 16, 211-241.
- Mary, H., & Brouhard, G. J. (2019). Kappa (κ): Analysis of Curvature in Biological Image Data using B-splines. *BioRxiv*, 852772.
- Kehelpannala, K. V. W. (1991). Structural evolution of high-grade terrains in Sri Lanka with special reference to the areas around Dodangaslanda and Kandy. *The crystalline crust of Sri Lanka, Part I, Summary of Research of the German-Sri Lankan Consortium. Geol. Surv. Dept. Sri Lanka, Prof. Paper*, 5, 69-88.
- Kehelpannala, K. W. (1993). *Structural evolution in the area surrounding the Kahatagaha-Kolongaha graphite mines, North-Northwest of Kandy, and the origin of vein graphite of Sri Lanka* (Doctoral dissertation, Johannes Gutenberg-Universität Mainz).
- Kehelpannala, K. W. (1997). Deformation of a high-grade Gondwana fragment, Sri Lanka. *Gondwana Research*, 1(1), 47-68.
- Kehelpannala, K. W. (2004). Arc accretion around Sri Lanka during the assembly of Gondwana. *Gondwana Research*, 7(4S), 41-46.
- Kehelpannala, K. W., & Ranaweera, L. (2007). Structural and Kinematic Evolution of a Possible PanéAfrican Suture Zone in Sri Lanka.
- Kehelpannala, K. W. (2016). Strongly deformed and mylonitized granulites of the Highland Complex of Sri Lanka along its boundary with the Wannu Complex. In *Geological Structures along the Wannu and Highland Complex boundary, Central Sri Lanka*, Guide Book on Field Geology Workshop 20-21, August 2016. Malaviarachchi, S.P.K. (ed.) Special Publication 11, Geological Society of Sri Lanka, 21-49.
- Kilian, R., Heilbronner, R., & Stünitz, H. (2011). Quartz grain size reduction in a granitoid rock and the transition from dislocation to diffusion creep. *Journal of Structural Geology*, 33(8), 1265-1284.
- Kleinschrodt, R., Voll, G., & Kehelpannala, W. (1991). A layered basic intrusion, deformed and metamorphosed in granulite facies of the Sri Lanka basement. *Geologische Rundschau*, 80(3), 779-800.
- Kleinschrodt, R. (1994). Large-scale thrusting in the lower crustal basement of Sri Lanka. *Precambrian Research*, 66(1-4), 39-57.
- Kleinschrodt, R., & Voll, G. (1994). Deformation and metamorphic evolution of a large-scale fold in the lower crust: the Dumbara synform, Sri Lanka. *Journal of Structural Geology*, 16(11), 1495-1507.
- Kleinschrodt, R., & McGrew, A. (2000). Garnet plasticity in the lower continental crust: implications for deformation mechanisms based on microstructures and SEM-electron channeling pattern analysis. *Journal of Structural Geology*, 22(6), 795-809.
- Kleinschrodt, R., & Duyster, J. P. (2002). HT-deformation of garnet: an EBSD study on granulites from Sri Lanka, India and the Ivrea Zone. *Journal of Structural Geology*, 24(11), 1829-1844.
- Kroll, H., Evangelakakis, C., & Voll, G. (1993). Two-feldspar geothermometry: a review and revision for slowly cooled rocks. *Contributions to Mineralogy and Petrology*, 114(4), 510-518.
- Kronenberg, A. K., & Wolf, G. H. (1990). Fourier transform infrared spectroscopy determinations of intragranular water content in quartz-bearing rocks: implications for hydrolytic weakening in the laboratory and within the earth. *Tectonophysics*, 172(3-4), 255-271.

- Kröner, A. (1991). Lithotectonic subdivision of the Precambrian basement in Sri Lanka. In *The Crystalline Crust of Sri Lanka, Part I. Summary and Research of the German-Sri Lanka Consortium. Geological Survey Department, Sri Lanka, Professional Paper, 5*, 5-21.
- Kröner, A., & Williams, I. S. (1993). Age of metamorphism in the high-grade rocks of Sri Lanka. *The journal of geology*, *101*(4), 513-521.
- Kröner, A., Jaeckel, P., & Williams, I. S. (1994). Pb-loss patterns in zircons from a high-grade metamorphic terrain as revealed by different dating methods: U-Pb and Pb-Pb ages for igneous and metamorphic zircons from northern Sri Lanka. *Precambrian Research*, *66*(1-4), 151-181.
- Kröner, A., Kehelpannala, K. V. W., & Hegner, E. (2003). Ca. 750–1100 Ma magmatic events and Grenville-age deformation in Sri Lanka: relevance for Rodinia supercontinent formation and dispersal, and Gondwana amalgamation. *Journal of Asian Earth Sciences*, *22*(3), 279-300.
- Kröner, A., Rojas-Agramonte, Y., Kehelpannala, K. V. W., Zack, T., Hegner, E., Geng, H. Y., ... & Barth, M. (2013). Age, Nd-Hf isotopes, and geochemistry of the Vijayan Complex of eastern and southern Sri Lanka: a Grenville-age magmatic arc of unknown derivation. *Precambrian Research*, *234*, 288-321.
- Kruhl, J. H. (1996). Prism-and basal-plane parallel subgrain boundaries in quartz: A microstructural geothermobarometer. *Journal of metamorphic Geology*, *14*(5), 581-589.
- Kruhl, J. H. (2001). Crystallographic control on the development of foam textures in quartz, plagioclase and analogue material. *International Journal of Earth Sciences*, *90*(1), 104-117.
- Kruhl, J. H., & Peternell, M. (2002). The equilibration of high-angle grain boundaries in dynamically recrystallized quartz: the effect of crystallography and temperature. *Journal of Structural geology*, *24*(6-7), 1125-1137.
- Kruse, R., Stünitz, H., & Kunze, K. (2001). Dynamic recrystallization processes in plagioclase porphyroclasts. *Journal of Structural Geology*, *23*(11), 1781-1802.
- Lafrance, B., John, B. E., & Frost, B. R. (1998). Ultra high-temperature and subsolidus shear zones: examples from the Poe Mountain anorthosite, Wyoming. *Journal of Structural Geology*, *20*(7), 945-955.
- Lapworth, T., Wheeler, J., & Prior, D. J. (2002). The deformation of plagioclase investigated using electron backscatter diffraction crystallographic preferred orientation data. *Journal of Structural Geology*, *24*(2), 387-399.
- Linckens, J., Herwegh, M., Müntener, O., & Mercolli, I. (2011). Evolution of a polymineralic mantle shear zone and the role of second phases in the localization of deformation. *Journal of Geophysical Research: Solid Earth*, *116*(B6).
- Lister, G. S., Paterson, M. S., & Hobbs, B. E. (1978). The simulation of fabric development in plastic deformation and its application to quartzite: the model. *Tectonophysics*, *45*(2-3), 107-158.
- Lister, G. S., & Dornsiepen, U. F. (1982). Fabric transitions in the Saxony granulite terrain. *Journal of Structural Geology*, *4*(1), 81-92.
- Little, T. A., Hacker, B. R., Brownlee, S. J., & Seward, G. (2013). Microstructures and quartz lattice-preferred orientations in the eclogite-bearing migmatitic gneisses of the D'Entrecasteaux Islands, Papua New Guinea. *Geochemistry, Geophysics, Geosystems*, *14*(6), 2030-2062.
- Liu, M., & Yund, R. A. (1992). NaSi-CaAl interdiffusion in plagioclase. *American Mineralogist*, *77*(3-4), 275-283.

- Lloyd, G. E., Farmer, A. B., & Mainprice, D. (1997). Misorientation analysis and the formation and orientation of subgrain and grain boundaries. *Tectonophysics*, 279(1-4), 55-78.
- Lloyd, G. E. (2004). Microstructural evolution in a mylonitic quartz simple shear zone: the significant roles of dauphine twinning and misorientation. *Geological Society, London, Special Publications*, 224(1), 39-61.
- Mainprice, D., Bouchez, J. L., Blumenfeld, P., & Tubià, J. M. (1986). Dominant c slip in naturally deformed quartz: Implications for dramatic plastic softening at high temperature. *Geology*, 14(10), 819-822.
- Malaviarachchi, S. P. (2018). Review on age of magmatism and crust formation in Sri Lanka: U-Pb and Lu-Hf isotopic perspectives. *Journal of the Indian Institute of Science*, 98(4), 417-427.
- Marshall, D. B., & McLaren, A. C. (1977a). The direct observation and analysis of dislocations in experimentally deformed plagioclase feldspars. *Journal of Materials Science*, 12(5), 893-903.
- Marshall, D. B., & McLaren, A. C. (1977b). Deformation mechanisms in experimentally deformed plagioclase feldspars. *Physics and chemistry of minerals*, 1(4), 351-370.
- Martelat, J. E., Schulmann, K., Lardeaux, J. M., Nicollet, C., & Cardon, H. (1999). Granulite microfabrics and deformation mechanisms in southern Madagascar. *Journal of Structural Geology*, 21(6), 671-687.
- McCaig, A., Covey-Crump, S. J., Ismaïl, W. B., & Lloyd, G. E. (2007). Fast diffusion along mobile grain boundaries in calcite. *Contributions to Mineralogy and Petrology*, 153(2), 159-175.
- Menegon, L., Piazzolo, S., & Pennacchioni, G. (2011a). The effect of Dauphiné twinning on plastic strain in quartz. *Contributions to Mineralogy and Petrology*, 161(4), 635-652.
- Menegon, L., Nasipuri, P., Stünitz, H., Behrens, H., & Ravna, E. (2011b). Dry and strong quartz during deformation of the lower crust in the presence of melt. *Journal of Geophysical Research: Solid Earth*, 116(B10).
- Menegon, L., Stünitz, H., Nasipuri, P., Heilbronner, R., & Svahnberg, H. (2013). Transition from fracturing to viscous flow in granulite facies perthitic feldspar (Lofoten, Norway). *Journal of Structural Geology*, 48, 95-112.
- Milisenda, C. C., Liew, T. C., Hofmann, A. W., & Kröner, A. (1988). Isotopic mapping of age provinces in Precambrian high-grade terrains: Sri Lanka. *The Journal of Geology*, 96(5), 608-615.
- Milisenda, C. C., Liew, T. C., Hofmann, A. W., & Köhler, H. (1994). Nd isotopic mapping of the Sri Lanka basement: update, and additional constraints from Sr isotopes. *Precambrian Research*, 66(1-4), 95-110.
- Minor, A., Rybacki, E., Sintubin, M., Vogel, S., & Wenk, H. R. (2018). Tracking mechanical Dauphiné twin evolution with applied stress in axial compression experiments on a low-grade metamorphic quartzite. *Journal of Structural Geology*, 112, 81-94.
- Miranda, E. A., Hirth, G., & John, B. E. (2016). Microstructural evidence for the transition from dislocation creep to dislocation-accommodated grain boundary sliding in naturally deformed plagioclase. *Journal of Structural Geology*, 92, 30-45.
- Montardi, Y., & Mainprice, D. (1987). A transmission electron microscopic study of natural plastic deformation of calcic plagioclases (An 68-70). *Bulletin de minéralogie*, 110(1), 1-14.

- Muto, J., Hirth, G., Heilbronner, R., & Tullis, J. (2011). Plastic anisotropy and fabric evolution in sheared and recrystallized quartz single crystals. *Journal of Geophysical Research: Solid Earth*, 116(B2).
- Nachlas, W. O., Whitney, D. L., Teyssier, C., Bagley, B., & Mulch, A. (2014). Titanium concentration in quartz as a record of multiple deformation mechanisms in an extensional shear zone. *Geochemistry, Geophysics, Geosystems*, 15(4), 1374-1397.
- Nachlas, W. O., Thomas, J. B., & Hirth, G. (2018). TitaniQ deformed: Experimental deformation of out-of-equilibrium quartz porphyroclasts. *Journal of Structural Geology*, 116, 207-222.
- Neumann, B. (2000). Texture development of recrystallised quartz polycrystals unravelled by orientation and misorientation characteristics. *Journal of Structural Geology*, 22(11-12), 1695-1711.
- Nicolas, A., & Poirier, J. P. (1976). Crystalline plasticity and solid state flow in metamorphic rocks.
- Nishikawa, S. & Kikuchi, S. (1928). "The diffraction of cathode rays by calcite". *Proc. Imperial Acad. Jpn.*, 4, 475-477.
- Osanai, Y., Sajeev, K., Nakano, N., Kitano, I., Kehelpannala, W. K., Kato, R., ... & Malaviarachchi, S. P. (2016a). UHT granulites of the Highland Complex, Sri Lanka I: Geological and petrological background. *Journal of Mineralogical and Petrological Sciences*, 111(3), 145-156.
- Osanai, Y., Sajeev, K., Nakano, N., Kitano, I., Kehelpannala, W. K., Kato, R., ... & Malaviarachchi, S. P. (2016b). UHT granulites of the Highland Complex, Sri Lanka II: geochronological constraints and implications for Gondwana correlation. *Journal of Mineralogical and Petrological Sciences*, 111(3), 157-169.
- Panozzo, R., & Hurlimann, H. (1983). A simple method for the quantitative discrimination of convex and convex-concave lines. *Microscopica Acta*, 87(2), 169-176.
- Passchier, C. W., & Trouw, R. A. (2005). *Microtectonics*. Springer Science & Business Media.
- Pennacchioni, G., Menegon, L., Leiss, B., Nestola, F., & Bromiley, G. (2010). Development of crystallographic preferred orientation and microstructure during plastic deformation of natural coarse-grained quartz veins. *Journal of Geophysical Research: Solid Earth*, 115(B12).
- Phillips, M. W., Colville, A. A., & Ribbe, P. H. (1971). The crystal structures of two oligoclases: A comparison with low and high albite. *Zeitschrift für Kristallographie-Crystalline Materials*, 133(1-6), 43-65.
- Piazolo, S., Prior, D. J., & Holness, M. D. (2005). The use of combined cathodoluminescence and EBSD analysis: a case study investigating grain boundary migration mechanisms in quartz. *Journal of Microscopy*, 217(2), 152-161.
- Piazolo, S., Bestmann, M., Prior, D. J., & Spiers, C. J. (2006). Temperature dependent grain boundary migration in deformed-then-annealed material: observations from experimentally deformed synthetic rocksalt. *Tectonophysics*, 427(1-4), 55-71.
- Pilugin, S. M., Fonarev, V. I., & Savko, K. A. (2009, March). Feldspar thermometry of ultrahigh-temperature ($\geq 1000^\circ\text{C}$) metapelites from the voronezh crystalline massif (Kursk-Besedino Granulite Block). In *Doklady Earth Sciences* (Vol. 425, No. 1, p. 201). Springer Nature BV.
- Platt, J. P., & Behr, W. M. (2011). Grainsize evolution in ductile shear zones: Implications for strain localization and the strength of the lithosphere. *Journal of Structural Geology*, 33(4), 537-550.

- Prior, D. J. (1999a). Problems in determining the misorientation axes, for small angular misorientations, using electron backscatter diffraction in the SEM. *Journal of Microscopy*, 195(3), 217-225.
- Prior, D. J., Boyle, A. P., Brenker, F., Cheadle, M. C., Day, A., Lopez, G., ... & Zetterstrom, L. (1999b). The application of electron backscatter diffraction and orientation contrast imaging in the SEM to textural problems in rocks. *American Mineralogist*, 84(11-12), 1741-1759.
- Prior, D. J., Wheeler, J., Peruzzo, L., Spiess, R., & Storey, C. (2002). Some garnet microstructures: an illustration of the potential of orientation maps and misorientation analysis in microstructural studies. *Journal of Structural Geology*, 24(6-7), 999-1011.
- Raase, P., & Schenk, V. (1994). Petrology of granulite-facies metapelites of the Highland Complex, Sri Lanka: implications for the metamorphic zonation and the PT path. *Precambrian research*, 66(1-4), 265-294.
- Raase, P. (1998). Feldspar thermometry; a valuable tool for deciphering the thermal history of granulite-facies rocks, as illustrated with metapelites from Sri Lanka. *The Canadian Mineralogist*, 36(1), 67-86.
- Ranalli, G. (2000). Rheology of the crust and its role in tectonic reactivation. *Journal of geodynamics*, 30(1-2), 3-15.
- Ranaweera, L. V., & Kehelpannala, K. W. (2019). Mesoscopic to microcopic structures associated with the Wannu Complex/Highland Complex Boundary Shear Zone in Sri Lanka. *Journal of the Geological Society of Sri Lanka*, 20(2).
- Reddy, S. M., & Buchan, C. (2005). Constraining kinematic rotation axes in high-strain zones: a potential microstructural method?. *Geological Society, London, Special Publications*, 243(1), 1-10.
- Riegger, O. K., & Van Vlack, L. (1960). Dihedral angle measurement: Metallurgical Society of the American Institute of Metallurgical Engineers Transactions, v. 218.
- Rosenberg, C. L., & Stünitz, H. (2003). Deformation and recrystallization of plagioclase along a temperature gradient: an example from the Bergell tonalite. *Journal of Structural Geology*, 25(3), 389-408.
- Rybacki, E., & Dresen, G. (2004). Deformation mechanism maps for feldspar rocks. *Tectonophysics*, 382(3-4), 173-187.
- Sajeev, K., Williams, I. S., & Osanai, Y. (2010). Sensitive high-resolution ion microprobe U-Pb dating of prograde and retrograde ultrahigh-temperature metamorphism as exemplified by Sri Lankan granulites. *Geology*, 38(11), 971-974.
- Sandiford, M., Powell, R., Martin, S. F., & Perera, L. R. K. (1988). Thermal and baric evolution of garnet granulites from Sri Lanka. *Journal of Metamorphic Geology*, 6(3), 351-364.
- Santosh, M., Tsunogae, T., Malaviarachchi, S. P., Zhang, Z., Ding, H., Tang, L., & Dharmapriya, P. L. (2014). Neoproterozoic crustal evolution in Sri Lanka: Insights from petrologic, geochemical and zircon U-Pb and Lu-Hf isotopic data and implications for Gondwana assembly. *Precambrian Research*, 255, 1-29.
- Scandale, E., Gandais, M., & Willaime, C. (1983). Transmission electron microscopic study of experimentally deformed K-feldspar single crystals. *Physics and Chemistry of Minerals*, 9(3), 182-187.

- Schenk, V., Raase, P., & Schumacher, R. (1988). Very high temperatures and isobaric cooling before tectonic uplift in the Highland Series of Sri Lanka. *Terra Cognita*, 8, 265.
- Schenk, V., Raase, P., & Schumacher, R. (1991). Metamorphic zonation and PT history of the Highland Complex in Sri Lanka. In *The Crystalline Crust of Sri Lanka, Part I. Summary of Research of the German-Sri Lankan Consortium* (Vol. 5, pp. 150-163). Geological Survey Department, Sri Lanka.
- Schindelin, J., Arganda-Carreras, I., Frise, E., Kaynig, V., Longair, M., Pietzsch, T., ... & Cardona, A. (2012). Fiji: an open-source platform for biological-image analysis. *Nature methods*, 9(7), 676-682.
- Schmid, E., & Boas, W. (1950). *Plasticity of crystals*. Hughes & Co, London.
- Schmid, S. M., & Casey, M. (1986). Complete fabric analysis of some commonly observed quartz c-axis patterns. *Geophysical Monograph*, 36(6), 263-286.
- Schulmann, K., Mlčoch, B., & Melka, R. (1996). High-temperature microstructures and rheology of deformed granite, Erzgebirge, Bohemian Massif. *Journal of Structural Geology*, 18(6), 719-733.
- Schumacher, R., Schenk, V., Raase, P., & Vitanage, P. W. (1990). Granulite facies metamorphism of metabasic and intermediate rocks in the Highland Series of Sri Lanka. In *High-temperature metamorphism and crustal anatexis* (pp. 235-271). Springer, Dordrecht.
- Schumacher, R., & Faulhaber, S. (1994). Summary and discussion of PT estimates from garnet-pyroxene-plagioclase-quartz-bearing granulite-facies rocks from Sri Lanka. *Precambrian Research*, 66(1-4), 295-308.
- Seck, H. A. (1971a). Koexistierende alkalifeldspäte und plagioklase im system NaAlSi₃O₈-KAlSi₃O₈-CaAl₂Si₂O₈-H₂O bei temperaturen von 650 C bis 900 C. *Neues Jahrbuch Mineralogie Abhandlungen*, 115, 315-345.
- Seck, H. A. (1971b). Der Einfluß des Drucks auf die Zusammensetzung koexistierender Alkalifeldspäte und Plagioklase im System NaAlSi₃O₈-KAlSi₃O₈-CaAl₂Si₂O₈-H₂O. *Contributions to Mineralogy and Petrology*, 31(1), 67-86.
- Smith, J. V. (1974). Feldspar Minerals. Volume 1. Crystal structure and physical properties, 625 p. *Springer-Verlag*, Berlin.
- Stipp, M., Stünitz, H., Heilbronner, R., & Schmid, S. M. (2002a). Dynamic recrystallization of quartz: correlation between natural and experimental conditions. *Geological Society, London, Special Publications*, 200(1), 171-190.
- Stipp, M., Stünitz, H., Heilbronner, R., & Schmid, S. M. (2002b). The eastern Tonale fault zone: a 'natural laboratory' for crystal plastic deformation of quartz over a temperature range from 250 to 700 C. *Journal of structural geology*, 24(12), 1861-1884.
- Stipp, M., Tullis, J., Scherwath, M., & Behrmann, J. H. (2010). A new perspective on paleopiezometry: Dynamically recrystallized grain size distributions indicate mechanism changes. *Geology*, 38(8), 759-762.
- Stöckhert, B., & Duyster, J. (1999). Discontinuous grain growth in recrystallised vein quartz—implications for grain boundary structure, grain boundary mobility, crystallographic preferred orientation, and stress history. *Journal of Structural Geology*, 21(10), 1477-1490.
- Stojakovic, D. (2012). Electron backscatter diffraction in materials characterization. *Processing and application of ceramics*, 6(1), 1-13.

- Stünitz, H., Gerald, J. F., & Tullis, J. (2003). Dislocation generation, slip systems, and dynamic recrystallization in experimentally deformed plagioclase single crystals. *Tectonophysics*, 372(3-4), 215-233.
- Svahnberg, H., & Piazzolo, S. (2010). The initiation of strain localisation in plagioclase-rich rocks: Insights from detailed microstructural analyses. *Journal of Structural Geology*, 32(10), 1404-1416.
- Takamura, Y., Tsunogae, T., Santosh, M., Malaviarachchi, S. P., & Tsutsumi, Y. (2015). Petrology and zircon U–Pb geochronology of metagabbro from the Highland Complex, Sri Lanka: implications for the correlation of Gondwana suture zones. *Journal of Asian Earth Sciences*, 113, 826-841.
- Takamura, Y., Tsunogae, T., Santosh, M., Malaviarachchi, S. P., & Tsutsumi, Y. (2016). U–Pb geochronology of detrital zircon in metasediments from Sri Lanka: Implications for the regional correlation of Gondwana fragments. *Precambrian Research*, 281, 434-452.
- Tholen, S. (2015). Der Einfluss der dynamischen Rekristallisation auf das Titan-in-Quarz-Geothermometer: Eine Fallstudie anhand unterschiedlicher Quarz-Mikrostrukturen in Metapeliten des Val Cannobina, nördliche Ivrea-Verbano-Zone. *Unpublished Master Thesis, University of Cologne*
- Thor, N. (2019). Rheology of Quartz-Feldspar Rocks: EBSD and EDX-Based Investigations in Lower Crustal Granulites. *Unpublished Master Thesis, University of Cologne*.
- Thomas, J. B., Watson, E. B., Spear, F. S., Shemella, P. T., Nayak, S. K., & Lanzirrotti, A. (2010). TitaniQ under pressure: the effect of pressure and temperature on the solubility of Ti in quartz. *Contributions to Mineralogy and Petrology*, 160(5), 743-759.
- Thomas, J. B., Watson, E. B., Spear, F. S., & Wark, D. A. (2015). TitaniQ recrystallized: experimental confirmation of the original Ti-in-quartz calibrations. *Contributions to Mineralogy and Petrology*, 169(3), 27.
- Tullis, J. (1970). Quartz: preferred orientation in rocks produced by Dauphiné twinning. *Science*, 168(3937), 1342-1344.
- Tullis, J. (1983). Deformation of feldspar. *Rev. Mineral.*, 2, 297-323.
- Tullis, J., & Yund, R. A. (1985). Dynamic recrystallization of feldspar: A mechanism for ductile shear zone formation. *Geology*, 13(4), 238-241.
- Tullis, J., & Yund, R. A. (1989). Hydrolytic weakening of quartz aggregates: The effects of water and pressure on recovery. *Geophysical Research Letters*, 16(11), 1343-1346.
- Tullis, J., & Yund, R. A. (1991). Diffusion creep in feldspar aggregates: experimental evidence. *Journal of Structural Geology*, 13(9), 987-1000.
- Tullis, J., & Yund, R. (1992). The brittle-ductile transition in feldspar aggregates: An experimental study. In *International geophysics* (Vol. 51, pp. 89-117). Academic press.
- Tullis, J. (2002). Deformation of granitic rocks: experimental studies and natural examples. *Reviews in Mineralogy and Geochemistry*, 51(1), 51-95.
- Urai, J. L., Means, W. D., & Lister, G. S. (1986). Dynamic recrystallization of minerals. In *Mineral and rock deformation: laboratory studies* (Vol. 36, pp. 161-199). Washington, DC: AGU.
- Vitanage, P. W. (1985). Tectonics and mineralization in Sri Lanka.
- Voll, G. (1969). Klastische Mineralien aus Sedimentgesteinen der schottischen Highlands und ihr Schicksal bei aufsteigender Regional-und Kontaktmetamorphose. *Habil. Schr., Tech. Univ. Berlin*.

- Voll, G., & Kleinschrodt, R. (1991). Sri Lanka: structural, magmatic and metamorphic development of a Gondwana fragment. In *The Crystalline Crust of Sri Lanka, Part I. Summary of Research of the German-Sri Lankan Consortium* (Vol. 5, pp. 22-51). Geological Survey Department, Sri Lanka, Professional Paper 5.
- Voll, G., Evangelakakis, C., & Kroll, H. (1994). Revised two-feldspar geothermometry applied to Sri Lankan feldspars. *Precambrian Research*, 66(1-4), 351-377.
- Wark, D. A., & Watson, E. B. (2006). TitaniQ: a titanium-in-quartz geothermometer. *Contributions to Mineralogy and Petrology*, 152(6), 743-754.
- Wen, S., & Nekvasil, H. (1994). SOLVALC: An interactive graphics program package for calculating the ternary feldspar solvus and for two-feldspar geothermometry. *Computers & Geosciences*, 20(6), 1025-1040.
- Wenk, H. R., Bortolotti, M., Barton, N., Oliver, E., & Brown, D. (2007). Dauphiné twinning and texture memory in polycrystalline quartz. *Physics and Chemistry of Minerals*, 34(9), 599-607.
- Wheeler, J., Prior, D., Jiang, Z., Spiess, R., & Trimby, P. (2001). The petrological significance of misorientations between grains. *Contributions to mineralogy and petrology*, 141(1), 109-124.
- Wijeratne, A. M. G. K., & Malaviarachchi, S. P. K. (2017). Preliminary geochemistry of Pottuvil Charnockites, Sri Lanka. *J Geol Soc Sri Lanka*, 18, 101-113.
- Willaime, C., Christie, J., & Kovacs, M. P. (1979). Experimental deformation of K-feldspar single crystals. *Bulletin de Mineralogie*, 102(2), 168-177.
- Yoshida, M., Kehelpannala, K. V. W., Hiroi, Y., & Vitanage, P. W. (1990). Sequence of deformation and metamorphism of granulites of Sri Lanka. *J Geosci, Osaka City Univ*, 33, 69-107.
- Yund, R. A. (1986). Interdiffusion of NaSi—CaAl in peristerite. *Physics and Chemistry of Minerals*, 13(1), 11-16.
- Yund, R. A., & Tullis, J. (1991). Compositional changes of minerals associated with dynamic recrystallization. *Contributions to Mineralogy and Petrology*, 108(3), 346-355.
- Zhanga, X., Harkness, R. M., & Last, N. C. (1992). Evaluation of connectivity characteristics of naturally jointed rock masses. *Engineering geology*, 33(1), 11-30.

Appendix

Appendix Table 1: Feldspar compositions and results of the Two-Feldspar geothermometry (calculated feldspar compositions after the method of Kroll et al., 1993; AP: antiperthite; SP: string/ spindle perthite).

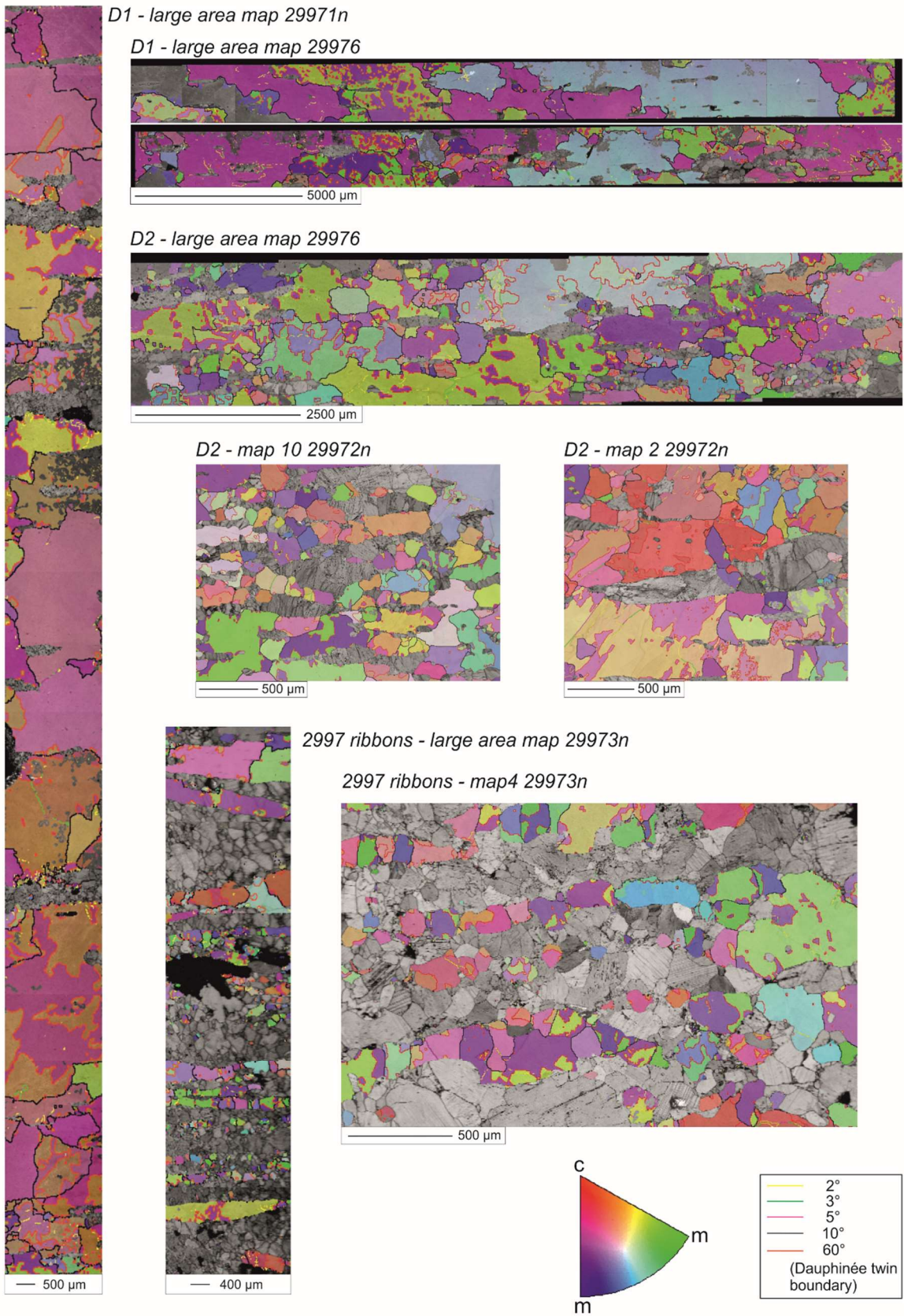
Sample	Fsp	Composition analyzed			Composition calculated			T (°C)
		Ab	Or	An	Ab	Or	An	
Quartz dominated domain								
<i>D1 A</i>								
N3P1	kfs	27.4	70.4	2.2	35.0	62.8	2.2	811
	pl	84.7	1.1	14.2	73.0	12.8	14.2	
N3P2	kfs	18.7	79.9	1.5	30.7	67.8	1.5	760
	pl	85.2	0.7	14.1	75.9	10.0	14.1	
N3P3	kfs	20.7	77.6	1.7	32.4	65.9	1.7	781
	pl	84.9	0.9	14.2	74.7	11.0	14.2	
N4P4	kfs	29.7	68.1	2.2	34.1	63.7	2.2	807
	pl	84.3	1.0	14.7	73.0	12.3	14.7	
N4P5	kfs	19.2	79.4	1.4	30.2	68.4	1.4	755
	pl	85.0	0.8	14.2	76.1	9.7	14.2	
N5P6	kfs	31.6	66.0	2.3	35.5	62.1	2.3	817
	pl	84.9	1.0	14.1	72.8	13.1	14.1	
N5P7	kfs	13.5	85.5	1.0	26.8	72.2	1.0	718
	pl	84.7	0.7	14.7	77.4	7.9	14.7	
N5P8	kfs	22.2	76.3	1.5	29.4	69.1	1.5	756
	pl	84.0	0.8	15.2	75.3	9.5	15.2	
N5P9	kfs	28.6	69.2	2.2	34.5	63.3	2.2	809
	pl	84.8	0.7	14.5	73.0	12.5	14.5	
N5P10	kfs	20.2	78.8	1.0	27.5	71.6	1.0	716
	pl	85.4	1.1	13.5	78.4	8.2	13.5	
mean	kfs	23.2	75.1	1.7	31.6	66.7	1.7	773 ± 36
	pl	84.8	0.9	14.3	75.0	10.7	14.3	
<i>D1L</i>								
P1	kfs	7.6	92.3	0.1	16.7	83.2	0.1	<u>579</u>
	pl	86.1	1.0	12.9	83.2	3.9	12.9	
P2	kfs	8.7	90.8	0.5	23.4	76.1	0.5	655
	pl	87.6	0.6	11.8	82.0	6.2	11.8	
P3	kfs	6.4	93.4	0.1	15.5	84.4	0.1	<u>565</u>
	pl	86.9	1.0	12.2	83.9	3.9	12.2	
P4	kfs	6.6	93.1	0.4	18.5	81.2	0.4	602
	pl	85.9	0.7	13.3	82.3	4.4	13.3	
P5	kfs	8.9	90.3	0.8	26.2	73.1	0.8	694
	pl	86.8	0.7	12.5	80.0	7.5	12.5	
P6	kfs	7.4	92.5	0.1	19.3	80.6	0.1	<u>577</u>
	pl	91.4	0.6	8.0	87.8	4.2	8.0	
P7	kfs	7.2	92.4	0.5	21.0	78.5	0.5	634
	pl	86.4	0.6	12.9	81.7	5.3	12.9	
P8	kfs	8.3	91.4	0.3	17.3	82.4	0.3	584
	pl	85.9	1.0	13.1	83.0	4.0	13.1	
mean	kfs	7.6	92.0	0.3	19.7	79.9	0.3	611 ± 42
	pl	87.1	0.8	12.1	83.0	4.9	12.1	
AP					77.8	12.8	9.5	
Feldspar dominated domain								

<i>kfs-rich</i>								
<i>(D3)</i>								
G1/ P1	kfs	12.9	86.7	0.4	18.4	81.1	0.4	611
	pl	84.0	0.9	15.0	80.6	4.4	15.0	
G2/ P2	kfs rim	15.8	83.6	0.6	21.1	78.3	0.6	646
	pl	84.2	1.1	14.8	79.8	5.4	14.8	
G2/ P2.2	kfs rim	11.6	87.7	0.6	21.3	78.1	0.6	654
	pl	83.6	0.7	15.6	78.8	5.5	15.6	
G4/ P4	kfs rim	13.9	85.6	0.4	18.4	81.2	0.4	611
	pl	83.9	0.9	15.2	80.4	4.4	15.2	
G5/ P5	kfs rim	14.6	84.8	0.7	22.3	77.0	0.7	664
	pl1	84.2	0.8	15.0	79.0	5.9	15.0	
G6/ P8	kfs	16.6	82.6	0.8	23.5	75.8	0.8	678
	pl	83.9	1.2	14.9	78.7	6.4	14.9	
G7/ P9	kfs	19.7	79.5	0.8	22.9	76.3	0.8	677
	pl	83.4	0.9	15.7	78.0	6.2	15.7	
G8/ P10	kfs	10.5	89.1	0.4	16.8	82.8	0.4	592
	pl	83.3	0.8	15.9	80.3	3.8	15.9	
G9/ P11	kfs	12.4	87.0	0.5	19.6	79.9	0.5	633
	pl	83.5	0.6	15.9	79.2	4.9	15.9	
G11/ P13	kfs	15.4	84.2	0.4	18.3	81.3	0.4	607
	pl	84.3	1.1	14.6	81.1	4.4	14.6	
mean	kfs	14.6	84.9	0.6	19.9	79.5	0.6	637 ± 28
	pl	83.8	0.9	15.3	79.6	5.1	15.3	
SP								
		14.0	85.4	0.6	20.8	78.6	0.6	
				21.4	77.0	1.6		
<i>D4</i>								
N1P1	kfs	14.9	84.7	0.5	18.8	80.7	0.5	619
	pl	83.5	1.1	15.4	80.0	4.6	15.4	
N1P2	kfs	17.6	81.1	1.3	27.7	71.1	1.3	737
	pl	83.5	0.9	15.5	75.9	8.5	15.5	
N1P3	kfs	13.7	85.9	0.4	18.0	81.6	0.4	608
	pl	83.6	1.0	15.4	80.3	4.3	15.4	
N1P4	kfs	19.5	79.3	1.2	27.1	71.6	1.2	732
	pl	83.0	1.2	15.8	75.9	8.3	15.8	
N1P5	kfs	19.5	79.6	0.9	24.5	74.7	0.9	693
	pl	84.0	0.9	15.1	78.0	6.9	15.1	
N2P6	kfs	22.9	75.6	1.5	29.5	69.0	1.5	759
	pl	83.7	0.8	15.5	75.0	9.5	15.5	
N2P7	kfs	22.1	76.3	1.6	29.9	68.5	1.6	763
	pl	83.7	0.9	15.4	74.9	9.8	15.4	
N2P8	kfs	23.4	75.4	1.2	27.2	71.6	1.2	730
	pl	83.7	0.9	15.4	76.4	8.3	15.4	
N2P9	kfs	19.4	79.3	1.2	28.1	70.7	1.2	737
	pl	83.9	1.2	15.0	76.4	8.7	15.0	
N2P10	kfs	21.3	77.2	1.4	29.4	69.2	1.4	753
	pl	84.1	0.9	15.0	75.6	9.4	15.0	
mean	kfs	19.4	79.4	1.1	26.0	72.9	1.1	713 ± 53
	pl	83.7	1.0	15.4	76.8	7.8	15.4	
<i>BL</i>								
P1	kfs	23.7	74.5	1.9	30.8	67.3	1.9	782
	pl	82.7	1.2	16.1	73.4	10.5	16.1	
P2	kfs	22.5	76.1	1.4	28.2	70.3	1.4	749

P3	pl	82.9	1.0	16.1	75.0	8.9	16.1	691
	kfs	16.5	82.6	0.9	23.8	75.3	0.9	
P4	pl	83.1	0.9	16.0	77.3	6.7	16.0	666
	kfs	14.8	84.5	0.7	21.7	77.6	0.7	
P5	pl	82.3	1.2	16.4	77.8	5.8	16.4	666
	kfs	12.6	86.7	0.7	21.9	77.3	0.7	
P6	pl	83.0	1.0	16.0	78.1	5.8	16.0	739
	kfs	23.1	75.6	1.3	28.1	70.6	1.3	
P7	pl	83.7	1.1	15.2	76.1	8.7	15.2	714
	kfs	21.4	77.6	1.0	26.1	72.9	1.0	
P8	pl	83.4	1.4	15.2	77.1	7.7	15.2	727
	kfs	21.0	77.9	1.1	27.4	71.5	1.1	
P9	pl	84.0	1.2	14.8	76.9	8.3	14.8	736
	kfs	19.1	79.6	1.3	27.0	71.6	1.3	
P10	pl	82.6	1.1	16.3	75.4	8.3	16.3	709
	kfs	22.3	76.6	1.1	24.7	74.2	1.1	
mean	kfs	19.7	79.1	1.2	26.0	72.9	1.2	718 ±
	pl	83.0	1.1	15.9	76.3	7.8	15.9	35

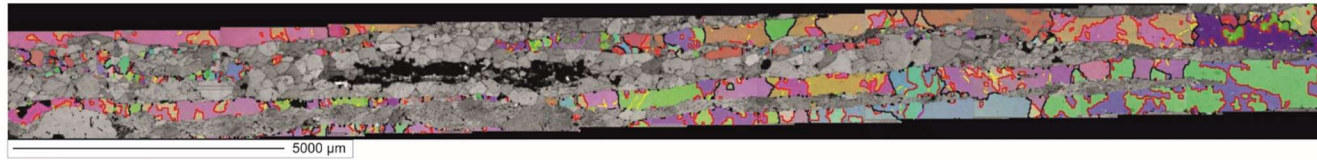
Appendix Table 2: Reintegrated perthite compositions.

String/ Spindle Perthite				Antiperthite			
Sample	Composition			Sample	Composition		
	Ab(kfs)	An(kfs)	Or(kfs)		Ab(pl)	An(pl)	Or(Pl)
G2	24.2	1.6	74.1	AP1	77.6	9.5	12.8
G4	21.4	1.6	77.0	AP2	79.7	9.9	10.4
G5	22.2	1.8	76.0	AP3	80.1	9.6	10.3
G8	18.5	1.2	80.3	AP4	73.4	8.8	17.8
P1	18.9	1.3	79.8				
P2	21.2	2.1	76.7				
P3	23.1	1.8	75.2				

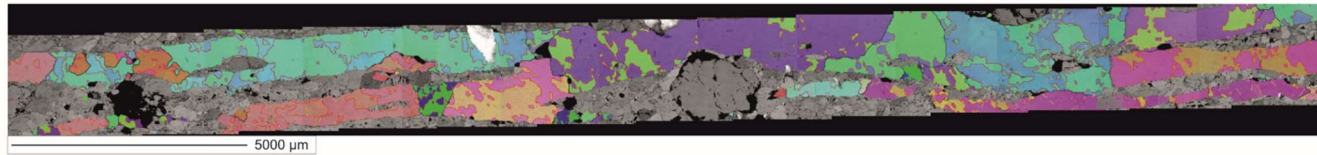


Appendix Fig. 1: EBSD Maps sample 2997 (Qdd) (maps are represented in XZ section with X parallel to the horizontal and Z parallel to the vertical).

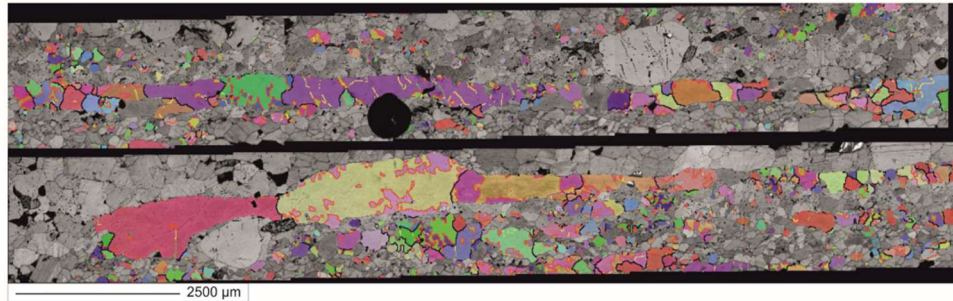
D3 - large area map 30545



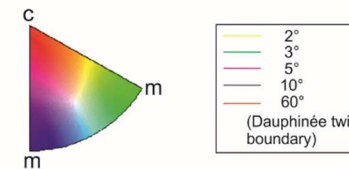
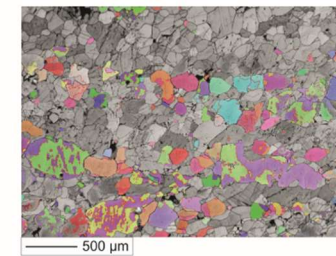
D3 - large area map 30545n



D4 - large area map 30544



Matrix - map2 30544



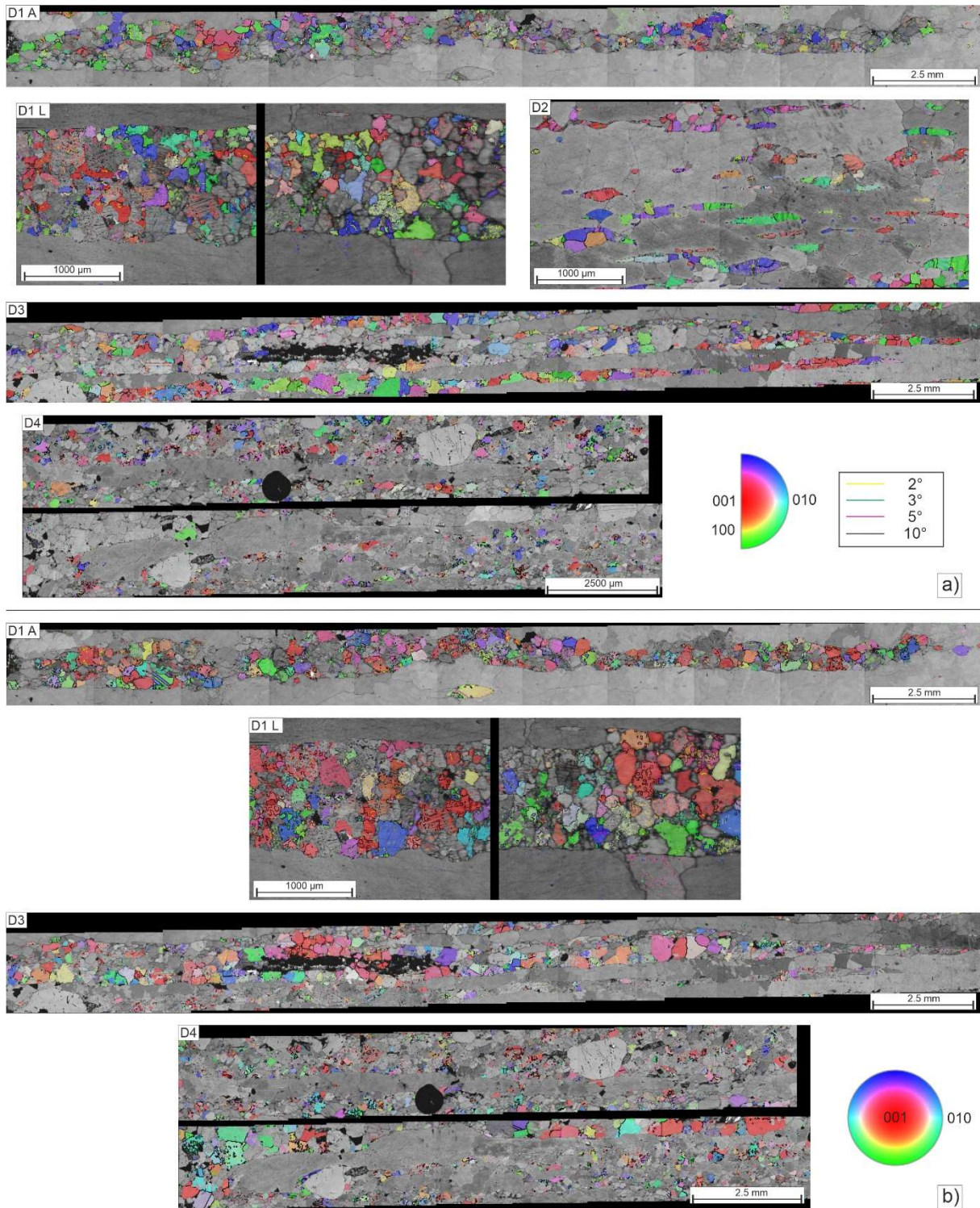
Appendix Fig. 2: EBSD Maps sample 3054 (Fdd) (maps are represented in XZ section with X parallel to the horizontal and Z parallel to the vertical).

Appendix Table 3: Results Boundary Trace Analysis of quartz (R II Ma: coincident rotation and misorientation axis, SP: Slip plane, SD: Slip direction, FII: Foliation subparallel slip plane; in individual cases multiple possible solutions are given).

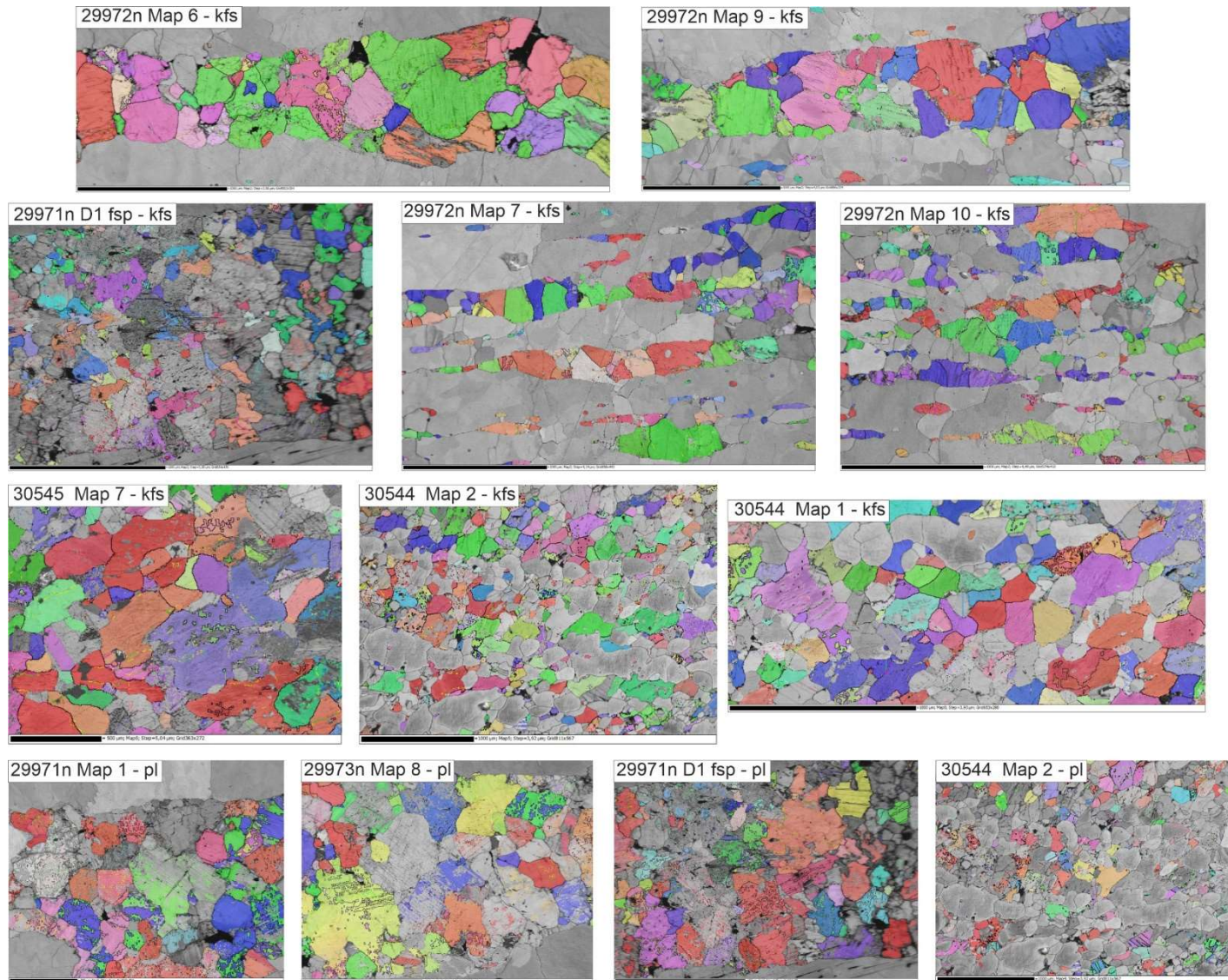
Domain/ Sample	Subset/ Boundary	R II Ma	SP	SD	Slip System	Comment	Category
D1							
Large map 29976	1/ 3	a	m	c	{m}[c]		C
	1/ 4	z	π	a	{ π }<a>	FII	C
	3/ 5	a	m	c	{m}[c]		C
	3/ 9	[20-21], a	r, m	a, a+c	{r}<a>+{m}<a>, {m}<a+c>	twist, combi	C
	b10	z	π	a	{ π }<a>		C
Large map 29971n	3/ 1	r	π'	a	{ π' }<a>	FII	C
	4/ 1	[11-22]	z, r	a	{z}+{r}<a>	twist	C
	4/ 2	a	m	c	{m}[c]	FII	C
	4/ 3	a	m	c	{a}[c]	FII	C
	5/ 3	a	m	c	{m}[c]		C
	5/ 4	m	a	c	{a}[c]	FII	C
	6/ 1	c	m	a	{m}<a>		C
	9/ 1	a	m	c	{m}[c]	FII	C
	10/ 2	z	π	a	{ π }<a>		C
	11/ 1	π'	r	a	{r}<a>	FII	C
	12.1/ 1	c	m	a	{m}<a>		C
	13/ 1	m	a	c	{a}[c]	FII	C
D2							
Large map 29976	1/ 4	z	π'	a	{ π' }<a>		C
	2/ 3	π'	r	a	{r}<a>		C
	2/ 5	π'	r	a	{r}<a>		C
	3/ 2	m	c	a	(c)<a>		C
	9/ 1	r	π'	a	{ π' }<a>		C
	12	π'	r	a	{r}<a>		C
29972 Map2	b1	c	m	a	{m}<a>		C
	b3	m	a	c	{c}<a>	FII	C
	b10	z	π	a	{ π }<a>		C
	b12	c	m	a	{m}<a>		C
	1/ 4	m	a	c	{a}[c]		B
	b4	m	c	a	{c}<a>	FII	B
29972 Map10	b3	[11-22]	r, z	a	{r+z}<a>	Twist	C
	b4	a	m	c	{m}[c]		C
	b6	c	m	a	{m}<a>		C

	b7	π'	r	a	$\{r\}\langle a \rangle$		C
	b10	[11-22]	r, z	a	$\{r+z\}\langle a \rangle$	FII, twist	C
	b12	r	π'	a	$\{\pi'\}\langle a \rangle$		C
	b13	z	π	a	$\{\pi\}\langle a \rangle$		C
2997 ribbons							
29973n Map4	1/ 2	π'	r	a	$\{r\}\langle a \rangle$		C
	5/ 1	z	π	a	$\{\pi\}\langle a \rangle$		A
	8/ 1	π	z	a	$\{z\}\langle a \rangle$	FII	A
	10/ 2	c	m	a	$\{m\}\langle a \rangle$		C
	10/ 3	z	π	a	$\{\pi\}\langle a \rangle$		C
	17/ 1	[20-21]	r, m	a, a+c	$\{r\}\langle a \rangle,$ $\{m\}\langle a \rangle, <$ $a+c>?$	twist	B
	25/ 1	z	π	a	$\{\pi\}\langle a \rangle$		C
	35/ 1	[20-21]	r, m	a, a+c	$\{r\}\langle a \rangle,$ $\{m\}\langle a \rangle, <$ $a+c>?$	twist	C
	37/ 1	c	m	a	$\{m\}\langle a \rangle$		B
	37/ 2	c	m	a	$\{m\}\langle a \rangle$		B
	37/ 3	c	m	a	$\{m\}\langle a \rangle$		B
	37/5	c	m	a	$\{m\}\langle a \rangle$		B
Large Map 29973n	b1	π	z	a	$\{z\}\langle a \rangle$	FII	A
	b2	π'	r	a	$\{r\}\langle a \rangle$		A
	31/1	r	π'	a	$\{\pi'\}\langle a \rangle$	FII	A
	31/2	m	c	a	$\{c\}\langle a \rangle$		A
	4	m	a	c	$\{a\}\langle c \rangle$		B
	5	π	z	a	$\{z\}\langle a \rangle$		B
D3							
30545n	1/ 1	r	π'	a	$\{\pi'\}\langle a \rangle$	FII	A
	1/ 3	π, r	z, π'	a	$\{z,$ $\{\pi'\}\langle a \rangle$	combi	A
	1/ 4	c	m	a	$\{m\}\langle a \rangle$		A
	2/ 1	a	m	c	$\{m\}\langle c \rangle$	FII	B
	2/ 2	m	a	c	$\{a\}\langle c \rangle$		B
	4/ 1	[11-23]	r, π'	a	$\{r+\pi'\}\langle a \rangle$	twist	A
	4/ 2	c	m	a	$\{m\}\langle a \rangle$	FII	A
	4/ 3	m	c	a	$\{c\}\langle a \rangle$		A
	5/ 1	a	m	c	$\{m\}\langle c \rangle$	FII	C
	5/ 2	[11-23], r	$\pi'+r, \pi'$	a	$\{r+\pi'\}\langle a \rangle,$ $\{\pi'\}\langle a \rangle$	twist, combi	C
	5/ 6	m, a	a, m	c	$\{a, m\}\langle c \rangle$	combi	C
	11/ 1	c	m	a	$\{m\}\langle a \rangle$		B
30545	2/ 1	m	c	a	$\{c\}\langle a \rangle$		C
	3/ 2	π'	r	a	$\{r\}\langle a \rangle$	FII	C
	4/ 1	π'	r	a	$\{r\}\langle a \rangle$		B

	6/ 1	π, r	π'	a	$\{\pi\}\langle a \rangle$		B
	7/ 1	r	π'	a	$\{\pi\}\langle a \rangle$		A
	8/ 1	r	π'	a	$\{\pi\}\langle a \rangle$	FII	C
	10/ 1	m	a	c	$\{a\}[c]$		C
D4							
30544	4/ 2	[11-22]	r+z	a	$\{r+z\}\langle a \rangle$	twist	C
	4/ 3	a	m	c	$\{m\}[c]$		C
	5/ 1	c	m	a	$\{m\}\langle a \rangle$	FII	A
	6/ 3	m	c	a	$(c)\langle a \rangle$		C
	6/ 4	[11-22]	r+z	a	$\{r+z\}\langle a \rangle$	twist	C
	7/ 1	m	a	c	$\{a\}[c]$		B
	8/ 1	[20-21], r, m	r+m, π', c	a	$\{r\}\langle a \rangle +$ $\{m\}\langle a \rangle,$ $\{\pi'\}\langle a \rangle,$ $(c)\langle a \rangle$	twist, combi	C
	8/ 2	a	m	c	$\{m\}[c]$		C
	11/ 1	c	m	a	$\{m\}\langle a \rangle$		A
	12/ 1	m	a	c	$\{a\}[c]$		C
	13/ 1	a	m	c	$\{m\}[c]$		C
	14/ 1	m	c	a	$(c)\langle a \rangle$		A
	15/ 2	ξ, π'	m, r	c+a, a	$\{m\}\langle c+a \rangle,$ $\{r\}\langle a \rangle$	twist, combi	B
	16/ 1	m	a	c	$\{a\}[c]$		C
	16/ 1	a	m	c	$\{m\}[c]$		C
	17/ 1	a	m	c	$\{m\}[c]$		C
	18	a	m	c	$\{m\}[c]$		B
	19	π'	r	a	$\{r\}\langle a \rangle$		B
	20	m	a	c	$\{a\}[c]$		B
	b21	[11-22]	r+z	a	$\{r+z\}\langle a \rangle$	twist, FII	B
	b22	[02-21]	z+m	a	$\{z\}\langle a \rangle +$ $\{m\}\langle a \rangle$	twist, FII	C
Matrix							
30544 Map2	1/1	z	π	a	$\{\pi\}\langle a \rangle$		C
	1/2	c	m	a	$\{m\}\langle a \rangle$		C
	1/3	[11-22]	r+z	a	$\{r+z\}\langle a \rangle$	twist	C
	3/1	r	π'	a	$\{\pi'\}\langle a \rangle$		B
	5/2	m	c	a	$(c)\langle a \rangle$		C
	5/3	π	z	a	$\{z\}\langle a \rangle$	FII	C
	6/1	m	a	c	$\{a\}[c]$	FII	C
	7/1	π'	r	a	$\{r\}\langle a \rangle$		B
	8/1	ξ	m	a+c	$\{m\}\langle a+c \rangle$		C
	8/2	[02-21]	z, m	a	$\{z\}\langle a \rangle +$ $\{m\}\langle a \rangle$	twist	C
	9/1	c	m	a	$\{m\}\langle a \rangle$		B
30544 large map							
	b1	π	z	a	$\{z\}\langle a \rangle$		B
	b2	π	z	a	$\{z\}\langle a \rangle$		A



Appendix Fig. 3: a) EBSD Maps displaying alkali feldspar; b) same maps displaying plagioclase (maps are represented in XZ section with X parallel to the horizontal and Z parallel to the vertical).



Appendix Fig. 4: EBSD Maps displaying alkali feldspar and plagioclase (maps are represented in XZ section with X parallel to the horizontal and Z parallel to the vertical; scale bars are 1 mm; in 30545 Map 7 - kfs and 29971n Map 1 - pl scale bars are 500 μ m).

Appendix Table 4: Results Boundary Trace Analysis of alkali feldspar (R II Ma: coincident rotation and misorientation axis, SP: Slip plane, SD: Slip direction, F II: Foliation (sub)parallel slip plane, (010) p: (010) plane perpendicular to the foliation; in individual cases multiple possible solutions are given).

Domain/ sample	Subset/ Boundary	R II Ma	SP	SD	Slip System	Comment
D1 A						
29972n Map6	2/ 1	[010]	(001)	[100]	(001)[100]	
	5/ 1	[012]	(110)	[1-12]	(110)[1-12]	
	6/ 1	[021]	(110)	[112], [-112]!	(110)[-112]	F II
	6/ 2	[101]	(1-1-1), (11-1)	[1-10, 110]	(1-1-1), (11-1)[1-10], [110]	F II
	7/ 1	[-21-1]	(001)	[110, 1-10]	[001][110], [1-10]	
	10/ 1	[001]	(110)	[1-12]	(110)[1-12]	
	11/ 2	[313]	(10-1)	[111], [1-11]	(10-1), [111], [1-11]	
	11/ 3	[111], [112]	(20-1)	[112], [1-12]	(20-1)[112], [1-12]	
	12/ 3	[001]	(010)	[101, 201]	(010)[101], [201]	
	13/ 1	[021], [112]	(110)	[1-12], [-112]!	(110)[1-12], [-112]	
	14/ 2	[021]	(20-1)	[112], [1-12]	(20-1)[112], [1-12]	F II
	14/ 3	[001]	(010)	[101], [201]	(010)[101], [201]	
29972n Map9	1/ 1	[112]	(11-1), (1-1-1)	[1-10], [110]	(11-1), (1-1-1)[1-10], [110]	
	2/ 1	[012]	(1-1-1), (11-1)	[1-10], [110]	(1-1-1), (11-1)[1-10], [110]	
	3/ 1	[111]	(001)	[100]	(001)[100]	
D1 L						
29971n D1fsp	1/ 1	[101]	(11-1), (1-1-1)	[1-10], [110]	(11-1)[1-10]	
	3/ 1	[021]	(001)	[100]	(001)[100]	
	4/ 2	[121], [010]	(20-1)	[102]	(20-1)[102]	
	6/ 1	[-10-1]	(110)	[1-12]	(110)[1-12]	
	7/ 3	[001]	(010)	[100]	(010)[100]	
29971n large map fsp	1/ 1	[121]	(001)	[100]	(001)[100]	
	2/ 1	[201]	(010)	[101]	(010)[101]	
	2/ 2	[-20-1]	(021)	[1-12]	[021][1-12]	
	3/ 1	[021]	(20-1)	[1-12]	(20-1)[1-12]	
	4/ 1	[-100]	(001)	[110], [1-10]	(001)[110], [1-10]	
	5/ 1	[-20-1]	(13-1)	[-112]	(13-1)[-112]	
	6/ 1	[112]	(1-20)	[001]	(1-20)[001]	F II

D2						
29972n Map7	4/ 1	[110]	(001)	[110, 1-10]	(001)[110], [1-10]	F II
	8/ 1	[-211]	(001)	[110], [1-10]	(001)[110], [1-10]	F II
	9/ 1	[112]	(10-1)	[111]	(10-1)[111]	F II
	10/ 1	[011]	(11-1)	[101]	(11-1)[101]	
	10/ 2	[-110]	(021)	[1-12]	(021)[1-12]	
	11/ 1	[-100]	(021), (001)	[1-12], [110], [1-10]	(021)[1-12], (001)[110], [1-10]	
	13/ 1	[001]	(010)	[100]	(010)[100]	F II
29972n Map 10	1/ 1	[-100]	(001)	[110], [1-10]	(001)[110], [1-10]	
	2/ 1	[101]	(1-1-1), (11-1)	[110], [1-10]	(1-1-1), (11-1)[110], [1-10]	
	3/ 1	[112]	(20-1)	[112, 1-12]	(201)[112], [1-12]	
	4/ 1	[-20-1]	(1-1-1), (10-1)	[110], [1-11]	(1-11)[110], (10-1)[1-11]	
	5/ 1	[-100]	(021)	[1-12]	(021)[1-12]	F II, (010) p
D3						
30545 Map 7	1/ 1	[112]	(1-1-1)	[110]	(1-1-1)[110]	
	2/ 2	[001]	(010)	[101, 201]	(010)[101], [201]	F II
	4/ 4	[-110]	(11-1)	[112]	(11-1)[112]	F II
	6/ 1	[201]	(021), (10-1)	[1-12], [111], [1-11]	(021)[1-12], (10-1)[111], [1-11]	(010) p
	8/ 1	[112]	(1-1-1)	[110]	(1-1-1)[110]	
	8/ 3	[010]	(001)	[100]	(001)[100]	
30545 large Map	1/ 1	[101]	(010)	[100]	(010)[100]	
	2/ 1	[001]	(010)	[100]	(010)[100]	
	3/ 1	[-20-1]	(010)	[001]	(010)[001]	
	4/ 1	[001]	(010)	[101]	(010)[101]	
	5/ 1	[101]	(1-1-1), (11-1)	[110], [1-10]	(1-1-1), (11-1)[110], [1-10]	
D4						
30544 Map 1	1/ 3	[-10-1]	(010)	[100], [201]	(010)[100], [201]	
	3/ 1	[012]	(110)	[1-12]	(110)[1-12]	F II
	3/ 2	[-10-1]	(010)	[201]	(010)[201]	
	6/ 1	[412], [-41-2], [201], [-20-1]	(021)	[1-12]	(021)[1-12]	(010) p
	7/ 2	[-20-1]	(010)	[001]	(010)[001]	F II

30544 Map 2	1/ 1	[021]	(20-1)	[102]	(20-1)[102]	F II
	2/ 1	[010]	(001)	[110], [1-10]	(001)[110], [1-10]	
	3/ 1	[-41-1]	(021)	[1-12]	(021)[1-12]	
	4/ 1	[-100]	(001)	[1-10]	(001)[1-10]	F II
	4/ 2	[001]	(110)	[1-12]	(110)[1-12]	
	7/ 1	[-20-1]	(010)	[001]	(010)[001]	
30544 large map	1/ 1	[-100]	(1-20)	[001]	(1-20)[001]	

Appendix Table 5: Results Boundary Trace Analysis in in plagioclase (R II Ma: coincident rotation and misorientation axis, R: Rotation axis, Ma: Misorientation axis, SP: Slip plane, SD: Slip direction, F II: Foliation (sub)parallel slip plane, (010) p: (010) plane perpendicular to the foliation; in individual cases multiple possible solutions are given).

Domain/ Sample	Subset/ Boundary	R II Ma	SP	SD	Slip System	Comment
D1 A						
29973n Map8	1/ 1	[101]	(13-1)	[-112]	(13-1)[-112]	
	2/ 1	[201]	(13-1)	[-112]	(13-1)[-112]	
	2/ 2	[201]	(010), (021)	[001], [1-12]	(010)[001], (021)[1-12]	
	3/ 1	[-1-10]	(10-1)	[1-11]	(10-1)[1-11]	
	3/ 2	[0-10]	(10-1)	[1-11]	(10-1)[1-11]	
	3/ 3	[111]	(20-1)	[1-12]	(20-1)[1-12]	
	5/ 2	[201]	(010)	[001]	(010)[001]	F II
	6/ 1	[-110]	(021)	[1-12]	(021)[1-12]	
	6/ 2	[-20-1]	(010)	[101]	(010)[101]	F II
	7/ 1	[-1-10]	(10-1)	[1-11]	(10-1)[1-11]	
	7/ 2	[-1-10]	(10-1)	[1-11]	(10-1)[1-11]	
	7/ 3	[-100]	(021)	[1-12]	(021)[1-12]	F II
	7/ 4	[111]	(10-1)	[1-11]	(10-1)[1-11]	
29971n Map1	1/ 2	[1-11]	(110)	[1-12]	(110)[1-12]	
	3/ 1	[-20-1]	(13-1)	[1-12]	(13-1)[1-12]	
	5/ 1	[101]	(010)	[100]	(010)[100]	
	6/ 1	[-100]	(010)	[101]	(010)[101]	
	6/ 2	[001]	(010)	[101]	(010)[101]	
D1 L						
29971n D1fsp	2/ 3	[-100]	(010)	[101]	(010)[101]	
	2/ 4	[112]	(1-20)	[001]	(1-20)[001]	
	3/ 1	[-1-10]	(010), (021)	[001], [1-12]	(010)[001], (021)[1-12]	(010) p
	1/ 2	[201]	(010)	[101]	(010)[101]	

29971n large map fsp	1/ 1	[001]	(010)	[101]	(010)[101]	
	2/ 1	[-100]	(021)	[1-12]	(021)[1-12]	
	3/ 1	[-100]	(010)	[001]	(010)[001]	
	4/ 1	[-100]	(010)	[001]	(010)[001]	F II
	5/ 1	[101]	(1-1-1)	[110]	(1-1-1)[110]	
	6/ 1	[101]	(1-1-1)	[110]	(1-1-1)[110]	
	7/ 1	[-100]	(010)	[001]	(010)[001]	
D3						
30544 large map	3/ 2	[-20-1]	(021)	[1-12]	(021)[1-12]	F II, (010) p
	3/ 3	[-100]	(021)	[1-12]	(021)[1-12]	(010) p
	3/ 1	[201]	(10-1)	[1-11]	(10-1)[1-11]	F II
	4/ 1	[001]	(110)	[1-12]	(110)[1-12]	
	6/ 1	[201]	(010)	[001]	(010)[001]	F II
	9/ 1	[001]	(010)	[201], [101]	(010)[201], [101]	
	9/ 2	[-100]	(021)	[1-12]	(021)[1-12]	(010) p
30545 large map	1/ 1	[-20-1]	(010)	[001]	(010)[001]	F II
	2/ 1	[-20-1]	(13-1)	[-112]	(13-1)[-112]	
	3/ 1	[-20-1]	(0219)	[1-12]	(021)[1-12]	(010) p
	3/ 2	[101]	(010)	[100]	(010)[100]	
D4						
30544 Map2	2/ 1	[-100]	(010), (021)	[101], [1-12]	(010)[101], (021)[1-12]	(010) p
	3/ 1	[201]	(021)	[1-12]	(021)[1-12]	(010) p
	3/ 2	[201]	(021)	[1-12]	(021)[1-12]	(010) p
	5/ 1	[100]	(010)	[001]	(010)[001]	
	5/ 3	[1-12]	(010)	[001]	(010)[001]	
	5/ 5	(010)	(20-1)	[1-12]	(20-1)[1-12]	F II
	7/ 1	[-1-10]	(20-1)	[1-12]	(20-1)[1-12]	
	8/ 1	[100]	(010)	[001]	(010)[001]	
	8/ 2	[001]	(010)	[201], [100]	(010)[201], [100]	
	9/ 1	[-100]	(001)	[110]	[001][110]	
30544 large Map	1/ 1	[100]	(010)	[001]	(010)[001]	

Appendix Table 6: Feldspar aggregate size (dp) and volume fraction (fp), Zener parameter (Z) and quartz grain size (D).

Sample/ domain	dp (μm) ^a	fp	Z (dp/fp)	D qtz (μm) ^a
D0				
25313	690	<0.01	492655	14535
25134	1460	0.01	98035	11694
D1				
2997-1n	10008	0.17	58884	15537
2997-5	6968	0.17	41555	12496
2997-6	2590	0.07	35691	13016
2997-2	5727	0.18	32277	10960
2997-3D1	3497	0.12	28452	12010
29974D1	5171	0.18	28006	8886
D2				
29976	2278	0.25	8987	2088
29972n	1869	0.19	9673	2626
2997-3D1	4524	0.20	22397	2725
29974D1	6779	0.26	25613	2484

^a area weighted mean size.

Erklärung zur Dissertation

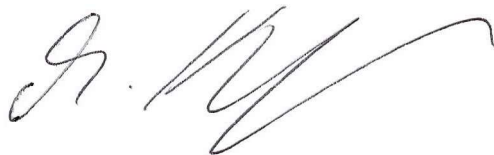
Gemäß der Promotionsordnung vom 02. Februar 2006 mit den Änderungen vom 10. Mai 2012, 16. Januar 2013 und 21. Februar 2014

Ich versichere, dass ich die von mir vorgelegte Dissertation selbstständig angefertigt, die benutzten Quellen und Hilfsmittel vollständig angegeben und die Stellen der Arbeit – einschließlich Tabellen, Karten und Abbildungen –, die anderen Werken im Wortlaut oder dem Sinn nach entnommen sind, in jedem Einzelfall als Entlehnung kenntlich gemacht habe; dass diese Dissertation noch keiner anderen Fakultät oder Universität zur Prüfung vorgelegen hat; dass sie – abgesehen von unten angegebenen Teilpublikationen – noch nicht veröffentlicht worden ist, sowie, dass ich eine solche Veröffentlichung vor Abschluss des Promotionsverfahrens nicht vornehmen werde.

Die Bestimmungen der Promotionsordnung sind mir bekannt. Die von mir vorgelegte Dissertation ist von Prof. Dr. Reiner Kleinschrodt betreut worden.

Teilpublikationen: keine

22.05.202

A handwritten signature in black ink, consisting of a stylized first letter 'G' followed by a series of loops and a long horizontal stroke extending to the right.